Engineering Broadband Response in Active and Passive Terahertz Metamaterials Using Planar and Multilayer Configurations

by

Bhagwat Singh Chouhan

A thesis submitted

in Partial Fulfilment of the Requirements for the Degree of

DOCTOR OF PHILOSOPHY

Department of Physics
Indian Institute of Technology Guwahati
Guwahati 781039, India.

February 2025

DECLARATION

The work presented in this thesis, entitled *"Engineering Broadband Response in Active and Passive Terahertz Metamaterials Using Planar and Multilayer Configurations"*, has been carried out by me under the supervision of **Prof. Gagan Kumar**, Department of Physics, Indian Institute of Technology Guwahati. No part of this thesis has been submitted elsewhere for the award of any other degree or qualification.

The research work described in this thesis was conducted during the period from **July 2020 to February 2024**. In keeping with the general practice of scientific reporting, appropriate acknowledgements have been made wherever the work is based on the findings of other investigations.

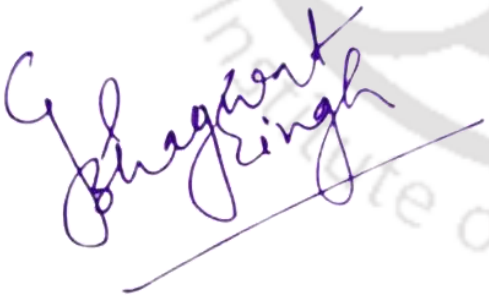

Bhagwat Singh Chouhan
Department of Physics
Indian Institute of Technology Guwahati
Guwahati-781039, Assam, India

Date: 04-02-2025

CERTIFICATE

This is to certify that the work presented in the thesis, entitled “Engineering Broadband Response in Active and Passive Terahertz Metamaterials Using Planar and Multilayer Configurations", by Mr. **Bhagwat Singh Chouhan,** a student of the Department of Physics, Indian Institute of Technology Guwahati, was carried out under my supervision and has not been submitted elsewhere for the award of any degree or qualification.

Prof. Gagan Kumar
Department of Physics
Indian Institute of Technology Guwahati
Guwahati-781039, Assam, India

Date: 04-02-2025

ACKNOWLEDGEMENT

As I look back on my entire journey at IIT Guwahati, I feel deep gratitude for the experiences, friendships, and challenges that have shaped my academic path. Writing this thesis is the result of years of dedication and determination, and I take this moment to express my sincere appreciation to those who have supported me along the way.

First and foremost, I extend my deepest gratitude to my supervisor, Prof. Gagan Kumar, for his constant support, patience, and encouragement throughout my Ph.D. journey. His guidance has been invaluable, always giving me the freedom to explore new ideas and make independent research decisions without hesitation. He never discouraged me from trying something different, and his trust in my abilities gave me the confidence to work autonomously and take ownership of my research. Because of his support, I always felt comfortable using lab resources and experimenting with new approaches, which played a crucial role in shaping my growth as a researcher. Beyond academics, he taught me many important life skills, including managing responsibilities, thinking critically, and staying motivated. He often said that a Ph.D. is not just about research but also about becoming a better professional and individual, a lesson I now truly understand as I reflect on these four years. His expertise in terahertz metamaterials and keen attention to detail helped me refine my work, making it stronger and more impactful. More than anything, his trust, kindness, and mentorship made my Ph.D. journey smooth and fulfilling. I will always be grateful for his guidance, which has shaped not only my research but also my confidence in facing challenges.

I am also deeply thankful to my doctoral committee members, whose valuable insights and critical evaluations have enriched this research. I extend my appreciation to Prof. Amarendra Kumar Sarma, Prof. Pravat Kumar Giri, and Dr. Mahima Arrawatia for their thoughtful feedback and encouragement, which greatly enhanced the quality of this thesis. Their constructive suggestions during my progress reviews played a crucial role in refining my ideas and strengthening my research.

I am grateful to my academic collaborators, whose support and resources significantly contributed to the success of my research. I acknowledge Prof. P. K. Giri (Department of Physics, IIT Guwahati), Dr. Anuraj Panwar (Department of Physics and Materials Science and Engineering, JIIT, Uttar Pradesh, India), and Amir Ahmad (College of Information Technology, United Arab Emirates University, UAE) for their valuable discussions and collaborative efforts.

I would like to express my sincere appreciation to the Center for Nanotechnology at IIT Guwahati for providing the cleanroom facilities, where I completed most of my fabrication work. I also thank the Department of Physics for allowing me to use the profilometer and UV spectroscopy. I am grateful to the former and current Head of the Department, faculty members, and staff for their support at various stages of my academic career. A special thanks to Prof. Bosanta R. Boruah, the current Head of the Department, for his support and accessibility in addressing academic-related matters.

I am deeply grateful to my seniors and colleagues, whose support and discussions have played an important role in my academic career. I especially thank Dr. S. Jagan Mohan Rao, who helped me choose the right supervisor. It was one of the best decisions I made during my Ph.D. I sincerely appreciate the guidance and support of Dr. Rakesh Sarkar, Dr. Dhriti Maurya, and Dr. Angana Bhattacharya, especially during the early phase of my research. I am also thankful to my friend and guru Bhai Bhairov K. Bhowmik, for his friendship, encouragement, and motivation. Working with him, spending time in the lab, and exploring Guwahati together made

this journey more enjoyable, and I will always cherish those memories. I also extend my gratitude to my juniors, Anshul Bhardwaj, Chandan Kumar, Lavi Kumar Vaswani, Asit Das, Harshita and Abhijit Das, for their support and cooperation. A special thanks to Rohith K. M., who, despite being my junior, has taught me many things. Our discussions helped me deepen my understanding of the field and broaden my knowledge. I am also grateful to my senior postdoctoral researcher, Dr. Arindom Phukan, for the valuable time we shared, even in a short period, which left a lasting impact on me.

I would like to thank my friends, whom I was fortunate to gain during this journey. After spending four years together, I can confidently say that I have found the best of friends with whom I have shared countless moments, both within and beyond academics. Without them, this journey would not have been as smooth and fulfilling. I cannot recall a single challenge where they were not by my side, offering their constant support. They are my extended family and strongest support system. I am deeply grateful to Swati, Sanu, Madan, Debraj, Dinesh, Sirendu, Himanshu, and Shilpi for their constant support, encouragement, and love throughout this journey.

I would also like to thank my childhood friends, who have always been there for me without ever needing to understand what I do. They are simply my friends, regardless of my work or achievements. A part of who I am today has been shaped by them, and I deeply value their friendship and character. I especially remember my childhood friend, the late Rahul, who sadly lost his life during the COVID-19 pandemic. His untimely passing is a constant reminder that life should not always be taken too seriously. I am also grateful to Rituraj, Sachin, Jeetendra, Shivshant, Yogesh, and Saurabh, not for any particular reason but simply because they are my friends, without conditions or expectations. A special thanks to Sahel Dey, my friend since M.Sc., who unknowingly taught me the value of hard work and perseverance. I have learned many things from him, even without him realizing it. I would also like to thank Ankit for his support during my M.Sc. Without his help, I might not have been able to complete my degree successfully. I also thank Manish for being a wonderful human being and my first-ever roommate in the hostel.

Finally, my deepest gratitude goes to my joint family, whose love and support have been an inseparable part of my life. Their contribution to my journey cannot be fully expressed in words, as I am not just a part of their family but a reflection of their values and guidance. Without them, this journey would not have been possible. Their unconditional love, patience, and sacrifices have been the foundation of my success. Their encouragement and selfless support allowed me to pursue my dreams without distractions. I bow down with deep respect to my grandfather, the late Babba, who has given me a genetic legacy that I carry forward with pride. His wisdom and presence continue to inspire me every day. I also express my heartfelt gratitude to Sadhguru, whose teachings in yoga and meditation have brought me clarity, strength, and peace. His guidance has been a source of inner stability, making this journey not only successful but also fulfilling.

This journey has been an incredible one, made meaningful by the constant support of my mentors, collaborators, colleagues, friends, and family. To each of them, I extend my sincerest thanks and appreciation.

(Bhagwat Singh Chouhan)

LIST OF PUBLICATIONS AND CONFERENCES ATTENDED

List of publications from the thesis work

1. **B. S. Chouhan**, B. Barman, L. K. Vaswani, A. Panwar, and G. Kumar, "Broadening of resonance with the bending of strongly coupled strip resonators in a planar terahertz metamaterial," *J. Lightwave Technol.*, vol. 42, no. 9, pp. 3283-3289, May 2024.
2. **B. S. Chouhan**, N. Acharyya, A. Panwar, D. R. Chowdhury, and G. Kumar, "Multi-stacked polarization-insensitive broadband terahertz metamaterial," *J. Appl. Phys.*, vol. 135, 173103, 2024.
3. **B. S. Chouhan**, A. Nawaz, A. Das, R. K. M, A. Ahmad, and G. Kumar, "Machine learning-driven ultra-broadband terahertz multilayer metamaterial," *J. Lightwave Technol*.
4. **B. S. Chouhan**, S. Ghosal, R. K. M, S. Ray, P. K. Giri, and G. Kumar, "Ultra-broadband actively tunable terahertz modulator based on multi-stacked metamaterial," *Scientific Report*
5. **B. S. Chouhan**, S. Ghosal, L. K. Vaswani, R. K. M, A. Panwar, P. K. Giri, and G. Kumar, "Multistacked toroidal metamaterial for ultra-broadband terahertz modulation," ,**under review**.

List of publications other than thesis work

6. A. Bhattacharya, **B. S. Chouhan**, K. Sharma, S. M. Halawani, A. Ahmad, and G. Kumar, "Terahertz binary computing in a coupled toroidal metasurface," *Sci. Rep.*, vol. 14, Article no. 8721, 2024.
7. L. K. Vaswani, **B. S. Chouhan**, A. Bhattacharya, A. Panwar, and G. Kumar, "Single and dual-band electromagnetically induced transparency in a strongly near-field coupled planar toroidal terahertz metamaterial," *Opt. Laser Technol.*, vol. 176, 111006, Sep. 2024.
8. L. K. Vaswani, **B. S. Chouhan**, A. Panwar, and G. Kumar, "Electromagnetically induced transparency in a strongly coupled orthogonal polarization-insensitive planar terahertz metamaterial," *J. Phys. D: Appl. Phys.*, vol. 57, 075103, 2024.
9. A. Bhattacharya, **B. S. Chouhan**, R. Singh, B. K. Bhowmik, and G. Kumar, "Polarization-independent lattice-coupled terahertz toroidal excitation," *J. Phys. D: Appl. Phys.*, vol. 56, 415101, 2023.
10. K. M. Dhriti, A. K. Chowdhary, **B. S. Chouhan**, D. Sikdar, and G. Kumar, "Tunable terahertz absorption modulation in graphene nanoribbon-assisted dielectric metamaterial," *J. Phys. D: Appl. Phys.*, vol. 55, no. 28, 2022.

List of Conference publications

1. **B. S. Chouhan**, "Modulating broadband terahertz in a graphene-assisted dielectric Metamaterial," *Workshop on Recent Advances in Photonics (WRAP)-2022*, published, DOI: 10.1109/WRAP54064.2022.9758283.

2. **B. S. Chouhan**, "Graphene-Dielectric based Tunable Terahertz Polarization Insensitive Modulator," *IEEE Photonics Conference (IPC)-2022*, published, DOI: 10.1109/IPC53466.2022.9975603.
3. **B. S. Chouhan**, "Metamaterial-based Terahertz broadband active modulator using VO2-resonators for the 6G communication systems," *Research and Industrial Conclave (RIC-2024)*, accepted, DOI: **Yet to generate.**
4. **B. S. Chouhan**, "Electromagnetically Induced Transparency in Broadside Coupled Toroidal Metasurfaces," *IEEE Workshop on Recent Advances in Photonics (WRAP-23)*, published, DOI: 10.1109/WRAP59682.2023.10712997.
5. **B. S. Chouhan**, "Polarization-Insensitive Ultra-Broadband Terahertz Metamaterials for 6G Applications," *The 14th International Conference on Metamaterials, Photonic Crystals and Plasmonics (META-2024)*, published, ISSN: 2429-1390.

List of Conferences, Symposiums, and Events attended during the thesis duration:

1. International Conference on "Frontiers in Terahertz Technology and Applications (**FTTA-2021**)" – 2021
2. **IEEE WRAP 2022**: IEEE Workshop on Recent Advances in Photonics – 2022
3. **IEEE Photonics Conference (IPC)-2022** – 2022
4. Research and Industrial Conclave Integration (**RIC**) 2022, IIT Guwahati – 2022
5. The Indian Nanoelectronics Users Program (**INUP**), IIT Guwahati 2022 – 2022
6. **ICTP Winter College** on Optics: Terahertz Optics and Photonics (**ICTP-2023**) – 2023
7. The Indo-French Conference on Photonics and Metamaterials (**IFCFPM - 2023**) – 2023
8. Frontier in Optics & Terahertz Photonics (**FiOTP-2023**) – 2023
9. International Conference on Advanced Nanomaterials & Nanotechnology (Centre for Nanotechnology, IIT-Guwahati, **ICANN-2023**) – 2023
10. **IEEE Sensors Winter School 2023** – 2023
11. India Semiconductor and Packaging Ecosystem Conference (**ISPEC**)-2024 – 2024
12. Frontier in Optics & Terahertz Photonics (**FiOTP-2024**) – 2024
13. Research and Industrial Conclave Integration (**RIC**) 2022, IIT Guwahati – 2024
14. **INUP** Users' Meet, Bombay, August 10, 2024 – 2024
15. 14th International Conference on Metamaterials, Photonic Crystals and Plasmonics (**META-2024**) – 2024
16. Workshop on Advancements and Applications of Analytical Instruments (**AAAI-2024**) – 2024
17. 7th Annual Conference on Quantum Condensed Matter (**QMAT-2024**)-2024

LIST OF PROFESSIONAL RECOGNITION, AWARDS, AND ACHIEVEMENTS

1. **Best Poster Award**, International Conference on "Frontiers in Terahertz Technology and Applications (**FTTA-2021**)" – 2021
2. **Best Poster Award**, **IEEE WRAP 2022**: IEEE Workshop on Recent Advances in Photonics – 2022
3. **First Prize**, **INUP-HACKATHONS** 5G & 6G Technology Hackathon – 2023

LIST OF PATENT PUBLICATION

1. **Title:** An ultra-broadband actively tunable terahertz modulator based on multi-stacked metamaterial and a method of preparation.

Application no.: **202431065241**

Status: First examination.

ABSTRACT

The terahertz (THz) region of the electromagnetic spectrum, spanning frequencies between the microwave and infrared domains, represents a promising frontier for advanced technologies, including high-speed communication, security screening, and medical imaging. Metamaterials, with their engineered subwavelength features, offer tailored electromagnetic properties beyond the capabilities of conventional materials. While narrowband metamaterials have been extensively studied for applications such as high-Q factor filtering, the growing demand for versatile and high-performance THz devices has driven the development of broadband designs. These designs overcome the limitations of narrowband structures by dynamically controlling THz waves across a wide frequency range, making them critical for spectroscopy, imaging, and next-generation wireless communication.

This thesis explores innovative approaches for designing broadband THz metamaterials, focusing on planar and multistacked resonator-based configurations. Researchers have developed planar metamaterials incorporating coupled resonators, symmetrically and asymmetrically paired resonators, and highly radiative metallic resonators. To further enhance the terahertz bandwidth using planar metamaterials, a novel bending-strip resonator-based planar metamaterial was developed. This structure exhibited significant resonance broadening, achieving a 350 GHz bandwidth through strong coupling between closely spaced resonators. While planar metamaterials offer a key advantage due to their ease of fabrication further improvements in planar designs experienced limitations, as increasing the density of resonators introduced trade-offs in resonance strength due to coupling effects and reduced resonator efficiency at specific frequencies. To overcome these challenges, multistacked resonator-based metamaterials were explored to achieve even greater bandwidth enhancement. A three-layered metamaterial design was developed, achieving a 500 GHz bandwidth by superimposing the individual resonances of closely stacked resonator layers. These broadband responses are crucial for communication and sensing applications, enabling high-performance THz technologies.

Active tunability is another critical feature of broadband THz metamaterial, enabling dynamic functionalities required for advanced modulators and filters. To achieve this, phase-transition semiconductors such as vanadium dioxide (VO_2) were integrated into multistacked metamaterials. This hybrid design combines broadband metamaterial structures with VO_2 layers, enabling tunable modulation. A novel transfer-and-peel-off fabrication method was developed to protect VO_2 films during processing, ensuring reliable band-pass filter functionality. These hybrid metamaterials exhibited an actively tunable full-width at half-maximum (FWHM) of 1.02 THz and a modulation depth exceeding 55% when the temperature increased from room temperature to 80°C. Additionally, toroidally excited multistacked metamaterials achieved tunable transitions from band-reject filters to broadband reflectors through temperature-driven active modulation, demonstrating their potential for advanced THz devices.

Despite these advancements, the design and fabrication of metamaterials remain challenging due to the complex interactions of subwavelength structures with electromagnetic waves. Traditional design approaches, which rely on computational simulations and extensive trial-and-error processes, are time-intensive. To address this, machine learning techniques were employed to accelerate design and optimization. Supervised learning algorithms, including random forests, XGBoost, and neural networks, were used to predict and refine electromagnetic responses with high accuracy, significantly reducing the reliance on time-consuming simulations and enabling faster innovation.

This thesis presents a comprehensive framework for broadband THz metamaterials, including actively tunable designs for real-time control of device performance. By integrating advanced fabrication methods and machine learning optimization, these innovations bridge the "terahertz gap" and establish a foundation for transformative applications in communication, sensing, and imaging, marking significant progress toward next-generation THz technologies.

LIST OF FIGURES

the first fundamental resonance, which arises from the circular currents flowing in the metallic SRRs. "DP1," "DP2," "DP3," and "DP4" refer to the dipolar resonances that occur after splitting.

- **Figure 1.12**: (a) Photomicrograph of the fabricated dual symmetrical split-ring resonator (SRR) sample. The unit cell of the metamaterial is highlighted in the white-edged box, with an inset showing the simulated SRRs along with the polarization of the incident wave. (b) Simulated transmission (in decibels) of the dual-band electric metamaterial is depicted by the solid line, while the individual symmetrical SRRs are represented by the dashed lines.
- **Figure 1.13**: (a) Geometric design of fractal metamaterial. (b) Transmission amplitude as the fractal level increases. (c) Transmission amplitude as the line width of the fractal resonance changes.
- **Figure 1.14**: Pictorial representation of charge and current distributions creating (a) electric dipole, (b) magnetic dipole, (c), (d) polar and axial toroidal dipole moments.
- **Figure 1.15**: (a) and (b) shows a schematic of the proposed metamaterial array with y-polarized terahertz radiation incident normally on the surface. (c) and (d) illustrate the surface current profile of the metamaterial at resonance. The arrows indicate the direction of the surface current flow. Magnetic moments are oriented out of the plane on the right-hand side and into the plane on the left-hand side of the metamolecule. Toroidal dipole excitation, labelled 'T', is aligned along the negative y-direction.
- **Figure 1.16**: Classification of metamaterials based on coupling effects. The diagram illustrates the transition from no coupling, where the average effect dominates (meta-gas), to strong coupling, which induces hybridization effects, leading to the formation of meta-molecules, meta-chains, and meta-crystals.
- **Figure 1.17**: (a) Structure of a magnetic dimer; (b) Equivalent LC circuit; (c) Metamaterial made of identical dimer elements.
- **Figure 1.18**: (a) Schematic of a neural network model showcasing forward design (input to output) and inverse design (output to input) through hidden layers. (b) Venn diagram illustrating the relationship between Artificial Intelligence (AI), Machine Learning (ML), Deep Learning (DL), and Data Science.
- **Figure 1.19**: Thesis organization chart outlining the progression of research on terahertz broadband metamaterials.
- **Figure 2.1**: (a) Trade-off between accuracy and speed: A good mesh achieves a good compromise between simulation speed and accuracy. (b) To ensure that the simulation is accurate across all frequencies of interest, the mesh needs to be fine enough to accurately represent the shortest wavelength in the simulation (at least 10 meshes per wavelength).
- **Figure 2.2**: Schematic showing the process for THz time-domain spectroscopy (THz-TDS) setup for transmission measurements. It details the fiber-coupled photoconductive antenna setup and sample positioning between parabolic mirrors.
- **Figure 2.3**: Schematic diagram of the fabrication steps performed to obtain a single-layer metamaterial structure. This includes cleaning, metallization, surface preparation, and etching stages.
- **Figure 2.4**: Flowchart illustrating the systematic fabrication process used to create the

multilayered metamaterial, from the preparation of the substrate to the deposition and patterning of the resonator layers.

- **Figure 2.5**: Comparison of the simulated and experimentally measured transmission spectra for the designed metamaterial with various spacer thicknesses.
- **Figure 2.6**: A graphical representation of the THz-TDS signal processing steps, from raw time-domain data to frequency-domain conversion using Fourier transform.
- **Figure 2.7**: Simulation setup for multi-layered metamaterial structures showing the alignment of the resonators in the design.
- **Figure 2.8**: Plot showing the calculated FWHM values as a function of polyimide spacer thickness, illustrating how the thickness influences the bandwidth of the metamaterial's transmission response.
- **Figure 2.9**: Optical path of the terahertz beam in the terahertz TDS for the sample measurement. For the reference measurement, the VO_2 thin film of the thickness 'd' will be replaced by the air medium.
- **Figure 2.10**: (a) and (c) Real and imaginary parts of the refractive index. (b) Real and imaginary parts of the conductivity of the VO_2 thin film. (d) The thickness of the VO_2 thin film was measured using a profilometer, and the inset FESEM image showing the cross-section view also confirms the approximate thickness of 1.5 μm.
- **Figure 3.1**: Depicts the design of a bending strip resonator-based metamaterial. The inset figure shows the unit cell of the metamaterial. The metamaterial consists of three strip resonators, two of which are bending at angles $\theta1 = 50°$ and $\theta2 = 8°$. The lengths of the resonators are L1 = 50 μm, L2 = 50 μm, and L3 = 52 μm, respectively. The width (w) of each resonator, the separation between two resonators, and the periodicity of the metamaterial are given as w = 5 μm, 2.5 μm, and 68 μm respectively.
- **Figure 3.2**: Depicts the unit cell and corresponding simulated transmission amplitude with respect to terahertz frequency. For a two resonator-based MM, the optimized angle (where the FWHM and RBW are maximum) is $\theta1 = 50°$ and for a three resonator-based MM, the optimized angle $\theta2=8°$ (keeping the $\theta1 = 50°$ fixed).
- **Figure 3.3**: Transmission spectra for different configurations of strip resonators, showing how the bending of the strips influences the overall bandwidth and transmission characteristics of the metamaterial.
- **Figure 3.4**: Experimental setup for fabricating and testing the bending strip resonator metamaterial. It shows the alignment of the resonators and the arrangement of the sample for THz-TDS measurements.
- **Figure 3.5**: Electric field distribution in the near field for various resonators at selected frequencies, highlighting the coupling mechanism between the resonators in the planar metamaterial configuration.
- **Figure 3.6**: A comparison of simulated and experimental results for the bending resonators, showing the effect of strip bending on the transmission spectra, including changes in resonance width and peak position.
- **Figure 3.7**: (a) Transmission amplitude as a function of THz frequency for various separation distances (d2). As the separation distance changes, the two merged resonances gradually separate, illustrating the decoupling of the resonators. (b) Transmission response for the three resonators, showing how increased separation

between them leads to distinct resonance peaks.

- **Figure 3.8**: Contour plots showing the coupling effect between the resonators in double and triple-strip-based metamaterials. As the separation between the resonators increases, the resonance frequencies move further apart from each other.
- **Figure 3.9**: (a) and (b) The coupling strength between the resonators as the separation between resonators and bending angle θ1 changes for two harmonic oscillator systems. (c) and (d) Shows the change in coupling strength as the separation distance between the resonators and bending angle θ1 changes, with θ2 fixed at 50°.
- **Figure 3.10**: Damping rates with respect to the separation distance between resonators and bending angles for the two and three-resonators-based metamaterial. (a) and (b) Show the variation of damping rates γ_1 and γ_2 as the separation between resonators and bending angle increases for the two-strip model. (c) and (d) Represent the variation of γ_1, γ_2, and γ_3 for the three-resonator configuration as separation and bending angle (θ2) increase.
- **Figure 4.1**: Schematic diagram of the designed hybrid metamaterial structure and the corresponding cross-sectional view for fabrication. The image shows the use of multiple layers of polyimide spacers and metallic resonators stacked to achieve broadband terahertz transmission.
- **Figure 4.2**: (a) and (b) Transmission spectra for different resonator configurations, demonstrating how changes in the number of stacked layers affect the transmission characteristics and bandwidth.
- **Figure 4.3**: Field distribution at the resonance frequencies for the metamaterial design, showcasing the contribution of individual resonators to the overall transmission response.
- **Figure 4.4**: (a) Transmission spectrum with respect to the thickness of the spacer. The optimized thickness of the spacer is between 40 μm to 55 μm. (b) For the fabrication, the thickness of the spacer, t=40 μm is taken since the FWHM at this thickness is relatively higher, and the transmission band is reasonably flat compared to other thicknesses of the spacer. (c) Transmission spectrum with respect to the relative positions of the resonators. Each resonator translates with small distances from the center of the metamaterial. Random combinations of translation distances of the resonators have been chosen and compared with the perpendicularly aligned resonator. The transmission amplitude is independent of the position of the resonators.
- **Figure 4.5**: The cross-sectional plane of field distribution (along the x-z plane, cuts through the center of resonators) and the front view of the metamaterial. Field distribution at three frequencies, 0.79 THz, 0.95 THz, and 1.35 THz plotted to realize coupling between the resonators.
- **Figure 4.6**: The simulated transmission spectra for different metamaterial configurations under varying environmental conditions, showing how the designed metamaterial responds to changes in temperature and external excitation.
- **Figure 5.1.1**: (a) Schematic of the multi-stacking and peel-off process of the metamaterial. (b) Transfer of the flexible metamaterial onto a VO_2 thin film on quartz, with the terahertz characterization scheme of the final MM. (c) Images of the flexible metamaterial, the peel-off process, and the fabricated sample.
- **Figure 5.1.2**: (a) FESEM image of VO_2 thin film surface morphology; insets show

zoomed and cross-sectional views, with thickness calculated as 1.5 µm. (b) Real and imaginary components of conductivity fitted using the Lorentz-Drude model. (c) Temperature-dependent Raman data revealing the phase transition behaviour of the VO_2 thin film. (d) Plasma frequency and relaxation time from Drude-Lorentz fitting.

- **Figure 5.1.3**: (a) Simulated, theoretically calculated, and experimentally measured transmission characteristics for a flexible MM, alongside their schematic and fabricated sample image. (b) VO_2 thin film, deposited on the quartz substrate, where the transmission amplitude decreases as the temperature changes from 50°C to 90°C. (c) Illustration of the multi-stacked MM integrated with the VO_2 thin film and transmission modulation w.r.t change in temperature.
- **Figure 5.1.4**: (a) Electric field distributions at four frequencies: F1 = 0.24 THz, F2 = 1.05 THz, F3 = 1.34 THz, and F4 = 1.90 THz. (b) Cross-sectional plane of the field distribution (along the x-z plane cutting through the edge of the resonators). (c–f) Side view of the MM and field distributions of the excited resonators at the four frequencies, illustrating coupling between the resonators.
- **Figure 5.1.5**: (a, b) Simulated and circuit-modeled transmission amplitudes for VO_2 in its dielectric (monoclinic) and metallic (tetragonal) phases, respectively, including their circuit representations. (c) Unit cell MM with its equivalent lumped circuital model. (d) Circuital model of the multistacked MM without the VO_2 layer, and (e) its corresponding simulated and calculated transmission amplitude. (f, h) Equivalent circuit representations of the multistacked MM when VO_2 is in the dielectric and metallic phases, respectively. (g, i) Corresponding transmission amplitudes fitted with circuit theory for the dielectric (DP) and metallic phases (MP).
- **Figure 5.2.1**: (a) and (b) Transmission spectra of the hybrid VO_2-based metamaterial, with and without phase transition of VO_2 at different temperatures. (c) Schematic of the VO_2-based hybrid metamaterial structure.
- **Figure 5.2.2**: (a) Cross-sectional FESEM image of the VO_2 thin film showing phase transition at different temperatures. (b) Temperature dependence of the transmission spectrum measured using THz-TDS, illustrating significant variation between the insulating and metallic phases of VO_2.
- **Figure 5.2.3**: (a) and (b) Multipolar analysis for single and multi-stacked configurations over the simulated frequency range, showing the dominance of toroidal dipolar excitation over electric and magnetic dipolar contributions. The red, black, and green curves represent power radiated by electric, toroidal, and magnetic dipoles, respectively.
- **Figure 5.2.4**: (a) Transmission response and electric field distribution for a single-layer toroidal resonator at the fundamental frequency $f=f_0$. (b) Transmission response and electric field distribution for a double-layer configuration at resonance frequencies $f=f_1$ and $f=f_2$. (c) Comparison of the scattering power of the single and multi-layered toroidal metamaterials.
- **Figure 5.2.5**: (a) Optical zoomed micrograph of the VO_2 film, with an inset showing a cross-sectional FESEM image indicating a thickness of 1.5 µm. (b) Raman spectra of the VO_2 film highlighting phase transition peaks. (c) Temperature-dependent transmission amplitudes extracted using THz-TDS. (d) Complex conductivity with respect to the variation of different temperatures.
- **Figure 5.2.6**: (a, c) Simulated transmission amplitude modulation for single and

double-layered metamaterials, respectively. (b, d) The corresponding experimentally measured transmission amplitude modulation. The graphs depict the temperature-dependent modulation, where an increase in temperature from 30°C to 120°C transforms the band-reject transmission filter into a reflector.

- **Figure 5.2.7**: Temperature-dependent transition of the band-reject filter into a broadband reflector. (a) Transmission response of the multistacked MM at low temperature behaving as a band-reject filter. (b) Transmission amplitude at higher temperature behaves as a broadband reflector.
- **Figure 6.1**: (a) Schematic illustration of the structure and working of a metamaterial. (b) Representation of how machine learning models predict the transmission response based on structural parameters of the metamaterial.
- **Figure 6.2**: (a) Comparison of transmission spectra with 100 data points (dashed line) and 1000 data points (green solid line). The negligible change justifies using 100 data points for output. (b) Transmission amplitude spectrum with each point (x, y) representing frequency and corresponding transmission amplitude. Only the y-values are used to form a 1-D array for the output data.
- **Figure 6.3**: (a) and (b) Verification of the forward method using two random test datasets, Data Set (1) and Data Set (2), tested with NN, RF, SVR, XGBoost, and RR methods. The bar charts represent input structural parameters (d1, d2, d3, d4, l1, l2, l3), and the plots compare the corresponding output transmission amplitudes. The dashed red line shows the predicted transmission from all models, while the green solid line represents the original transmission amplitude from the CST simulation.
- **Figure 6.4**: (a) and (b) Verification of the inverse method using two randomly selected test datasets. The transmission amplitude spectrum (100 data points) is taken as input, while the 7 structural parameters (d1, d2, d3, d4, l1, l2, l3) are the output. The green chart bars represent the predicted structural parameters, and the red chart bars represent the original parameters from the CST simulation. Additionally, the transmission amplitude from CST simulation using the predicted parameters is compared with the original transmission amplitude.
- **Figure 6.5**: Illustration of the electric field distribution at different resonances: (a) field resulting from a single resonator, (b) and (c) field distribution caused by double and triple resonators based on metamaterials (MM). The single resonance is attributed to dipole interaction in the single straight resonators, while the merging of two or three resonances (broadening of resonance) is a result of coupling between the two or three resonators.
- **Figure 6.6**: Illustration of the hybridization scheme of plasmon modes in multistacked metamaterials. The z-components of the electric field distributions for TE-polarized light are shown at four frequencies: f1 = 0.90 THz, f2 = 0.90 THz, f+ = 0.96 THz, and f- = 0.81 THz. The antisymmetric mode (low-energy) and symmetric mode (high-frequency) arise from in-phase and out-of-phase charge oscillations, respectively.
- **Figure 6.7**: (a) Electric field distribution due to the bottom resonator. (b) Electric field distribution due to the top resonator. (c) Electric field distribution due to multistacked resonators. The individual resonators (hexagonal or cross) have a resonance dip at f0 = 0.90 THz. When stacked (multistacked configuration), this dip splits into two resonances (f- and f+), broadening the transmission amplitude. The coupling between the resonators hybridizes the single mode into two plasmon modes.

- **Figure A1:** (a) Schematic diagram of the CVD setup for the synthesis of VO_2 thin films. (b) Raman spectrum of as-grown VO_2 thin films. (c) XRD pattern of the same.
- **Figure A2:** (a) Transmission spectrum with respect to the thickness of the spacer, highlighting the optimized spacer thickness of 50 μm. (b) FWHM of multistacked MM w.r.t spacer thickness. (c) Transmission spectrum with respect to the relative positions of the resonators. Each resonator is shifted by small distances from the center of the metamaterial's resonator, indicating that the transmission amplitude is largely independent of the resonators' positions. (d) A 3D view of the resonators shifted with respect to the center of the resonators, visually illustrating the experimental setup and findings.
- **Figure A3:** Simulated and experimental terahertz transmission of hybrid multi-stacked metamaterial samples. (a, b) Sample (1) with varying VO_2 conductivity and temperature. (c, d) Sample (2) with improved spacer thickness control, showing better agreement between simulation and experiment.

Contents

Chapter 1: Introduction

1.1 Terahertz Radiation (THz)

The electromagnetic spectrum has been a driving force behind numerous technological advancements that have transformed our lives. For example, radio waves have enabled global communication networks and broadcasting[1, 2], microwaves have powered wireless data transmission and radar systems[3, 4], infrared radiation has found applications in remote sensing and thermal imaging[5, 6], and visible light is fundamental to everything from photography to fibre-optic communication[7, 8]. Meanwhile, ultraviolet radiation plays a crucial role in sterilization and medical imaging, X-rays are indispensable in medical diagnostics and security scanning, and gamma rays are used in cancer treatment[9] and astrophysical research. Each region of the spectrum has been harnessed for unique applications, contributing to advancements in science, medicine, communications, and industry, enhancing our understanding of the universe and improving the quality of life. However, one region within this spectrum, the THz band, situated between the domains of electronics and photonics, remained largely unexplored for many years and is generally known as the "terahertz gap[10-13]." This terahertz gap emerged primarily due to the lack of natural materials capable of effectively interacting with THz frequencies. At lower frequencies, where free electron motion governs electronic devices, the output power of electromagnetic waves decreases as frequency increases due to factors such as the carrier saturation velocity, typically around 10^5 m/s, and the maximum electric field a device can support before breaking down. As frequencies

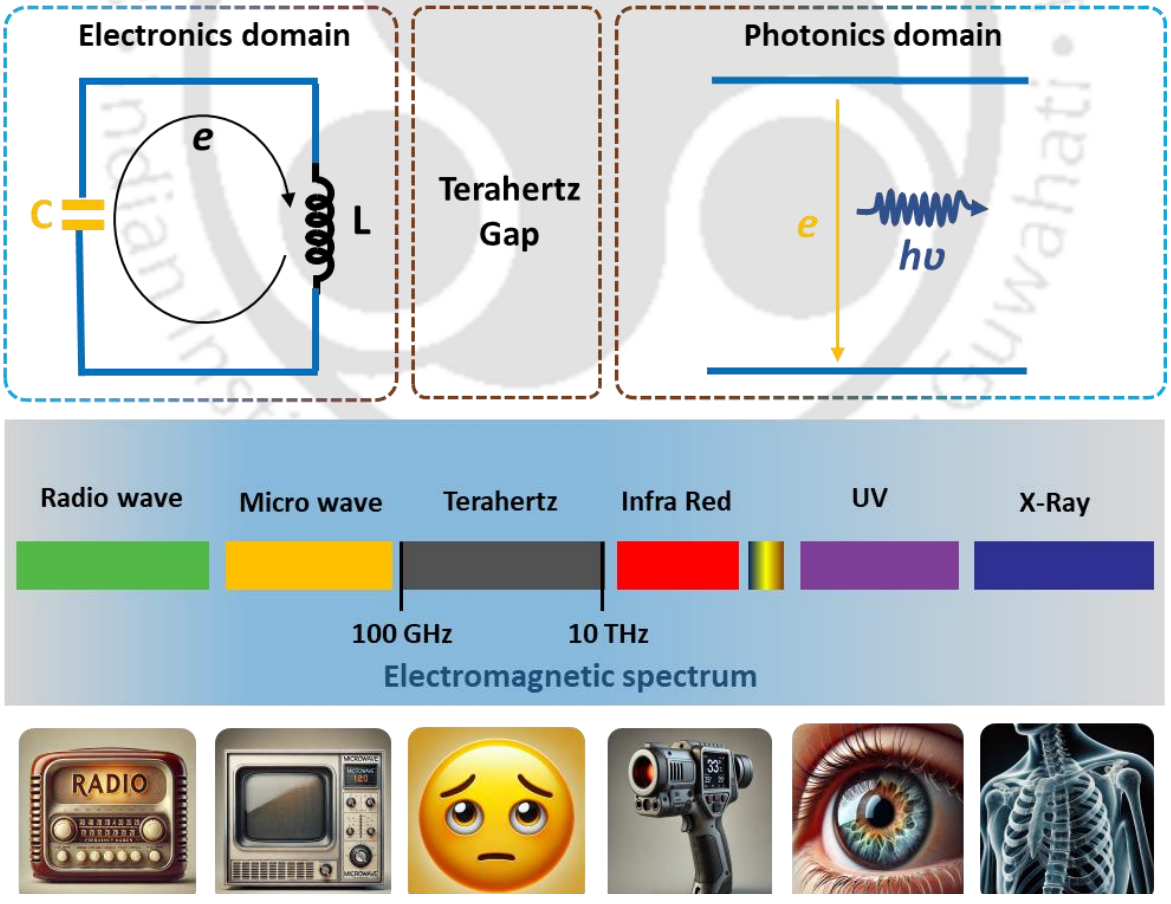

Figure 1.1: The figure depicts the position of the terahertz (THz) band (100 GHz–10 THz) within the electromagnetic spectrum, situated between the electronics and photonics regions, and highlights various applications of different spectral bands, including communication, imaging, and diagnostics.

approach the THz range, these limitations become particularly significant, reducing source power to sub-milliwatt levels near 300 GHz and even further to a few microwatts near 1 THz[14].

Similarly, in the photonics region, which spans from the infrared to the ultraviolet range (as shown in Figure 1.1), the output power decreases as the frequency approaches the terahertz range. This occurs due to a lack of natural materials with suitable bandgaps for photonic sources. Semiconductor materials, with bandgaps on the order of electron volts (eV), are not well-suited for generating terahertz photons, whose energy is on the millielectronvolt (meV) scale ($E_{(1\ THz)} \approx 4.1$ meV). Also, since THz waves have very low photon energy, thermal relaxation can easily obscure the distinction between the two states, the difference of which is equal to that of a THz photon. This dual challenge of insufficient power output from electronic devices and unsuitable bandgaps in photonic materials has hindered progress in the generation, detection, and manipulation of terahertz waves, contributing to the persistent "terahertz gap[13, 15-17]."

However, In the last two decades, significant advancements have emerged in terahertz technology as researchers have made substantial efforts to bridge this gap. Pioneering work on terahertz generation using photoconductive switches and nonlinear frequency mixing techniques, along with the development of terahertz detection methods using photoconductive antennas and nonlinear crystals like ZnTe, has played a crucial role in this progress. These innovations led to the development of terahertz time-domain spectroscopy (THz-TDS), which laid the foundation for modern terahertz technology. As a result of these advancements, terahertz radiation has found widespread potential applications across various fields, including medicine, microelectronics, agriculture, forensic science, and many others.

1.1.1 Terahertz Properties and its Applications

The THz frequency range has gained significant interest due to its unique properties and various applications in imaging, spectroscopy, sensing, and wireless communication[18]. THz waves act as a bridge between microwave and infrared frequencies, offering several advantages despite the technological challenges encountered in the past. Below are a few important applications of terahertz radiation.

Safe and Non-Ionizing Radiation

THz radiation, with photon energies ranging from 0.1 to 12.4 meV (corresponding to frequencies of 0.1 THz to 3 THz), is non-ionizing, making it much safer for biological tissues compared to ionizing radiation such as ultraviolet (UV)[19], X-rays, and gamma rays. Unlike ionizing radiation, which can dislodge electrons from atoms or molecules (requiring energies around 12 eV), THz photons are three orders of magnitude weaker and do not pose the same risks. Ionizing radiation can generate free radicals, leading to potential health hazards such as cancer, requiring extreme caution during use. In contrast, THz waves do not penetrate deeply into the human body due to high absorption by water, making them ideal for surface-level medical imaging applications, such as skin cancer and dental diagnostics. This non-ionizing nature ensures that THz frequencies are safe for various biomedical applications without the inherent dangers associated with ionizing radiation.

Penetration of Dielectric Materials

Due to their longer wavelengths compared to visible and infrared light, THz waves can penetrate through various dielectric materials, such as paper, plastics, ceramics, wood, and fabrics. This property makes THz radiation invaluable for nondestructive testing, security screening, and material characterization. For instance, THz waves can detect concealed objects like weapons, explosives, and drugs by penetrating non-conductive surfaces that typically block

other forms of radiation[20, 21]. THz sensing and positioning techniques offer high resolution for identifying hidden objects and are also capable of detecting structural defects, hidden layers, and features beneath surfaces.

These characteristics are particularly beneficial in areas such as security screening, quality control, industrial process monitoring, and multilayer material inspection. Figure 3(a) illustrates a schematic diagram (AI-generated) of a security screening scenario, where THz imaging is used as an alternative to X-ray systems. The figure highlights how THz waves can penetrate clothing to detect concealed metallic components, offering a safer approach that does not involve ionizing radiation or pose risks to human skin.

In addition to security screening, the penetration ability of THz radiation is particularly useful in inspecting multi-layered dielectric structures, such as composite materials, coatings, and packaging systems, where different material layers are stacked on top of one another. As shown in Figure 2(e), THz imaging can reveal internal features and layer boundaries that are otherwise invisible using ultraviolet (UV), visible, or infrared (IR) light, which typically exhibit poor transmission through many dielectric media. Unlike these shorter-wavelength bands, THz radiation can transmit through non-metallic and non-polar materials such as plastics, foams, ceramics, and paper, enabling non-destructive and contactless inspection.

This property is widely utilized in industrial quality control (e.g., inspecting adhesive layers, paint coatings, and semiconductor wafers), cultural heritage conservation (e.g., revealing hidden artwork or layers in historical documents), and aerospace engineering (e.g., detecting delamination or foreign inclusions in composite materials). THz systems can thus provide

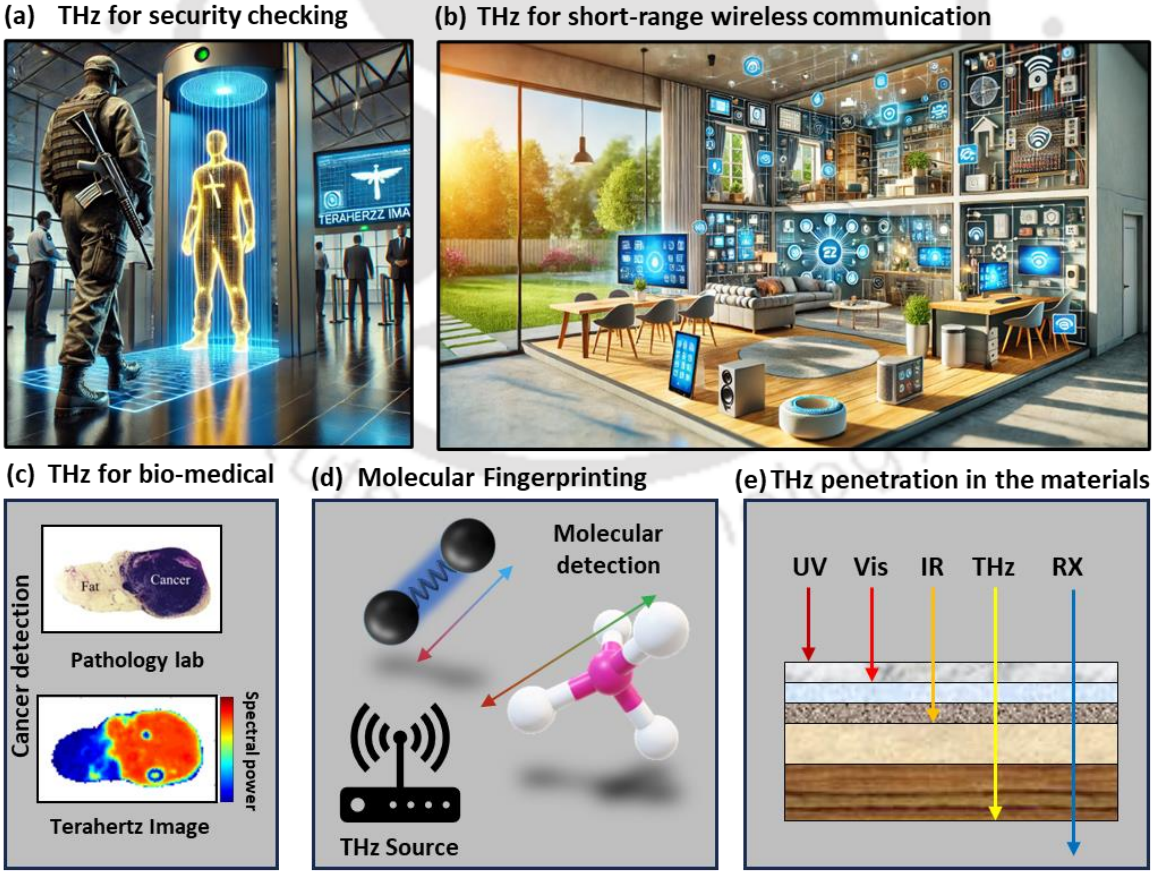

Figure 1.2: Illustrates diverse applications of terahertz (THz) radiation, including security screening, wireless communication, cancer detection, molecular analysis, and advanced material characterization.

critical insight into internal structures without damaging the sample or requiring physical disassembly.

Molecular Fingerprinting

Terahertz radiation is highly effective for molecular fingerprinting because many molecules exhibit unique absorption and dispersion features in the THz frequency range, which correspond to their characteristic rotational and vibrational transitions. As illustrated in Figure 3(d), different molecular structures display distinct rotational and vibrational modes, leading to unique THz absorption and dispersion profiles. These molecular "fingerprints" enable the precise identification and differentiation of chemical substances, allowing THz spectroscopy to analyze material composition at the molecular level with high specificity. This capability is particularly valuable for detecting hazardous materials such as explosives, illicit drugs, and other chemicals that have well-defined spectral signatures within the THz band[20, 21].

Imaging and Detection

THz imaging excels in differentiating materials with varying water content, as THz waves are highly absorbed by water molecules. This makes it particularly useful in medical applications, where it can effectively detect abnormalities such as tumors, burns, and skin conditions that alter tissue hydration levels. In security applications, the contrast between hydrated and dry materials enhances the detection of organic substances, such as explosives and drugs, which often contain water or moisture. Additionally, THz waves are fully reflected by metals, making THz imaging an excellent tool for detecting concealed metallic objects, such as weapons, under clothing or inside packages. Since THz radiation is non-ionizing and poses no health risks, it is a safer alternative for security screening in airports and other high-security areas[22].

For example, in Figure 3(c)[23], a comparison is presented between a pathology-confirmed cancer sample and its corresponding terahertz reflection image. The THz image clearly shows that the cancerous region exhibits higher reflectivity than the adjacent fatty tissue. This contrast is attributed to differences in water content and structural properties between the malignant and non-malignant areas. The close correlation between the THz image and the pathological diagnosis supports the utility of THz imaging for identifying cancerous tissue boundaries in biomedical diagnostics.

Transmission and Reflection: Short-Range Wireless Terahertz Communication Systems: In short-range wireless communication systems, THz waves offer a promising solution due to their ability to support ultra-high data rates while maintaining low latency. The unique propagation characteristics of THz radiation, such as low penetration in metals and strong reflection from conductive surfaces, enable the design of highly directional and secure communication links. Although THz waves are strongly absorbed by atmospheric moisture over long distances, they are well-suited for short-range indoor environments where controlled conditions minimize signal degradation.

As illustrated in Figure 1.2(b), a typical THz communication setup can involve a central THz emitter connected to multiple user devices within a confined space. These systems operate at frequencies beyond 100 GHz, with bandwidths that allow data rates exceeding 1 terabit per second (Tbps), far surpassing conventional wireless technologies. This capability makes THz communication ideal for high-density, high-speed applications such as wireless data centers, chip-to-chip interconnects, augmented/virtual reality environments, and next-generation IoT networks. The integration of THz systems with advanced modulation schemes and beamforming techniques further enhances spectral efficiency and link reliability. The more details on the wireless communication is discussed in detail in section 1.4.1.

1.2 Metamaterials (MMs)

The interaction between electromagnetic waves and materials is fundamentally governed by Maxwell's equations. In isotropic bulk materials, this interaction is typically characterized by two key parameters: effective permittivity (ε) and permeability (μ). These parameters define how the material responds to electric and magnetic fields, respectively. For most natural materials, the permittivity and permeability are referenced relative to their free-space

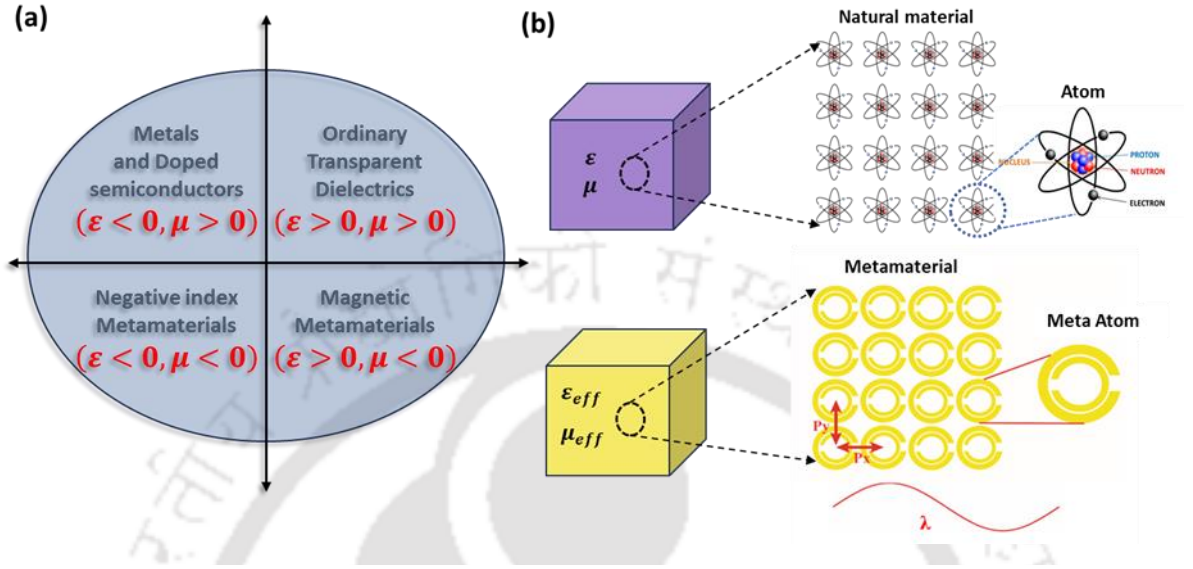

Figure 1.3: (a) Material classification in ε-μ space, showing. The diagram illustrates four quadrants, each representing a different type of material. The fourth quadrant, where both μ and ϵ are negative, indicates a negative refractive index material. (b) The comparison of natural materials with metamaterial.

counterparts, represented as $\varepsilon_r = \varepsilon/\varepsilon_0$ and $\mu_r = \mu/\mu_0$ where ε_r and μ_r are the relative permittivity and permeability of the material, ε_0 and μ_0 represent the permittivity and permeability of free space, respectively. In the ε–μ space, materials are classified into four quadrants based on the signs of their permittivity and permeability. The first quadrant ($\varepsilon > 0$, $\mu > 0$) includes most naturally occurring dielectric materials, known as right-handed materials (RHM), where the electric field (E), magnetic field (H), and wave propagation direction (k) form a right-handed triplet following the right-hand rule. The second quadrant ($\varepsilon < 0$, $\mu > 0$) encompasses plasmonic materials like gold (Au) and silver (Ag) at visible and ultraviolet frequencies, where electromagnetic waves generate evanescent fields that decay exponentially rather than propagating through the medium. The third quadrant ($\varepsilon < 0$, $\mu < 0$) represents left-handed materials (LHM) that exhibit unusual electromagnetic behaviours such as negative refractive index and backward wave propagation. Lastly, the fourth quadrant ($\varepsilon > 0$, $\mu < 0$) includes rare materials often referred to as magnetic plasmas, which support evanescent waves, with few examples like certain ferromagnetic materials at sub-GHz frequencies. Figure 1.3(a) illustrates a broad classification of materials based on intrinsic properties: the first and second quadrants represent naturally occurring dielectrics and metals, respectively, while the third and fourth quadrants represent a special class of materials, generally man-made, called metamaterials[24-26]. Unlike natural materials, metamaterials are engineered structures whose electromagnetic properties arise not from their constituent substances but from their designed unit cells or meta-atoms (Figure 1.3b). A key feature of metamaterials is that their inhomogeneity scale, typically the size of the unit cell, is much smaller than the wavelength of the interacting electromagnetic waves. This allows the material to behave as a homogeneous medium on a macroscopic scale, enabling the effective permittivity and permeability to be precisely tuned to desired values[27].

A major advantage of metamaterials is the ability to engineer the size, shape, and arrangement of their unit cells to control electromagnetic wave interactions. This tunability enables the

creation of materials with properties not found in nature, such as negative refractive index or perfect lensing. By scaling the unit cell size relative to the wavelength, the interaction characteristics can be manipulated for a wide range of applications, from cloaking devices to highly efficient lenses and antennas. Consequently, metamaterials have emerged as a revolutionary class of materials in modern science, enabling advanced control of light, sound, and electromagnetic waves across various frequency ranges[27].

One of the essential conditions for electromagnetic metamaterials is that the size of their unit cells, or meta-atoms, must be much smaller than the wavelength of the interacting electromagnetic waves. This subwavelength scale of inhomogeneity gives metamaterials a macroscopically uniform appearance, allowing them to be classified as "materials" rather than devices. At this scale, the complex interactions between electromagnetic fields and meta-atoms can be effectively characterized by macroscopic parameters such as permittivity (ε) and permeability (μ).

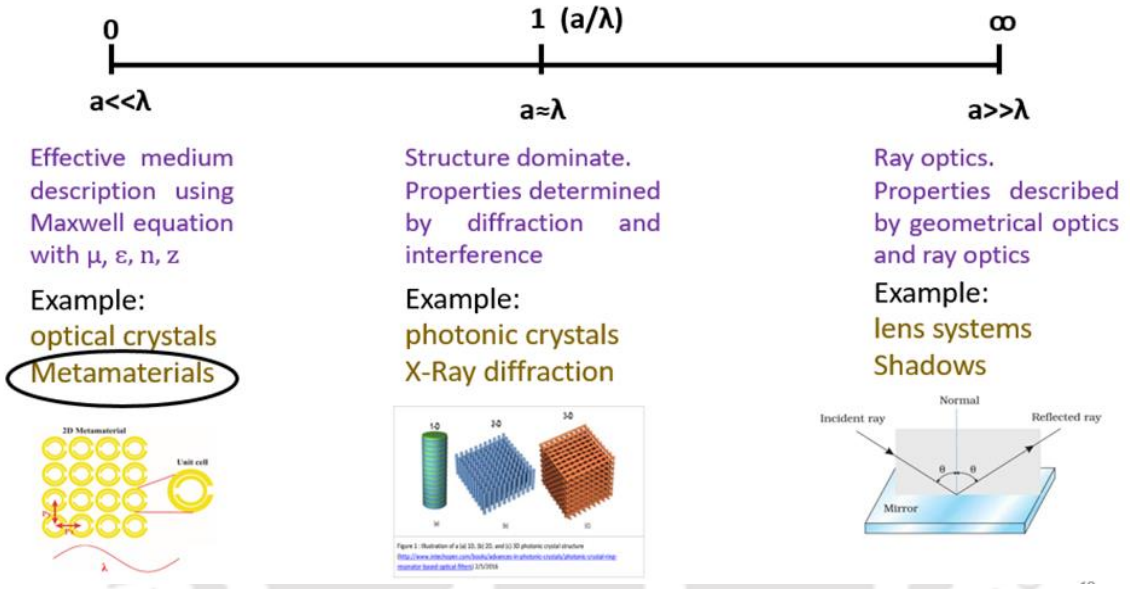

Figure 1.4: Levels of inhomogeneity in Optical materials: Subwavelength structures, such as metamaterials, are made of meta-atoms smaller than the wavelength, resulting in a uniform appearance. At the wavelength scale, diffraction and interference dominate, as seen in photonic crystals. At larger scales, geometrical optics and ray tracing apply.

As illustrated in Figure 1.4, when the relative size of the inhomogeneities increases compared to the wavelength, the interaction properties of the material change significantly. Structures with dimensions much smaller than the wavelength can behave as effective mediums, while structures approaching the wavelength exhibit dominant wave phenomena such as diffraction and interference, which are observed in systems like X-ray diffraction in crystals and photonic crystals in optics. For inhomogeneities much larger than the wavelength, electromagnetic interactions are typically analyzed using geometrical optics and ray tracing techniques, where the wave nature is approximated by straight-line rays that reflect and refract at interfaces.

It is important to note that while metamaterials are primarily categorized in the third and fourth quadrants of the ε-μ space, electrically excited metamaterials typically fall into the second quadrant, where $\varepsilon < 1$ and $\mu \geq 1$. Traditionally, metamaterials have been designed with periodic structures, which provide predictable and well-defined electromagnetic properties. However, recent advancements have led to the development of metamaterials with random shapes and non-uniform periodicity for various applications. For instance, machine learning techniques are now being employed to design materials incorporating unique geometries. These designs, often appearing random and non-intuitive, achieve highly optimized and application-specific

electromagnetic responses.

1.3 Electric and magnetic metamaterial

Over the past decade, various types of subwavelength resonators have been introduced as fundamental building blocks for metamaterials. Examples include thin wires[28, 29], Swiss

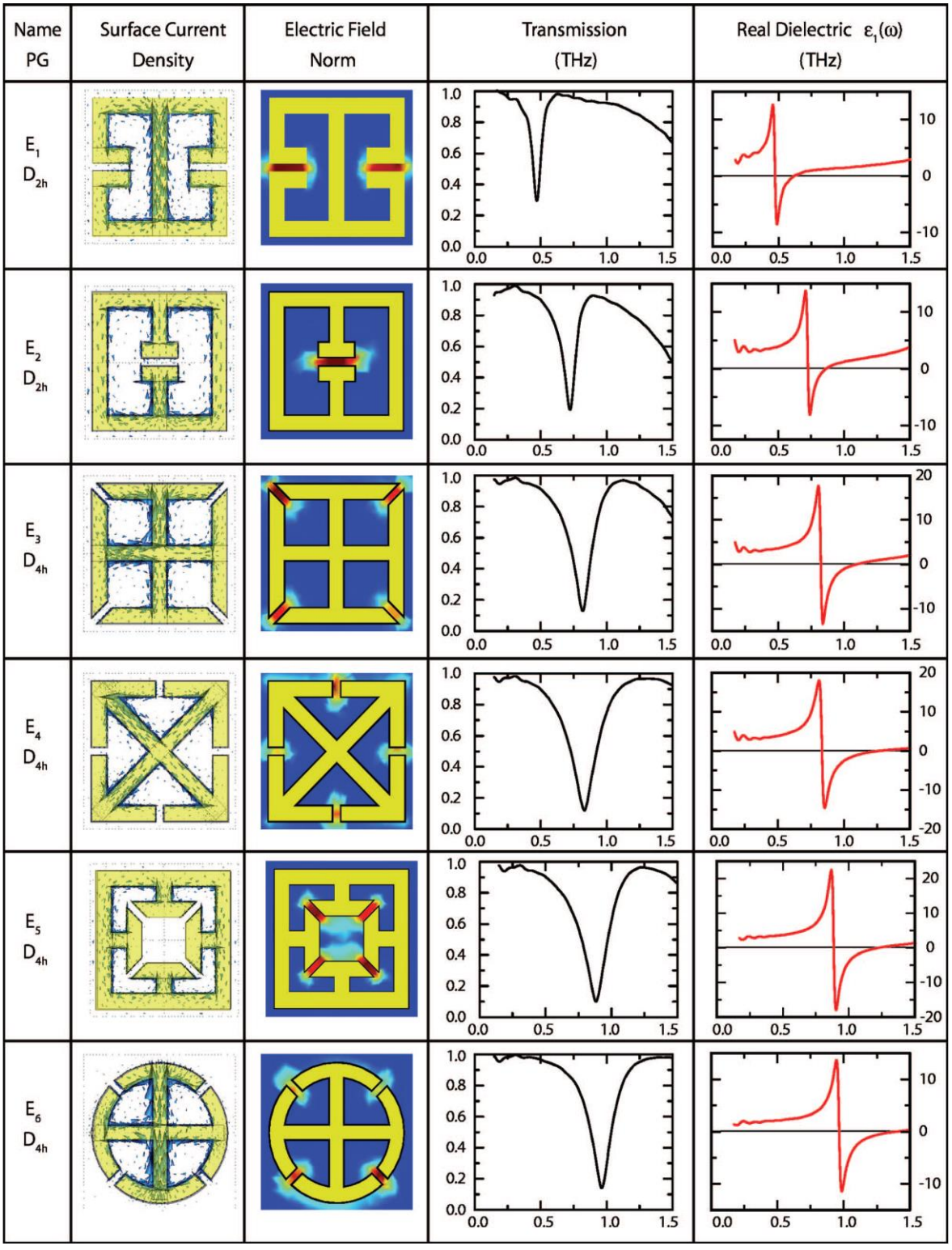

Figure 1.5 presents simulation and experimental results for electric metamaterial particles. The left column lists the names of the particles as referenced in the article [30], along with their corresponding point groups. The second and third columns show the surface current density and the electric field at resonance, respectively. Finally, the fourth and fifth columns display the experimentally measured transmission (T) and the real part of the dielectric function.

rolls[30], split-ring resonators (SRRs)[31, 32], parallel rods[31], pairs of crosses[33], and fishnet structures[34, 35], among others. Some of these resonators are designed to exhibit either an electric or magnetic response, while others show a negative refractive index. Since the first realization of terahertz metamaterials in 2004[36], nearly all metamaterial designs that demonstrate electric, magnetic, or dual responses have been scaled and studied in the terahertz regime. The following sections will explore the electric and magnetic responses of metamaterials, which are essential components in the foundational study of metamaterials.

1.3.1 Electric Metamaterials

Electric metamaterials are designed to effectively manipulate the electric component of electromagnetic waves. Among the most commonly used structures for achieving electric responses are electric split-ring resonators (eSRRs)[31]. These consist of periodically arranged split-ring structures, where the electric field of the incident wave couples to the split gaps, inducing resonant currents. This coupling enables unique electromagnetic properties not found in natural materials. The effective permittivity (ε_{eff}) of eSRR-based metamaterials is described by a Drude-Lorentz model[34]:

$$\varepsilon_{eff} = \varepsilon_{\infty} + \frac{F \cdot \omega_p^2}{(\omega_0^2 - \omega^2 - i\gamma\omega)}, \tag{1.1}$$

where ε_{∞} is the high-frequency permittivity limit (frequency-independent dielectric constant), ω_p is the plasma frequency, ω_0 is the resonance frequency, γ represents the damping factor (associated with losses), ω is the angular frequency and F is the oscillator strength. In the context of metamaterials, oscillator strength (F) is a dimensionless parameter that quantifies the intensity of interaction between the incident electric field and the resonant unit cell. It is closely related to the filling factor, which is defined as the ratio of the resonator volume to the unit cell volume. A larger oscillator strength (or higher filling factor) indicates a stronger electromagnetic response, resulting in a more pronounced resonance in the effective permittivity. Thus, tuning the geometry and arrangement of eSRRs allows for the control of F, enabling tailored response.

In artificial electromagnetic materials, parameters such as the carrier density (n) and the effective mass of electrons (m^*) are governed by the geometrical dimensions and arrangements of the resonator elements. This geometrical dependence offers significant flexibility to tune ε_{eff}, allowing for a wide range of electromagnetic responses that are not possible with natural materials. Near the resonance frequency (ω_0) real part of ε_{eff} can become negative. This property facilitates advanced phenomena such as electromagnetic field confinement, negative [37]refraction, and enhanced wave manipulation, making eSRR-based metamaterials critical for applications in lenses, cloaking devices, and waveguides. Figure (1.5) presents a class of metamaterials that exhibit a tailored response to the electrical component of terahertz radiation. These electric metamaterials are investigated theoretically, computationally, and experimentally using terahertz time-domain spectroscopy. These structures display a resonant response, including regions of negative permittivity ranging from 500 GHz to 1 THz.

The functionality of the metamaterials shown in Figure 1.5 is rooted in the resonant LC behavior of the split-ring resonators. Each SRR consists of a metallic ring with a narrow gap, functioning as an LC circuit, where the ring provides inductance (L) and the gap forms a capacitor (C). When the incident THz electric field is polarized appropriately, it induces an oscillating current around the ring. This leads to charge accumulation across the gap, generating a strong localized electric field and establishing the LC resonance.

Furthermore, as illustrated in the second column of Figure 1.5, the circulating currents in

adjacent eSRRs exhibit clockwise and counterclockwise rotation, respectively. This anti-symmetric current distribution results in the cancellation of the net magnetic dipole moment, confirming that the resonators do not support a magnetic response. Instead, the resonant behavior arises entirely from electric dipole interactions, validating that the metamaterial class shown is a purely electric metamaterial with no magnetic contribution to the resonance.

1.3.2 Magnetic Metamaterials

Magnetic metamaterials are specially designed to display strong magnetic responses, even when made from non-magnetic materials. One of the most commonly used structures to achieve this effect is the magnetic split-ring resonator (mSRR). An mSRR consists of concentric metallic loops with splits that enable the generation of circulating currents when exposed to a magnetic field[36]. These induced currents create magnetic dipole moments, which result in an effective permeability described by the Lorentz model[38]:

$$\mu_{eff} = 1 + \frac{F\omega^2}{(\omega_m^2 - \omega^2 - i\gamma\omega)}, \tag{1.2}$$

Here, ω_m is the resonance frequency, γ represents the damping factor (associated with losses), F is the oscillator strength, and ω is the angular frequency. The plasma frequency at which permeability crosses zero is expressed as:

$$\omega_{mp}^2 = \omega_m^2/(1 - F), \tag{1.3}$$

At frequencies below the resonance frequency ω_m , the mSRRs exhibit a positive magnetic response. Between the resonance and plasma frequencies, however, the response becomes negative. This dispersive behaviour allows the structure to support both paramagnetism($\mu_{eff} > 1$) and diamagnetism($\mu_{eff} < 1$), including the phenomenon of negative permeability.

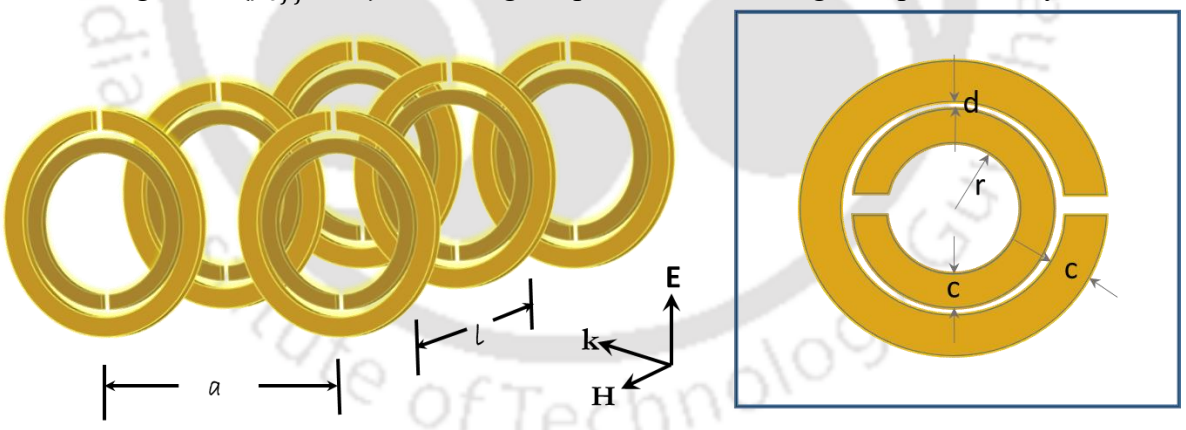

Figure 1.6: Double SRR: When excited by a magnetic field parallel to the SRR axis, the structure exhibits a Lorentzian resonance in its effective permeability. The electric field is parallel to the gap and, therefore, does not couple to the SRRs.

To experimentally demonstrate that a magnetic split-ring resonator (mSRR) metamaterial exhibits negative magnetic permeability (μ < 0), a magnetic field component perpendicular to the SRR plane is required. Ideally, this condition is realized by aligning the wave propagation vector (k) parallel to the SRR plane. However, this arrangement is challenging for thin, planar metamaterials due to practical limitations in experimental setups.

Instead, oblique incidence is typically employed (figure 1.7a), introducing a component of the magnetic field (H⊥) perpendicular to the SRR plane. This perpendicular magnetic component induces circulating currents within each resonator ring, as illustrated in Figure 1.7(d). At

resonance, these induced circular currents generate a strong magnetic dipole moment directed opposite to the applied magnetic field, H⊥. This phenomenon leads to an effective negative magnetic permeability. As depicted in Figure 1.7(d), the surface currents within each individual ring circulate consistently in one direction (typically anticlockwise or clockwise), and crucially, the currents in adjacent resonators are aligned similarly, without intersecting. This uniform circulation and coherent alignment of currents confirm that these resonators exhibit a magnetic resonance, distinguishing their response from purely electric metamaterials.

The first experimental demonstration of this magnetic resonance effect at terahertz frequencies utilized arrays of planar double-ring mSRRs, achieving a strong magnetic resonance near 1.2

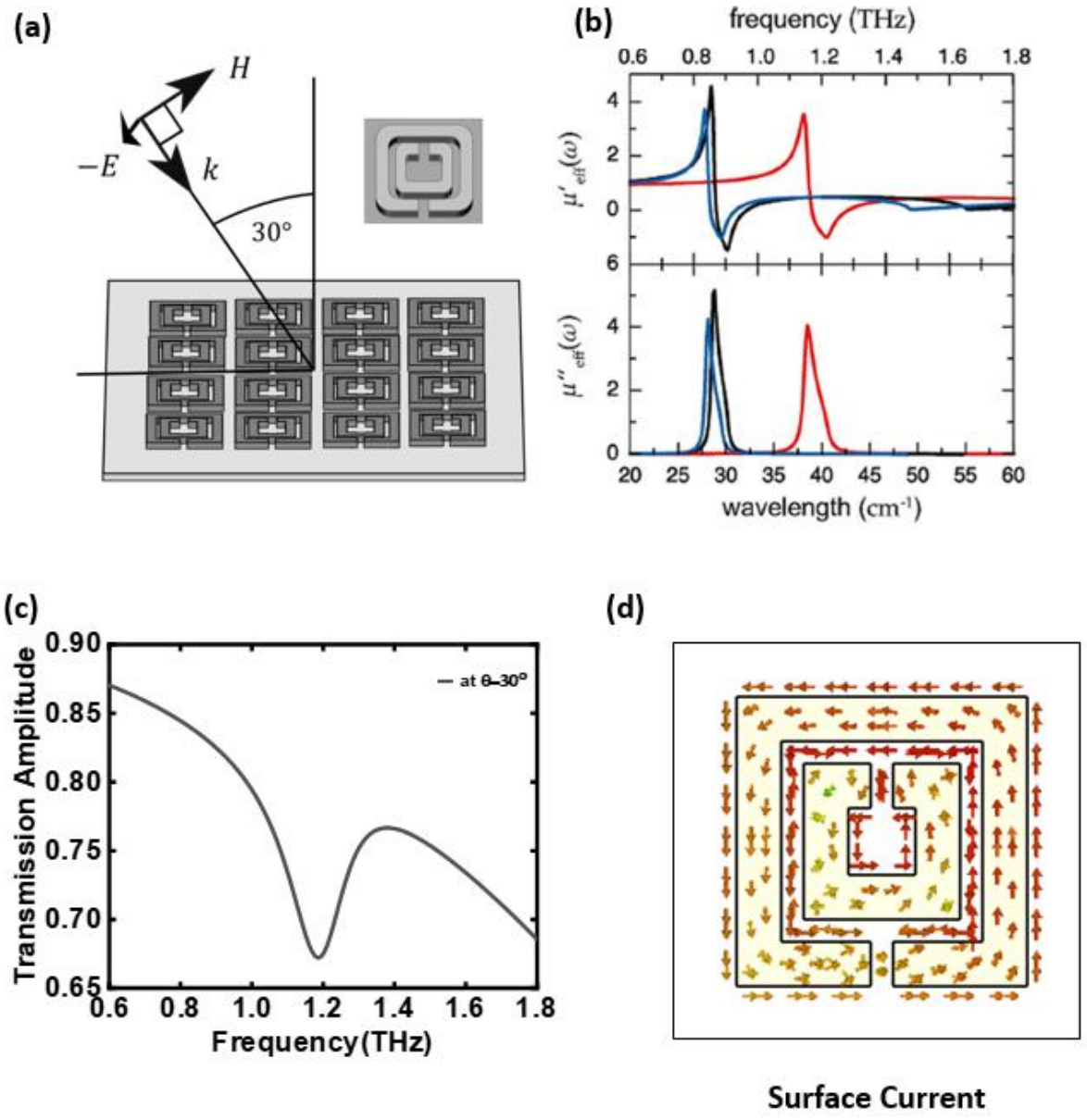

Figure 1.7: Magnetically coupled split-ring resonators (SRRs). (a) Oblique incidence (30°) of THz radiation enabling magnetic coupling. (b) Complex magnetic permeabilities for different geometries [35]. (c) Transmission response. (d) Surface currents confirming magnetic resonance.

THz under oblique incidence. These artificial structures exhibited magnetic responses significantly stronger than those found in natural magnetic materials. Further experiments using single-ring SRRs have successfully demonstrated similar magnetic resonances at even higher

frequencies, such as 6 THz, underscoring the broad applicability and versatility of mSRRs-based metamaterials at terahertz frequencies [39].

1.3.3 Classification of metamaterial

Metamaterials can be broadly categorized based on their operational principles, design methodologies, and structural configurations. This classification provides an essential framework for understanding their functionality and diverse applications. Fundamentally, metamaterials are classified into two primary types: passive metamaterials and active metamaterials. Passive metamaterials derive their properties purely from their geometric structure and material composition, while active metamaterials incorporate external stimuli, such as electric, magnetic, or thermal inputs, to dynamically alter their properties. Below is the detailed information on the different types of metamaterials.

Passive Metamaterials

Passive metamaterials derive their electromagnetic properties from the intrinsic design of their unit cells and the choice of constituent materials. These unit cells, typically on the sub-wavelength scale ($\approx \lambda/4$), are fabricated from a combination of dielectric materials and structured metallic patterns. Examples of passive metamaterial designs include split-ring resonators, strip resonators, crosswire resonators, and their variations.

Passive metamaterials offer a degree of control over electromagnetic waves that surpass natural materials, enabling applications such as optical pulse manipulation, frequency filtering, and resonance-based sensing.

Active Metamaterials

Unlike passive metamaterials, active metamaterials feature tunable electromagnetic properties that can be dynamically adjusted through external stimuli such as voltage, temperature, or [40]optical pumping. The development of active metamaterials began in 2006 when Padilla and his team demonstrated the ability to control the electric response of split-ring resonators through the photoexcitation of free carriers in the substrate[41]. Building on this breakthrough, Chen and colleagues later introduced electrical control of metamaterials using an applied electric bias in the terahertz range[42]. These foundational efforts catalysed rapid advancements in active metamaterials, significantly expanding their applications.

Active metamaterials have primarily been explored through dynamic control mechanisms utilizing optical, electrical, thermal, and mechanical stimuli, each offering distinct advantages and limitations. For instance, optical control is particularly well-suited for ultrafast devices due to its high-speed tunability. The incorporation of functional materials such as vanadium dioxide (VO_2), graphene, or liquid crystals further enhances the capabilities of active metamaterials[43-45]. These materials enable a responsive interaction with external triggers, paving the way for applications in adaptive optics, reconfigurable filters, and active modulators.

1.4 Terahertz metamaterial

Metamaterials have transformed the ability to manipulate electromagnetic waves by enabling precise control over optical properties through the design of their unit cells' geometric parameters. One significant advantage of these engineered structures is their scalability: by adjusting the size of the unit cell, metamaterials can be tuned to respond across a broad spectrum of frequencies, from microwaves to optical domains.

In the THz frequency range, typically spanning 0.1 to 2.0 THz (with corresponding wavelengths from approximately 3,000 to 150 μm), metamaterials offer unique opportunities due to the lack of natural materials with strong electromagnetic responses in this spectrum.

Achieving resonance in this range requires feature sizes on the order of 10 to 100 μm, making them well-suited for fabrication using standard micro-photolithography techniques. These fabrication methods are not only accessible but also cost-effective, supporting the practical implementation of THz metamaterials in real-world devices.

It is important to note that the 0.1–2.0 THz range has been consistently adopted throughout this thesis, as it represents a region that is both experimentally accessible with current THz emitters and widely supported in the literature for metamaterial-based applications, particularly in terahertz communication systems, sensors, modulators, and other functional devices.

A notable class of terahertz metamaterials includes split-ring resonators, which are capable of exhibiting negative permittivity and permeability near their resonance frequencies. This enables the realization of exotic electromagnetic properties such as negative refractive index and artificial magnetism. In the THz regime, where most conventional materials lack strong interaction with electromagnetic fields, metamaterials provide a flexible and tunable platform to manipulate both the electric and magnetic components of incident waves. This dual control is essential for developing compact, high-performance THz components with tailored spectral responses and dynamic tunability.

1.5 Applications of THz metamaterials

Metamaterials, with their unique electromagnetic properties and sub-wavelength structural features, have revolutionized various advanced fields. Their compactness and lightweight nature make them ideal for aerospace applications, such as developing filters and modulators for space technology. In medical science, they facilitate the production of biosensors and spectroscopic components[40, 46]. Metamaterials enhance the efficiency and durability of solar power systems and are instrumental in creating nanoscale chips and integrated circuits in

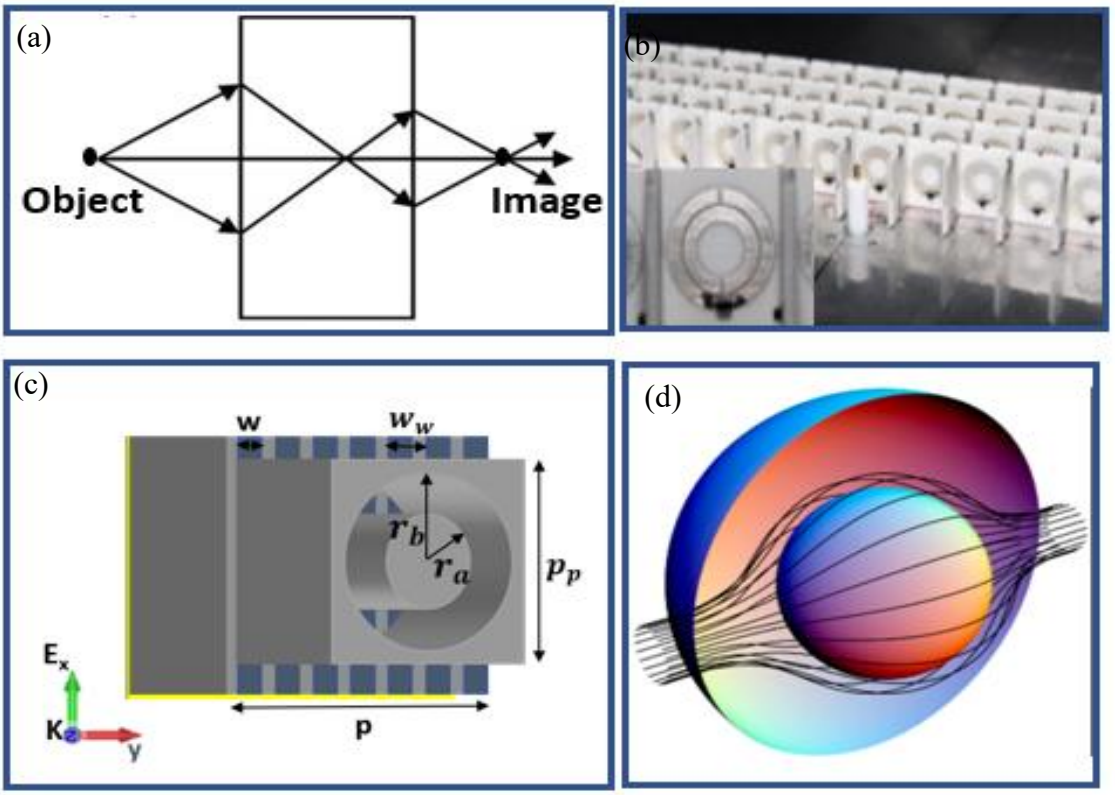

Figure 1.8: Application of Metamaterials in (a)perfect lens [47], (b)negative index material [48], (c)perfect absorbers and modulators [62], and (d)cloaking.

electronics[47]. They also enable unique devices like perfect lenses[48], negative index materials[49], optical cloaking devices, and advanced communication components[18]. In the THz domain, metamaterials are particularly valuable for manipulating electromagnetic waves at THz frequencies. The development of THz technology relies on highly efficient devices capable of generating, controlling, and detecting THz radiation. Metamaterials serve as the foundation for such devices, including filters, switches, sensors, lenses, modulators, and waveguides. Below are the different applications of metamaterials for various purposes:

Filters: Metamaterial-based THz filters selectively transmit specific frequency ranges while blocking others. Designed as long-pass, short-pass, or band-pass filters, they modulate the amplitude and phase of THz waves. These filters are crucial in THz spectroscopy, aerospace applications, electronic devices, and biosensing technologies[50-52].

Switches: THz switches utilize metamaterials to control the transmission or reflection of terahertz waves. By altering the properties of these metamaterials using external stimuli such as electric or magnetic fields, it becomes possible to rapidly modulate THz waves. This capability paves the way for faster and more efficient THz communication systems[42, 53, 54].

Sensors: Advanced metamaterial designs, including those that utilize high-quality resonances from Bound States in the Continuum (BIC) and toroidal metamaterials, significantly enhance the performance of terahertz sensors. BIC resonances arise from destructive interference between radiating modes, resulting in states that are highly localized and do not couple to free-space radiation, thereby producing extremely high-Q resonances. Similarly, toroidal resonances are generated by toroidal dipole moments, which are associated with circulating magnetic fields confined in a donut-shaped configuration, offering strong field localization and minimal radiative loss. These innovative, high-Q factor-based narrow resonances enable the detection of even the smallest changes in the refractive index of biomolecules and other materials, making them highly effective for applications such as early disease detection, environmental monitoring, and material analysis. By harnessing the ultra-narrow linewidths and strong electromagnetic field confinement associated with BIC and toroidal resonances, these sensors achieve exceptional sensitivity and precision. This capability allows for the identification of subtle molecular or structural changes, paving the way for breakthroughs in both scientific research and real-world applications.[55-58].

Lenses: Traditional terahertz lenses are constrained by diffraction limits due to the relatively long wavelengths of THz radiation, resulting in lower resolution. Metamaterial-based THz lenses overcome this limitation by incorporating sub-wavelength structures that effectively manipulate[48] THz waves. For instance, super-oscillatory lenses (SOLs) have been developed to achieve sub-diffraction focusing[59], enabling multiple focal points smaller than the diffraction limit. Additionally, gradient index (GRIN) lenses designed with metamaterials can focus THz radiation to spot sizes smaller than the wavelength[60, 61], significantly [62]enhancing spatial resolution. These advancements facilitate high-resolution THz imaging and sensing applications.

Modulators: Metamaterial-based THz modulators are capable of adjusting the phase, amplitude[63], and polarization of THz waves with high precision. These modulators are essential for THz communication and imaging, enabling the control of THz wave transmission, generation, and detection (A schematic diagram is shown in Figure 1.9). Electrically tunable solid-state modulators offer broadband operation and can efficiently replace traditional mechanical choppers in time-domain spectroscopy systems, enhancing speed and reliability. Using advanced metamaterial designs, these modulators achieve superior performance in terms of speed, sensitivity, and tunability, supporting the development of next-generation THz technologies[62, 64].

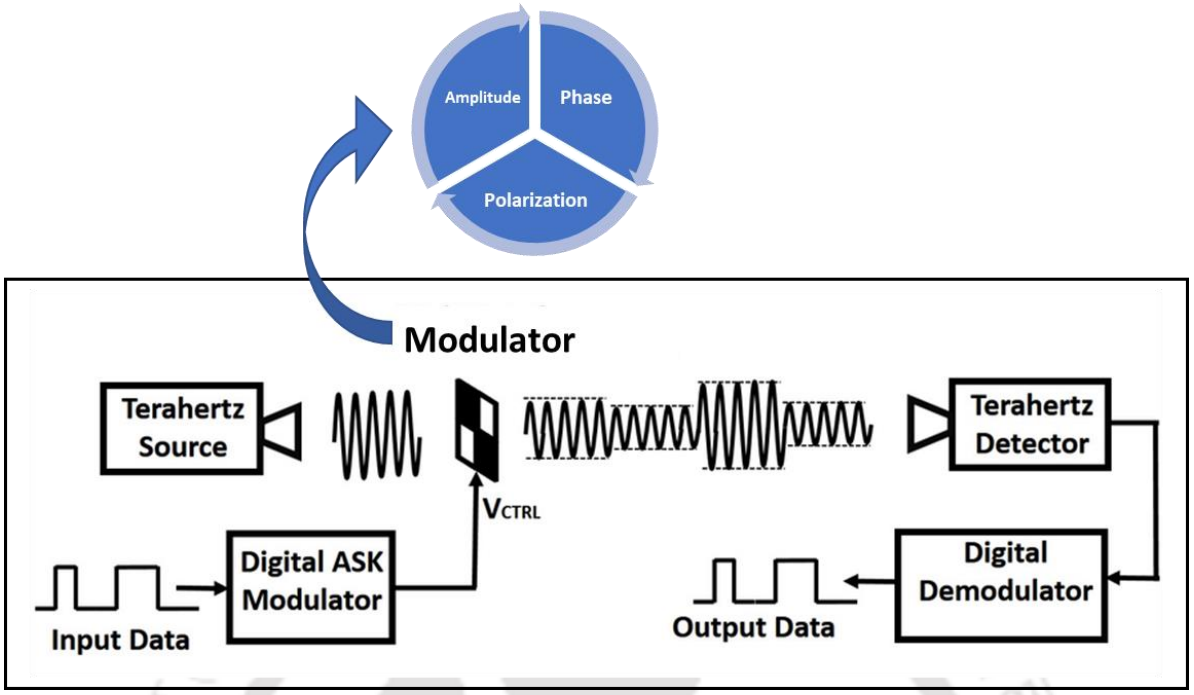

Figure 1.9: Schematic diagram showing the use of terahertz modulators in manipulating the incident source amplitude, phase, and polarization.

1.6 Broadband terahertz metamaterial: Filter and modulators

Broadband terahertz metamaterials are crucial to advancing next-generation communication, imaging, and sensing systems. These MMs offer dynamic control over the phase, amplitude, and polarization of THz waves, meeting critical requirements for applications such as spectroscopy, high-resolution sensing, and ultra-fast wireless communication. The ability of these metamaterials to support ultra-wideband operations is essential for creating filters, modulators, and waveguides capable of functioning across the extensive THz spectrum. Two primary design approaches are utilized to achieve a broadband transmission response: planar and multi-stacked metamaterials[51, 62, 64].

Planar Metamaterials: Planar terahertz metamaterials consist of single-layer metasurfaces with resonator structures arranged in a two-dimensional array. These designs are highly valued for their ability to achieve high-Q resonances, which are crucial for applications such as narrowband filtering, precision sensing, and frequency selection. Beyond these traditional uses, planar metamaterials have demonstrated significant potential for broadband functionality[58, 65-70].

Broadband performance in planar metamaterials can be achieved through various advanced design approaches, such as exploiting multiple resonances, introducing geometric asymmetries in the resonator structures[71], employing nested planar configurations[72], or using fractal metamaterials to extend bandwidth[73]. Additionally, coupling multiple resonators within a single unit cell enables multi-resonance phenomena[74], further enhancing their operational range.

However, achieving substantial enhancements in planar metamaterials remains challenging due to inherent limitations, such as geometric constraints and material losses. These limitations and potential solutions are discussed in greater detail in Section 1.6.1.

Multi-Stacked Metamaterials

Multi-stacked metamaterials utilize the layered arrangement of metasurfaces separated by dielectric spacers to achieve broadband responses. This configuration enables subwavelength coupling between resonances in vertically stacked layers, leading to hybridization and mode splitting, which in turn enhances the overall bandwidth of the metamaterial response[51]. Key aspects of multi-stacked metamaterials include:

- **Spacer Optimization:** The thickness and refractive index of the dielectric spacers are optimized to manage interlayer coupling and achieve constructive interference between resonances.
- **Resonator Design:** Resonator geometries in each layer are tailored to target specific frequency ranges, creating overlapping resonances that span a broad spectrum.
- **Enhanced Performance:** Multi-stacked designs are particularly effective in creating broadband filters, polarization-insensitive modulators, and highly efficient absorbers.

By combining both approaches, planar and multi-stacked metamaterials, broadband THz responses can be achieved. While planar designs offer simplicity and ease of fabrication, multi-stacked configurations excel in delivering extended bandwidth and enhanced functionality. Together, these approaches play a crucial role in the development of advanced THz devices for modern technological applications. In the next section, we will discuss the need for broadband terahertz metamaterials, especially in the field of communications.

1.6.1 Broadband Terahertz Metamaterial in the Communication System

In recent years, terahertz technology has emerged as a crucial enabler for future communication systems, particularly with the advent of 6G networks. At the 2019 World Radiocommunication Conference (WRC-19), the International Telecommunication Union (ITU) allocated portions of the spectrum for millimeter-wave (mmWave) frequencies to support 5G networks. However,

the current mmWave frequencies (30 GHz to 100 GHz) may not be sufficient to meet the increasing demands of future communication systems[18, 75].

Disruptive applications such as virtual and augmented reality, the Internet of Things (IoT), Industry 4.0, connected and autonomous vehicles, and emerging use cases like the Metaverse, holographic telepresence, Tactile Internet, digital twins, and fully immersive experiences require hyper-fast data rates, ultra-reliability, near-zero latency, and massive connectivity. These demands, reaching into terabits per second (Tbps), far exceed the capabilities of 5G networks[18, 64].

Sub-6 GHz bands, widely used in 4G and 5G, are now congested, and even advanced technologies like massive MIMO and high-order modulation cannot overcome the bandwidth scarcity. In contrast, THz frequencies, ranging from 100 GHz to 10 THz, offer significantly broader bandwidth, enabling data rates of up to 1 terabit per second (Tbps). This opens the door for future applications such as ultra-high-definition video streaming, fully immersive virtual and augmented reality, and the Internet of Everything (IoE), which require vast data capacities. Although mmWave frequencies have been instrumental for 5G, they typically operate within a

Table 1.1: Comparison of the different EM band with the Terahertz band for the utilization in the wireless communication system.

Technology	**MM Wave**	**Terahertz**	**Infrared (IR)**	**Visible Light**
Frequency	30 GHz - 100 GHz	100 GHz -10 THz	10 THz - 430 THz	430 THz -770 THz

Data Rate	Up to 10 Gbps	Up to 1 Tbps	10 to 800 Gbps	10 to 800 Gbps
Range	Short	Short/Medium	Short/ Long	Short
Propagation path	LOS/ NLOS*	LOS/ NLOS*	LOS	LOS
Bandwidth	Narrow	Very wide	Wide	Moderate
Attenuation	High, affected by rain/obstacles	High, affected by the atmosphere	Moderate, affected by weather	Low, blocked by objects
Applications	5G networks, fixed access	6G, high-speed communication, sensing	Remote controls, thermal imaging	Indoor data transmission (VLC)
Challenges	Short-range, atmospheric loss	Signal attenuation, tech complexity	Requires line-of-sight, weather-sensitive	Line-of-sight, range limits

bandwidth of only around 10 GHz, limiting their ability to achieve Tbps data rates. Additionally, mmWave signals are highly susceptible to signal attenuation, especially when obstructed by obstacles or impacted by atmospheric absorption, making them less reliable for long-distance communication.

On the other end of the spectrum, infrared (IR) and visible light technologies offer large spectral resources but come with their own challenges. These technologies generally require line-of-sight (LOS) propagation and are highly sensitive to environmental factors such as fog, rain, or dust, which can severely degrade their performance. Furthermore, while IR and visible light communication are well-suited for short-range or indoor applications, they lack the imaging and sensing capabilities that THz frequencies provide, making THz technology more versatile and suitable for large-scale communication and sensing applications. Table 1.1 shows a comparative study of different communication bands with the Terahertz band[18].

A major advantage of THz technology is its safety compared to higher-frequency bands. Frequencies such as ultraviolet (UV), X-ray, and gamma-ray are classified as ionizing radiation, meaning they carry enough energy to remove electrons from atoms, which can be harmful to human health. These ionizing bands are used in specialized fields like radiotherapy or industrial applications but are unsuitable for widespread personal communication due to health risks. In contrast, THz frequencies are non-ionizing, with photon energies well below the threshold required to dislodge electrons, making THz radiation much safer for everyday communication technologies. This positions THz technology as a reliable and secure option for future communication networks.

One of the main features of metamaterials in THz modulation is the ability to extend the bandwidth, which is crucial for high-speed communication applications. Ultra-broadband THz modulators are particularly valuable for this purpose as they allow for dynamic control over both the amplitude and phase of THz signals across a wide frequency range. This broadening of the operational bandwidth directly enhances the capacity of communication systems, as described by the Shannon-Hartley theorem[76, 77]:

$$C = B \times log_2 \left(1 + \frac{S}{N}\right) \tag{1.4}$$

where C is the channel capacity, B is the bandwidth, and S/N is the signal-to-noise ratio. By increasing the bandwidth B, the overall data transmission capacity C is increased, which is crucial for achieving terabits-per-second data rates in future 6G wireless systems.

1.7 Motivation:

The terahertz region of the electromagnetic spectrum, which spans frequencies from 0.1 to 10 THz, has historically been underutilized. This is mainly due to its position between the microwave and infrared frequencies, as well as the lack of natural materials that can strongly interact within this range (as discussed in section 1.1). As a result, the "terahertz gap" has constrained the development of efficient devices for high-speed communication, imaging, and sensing applications. However, recent advancements in engineered materials and fabrication technologies are beginning to unlock the potential of THz frequencies. Notably, metamaterials (MMs) have demonstrated significant promise for manipulating THz waves. This thesis is driven by the need to bridge the terahertz gap through the innovative design of broadband THz metamaterials.

1.7.1 Bandwidth Enhancement in Coupled Planar Metamaterial Systems

Planar metamaterials with geometries like split-ring resonators, cross-shaped resonators, and square-ring resonators have been extensively studied for narrowband terahertz applications. These planar configurations provide functionalities such as filtering, modulation, and sensing[58, 65, 66]; however, they typically have limited bandwidth. This restriction on bandwidth impacts their effectiveness for emerging THz applications, including high-speed communication, broadband sensing, and cloaking.

To address these challenges, researchers have explored various designs to expand resonance. For instance, Yuan et al. developed dual-band planar metamaterials aimed at enhancing broadband THz applications[71], while Dibakar et al. proposed nested resonator configurations to improve dipole resonance broadening[72]. Several other techniques have been employed by researchers to enhance the bandwidth of terahertz resonance[78], as discussed in section 1.6.1. This thesis delves deeper into planar metamaterials by introducing a novel design featuring strongly coupled bending strip resonators. This design achieves significant broadening of the fundamental resonance by optimizing the bending angles, demonstrating the potential of planar geometries to enhance bandwidth for specific THz applications.

Despite these advancements, planar architectures face inherent limitations, including restricted inter-resonator coupling and low resonator density, which hinder their bandwidth and resonance strength. To overcome these challenges, alternative design strategies are necessary to achieve ultra-broadband responses.

1.7.2 Utilization of Multistacked Metamaterials for Ultrawideband Responses

Multistacked metamaterials have emerged as a promising approach to overcome the limitations of planar designs. By stacking multiple layers of resonators, these structures allow for enhanced interlayer coupling, resulting in significantly broader resonances while maintaining strong resonance characteristics. Previous studies, such as Han et al.'s multistacked split-ring resonator and Ruan et al.'s broadband metamaterial filter, have demonstrated that stacking can lead to ultra-broadband responses[78, 79]. Building on this research, this thesis investigates polarization-insensitive, multistacked terahertz metamaterials by optimizing parameters such as layer thickness and resonator dimensions. These multistacked designs provide excellent scalability and compatibility with various THz photonic and wireless communication applications.

1.7.3 Dynamic Tunability with Vanadium Dioxide (VO_2)

Dynamic tunability is essential for developing reconfigurable THz devices such as filters and modulators. While planar metamaterials have laid the groundwork for many tunable designs, broadband applications require tunability in multi-layered structures. In this thesis, vanadium dioxide (VO_2), known for its insulator-to-metal phase transition induced by temperature

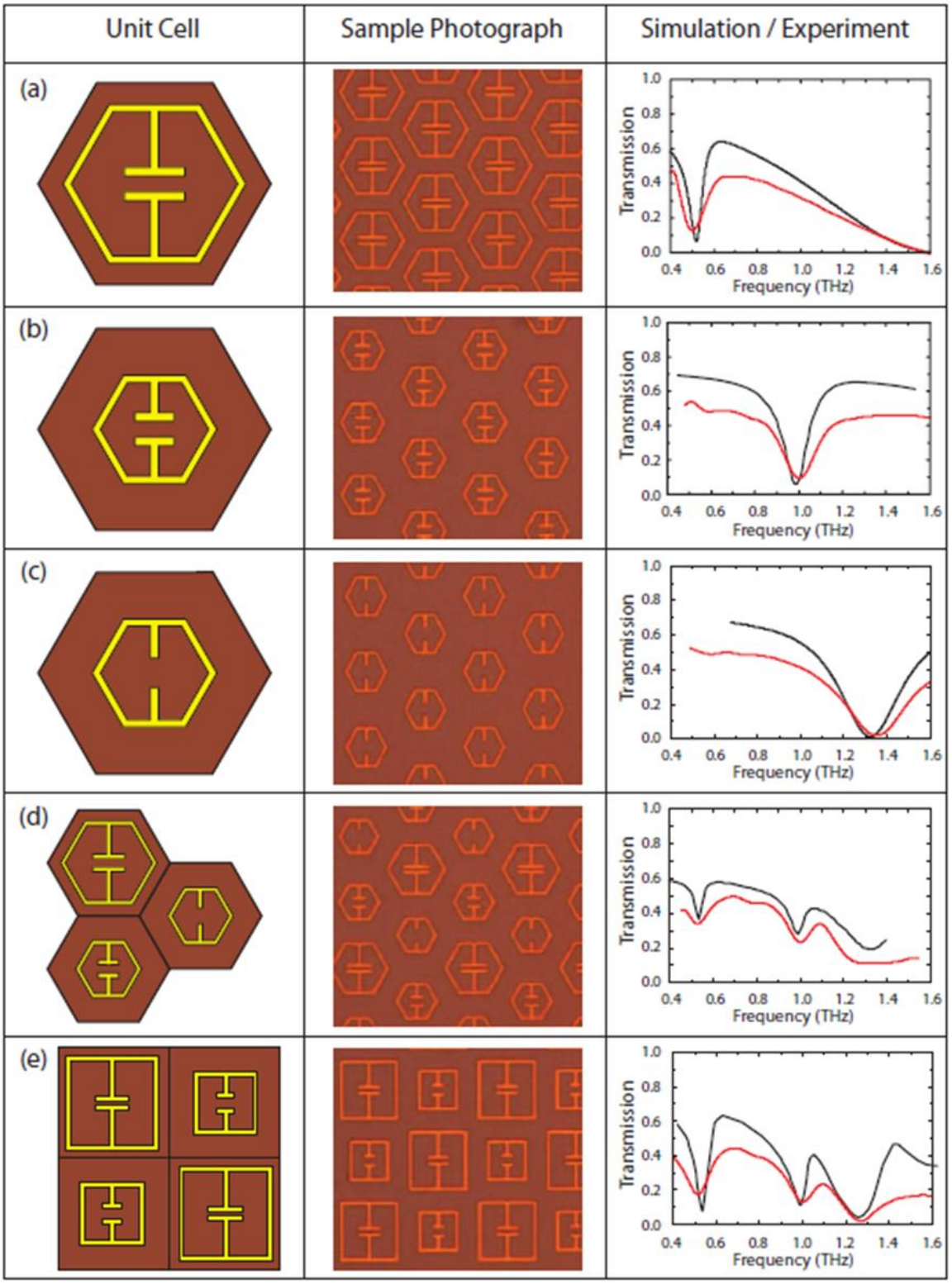

Figure 1.10: Simulation and experimental results for different primitive meta-unit cells. The left column displays the unit cell models, the middle column contains images of the fabricated samples, and the right column shows the plots of simulated data (black curve) and experimental data (red curve) [75].

changes[80], is incorporated into these multi-layered designs. This integration allows for significant variations in conductivity and permittivity, enabling substantial modulation and across a wide range of frequencies. By optimizing the arrangement of VO_2 layers and refining the overall structure, this research enhances tunable multi-layered metamaterials, paving the way for the next generation of THz devices.

1.7.4 Expediting Design of Metamaterials with Machine Learning

The design of metamaterials requires precise control over subwavelength structures; however, conventional simulation methods, such as Finite-Difference Time-Domain (FDTD), can become computationally expensive for large-scale parameter sweeps. To streamline this process, this thesis utilizes machine learning (ML) models, including neural networks, to predict and optimize the performance of metamaterials. By training on extensive simulation datasets, ML-driven approaches significantly reduce iteration times, allowing for the rapid exploration of vast parameter spaces.

In summary, this thesis addresses the challenges associated with the terahertz gap by advancing metamaterial design beyond conventional planar architectures. It integrates tunable materials, such as VO_2, and leverages ML-driven optimization techniques. Together, these contributions aim to facilitate the development of high-performance, scalable THz devices, establishing a solid foundation for transformative applications in photonics, communication, and sensing.

1.8 Important Concepts related to the thesis:

In this section, we have explored several important concepts that play a crucial role in our research. These concepts have been referenced repeatedly throughout various thesis works, underscoring their significance in our field of study. By examining these foundational ideas in detail, we aim to establish a stronger framework for understanding and analyzing the topics at hand.

1.8.1 Coupled MM for Ultra-Broadband Resonance in Planar Configuration:

The design of planar metamaterials has been crucial in advancing applications requiring precise control of electromagnetic resonances. A key objective in this domain is achieving ultra-broadband enhancement of resonance to expand the operational bandwidth, which is critical for applications in sensing, imaging, and communication. However, a recurring limitation in planar metamaterials is the intrinsic trade-off between bandwidth broadening and the strength of the resonance. This section explores various strategies employed for resonance broadening and highlights the challenges in overcoming this trade-off.

Multiresonance Configurations: The multiresonance approach uses multiple resonators with different shapes and sizes within a single unit cell. Patterns like checkerboard and beehive arrangements allow multiple resonance frequencies to exist together, with the number of different resonators determining the range of frequencies covered[81]. Figure 1.10 shows examples of metamaterial geometries that can be arranged in various planar patterns, expanding the range of possible designs beyond simple square lattices of wires and split-ring resonators. These new metamaterials can help overcome the narrow-band response of traditional designs by enabling multi-frequency behaviour without greatly reducing their "electromagnetic strength." However, multiresonance structures naturally reduce resonance strength because there are fewer identical resonators, and different resonators can interfere with each other. In extreme cases, these effects can completely suppress the desired properties.

Nested Structures in Split-Ring Resonators: A more sophisticated approach for broadening the resonance involves nested structures in split-ring resonators. Dibakar et al. proposed a design in which progressively smaller interconnected rings are added within the SRR unit cell,

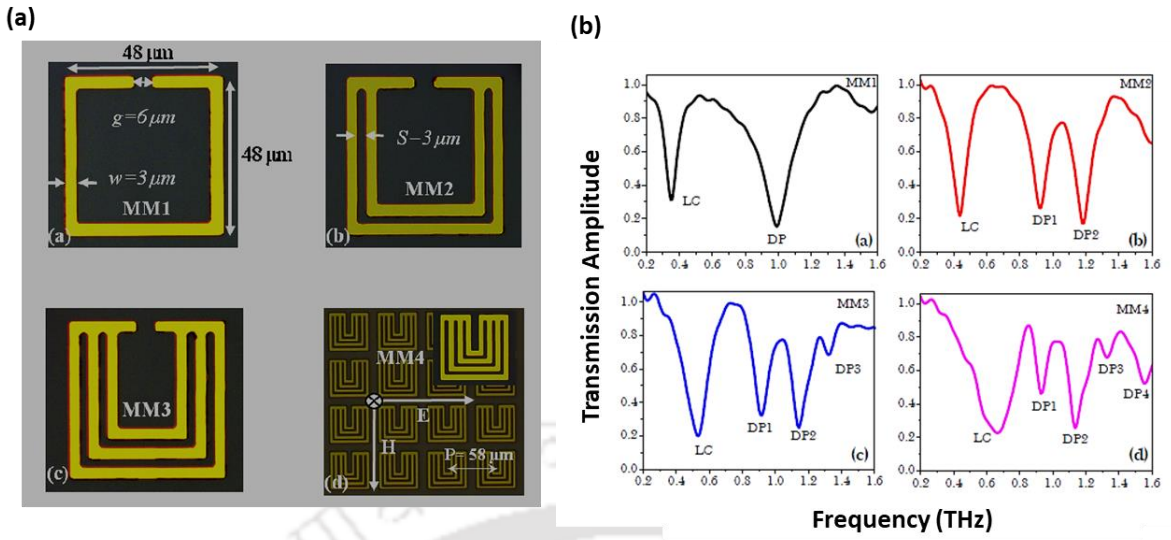

Figure 1.11 (a) Microscopic images of the fabricated metamaterial samples. The original split-ring resonator (SRR) unit cell is designated as MM1. MM2 features one inner ring, MM3 has two inner rings, and MM4 contains three inner rings. (b) Measured transmission amplitudes for the samples MM1, MM2, MM3, and MM4. "LC" denotes the first fundamental resonance, which arises from the circular currents flowing in the metallic SRRs. "DP1," "DP2," "DP3," and "DP4" refer to the dipolar resonances that occur after splitting [66].

reducing the effective inductance and resulting in both a blue shift and significant resonance broadening[72]. For example, transitioning from a single-ring SRR to a four-ring nested structure achieved a fourfold increase in full-width at half-maximum (FWHM), expanding the resonance linewidth from 70 GHz to 280 GHz (see Figure 1.11). Importantly, the resonance minima were preserved, ensuring reasonable transmission strength. While effective, this approach still falls short for ultra-broadband applications, as the structural complexity and associated losses impose practical limits on further bandwidth enhancement.

Coupling-Based Dual-Resonance Designs: Coupling mechanisms between asymmetric resonators provide yet another strategy for bandwidth enhancement. For instance, Yu Yuan et al. introduced a dual-band planar metamaterial with resonances at 1.0 and 1.2 THz by

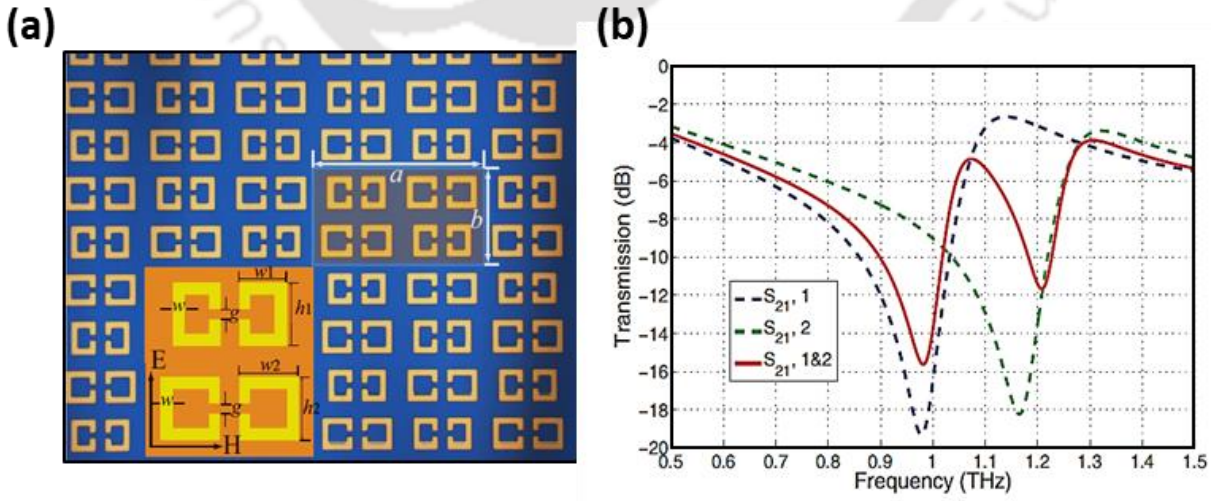

Figure 1.12: (a) Photomicrograph of the fabricated dual symmetrical split-ring resonator (SRR) sample. The unit cell of the metamaterial is highlighted in the white-edged box, with an inset showing the simulated SRRs along with the polarization of the incident wave. (b) Simulated transmission (in decibels) of the dual-band electric metamaterial is depicted by the solid line, while the individual symmetrical SRRs are represented by the dashed lines [65].

combining two asymmetric SRR pairs in a single unit cell, as shown in Figure 1.12[71]. The mutual inductance between the resonators broadened the operational frequency range but weakened the resonance strength, especially at higher frequencies, due to polarizability cancellation. While this approach successfully extends the spectral coverage, the loss in resonance strength highlights the trade-off inherent in coupling-based designs.

Fractal Design: Fractal-based designs present a unique approach to achieving broad resonance behaviour through self-similar patterns. For instance, when the electric field is oriented in the y-direction, as illustrated in Figure 1.13a,[73] the fractal geometries exhibit a sharp dip in the transmission spectrum. This dip has a narrow full width at half maximum (FWHM) at lower fractal levels, indicating strong and localized resonances. However, as the fractal level increases, the effective resonator length also increases, resulting in a redshift in resonance frequency and a corresponding increase in FWHM, as shown in Figure 1.13b.

Additionally, the FWHM of the terahertz can be controlled through the width of the fractal resonance, as observed in Figure 1.13c. As the fractal width decreases, FWHM increases, but this comes at the cost of compromised resonance strength. While fractal designs can broaden the resonance spectrum, they also pose practical challenges, particularly in fabricating finer self-similar features at higher levels. Complex geometries can lead to coupling effects that may degrade overall performance, and the resolution limits of fabrication techniques can hinder further bandwidth expansion.

Despite the diversity of strategies, ranging from nested structures to multi-resonance configurations and coupling-based designs, a fundamental limitation persists. Ultra-broadband resonance enhancement in planar metamaterials inevitably involves a trade-off with resonance strength. This trade-off arises from intrinsic electromagnetic phenomena, including non-radiative losses, mutual inductance, and coupling effects, which dictate the behaviour of these structures. Consequently, achieving both ultra-broadband FWHM and high resonance strength simultaneously remains an unresolved challenge in planar designs. Future advancements may

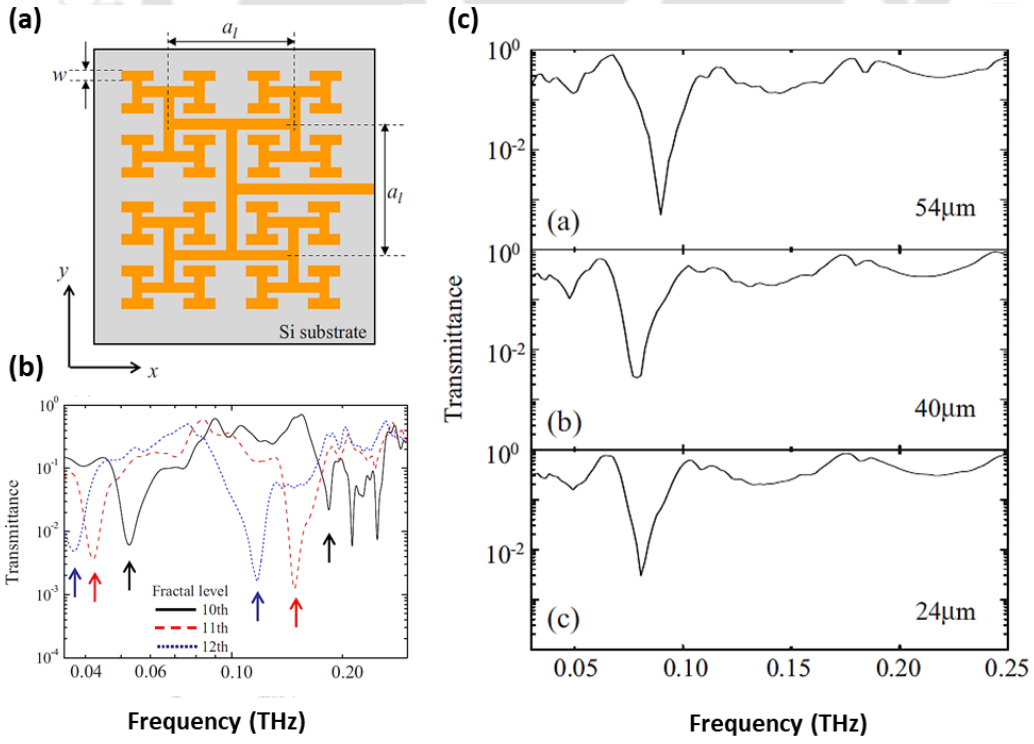

Figure 1.13: (a) Geometric design of fractal metamaterial. (b) Transmission amplitude as the fractal level increases. (c) Transmission amplitude as the line width of the fractal resonance changes [67].

require exploring alternative material architectures, such as hybrid or three-dimensional metamaterials, to overcome these inherent limitations.

1.8.2 Toroidal metamaterials:

Toroidal resonances are a distinctive class of electromagnetic excitations arising from unconventional current distributions within metasurfaces. These resonances emerge when magnetic dipoles are arranged in a head-to-tail configuration, forming poloidal current loops that collectively generate a pronounced toroidal dipole moment, as depicted in Figure 1.14. This current and charge organization, illustrated in Figures 1.14(c) and 1.14(d), creates toroidal moments fundamentally distinct from conventional electric or magnetic dipoles.

A planar split-ring resonator metasurface design supporting toroidal dipole modes is shown in Figure 1.15[82]. In this structure, counter-propagating currents in adjacent resonators induce head-to-tail magnetic dipole configurations, leading to the formation of a toroidal dipole. The geometric parameters of the SRRs, such as the slit gap, the separation between resonators, and the SRR width, critically influence the resonance frequency and quality factor (Q). Precise tuning of these parameters allows optimization of the toroidal resonance.

The unique attributes of toroidal resonances make them highly advantageous for advanced photonic applications. Their high-Q resonances enable sharp spectral features, which are invaluable for sensing, filtering, and slow-light applications. Additionally, the head-to-tail

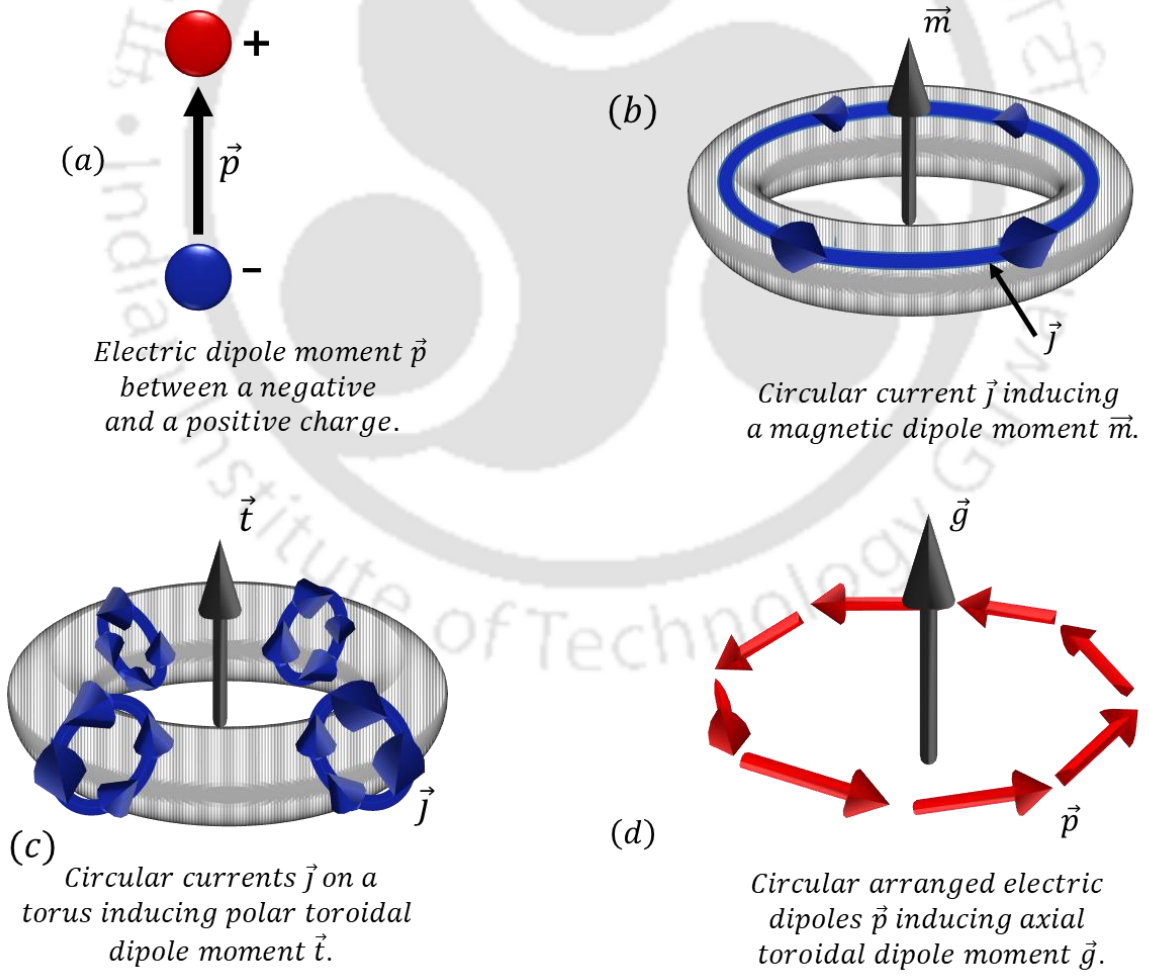

Figure 1.14: Pictorial representation of charge and current distributions creating (a) electric dipole, (b) magnetic dipole, (c), (d) polar and axial toroidal dipole moments.

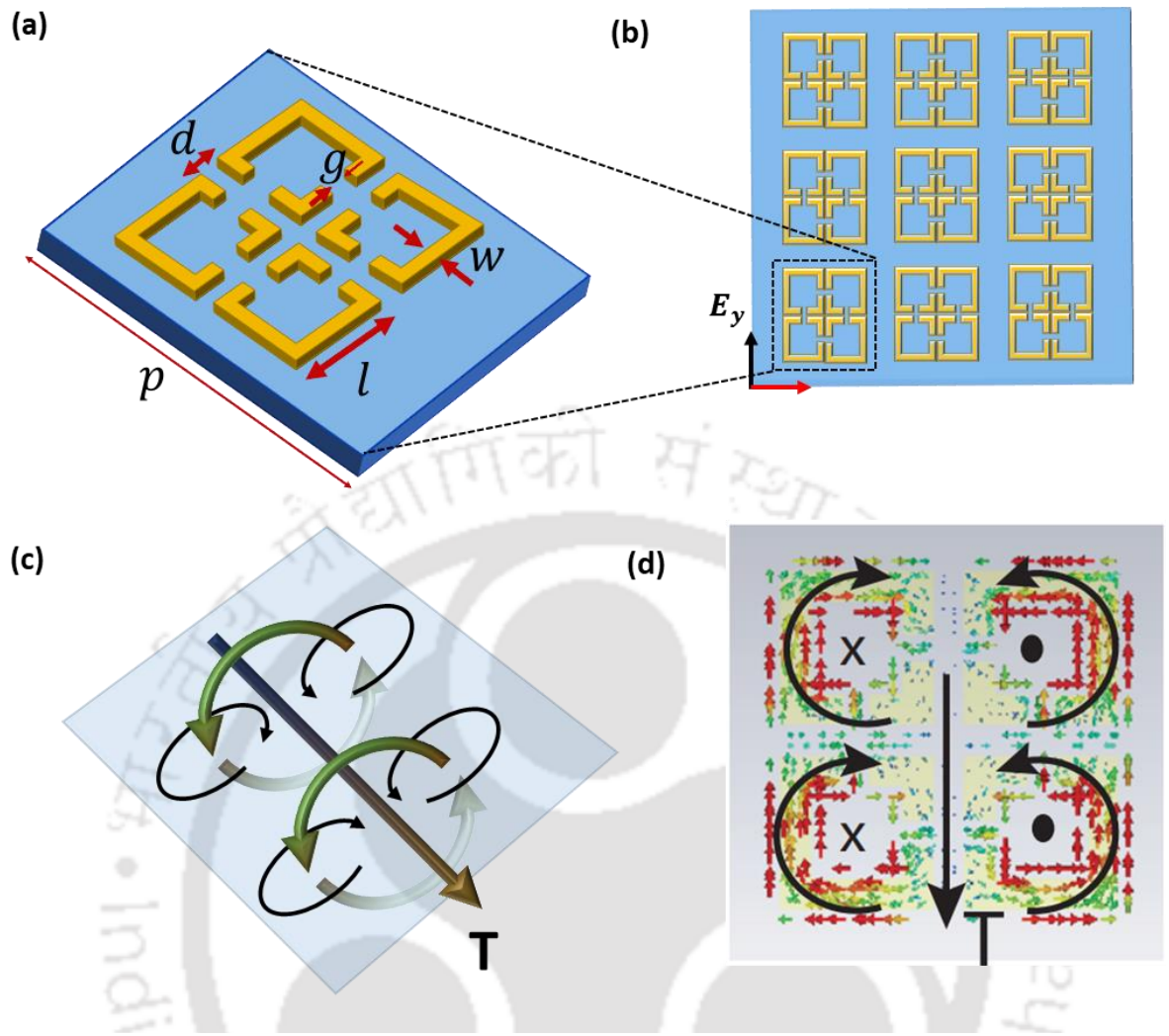

Figure 1.15: (a) and (b) shows a schematic of the proposed metamaterial array with y-polarized terahertz radiation incident normally on the surface. (c) and (d) illustrate the surface current profile of the metamaterial at resonance. The arrows indicate the direction of the surface current flow. Magnetic moments are oriented out of the plane on the right-hand side and into the plane on the left-hand side of the metamolecule. Toroidal dipole excitation, labelled 'T', is aligned along the negative y-direction.

arrangement of magnetic dipoles suppresses radiative losses, facilitating efficient energy storage and minimizing signal loss. These properties are particularly beneficial for high-sensitivity detectors, energy-harvesting devices, and systems requiring minimal power dissipation, further highlighting the transformative potential of toroidal resonances in photonic technologies.

1.8.3 Mode Splitting and Hybridization in Metamaterials

As discussed in section 1.2, Metamaterials are composite materials made up of numerous artificially structured "meta-atoms" arranged in specific configurations. In the simplest effective-media model, the interactions among these meta-atoms are often ignored, treating the metamaterial as an "averaged" medium. In this view, the overall response of the metamaterial is attributed to the individual resonant properties of its constituent elements. While this approach can be a useful approximation, it fails to consider the inter-element coupling that occurs when meta-atoms are placed closely together. This coupling can lead to significant changes in the metamaterial's overall response. One notable consequence of this coupling is mode splitting[83]: instead of exhibiting a single resonance, multiple discrete modes emerge due to the hybridization of the individual resonances, as shown in Figure 1.16. In other words,

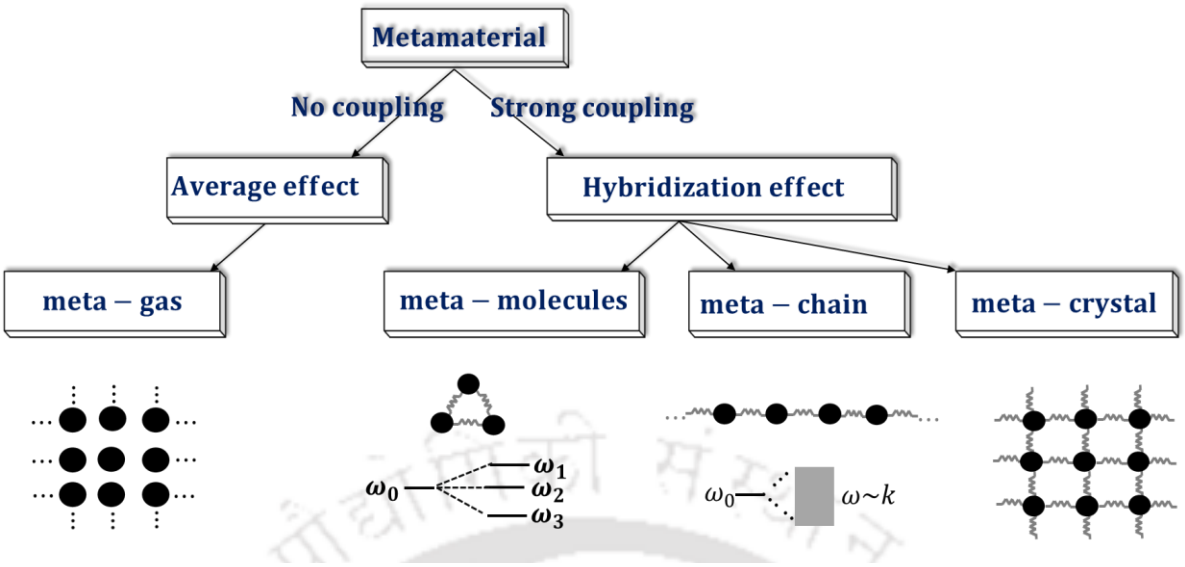

Figure 1.16: Classification of metamaterials based on coupling effects. The diagram illustrates the transition from no coupling, where the average effect dominates (meta-gas), to strong coupling, which induces hybridization effects, leading to the formation of meta-molecules, meta-chains, and meta-crystals.

the collective behaviour of the coupled resonators can be quite different from simply combining their isolated responses.

A clear and illustrative example of mode splitting can be observed in coupled split-ring resonators, as shown in Figure 1.17. When two SRRs are configured as a magnetic dimer (MD), they interact through mutual inductance, which causes the hybridization of their resonant states[83]. Each SRR functions as an LC circuit with its own natural resonance frequency $\omega_0 = 1/\sqrt{LC}$, where L is the inductance of the metallic loop, and C is the capacitance associated with the gap (Figure 1.17c). The Lagrangian for a single SRR is given as:

$$\boldsymbol{L} = \left(\frac{L}{2}\dot{Q}^2\right) - \left(\frac{Q^2}{2C}\right), \tag{1.5}$$

where Q is the charge accumulated in the gap of the SRR, $\dot{Q}$ represents the induced current, $\left(\frac{L}{2}\dot{Q}^2\right)$ corresponds to the kinetic energy of the oscillatory current, and $\left(\frac{Q^2}{2C}\right)$ is the electrostatic energy stored in the capacitor.

When two SRRs are coupled to form a dimer, the system's Lagrangian includes an additional mutual inductance term, M to account for their interaction:

$$\boldsymbol{L} = \frac{L}{2}\left(\dot{Q}_1^2 - \omega_o^2 Q_1^2\right) + \frac{L}{2}\left(\dot{Q}_2^2 - \omega_o^2 Q_2^2\right) + M\dot{Q}_1\dot{Q}_2 \tag{1.6}$$

where Q_1 and Q_2 are the charges in the gaps of the two SRRs, and the mutual inductance M characterizes the coupling strength.

From this coupled Lagrangian, the eigenfrequencies are derived:

$$\omega_{\pm} = \omega^0/\sqrt{(1 \mp \kappa)}, \qquad \kappa = M/L \tag{1.7}$$

representing the bonding (low energy, ω_-) and anti-bonding (high-energy, ω_+) modes. The bonding mode exhibits symmetric charge oscillations ($Q_1 = Q_2$), leading to reduced radiative loss and a higher Q-factor. In contrast, the anti-bonding mode has antisymmetric oscillations ($Q_1 = -Q_2$), resulting in enhanced radiation loss. The frequency splitting $\Delta\omega = \omega_+ - \omega_-$ increases with the coupling strength κ, which is determined by the distance and alignment of the SRRs. Hybridization in coupled systems leads to the formation of bonding and anti-bonding resonant modes. The frequency separation between these modes depends on the coupling strength, which can be tuned by adjusting the spacing, orientation, or arrangement of the resonators. The bonding mode, with its reduced radiative loss and higher Q-factor, is particularly advantageous for applications such as high-Q cavities, optical sensors, and enhanced nonlinear optical processes. Moreover, in extended systems like one-dimensional arrays, the coupling can induce collective effects such as magnetic plasmon (MP) waves, enabling subwavelength waveguiding and tunable dispersion. In other configurations, like fishnet metamaterials, hybridization can enhance the negative refractive index and improve optical transmission efficiency.

1.8.4 Machine learning in metamaterials

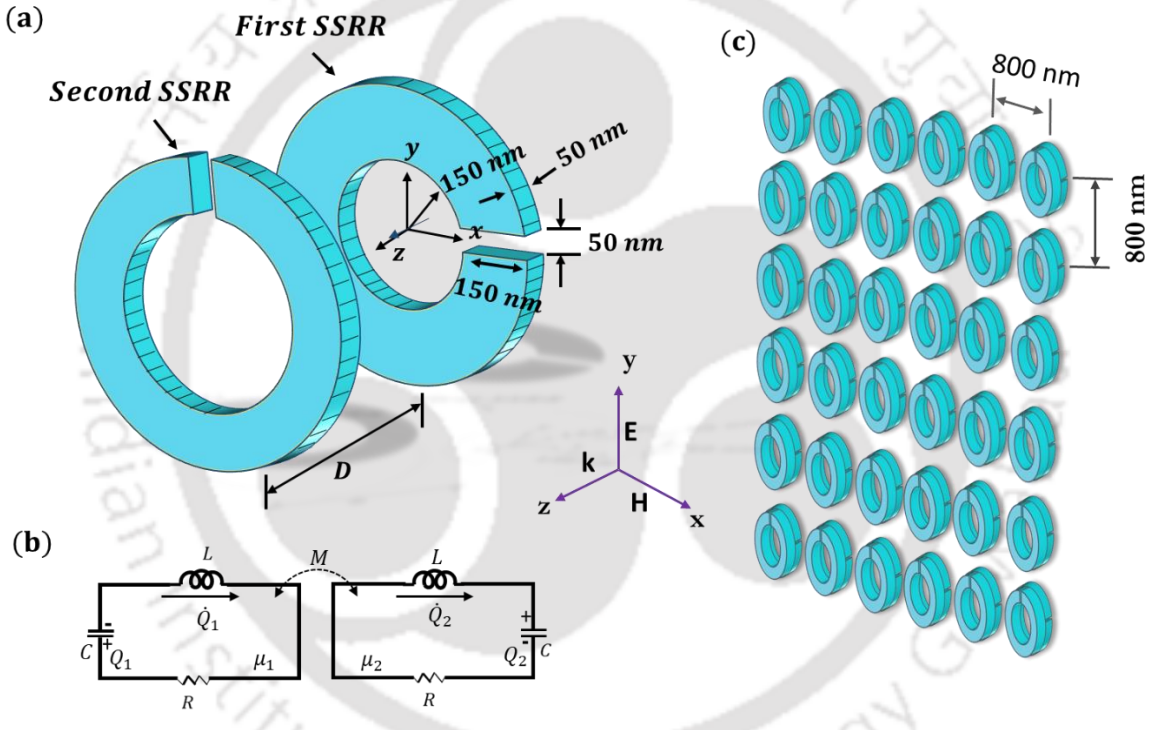

Figure 1.17:(a) Structure of a magnetic dimer; (b) Equivalent LC circuit; (c) Metamaterial made of identical dimer elements.

Machine learning (ML), a subset of artificial intelligence (Figure 1.18b), focuses on developing algorithms that learn from data and make decisions or predictions with minimal human intervention. Over the past decade, ML has emerged as a powerful tool in diverse domains, ranging from healthcare and finance to computer vision. In the context of metamaterials, ML significantly broadens the scope of design exploration. By leveraging data-driven models, researchers can predict metamaterial behaviour more efficiently, reduce the reliance on lengthy simulations, and optimize structural parameters without exhaustive trial-and-error.

One of the most transformative advantages of ML in metamaterial and nanophotonic research, as highlighted by Khaireh-Walieh et al. (2023)[84], is its inverse-design capability. Traditional approaches typically involve either manual parameter tuning or extensive physical simulations. In contrast, ML-based methods can directly map a desired performance goal (e.g., a specific resonance frequency) back to its optimal structural configuration. This approach not only

accelerates innovation but also reduces computational overhead and can reveal non-intuitive design solutions that conventional methods might lack.

Machine learning (ML) algorithms can generally be grouped into three major categories: supervised, unsupervised, and reinforcement learning[85]. In supervised learning, models are trained on labelled datasets to accurately map inputs (e.g., metamaterial structural parameters) to known outputs (mechanical or electromagnetic properties). By contrast, unsupervised learning uncovers hidden patterns in unlabelled data, making it ideal for identifying novel structural features or clustering metamaterial designs with similar characteristics. Lastly, reinforcement learning (RL) focuses on sequential decision-making to maximize a reward, which is particularly useful for navigating large parametric spaces and iteratively refining metamaterial designs toward desired performance targets.

Although unsupervised and reinforcement learning is promising for innovative metamaterial discovery, this thesis primarily utilizes supervised learning, the foundation for many predictive tasks in metamaterial research.

1.8.4.1 Supervised Learning in Metamaterial Design

Supervised learning train models using labelled examples, making it ideal for predicting metamaterial properties based on design parameters. Two main supervised learning tasks are:

- **Classification**: Predicting discrete classes or categories (e.g., determining whether a given metamaterial design will exhibit a particular resonant frequency).
- **Regression**: Predicting continuous output values (e.g., estimating the effective refractive index of a metamaterial based on design parameters).

Given the need to forecast performance metrics like bandgap frequencies and electromagnetic responses, regression methods and classification methods both play an important role in metamaterial research.

Common Supervised Learning Algorithms: Below are widely used supervised algorithms, each offering unique benefits for modelling and optimization:

- **Linear Regression**: A fundamental regression method that assumes a linear relationship between input features and a continuous target[86, 87].
- **Decision Trees**: Tree-like models that split data based on feature values, offering high interpretability[88].
- **Random Forest**: An ensemble of decision trees that improves prediction accuracy by aggregating outputs from multiple trees[89].
- **Support Vector Machine (SVM)**: Constructs an optimal hyperplane (or set of hyperplanes) in a high-dimensional space for classification or regression[90].
- **k-Nearest Neighbours (k-NN)**: Makes predictions by examining the k closest examples in the training set, suitable for smaller datasets and intuitive to implement[91].
- **Gradient Boosting**: Sequentially adds weak learners (e.g., small decision trees) to correct errors made by previous models, often yielding highly accurate predictions[92].

Incorporating these supervised algorithms into metamaterial studies enables more rapid discovery of high-performance designs. By precisely predicting how structural parameters impact material properties, researchers can guide simulations and experiments toward the most promising configurations, accelerating innovation in next-generation metamaterials.

1.8.4.2 Neural Networks

Artificial Neural Networks (ANNs) are versatile models that can be used for supervised, unsupervised, or reinforcement learning. In metamaterial research, however, they are most commonly applied in a supervised setting to capture the often-nonlinear relationships between geometric parameters and metamaterial responses. ANNs consist of multiple layers of interconnected nodes known as neurons. Each neuron processes input signals through weighted connections and applies an activation function, such as the Rectified Linear Unit, defined as (ReLU, max(0, x)), to introduce nonlinearity. Other popular activation functions include sigmoid and hyperbolic tangent (tanh), which can be selected based on the specific requirements of the problem. By adjusting the depth (the number of layers) and the width (the number of neurons per layer) of the network, researchers can tailor the network's capacity to tasks such as predicting bandgap frequencies or electromagnetic spectra[93].

Deep Neural Networks (DNNs), which stack many hidden layers, can learn complex feature representations from large datasets. Specialized architectures such as Convolutional Neural

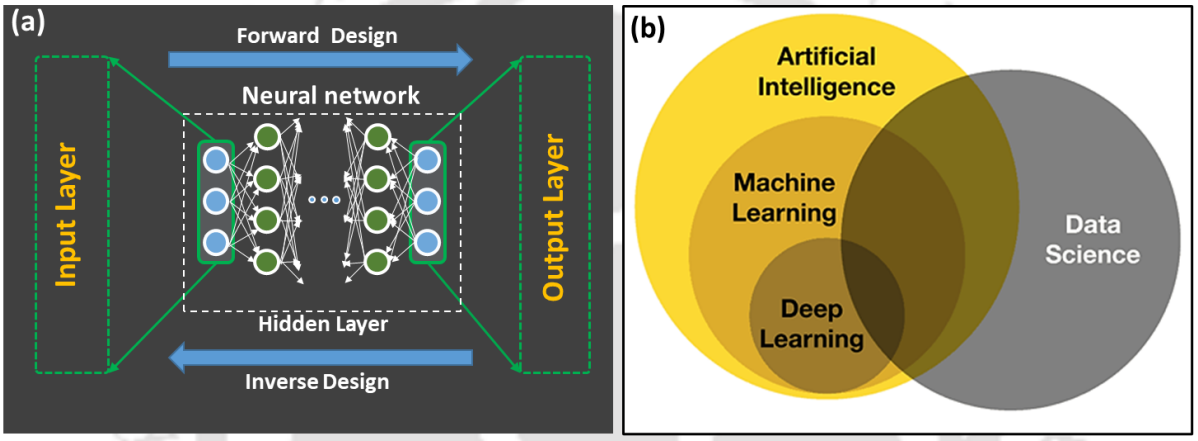

Figure 1.18: (a) Schematic of a neural network model showcasing forward design (input to output) and inverse design (output to input) through hidden layers. (b) Venn diagram illustrating the relationship between Artificial Intelligence (AI), Machine Learning (ML), Deep Learning (DL), and Data Science.

Networks (CNNs) handle spatial or image-like data efficiently, while Recurrent Neural Networks (RNNs) are better suited for sequence-based tasks. According to Khaireh-Walieh et al. (2023)[84], these advanced networks greatly facilitate the *inverse-design* process by mapping performance targets (e.g., a desired reflection spectrum) directly to structural parameters, thereby reducing computational costs and uncovering non-intuitive solutions. Consequently, neural networks have become indispensable for rapid, data-driven metamaterial design, pushing innovation forward by enabling more thorough and efficient exploration of vast parametric spaces.

1.9 Thesis organisation

This thesis is structured into seven chapters. The **first chapter** gives an overview of research and development in terahertz metamaterials, with a focus on broadband terahertz metamaterials. The **second chapter** outlines the technical details of the methods used in this research.

In the **third chapter**, we designed and fabricated planar metamaterials incorporating multiple bending strip resonators. These resonators were specifically aimed at enhancing bandwidth through subwavelength coupling mechanisms. However, after a thorough investigation, we concluded that further enhancement of planar metamaterials is not feasible due to inherent

limitations, such as increased losses and fabrication challenges associated with higher resonator densities.

To address these limitations, in **chapter four**, we designed passive multistacked metamaterials. By stacking multiple layers of resonators, we achieved broadband resonance without sacrificing resonance strength. This approach effectively broadened the spectral response, making it more suitable for broadband terahertz applications. The multistacked structures were meticulously engineered to optimize interlayer coupling and minimize losses, resulting in enhanced performance compared to traditional planar designs.

Recognizing the need for active control in terahertz devices, in **chapter five**, we designed actively tunable terahertz broadband modulators, specifically focusing on band-pass and band-reject filters. We explored the use of vanadium dioxide (VO_2) for active modulation in terahertz metamaterials. VO_2 exhibits a phase transition from an insulating to a metallic state when heated above a certain temperature, resulting in significant changes in its electrical and optical properties. By integrating VO_2 into metamaterial designs, we achieved dynamic control over the terahertz response. We carefully engineered the VO_2 layers within the metamaterial structure to optimize the modulation depth and operational bandwidth. Thermal activation of VO_2 allowed us to switch the metamaterial's properties rapidly, enabling applications in tunable filters and modulators.

Designing and fabricating metamaterials is inherently challenging due to the complex interactions between their subwavelength structures and electromagnetic waves. Traditional design methods involve extensive computational techniques, such as Finite-Difference time domain (FDTD) simulations and genetic algorithms, which are computationally intensive and often rely on a trial-and-error approach. To streamline the design process, in **chapter six**, we employed machine learning (ML) techniques, particularly deep learning, for the design and optimization of metamaterials. We developed a neural network model trained on a dataset of metamaterial structures and their corresponding electromagnetic responses. This model enabled rapid prediction of metamaterial properties based on structural parameters, significantly reducing the need for time-consuming simulations. By utilizing ML algorithms, we efficiently explored a vast design space, identified optimal configurations, and accelerated

<table>
<tr><td colspan="4">Chapter 1 : Introduction of Terahertz, Metamaterial and Broadband Modulator.</td></tr>
<tr><td colspan="4">Chapter 2: Methods and models.</td></tr>
<tr><td>Theis Organization</td><td>Passive MM</td><td>Active MM</td><td>ML-MM</td></tr>
<tr><td>Planar MM</td><td>Chapter 3: Bending strip-based MM.</td><td colspan="2">Further enhancement of the FWHM is not possible without compromising the strength of the resonance.</td></tr>
<tr><td>Multistacked MM</td><td>Chapter 4: Multistacked MM, an ultrabroad band reject filter.</td><td>Chapter 5: Tunable band pass and band reject filter using VO_2-based Hybrid metamaterial.</td><td>Chapter 6: Ultra-broadband band reject filter using Machine learning.</td></tr>
<tr><td colspan="4">Chapter 7: Summary of the thesis and future possibilities.</td></tr>
</table>

Figure 1.19: Thesis organization chart outlining the progression of research on terahertz broadband metamaterials.

the development of new metamaterial structures with desired properties.

In the final chapter, **chapter seven**, we summarize the thesis and discuss future possibilities for the work. We reflect on the advancements made in broadband terahertz metamaterial design, the integration of active tuning mechanisms using VO_2, and the application of machine learning in metamaterial optimization. Additionally, we outline potential future research directions, including further exploration of tunable materials, scaling the designs to higher frequencies or different spectral regions, and the development of metamaterial-based devices for specific applications in communication and sensing technologies.

In summary, this thesis presents comprehensive research on the development of broadband terahertz metamaterials. Through innovative design strategies, including the use of multiple bending strip resonators in planar metamaterials, the advancement to passive multistacked structures, and the integration of VO_2 for active tuning, we have addressed key challenges in enhancing bandwidth and achieving tunability. Additionally, the application of machine learning techniques has significantly improved the metamaterial design process, enabling more efficient and effective development of advanced terahertz devices.

Chapter 2: Methodology

This chapter provides a comprehensive overview of the methods used to design, fabricate, and characterize terahertz metasurface devices. Section 2.1 discusses the computational approach utilizing CST Microwave Studio, detailing the essential steps involved in modelling and simulating metasurface structures. Section 2.2 describes the cleanroom fabrication processes, emphasizing the specialized equipment and precise techniques necessary for producing high-quality samples. Section 2.3 introduces the terahertz time-domain spectroscopy (THz-TDS) method, explaining how it is used to experimentally assess and validate the performance of the fabricated metasurfaces.

2.1 Design through numerical simulation

The design and analysis of metasurfaces were carried out using CST Microwave Studio Suite, a powerful 3D electromagnetic simulation software. CST solves Maxwell's equations through advanced numerical techniques like the Finite Integration Technique (FIT) and Finite Element Method (FEM), ensuring accurate modelling of complex electromagnetic structures. Its comprehensive material library, along with options to define custom materials, supports frequency-dependent models such as Drude and Lorentz, enabling precise simulations. By extracting key parameters like transmission (S_{21}), reflection (S_{11}), and detailed field distributions, CST provides valuable insights into resonance behaviour and aids in the efficient optimization of metasurface designs.

2.1.1 Selection of Solvers:

CST offers various kinds of solvers, each suited to specific scenarios:

- **Time-domain solver**: This approach uses the Finite Integration Technique (FIT) to discretize Maxwell's integral equations and efficiently compute broadband responses in a single simulation run. The results are then converted into frequency spectra using Fast Fourier Transform (FFT). This solver is particularly effective for electrically large structures, as it captures fine frequency details without requiring additional computational effort.
- **Frequency-domain solver**: This solver employs the Finite Element Method (FEM) and performs simulations at discrete frequencies, making it particularly efficient for electrically small or narrowband structures. It includes adaptive meshing to enhance accuracy across specified frequency steps.
- **Asymptotic solver**: This solver applies the Shooting Bouncing Ray (SBR) method, an advanced ray-tracing approach that extends physical optics for high-frequency analysis. It is ideal for electrically very large models where full-wave methods are impractical, and is commonly used for installed antenna performance, radar cross-section analysis, and large-scale scattering problems.
- **Eigenmode solver**: Designed for analyzing resonant behaviors, this solver uses the Advanced Krylov Subspace (AKS) method and the Jacobi-Davidson method (JDM) to compute eigenfrequencies and field distributions. It is ideal for high-Q structures such as filters, cavities, and slow-wave devices. Sensitivity analysis is also supported to evaluate performance under structural variations.
- **Hybrid solver**: This solver combines multiple numerical methods, such as full-wave and asymptotic techniques, within a unified simulation environment. It enables co-simulation of different regions in a single setup, making it well-suited for multiscale

problems, complex system integration, EMC/EMI analysis, and antenna placement on large platforms.

2.1.2 Meshing and Boundary Conditions

Meshing is a crucial step in electromagnetic simulations, involving the division of the computational domain into smaller regions known as mesh cells. These cells serve as the basis for solving Maxwell's equations, enabling the calculation of electric and magnetic fields within each cell. The quality of the mesh, determined by the size, shape, and number of these cells, directly impacts both the simulation's accuracy and its computational efficiency. A finer mesh can capture rapid variations in electromagnetic fields with greater precision, particularly in regions of high field gradients. However, this increased accuracy comes at the cost of greater computational effort and longer simulation times. Conversely, coarser meshing reduces computational demands but risks oversimplifying critical details, leading to inaccuracies in the results. Figure 2(a) illustrates the trade-off between simulation accuracy and speed. Optimal meshing can be achieved by carefully balancing the need for accuracy with computational efficiency.

In frequency-domain simulations, tetrahedral meshing is typically employed. This type of meshing adapts well to complex geometries and automatically refines itself in regions where the field gradients are significant. Such refinement ensures high accuracy, especially for intricate designs. Frequency-domain simulations involve transforming Maxwell's integral equations into the frequency domain using Fourier analysis, where the time derivative operator $\frac{\partial}{\partial t}$ is replaced by its frequency-domain counterpart, $i\omega$. This approach is particularly effective for analysing resonance phenomena, narrowband responses, and systems requiring steady-state solutions. Additionally, it provides results for all ports in a single calculation, offering computational efficiency for specific applications.

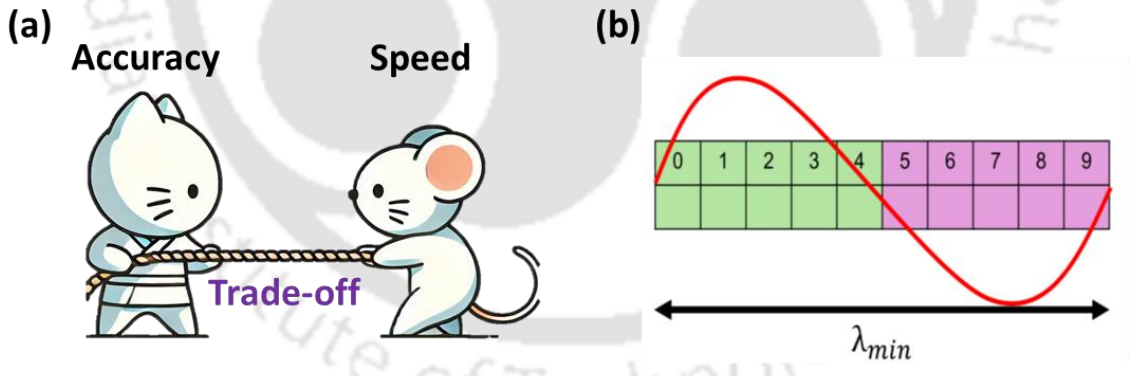

Figure 2.1: (a) Trade-off between accuracy and speed: A good mesh achieves a good compromise between simulation speed and accuracy. (b) To ensure that the simulation is accurate across all frequencies of interest, the mesh needs to be fine enough to accurately represent the shortest wavelength in the simulation (at least 10 meshes cells per wavelength).

In contrast, time-domain simulations utilise hexahedral meshing composed of uniform cuboidal cells. This meshing type is well-suited for broadband simulations, such as those involving Gaussian pulses, as it allows the capture of a wide range of frequencies in a single run. The uniform structure of hexahedral meshes ensures computational stability while maintaining sufficient accuracy for broadband analyses. The resolution of the mesh is a critical factor in ensuring simulation accuracy. To minimise numerical dispersion, where different frequencies propagate at slightly different speeds due to spatial discretisation, the shortest wavelength of interest must be sampled by at least 10 mesh cells. Failure to meet this criterion can lead to

distorted results, particularly at higher frequencies. In time-domain simulations, the Courant stability condition governs the maximum allowable time step, linking it to the smallest mesh cell size. The time step is mathematically expressed as[94]:

$$\Delta t_{max} \leq \left(u_{max} \sqrt{\frac{1}{\Delta x^2} + \frac{1}{\Delta y^2} + \frac{1}{\Delta z^2}} \right)^{-1}, \tag{2.1}$$

Where Δx, Δy and Δz are the dimensions of the mesh cell, and u_{max} is the maximum wave phase velocity. For uniform cuboid mesh cells ($\Delta x = \Delta y = \Delta z = \Delta l$), the formula simplifies to:

$$\Delta t_{max} \leq \left(\frac{\Delta l}{\sqrt{3} u_{max}} \right). \tag{2.2}$$

This relationship underscores a trade-off: smaller mesh cells enhance resolution and accuracy but require smaller time steps, significantly increasing simulation time. Larger mesh cells, while reducing computational effort, may compromise accuracy, especially in regions with high field gradients or intricate structural details.

Advanced simulation tools, such as CST Microwave Studio, employ techniques like adaptive meshing to balance accuracy and computational efficiency. Adaptive meshing dynamically refines the grid in critical regions with rapid field variations while allowing coarser meshing in less significant areas. This approach minimizes computational demands without sacrificing precision, ensuring reliable and efficient simulation outcomes.

Boundary Conditions: After setting up the mesh, defining appropriate boundary conditions is equally important for ensuring accurate and realistic simulation outcomes. In frequency-domain simulations, boundary conditions in the XY plane are often configured as 'Unit Cell' to efficiently model a periodic metamaterial array, emulating an infinite arrangement of identical cells while minimising computational load. In the *Z* direction, an 'Open' boundary

Figure 2.2: The steps and required details for proceeding with the CST software.

condition is typically used to simulate free-space propagation, allowing waves to exit the domain without reflecting back into the structure. To reduce the impact of fringing fields near Z_{max} $(+Z)$, CST introduces an 'Open (add space)' boundary by default, adding a gap of $(\lambda_{central}/4)$. This setup is critical for maintaining accurate phase and amplitude responses in metamaterial simulations. By carefully refining the mesh and selecting boundary conditions tailored to the geometry and physics of the problem, simulations can closely match real-world behaviour while remaining computationally feasible. Figure 1.2 provides a flow chart for designing the metamaterial using CST software.

Port Definition: In order to excite the metamaterial and analyze its transmission characteristics, ports were placed at both ends of the Z-direction. Waveguide ports were used, which are ideal for planar structures and allow CST to calculate S-parameters such as S_{11} and S_{21}. These ports were defined with a characteristic impedance of 50 ohms, and the fundamental mode was selected to ensure that the correct excitation profile is used for the incoming wave. Proper placement and sizing of the ports are essential to avoid exciting higher-order modes or causing impedance mismatches, which could distort the results. For certain specific applications, discrete or lumped ports can also be used, but waveguide ports remain the standard choice in metamaterial transmission mode analysis due to their accuracy and compatibility with periodic boundaries.

Post-Processing: After completing the simulation, post-processing in CST Studio Suite is a critical phase for interpreting and analysing the results to extract meaningful electromagnetic parameters. The primary outputs are the S-parameters, particularly S_{21} (transmission coefficient) and S_{11} (reflection coefficient), which provide insights into the frequency-dependent response of the metamaterial. These parameters are essential for identifying resonance frequencies, operating bandwidths, and transmission efficiency.

Beyond S-parameters, CST Studio Suite offers a comprehensive suite of post-processing tools to visualise and analyse the electromagnetic behaviour within the metamaterial structure. Field plots, including electric (E-field) and magnetic (H-field) distributions, are generated to examine internal phenomena such as field confinement, enhancement, and interaction with subwavelength features. Surface current distributions can also be visualised to understand the current flow patterns, which are crucial for identifying resonant modes and potential loss mechanisms.

For metamaterial characterisation, CST provides specialised templates to extract effective material parameters such as permittivity (ε), permeability (μ), and refractive index (n) from the simulated S-parameter data. These templates utilise retrieval methods based on established algorithms to compute the effective parameters, facilitating the assessment of the metamaterial's electromagnetic properties. Furthermore, CST Studio Suite includes advanced post-processing capabilities such as parameter sweeps and optimisation tools. Parameter sweeps allow for systematic variation of geometric or material properties to study their impact on performance metrics like resonance frequency and bandwidth. Optimisation tools enable automated tuning of design parameters to achieve desired electromagnetic responses, enhancing the efficiency of the design process.

By leveraging these post-processing features, simulations can closely replicate real-world behaviour, providing a robust platform for the accurate design and analysis of high-performance metamaterials. Figure 1.2 provides a flow chart outlining the major steps involved in designing and simulating the metamaterial structure using CST Studio Suite, beginning from geometry creation to boundary setup, excitation, simulation, and post-processing analysis.

2.2 Fabrication of Metamaterials

Fabrication of metamaterials can mainly be done using two different approaches: the etching method and the lift-off method. In the etching method, a photoresist pattern is used to selectively remove portions of a deposited metal layer, leaving behind the desired metamaterial structure. This technique is widely adopted for high-precision pattern transfer and is particularly useful for multilayer metamaterial fabrication. One key advantage of this method is that it significantly reduces the risk of unintentionally removing or lifting off the entire structure during the resist removal stage, which can be a concern with the lift-off approach. On the other hand, the lift-off method involves first patterning the photoresist, followed by metal deposition. The photoresist is then dissolved, lifting away the metal on top of it and leaving behind the desired patterned metal features. This method is generally useful for clean edge definition and when working with sensitive substrates.

In the present thesis, the etching method was employed for the fabrication of all planar and multilayer metamaterial samples, except in Chapter 2, where the lift-off method was used for a specific structure and is discussed separately in that chapter. Fabricating planar and multilayer metamaterials requires a meticulous lithography process to ensure high-quality and reproducible structures. This section outlines the fabrication workflow, from substrate preparation to metal etching, used to create the metamaterials presented in the thesis work. The detailed steps of the planar metamaterial fabrication are given as follows:

1. **Substrate Cleaning**: The process begins with cleaning the substrate to ensure surface quality and reproducibility. Loosely adhering contaminants are removed by blowing a strong nitrogen (N_2) flow over the substrate. The substrate is then immersed in a heated acetone bath at 80°C and subjected to ultrasonic cleaning for 10 minutes to dislodge stubborn organic residues. After cleaning, the substrate is taken out of the acetone, dried with N_2 gas, and polished gently using acetone-soaked lens-cleaning paper. This process is repeated until no visible residues remain, verified by illuminating the substrate under a strong light source. The substrate is rinsed with isopropyl alcohol (IPA) and dried again with N_2 gas. To remove residual moisture, the substrate is heated at 100°C on a hot plate for 10 minutes.
2. **Metallization**: A 200 nm-thick aluminium layer is deposited on the cleaned substrate using a thermal evaporator. This thickness exceeds the skin depth of aluminium in the terahertz frequency range, minimising partial transmission through the resonators. The deposited aluminium layer forms the foundation for the metamaterial features to be defined in subsequent steps.
3. **Surface Preparation with HMDS**: To improve the adhesion of the photoresist layer, the substrate is treated with hexamethyldisilazane (HMDS). The HMDS is applied using a spin coater at 3500 RPM for 60 seconds, followed by heating the sample at 150°C for 30 minutes to ensure optimal bonding.
4. **Photoresist Spin Coating and Pre-Bake**: A positive photoresist (S1813) is spin-coated onto the substrate to achieve a thickness of 1.3 µm. This is done by spinning the sample at 3000 RPM for 60 seconds. After coating, the substrate undergoes a soft-bake process on a hot plate at 120°C for 2 minutes to remove excess solvent and improve uniformity and adhesion.
5. **UV Exposure or Mask Writing:** The photoresist-coated substrate is patterned using either UV exposure or direct laser writing. In the case of UV exposure, the substrate is aligned under a photomask, and UV light is applied using a mask aligner. Alternatively, a mask writer can be used to write the desired pattern directly at the micrometre level. For most of the work presented in this thesis, direct laser writing was performed using a DILASE-250 mask writer, which enables high-resolution pattern generation.

6. **Development**: After UV exposure, the substrate is immersed in the M319 developer solution for 60 seconds to remove the exposed photoresist regions. The unexposed areas remain intact, serving as a mask for the subsequent etching step. The substrate is then rinsed with deionized water and dried with N_2 gas.
7. **Pattern Transfer by Metal Etching**: The developed photoresist serves as a mask for the underlying metal. The substrate is immersed in an aluminium etchant for 2 to 3 minutes to selectively remove the unmasked aluminium regions. After etching, the remaining photoresist is stripped away using acetone or a dedicated resist remover, leaving the metal pattern that defines the metamaterial structures.
8. **Post-Processing**: The substrate is cleaned using acetone and deionized water, dried with N_2 gas, and heated on a hot plate at 100°C for 5 minutes to remove residual moisture. The fabricated samples are inspected using optical microscopy, profilometry, or scanning electron microscopy (SEM) to confirm the patterned features.

By following the systematic steps of cleaning, metallization, surface preparation, photoresist coating, UV exposure, development, and metal etching, high-quality planar metamaterial structures can be reliably fabricated. Precise control of each parameter in this lithography process ensures reproducibility and optimal performance of the fabricated devices. The presented fabrication methodology was consistently used throughout this thesis to create periodic metamaterial arrays with excellent pattern fidelity and robust functionality. For the multistacked metasurface structures, where multiple layers are aligned one over the other, we used either a double-sided mask aligner or a mask writer for precise alignment of the meta-atoms. The methodology for multilayer stacking is discussed in the specific chapter where multistacked metamaterial studies are presented.

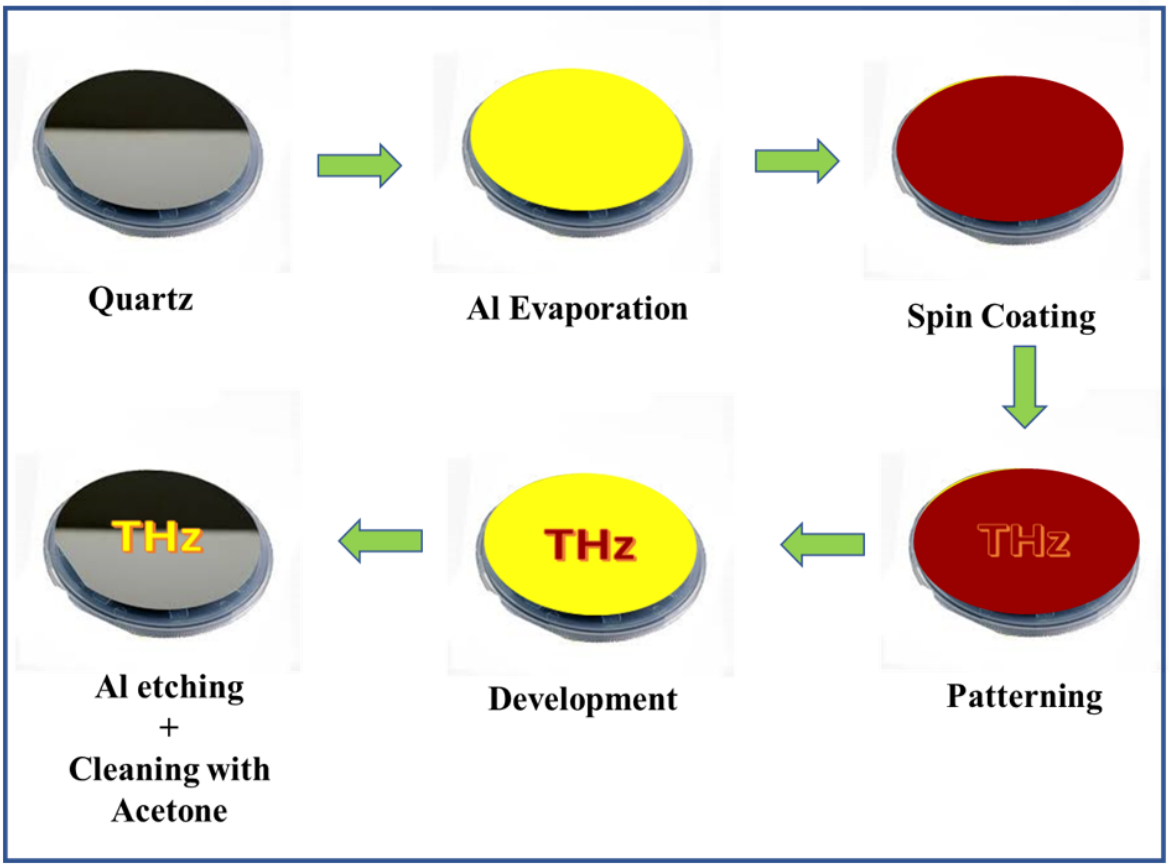

Figure 2.3: Schematic diagram of the fabrication steps performed to obtain a single-layer metamaterial structure.

2.3 Terahertz Time Domain Spectroscopy and Metamaterials Characterisation

Terahertz time-domain spectroscopy (THz-TDS) is a powerful technique for characterizing metamaterials in the terahertz frequency range. In this section, we discuss how terahertz waves can be generated using photoconductive antennas (PCAs) and optical rectification in nonlinear crystals. We also describe the detection of terahertz signals through PCAs and ZnTe crystals. Following this, we present a typical THz-TDS setup, highlighting the working principles of photoconductive antennas, the role of optical crystals for detection, and the importance of the delay line in obtaining time-resolved signals. Finally, we conclude with a discussion on the practical applications of THz-TDS, emphasizing its usefulness in characterizing terahertz metamaterials and its broader applicability in other fields.

2.3.1 Terahertz generation

Terahertz sources are generally categorized based on their operating principle, frequency range, and emission mode, with two main types: continuous wave (CW) and pulsed (time-domain) systems. In CW systems, the THz emission typically arises from frequency multiplication, and most operate at frequencies of up to about 0.8 THz in a narrowband manner with limited tunability. However, they can achieve high spectral resolution (around 100 MHz), which is particularly advantageous for spectroscopic applications. Certain CW sources, such as quantum cascade lasers and backward-wave oscillators, can reach up to 5 THz but are expensive and often require cryogenic cooling to function effectively. These CW systems can operate in passive or active modes and generally provide higher output power than pulsed sources. In contrast, pulsed or time-domain THz systems use ultrafast femtosecond lasers to produce picosecond-duration electromagnetic transients. This can be achieved using photoconductive antennas (PCAs) or by leveraging the nonlinear optical response of bound electrons in materials like ZnTe. Because the femtosecond pulses contain a broad range of frequencies, the resulting THz emission is inherently broadband. Pulsed THz sources also offer simultaneous amplitude and phase measurements (i.e., they are coherent) and enable time-of-flight techniques for depth or thickness profiling in samples.

2.3.1.1 Photo-Conducting Antenna (PCA)

Photoconductive antennas (PCAs) are widely used for generating and detecting terahertz radiation because they can operate at room temperature and do not require high-power laser sources. By utilizing a femtosecond laser pulse along with a moderate bias voltage, PCAs are capable of producing relatively high-power THz radiation with a reasonable bandwidth.

The operating principle of THz generation using a photoconductive antenna is illustrated in Figure 2.4(b). A PCA consists of two metal electrodes that are deposited on a semiconductor

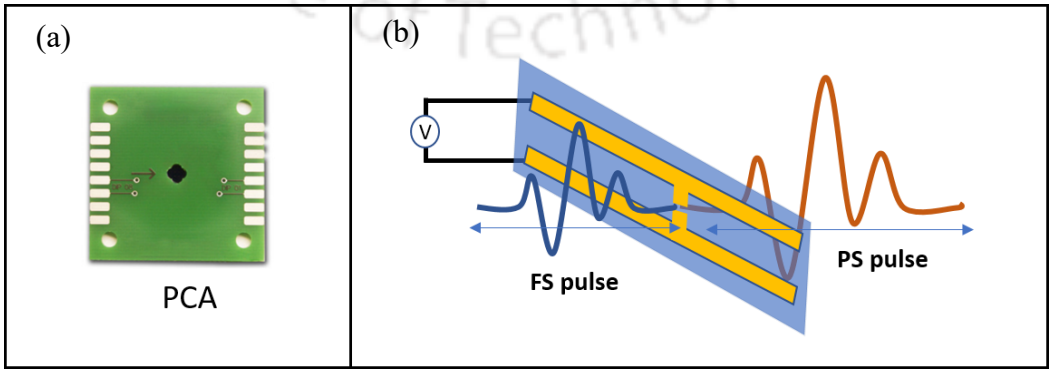

Figure 2.4:(a) shows the picture of PCA antenna. (b)A schematic of the photo-conductive antenna. The transient current is generated when the fs-laser pulse hits the electrode's gap. This transient current will produce the EM pulse of ps-duration.

substrate[95, 96]. These electrodes are connected to a DC voltage and separated by a small gap that is typically larger than the semiconductor's bandgap. When a focused femtosecond laser pulse strikes this gap, it generates electron-hole pairs within the semiconductor. These charge carriers are then rapidly accelerated by the external bias field, producing a transient photocurrent that lasts for approximately sub-picoseconds.

According to Maxwell's equations, this rapidly changing photocurrent emits an electromagnetic pulse of a similar duration. The current density J(t) within the gap can be expressed as:

$$\boldsymbol{J}(t) = N(t)\mu e\boldsymbol{E_b} \tag{2.3}$$

Where N, μ, e, and E_b are the density of charge carriers, mobility of carriers, electric charge and biasing electric field, respectively. The electric field generated by the time-varying photocurrent is given by

$$\boldsymbol{E}_{THz} \propto \frac{d\boldsymbol{J}(t)}{dt} \propto \frac{d\boldsymbol{N}(t)}{dt}. \tag{2.4}$$

The energy of the terahertz field originates from the electrical potential energy stored in the biased gap of a photoconductive antenna (PCA). Prior to optical excitation, this energy is stored in the form of a capacitive charge across the gap. When a laser pulse generates charge carriers (electron-hole pairs), the sudden increase in carrier concentration causes a drop in resistivity, allowing current to flow. The rapid change in current, driven by the bias field, results in the emission of THz radiation. This process converts a portion of the stored electrical energy into electromagnetic radiation in the terahertz frequency range.

The efficiency of this process is influenced by several factors, including the properties of the photoconductive material, the bias voltage, and the characteristics of the laser pulse. A higher generation of charge carriers leads to greater conversion of stored energy into THz radiation.

The performance of photoconductive antennas depends on various parameters, such as the semiconductor's bandgap, carrier lifetime and mobility, electrode gap, and bias voltage. PCAs can be designed as either resonant or non-resonant. Resonant PCAs produce THz radiation centred around a specific frequency determined by the spacing of the electrodes, whereas non-resonant PCAs, with adjustable electrode gaps, provide a broader frequency bandwidth.

2.3.1.2 Optical Rectification

Optical rectification is another well-established method for generating THz radiation. Under low incident-light intensities, the polarization $\boldsymbol{P}$ of a material is directly proportional to the electric field $\boldsymbol{E}$, as shown in[97]

$$\boldsymbol{P}(\boldsymbol{r},t) = \chi\boldsymbol{E}(\boldsymbol{r},t) \tag{2.5}$$

However, in nonlinear materials exposed to intense laser pulses (typically ultrafast femtosecond pulses), higher-order terms become significant, and the polarization can be expressed as

$$\boldsymbol{P}(\boldsymbol{r},t) = \chi^{(1)}\!:\boldsymbol{E}(\boldsymbol{r},t) + \chi^{(2)}\!:\boldsymbol{E}(\boldsymbol{r},t)\boldsymbol{E}(\boldsymbol{r},t) + \chi^{(3)}\!:\boldsymbol{E}(\boldsymbol{r},t)\boldsymbol{E}(\boldsymbol{r},t)\boldsymbol{E}(\boldsymbol{r},t) + \cdots \tag{2.6}$$

When the second-order susceptibility $\chi^{(2)}$ is nonzero, this leads to optical rectification, which can be understood as a difference-frequency mixing process in which various frequency components of the laser pulse interfere to generate lower-frequency radiation in the THz range. For an incident plane wave, the time-dependent polarization that contributes to the THz field

may be written as

$$\boldsymbol{P_{OR}(t) = 2\chi^{(2)} \iint_0^\infty E(w+\Omega)E'(w)e^{-i\Omega r}\, d\Omega dw} \tag{2.7}$$

Here, $\boldsymbol{\Omega}$ is the difference between the two frequency components of the laser pulse, whereas $\chi^{(2)}$ is the second-order susceptibility, depending on the material crystalline structure. The radiated electric field due to the EO-induced polarization can be expressed as follows

$$\boldsymbol{E_{THz} \propto \frac{\partial J(t)}{\partial t} \propto \frac{\partial^2 p(t)}{\partial t^2} \propto \chi^{(2)} \frac{\partial^2}{\partial t^2} E_{laser}(t)} \tag{2.8}$$

which shows that no external bias voltage is required, unlike in photoconductive antenna-based THz sources. Several factors influence the efficiency of THz generation by optical rectification, including the material's nonlinear coefficients, phase-matching conditions, crystal thickness, and absorption or dispersion in both the optical and THz frequency ranges. ZnTe is a commonly used crystal for THz generation because it has a relatively high second-order nonlinear susceptibility ($\chi^{(2)}$), favourable phase-matching conditions for near-infrared pulses (such as those at 800 nm), and moderate phonon absorption in the THz range. Other options include GaP, GaSe, and $LiNbO_3$, which can be used depending on the desired bandwidth, laser wavelength, and acceptable absorption characteristics.

A significant advantage of optical rectification is that it is a non-resonant process. This means

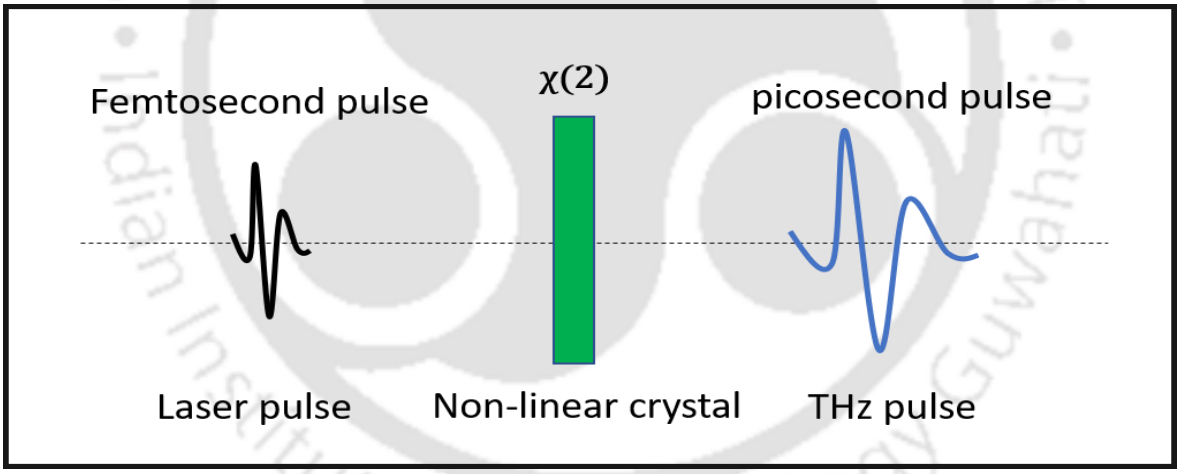

Figure 2.5: Schematic of terahertz generation by the optical-rectification method. When the fs-pulse passes through a non-linear medium, it converts into ps-pulse due to the optical rectification effect.

the THz pulse bandwidth is not limited by the intrinsic response time of the medium but rather by the duration of the ultrafast laser pulse and by phonon absorption in the crystal. Additionally, the absence of an external bias circuit simplifies the experimental setup when compared to photoconductive emitters. Besides optical rectification and photoconductive antennas, other methods for generating THz radiation include Photo-mixing, the Photo-Dember effect, and backwards-wave oscillators. Each method has its own advantages and limitations (see table 2.1), which depend on factors like wavelength tunability, output power, and spectral coverage.

2.3.2 Terahertz detection

Table 2.1: Advantages and limitations of the different THz sources

Source	Advantages	Limitations
Photoconductive antenna	✓ Broadband	✗ Small output power ✗ Bulky
Electro-optical conversion	✓ Broadband	✗ Small output power ✗ Bulky
Optical Rectification	✓Moderate output power ✓ High frequency	✗ Bulk
QC laser	✓ High integration ✓ Moderate output power	✗ Low frequency ✗ Small tunability
BW oscillator	✓ High tunability ✓ High output power	✗ Bulky ✗ Low frequency

A key characteristic of any terahertz detector is its frequency sensitivity range. In practice, broadband THz detectors are primarily divided into two categories: thermal detectors (Class A) and pulsed detectors (Class E). Thermal detectors, mainly bolometers, are traditionally used in Fourier-transform spectroscopy, while pulsed detectors are employed in time-domain spectroscopy (TDS). As a result, Class A and Class E detectors are the most suitable for THz spectroscopy. This discussion will focus on THz detection using pulsed methods.

2.3.2.1 Terahertz Detection through PCA

Detection of terahertz radiation using a photoconductive antenna (PCA) operates on a principle

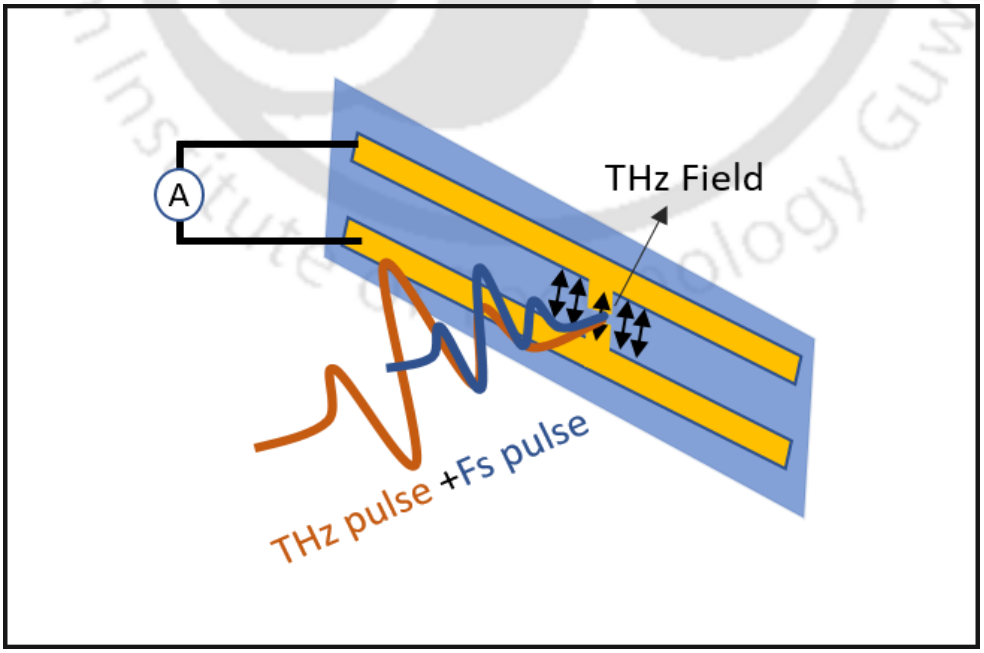

Figure 2.6: Detection of terahertz wave using photo conducting antenna. Laser pulse and THz wave hit simultaneously on the gap of the antenna. The fs pulse generates carriers and the THz wave act as a bipolar field that biases the antenna.

similar to PCA-based THz generation, but it does not require an external DC bias voltage. Instead, an ammeter is connected in place of the voltage source to measure the current generated by the terahertz radiation field. Both the generated THz radiation and the femtosecond (fs) laser pulse are directed to arrive simultaneously at the antenna's gap region. The fs pulse excites charge carriers in the semiconductor substrate, while the incoming THz field itself biases the antenna, resulting in a transient current that is proportional to the instantaneous THz field. Figure 6 illustrates the operating principle of a photoconductive antenna in detection mode[96].

It is important to understand that photoconductive antennas (PCAs) designed for detection are different from those intended for terahertz emission. Detection PCAs typically have much narrower antenna gaps, around 10 µm, which allows for a smaller electric field to generate a measurable current. In contrast, emission PCAs can have gaps that exceed 50 µm. The factors that influence the performance of PCAs in detection are similar to those that affect PCA emitters, including the semiconductor bandgap, carrier lifetime and mobility, and the dimensions of the antenna gaps.

2.3.2.2 Terahertz detection using EO Crystal

Terahertz detection in non-centrosymmetric materials is facilitated by the Pockels effect, which induces a refractive index change proportional to the external electric field. This phenomenon modifies the material's birefringence so that when a femtosecond (fs) optical probe pulse and a THz pulse propagate simultaneously through the crystal, the fs pulse undergoes a phase modulation tied to the THz-induced refractive-index change. Because the probe pulse is much shorter than the THz pulse, it effectively samples a nearly static electric field at each point in time. The phase modulation of the probe manifests as a polarization change, which is then converted into an intensity difference through an appropriate detection scheme[98] (See Figure 2.7).

In practice, a linearly polarised probe pulse first passes through a polariser before entering the electro-optic (EO) crystal. In the absence of a THz field, the probe remains linearly polarised, and the quarter-wave plate (QWP) is aligned such that it converts this linear polarisation into

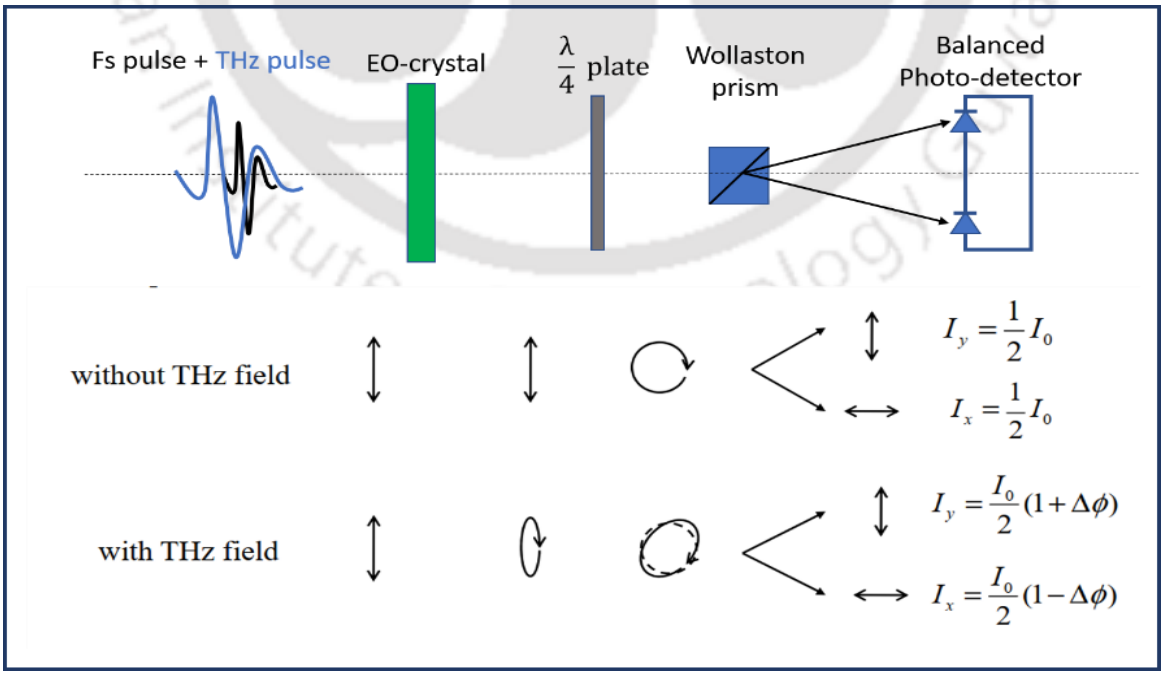

Figure 2.7: Terahertz detection using EO-crystal. Laser pulse and THz pulse co-propagate through the nonlinear medium. The phase of the fs pulse is modulated due to the induced refractive index caused by the THz field. Phase change can be measured by measuring intensity change at the detector end.

circular polarisation. A Wollaston prism splits this circularly polarized light into two orthogonal components of equal intensity, and a balanced photodiode pair then produces a zero differential signal. However, when a THz field is present, it alters the refractive index of the crystal differently along orthogonal axes. As a result, the probe's polarization acquires an additional phase shift proportional to the strength of the THz field. After passing through the QWP, the probe becomes slightly elliptical; the Wollaston prism thus generates two beams with unequal intensities. A photodiode assembly in differential mode measures the resulting intensity difference, which is directly related to the THz field amplitude. By controlling the temporal overlap of the fs and THz pulses, it is possible to map out the THz waveform in time. The detection scheme is provided in Figure 2.7.

A key advantage of electro-optic sampling (EOS) is its ability to directly and quantitatively measure the electric field amplitude of a THz pulse with sub-picosecond resolution. This phase-resolved detection allows reconstruction of both the magnitude and polarity of the THz waveform. Unlike photoconductive antennas, which may degrade under high-intensity optical probing, EOS is more robust as it involves no current flow through the crystal. These attributes make electro-optic sampling the preferred method for high-field THz measurements, providing reliable, sensitive detection of ultrafast THz signals. The comparison of the strengths and weaknesses of both techniques is given in Table 2.2.

Table 2.2: Advantages and limitations of different THz detectors.

Detector	Advantages	Limitations
Photoconductive antenna	✓ Fast response ✓ Moderate sensitivity	✗ Low detection current ✗ Relatively expensive
Electro-optical conversion	✓ Broad spectral response ✓ Fast response ✓ Moderate sensitivity	✗ Complex readout ✗ Relatively expensive

2.3.3 Terahertz Time Domain Spectroscopy (THz-TDS): Working principle

Terahertz Time-Domain Spectroscopy (THz-TDS) is a powerful spectroscopic technique that employs short pulses of terahertz radiation to probe and characterize the intrinsic properties of various materials. Unlike conventional Fourier-transform spectroscopy, which is primarily sensitive to the amplitude of spectral components, THz-TDS captures both the amplitude and phase information of the THz wave[99, 100]. This dual-domain analysis allows for a more comprehensive understanding of material properties such as refractive index and absorption coefficients. In a typical THz-TDS setup, an ultrashort near-infrared (NIR) laser pulse, typically shorter than 100 femtoseconds (fs), is first split into two distinct beams using a beam splitter. The beam with a higher power, known as the pump beam, is directed towards a photoconductive (PC) antenna to generate the THz pulse (The detailed working principle is discussed in section 2.31.1)

Simultaneously, the lower power beam, referred to as the probe beam, is directed towards a mechanical delay line. The mechanical delay line, typically consisting of a movable mirror (more specifically, a retroreflector) mounted on a translation stage, precisely controls the temporal overlap between the probe and the THz pulses by adjusting the optical path length of the probe beam. This precise temporal control is essential for sampling the time-dependent electric field of the THz pulse at different moments, thereby enabling the reconstruction of the full time-domain waveform of the THz signal through successive measurements.

For detection, the probe beam interacts with the THz-induced electric field within a zinc

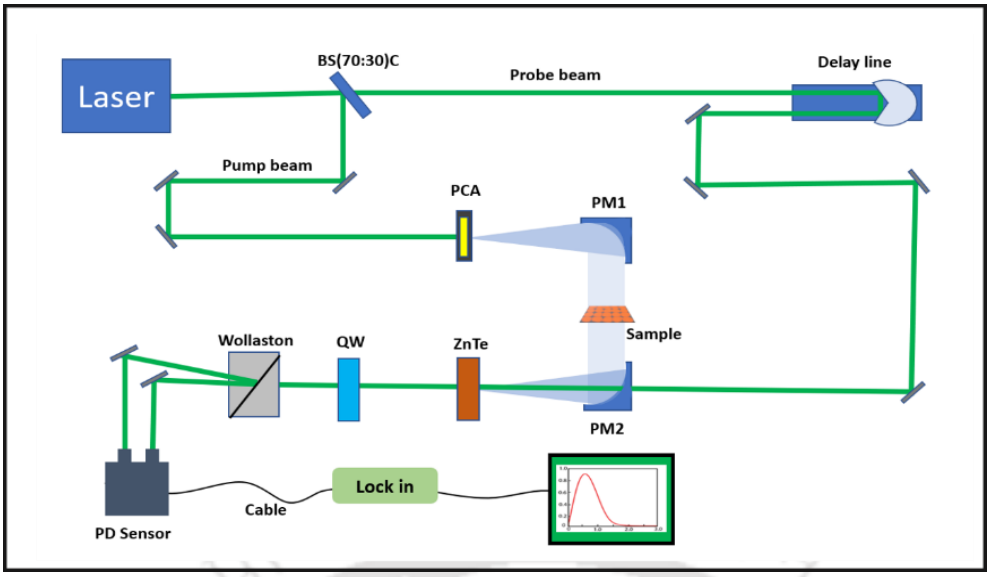

Figure 2.8: Schematic of THz-TDS setup. PCA is used for generation, and ZnTe for the detection of THz radiation.

telluride (ZnTe) electro-optic (EO) crystal via the Pockels effect. The Pockels effect causes a linear change in the refractive index of the ZnTe crystal in response to the external THz electric field, thereby modifying the crystal's birefringence. As the femtosecond probe pulse propagates through the EO crystal, the induced birefringence results in a phase modulation of the probe beam's polarization state. If the probe beam is initially linearly polarized at 45° to the principal axes of the ZnTe crystal, the THz field induces a slight ellipticity in its polarization after passing through the crystal.

After exiting the EO crystal, the probe beam passes through a quarter-wave (λ/4) plate, which introduces a 90° phase shift between the orthogonal ordinary (o-ray) and extraordinary (e-ray) polarization components, effectively converting the slightly elliptically polarized light into circularly polarized light. This circular polarization is then split into two orthogonal, linearly polarized beams of equal intensity by a Wollaston prism. In the absence of a THz field, both beams have equal intensities, and a pair of balanced photodiodes arranged in a differential configuration detect no net current. However, when a THz pulse is present, the induced birefringence in the ZnTe crystal alters the probe beam's polarization state, resulting in an imbalance between the intensities of the two orthogonal beams. This intensity difference (I_s=I_x-I_y) is directly proportional to the amplitude of the THz electric field. The schematic ray diagram of the THz-TDS is shown in Figure 2.8.

The differential current generated by the photodiodes is amplified and converted into a voltage signal by a preamplifier. A lock-in amplifier is employed to accurately extract the THz-induced modulation from the probe beam. The lock-in amplifier synchronizes with modulation frequency of bias voltage applied to the photoconductive emitter, effectively enhancing the signal-to-noise ratio by filtering out extraneous noise and isolating the signal corresponding to the THz modulation. To measure the spectral response of a sample, we first have to record the reference waveform of this THz radiation (spectrum without sample) and then the signal waveform (THz-wave transmitted through the sample). If the Fourier transform of reference waveform and signal waveform is given by $A_r(w)e^{-i\emptyset_r(w)}$ and $A_s(w)e^{-i\emptyset_s(w)}$, The spectrum properties such as absorption and refractive index of the sample can be calculated by[101]

$$\alpha(w) = \frac{1}{d} ln \frac{A_r(w)}{A_s(w)} \tag{2.9}$$

$$\eta = 1 + \frac{\{\emptyset_s(w) - \emptyset_r(w)\}c}{wd} \tag{2.10}$$

Where *d* is the thickness of the sample and *c* is the speed of light in a vacuum. These equations are valid for transmission mode only. The complex value of the refractive index can also be calculated by reflection spectroscopy, which can be used to calculate the complex electric permeability.

Chapter 3: Broadening of resonance in the planar terahertz metamaterial

Introduction

As discussed in section 1.4, recent years have seen extensive research into various metamaterial designs, including split-ring resonators, single-strip resonators, fishnet structures, and cross-shaped geometries. These designs are known for their ability to produce narrowband resonances, which are valuable in applications such as filtering, sensing, frequency selection, and modulation. However, there is a growing interest in expanding the capabilities of metamaterials to include applications that require a broad spectral response, such as cloaking devices, broadband filtering, and absorption.

Despite some advancements, achieving broadband terahertz responses in planar metamaterials remains challenging. Most planar metamaterials primarily focus on creating multiband resonance dips, where the fundamental resonance mode typically dominates. Applications requiring broad spectral coverage necessitate the enhancement and broadening of these fundamental resonances. To address this need, we explored a novel planar metamaterial geometry designed to broaden the fundamental resonance while maintaining strong

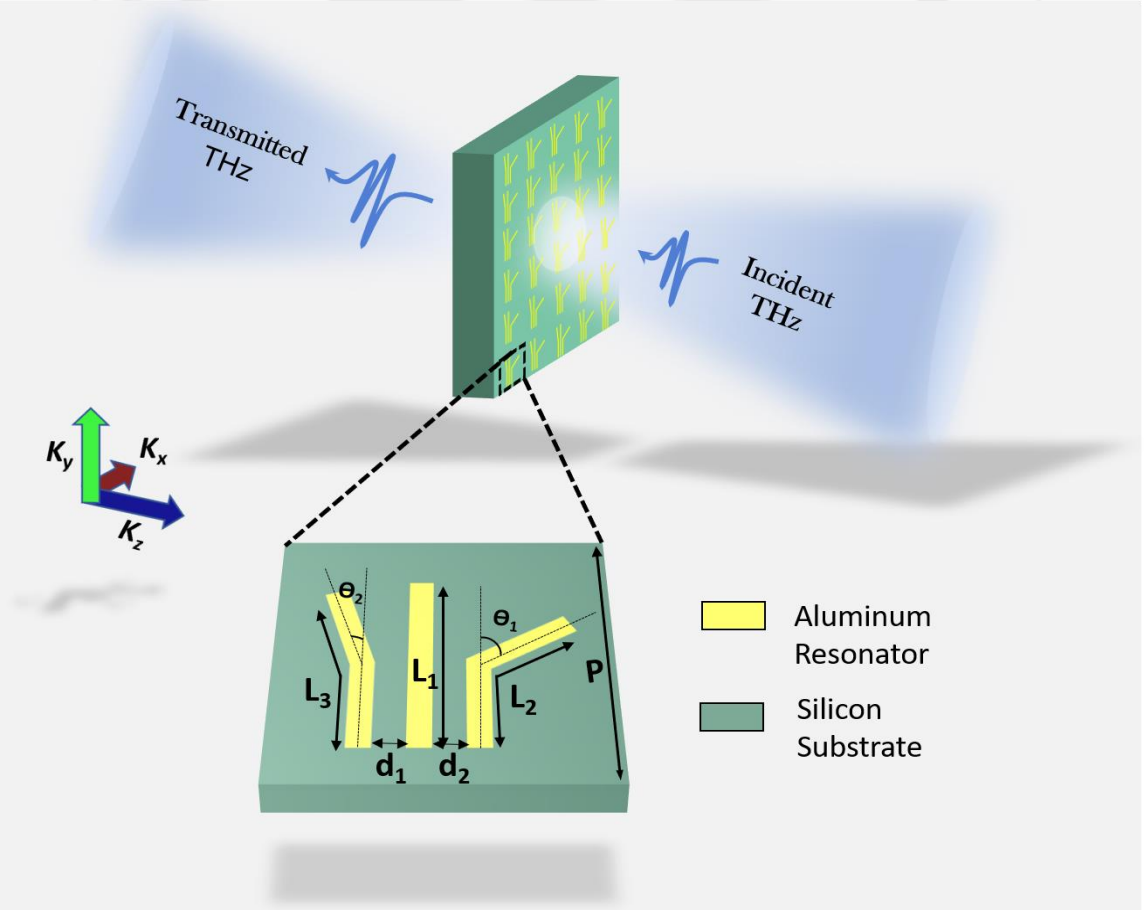

Figure 3.1: depicts the design of a bending strip resonator-based metamaterial. The inset figure shows the unit cell of the metamaterial. The metamaterial consists of three strip resonators, two of which are bending at angles $\theta_1 = 50°$ and $\theta_2 = 8°$. The lengths of the resonator are $L_1 = 50$ µm, $L_2 = 50$ µm, and $L_3 = 52$ µm, respectively. The width (w) of each resonator, the separation between two resonators, and the periodicity of the metamaterial are given as $w = 5$ µm, 2.5 µm, and 68 µm respectively.

electromagnetic interactions.

This work presents a planar metamaterial design consisting of three-strip resonators. The central resonator initially exhibits narrowband behaviour. However, the strategically positioned and optimally bent additional strips enhance coupling, resulting in a significant broadening of the resonance. Section 3.2 details the design process and includes a parametric study focused on the bending of the resonators. In Section 3.3, we examine how the geometry of the resonators affects broadband transmission. The fabrication and characterisation of these designs are discussed in Section 3.4, along with a comparison between simulation and experimental results. Section 3.5 analyses the coupling mechanisms by exploring electric field distributions and contour plots. Section 3.6 employs a harmonic oscillator model to clarify the observed broadening behaviour. Finally, Section 3.7 summarises the findings and discusses their implications for terahertz applications.

3.1 Design and Simulation

To design the planner broadband MM, we utilized CST Microwave Studio Suite, a commercially available numerical software. This software employs the finite-element method (FEM) to iteratively solve Maxwell's equations with user-defined boundary conditions, as discussed in detail in section 2.1. Our study focused on three specific designs of strip resonators. Initially, we designed a single-strip resonator (SR_1) that exhibited a sharp resonance at 0.96 THz. The full width at half maximum (FWHM) and reject bandwidth (RBW) at 20% transmission were calculated to be 160 GHz and 63 GHz, respectively. To achieve a broader resonance dip, we introduced a second strip resonator (SR_2), bent at an optimized angle of $\theta_1 = 50°$ from the middle of the strip, as shown in Figure (3.2b). The intention was to maximize the broadening effect in the fundamental resonance dip. In this case, the FWHM and RBW were calculated to be 270 GHz and 120 GHz, respectively. In order to further enhance the FWHM

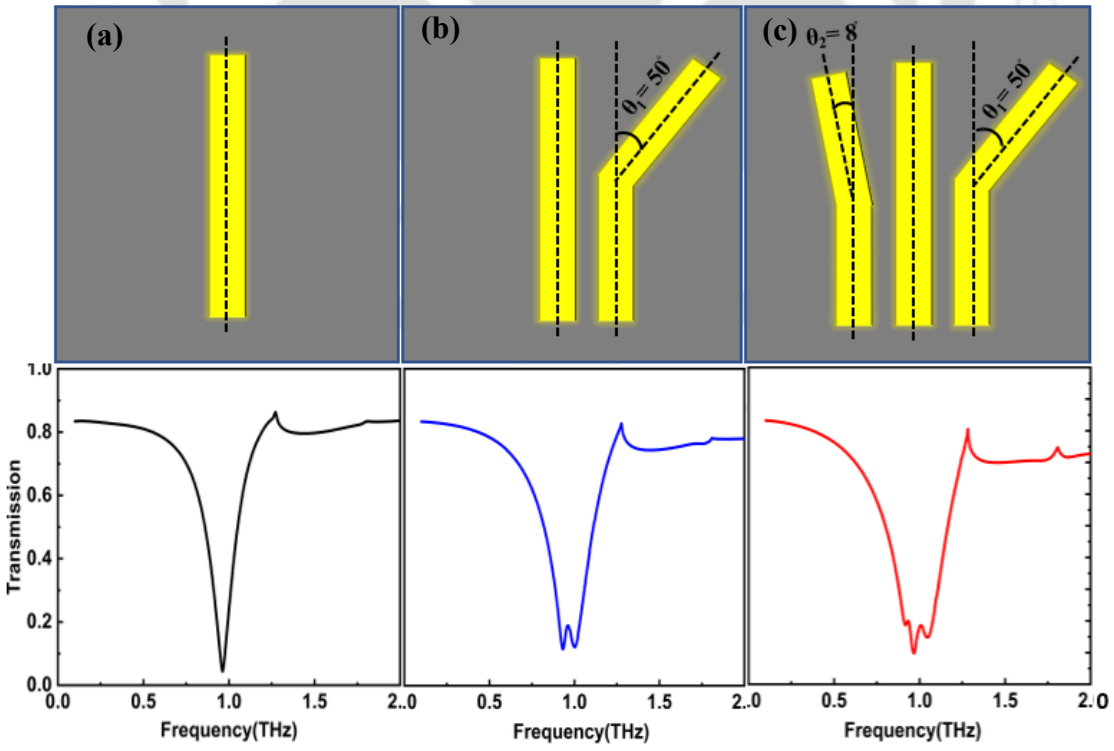

Figure 3.2: Depicts the unit cell and corresponding simulated transmission amplitude with respect to terahertz frequency. For two resonator-based MM the optimized angle (where the FWHM and RBW are maximum) is $\theta_1 = 50°$ and for three resonators-based MM the optimized angle $\theta_2=8°$ (keeping the $\theta_1 = 50°$ fixed).

and RBW, we again incorporated an additional strip resonator (SR_3) at an optimum angle of θ_2 = 8° (see Figure (3.2c)). In this case, the maximum FWHM and RBW were calculated to be 350 GHz and 160 GHz, respectively. All resonators were designed on a silicon substrate, with strip resonators made of aluminium. The lengths of the strip resonators were taken as follows: L_1 = 50 µm, L_2 = 50 µm, and L_3 = 52 µm. The width (w) of each resonator, the separation between two resonators, and the periodicity of the MM were w = 5 µm, d=2.5 µm, and p=68 µm, respectively. To ensure accurate modelling, we employed a finite mesh size of λ/10. The unit cell boundary conditions were applied to the x and y-axis, while an open boundary condition was imposed along the positive and negative z-axis. The incident terahertz radiation was predominantly oriented perpendicular to the sample plane, with the electric field (E-field) aligned parallel to the strip resonators. In our study, we considered the silicon substrate to be loss-free, and the aluminium metal serving as the material for the strip resonators was considered to be lossy, with an electrical conductivity of 3.5×10^7 S m^{-1}. The schematic diagram and unit cell of the proposed planar MM is given in Figure 3.1.

3.2 Effect of bending the strip resonators on transmission

To understand the role of bending strip resonators SR_2 and SR_3 in broadening the resonance, we bend SR_2 and SR_3 from the middle at angles θ_1 and θ_2, respectively. Initially, in the two-resonator strip-based metamaterial design, we varied the bending angle θ_1 from 0° to 60° while keeping all other parameters fixed. Figure 3(a) illustrates that as θ_1 increases, the FWHM of the fundamental resonance dip increases until 50° and then starts decreasing. A similar response

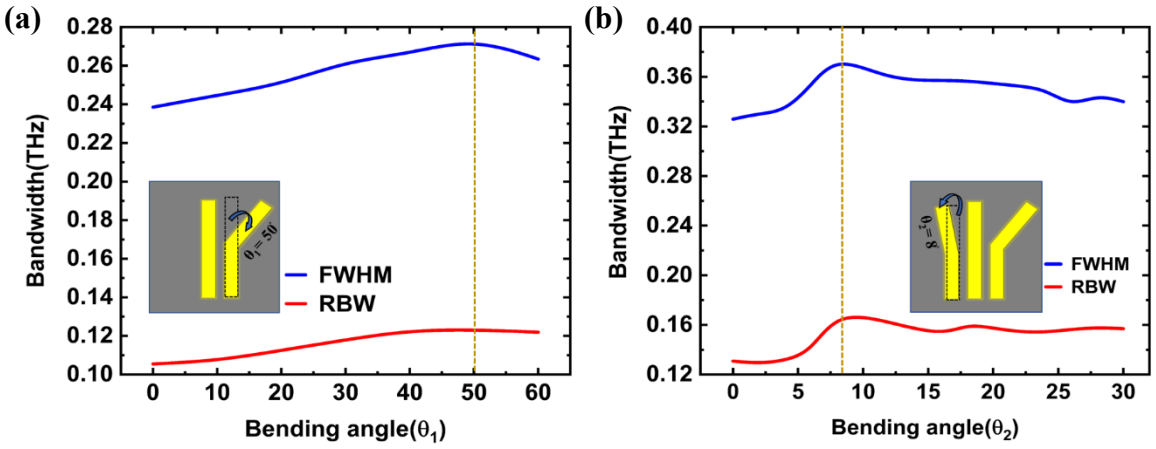

Figure 3.3: shows the FWHM and RBW corresponding to the different bending angles for the two resonators and three resonators-based MM. Optimized bending angles for the two resonators-based MM is θ_1 = 50°. and the optimized bending angle for the three resonators-based MM is θ_2 = 8° keeping the θ_1 fixed at 50°.

can be observed for the RBW, it increases until θ_1 = 50° and then remains constant as the angle θ_1 is further increased. Therefore, the maximum resonance bandwidth for the two-resonator-based MM can be achieved at an optimum angle of 50°. To further enhance the broadening of the transmission resonance dip, an additional strip, SR_3, was added to the left side of strip SR_1. By varying the bending angle θ_2, keeping θ_1 fixed at 50° along with the other parameters, we observed that the FWHM and the RBW could be enhanced up to 350 THz and 160 THz, respectively, when θ_2 reached 8° (see Figure 3.3(b)). However, beyond θ_2 = 8°, the FWHM and RBW start decreasing. This parametric sweep helped us obtain optimum angles of bending for maximum enhancement in FWHM. At θ_1 = 50 and θ_2 = 8°, the total enhancement in FWHM and RBW compared to the single strip configuration was obtained at 195 THz and 65 THz, respectively. The bending of strips at optimum angle resulted in the enhancement of over 200

% in FWHM. This is believed to be caused by strong coupling between resonators, which is discussed in section 3.5.

3.3 Experiment: Fabrication and characterization

To experimentally verify the boarding effect of resonance in transmission, a series of fabrication steps were followed to create the desired pattern on a silicon substrate. Initially, the silicon sample was thoroughly cleaned using acetone, isopropyl alcohol (IPA), and distilled or deionized (DI) water to eliminate any impurities. Subsequently, the sample was dried using N_2 gas and heated at 100°C for 10 minutes using a hot plate to ensure complete moisture removal. A 200 nm thick layer of aluminium metal was then deposited onto the clean substrate using a thermal evaporator. The thickness of the metal was chosen to be higher than the skin depth of the metal in the terahertz range to avoid partial transmission from the resonators. To enhance the adhesion of the photoresist to the substrate, a coating of hexamethyldisilazane (HMDS) was applied at a rotational speed of 3500 RPM for 60 seconds, followed by heating the sample at 150°C for 30 minutes to facilitate optimal bonding. The pre-coated substrate was further coated

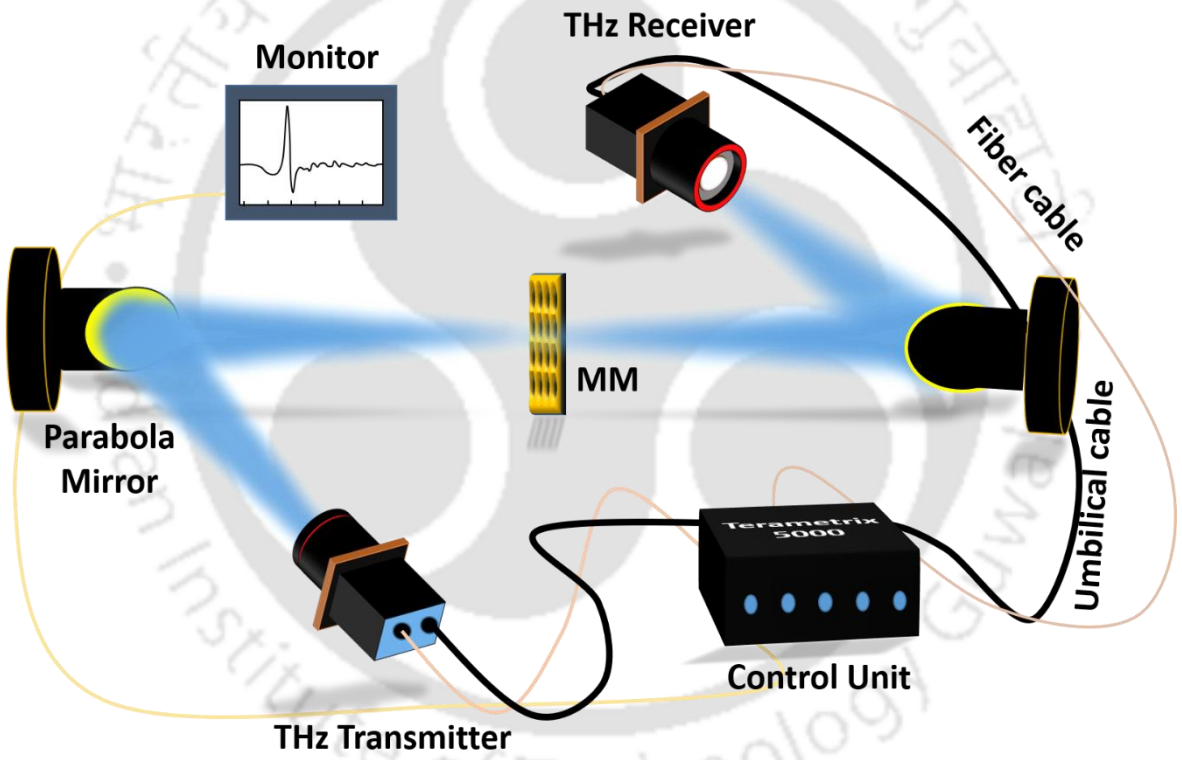

Figure 3.4: Schematic of the THz-TDS setup used for experimental characterization of the metamaterial: The T-RAY 5000 control unit delivers precisely controlled optical signals to the fiber-coupled photoconductive antennas for THz generation and detection. The metamaterial sample is positioned between tightly focused parabolic mirrors, and the THz-TDS signal is obtained on the monitor in the time domain. It is then converted to the frequency domain using FFT.

with a positive photoresist (S1813) of thickness 1.3 um, by spinning the sample at 3000 RPM for 60 seconds. Subsequently, the photoresist-coated substrate underwent a 2-minute baking process at 100°C to promote uniformity and stability. For pattern generation, a hard mask was employed, and the sample was exposed to UV light to induce the desired pattern formation. After exposure, the sample was developed in M319 solution for 60 seconds, selectively removing the photoresist from the exposed areas, thus leaving the desired pattern on the substrate. To selectively etch the unmasked metallic part, an aluminum etchant was utilized for

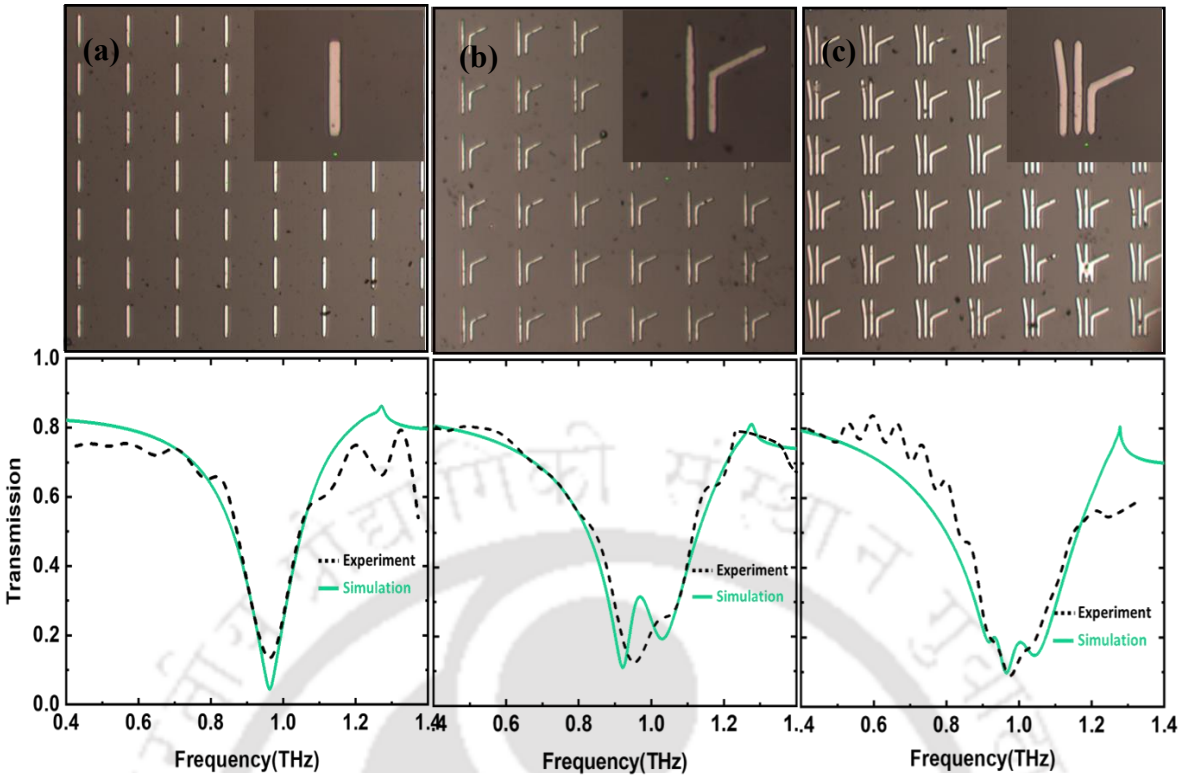

Figure 3.5. (a), (b), and (c) illustrates the fabricated samples for single, double, and triple strip resonator-based metamaterials respectively. Corresponding measured and simulated transmission with respect to frequency plots are provided below each metamaterial structure. The simulation and measured transmission spectra exhibit a close match, demonstrating FHWM broadening as the number of bending resonators was gradually increased with an optimum angle.

a duration of 2 to 3 minutes, resulting in the formation of the desired pattern. Following the fabrication process, the sample underwent thorough cleaning with acetone and DI water, followed by drying using N_2 gas. Final drying was achieved by heating the sample for 5 minutes at 100°C to ensure complete removal of any residual moisture. The fabricated metamaterial samples consisted of periodic arrays of designed metamaterial that were prepared on a 1 cm × 1 cm region. Three sets of samples were fabricated, including single-strip, double-strip, and triple-strip-based metamaterials. Terahertz transmission measurements were conducted using a switch-based THz time-domain spectroscopy (THz-TDS) setup from LUNA Innovations (Terametrix 5000 T-Ray). Fibre-coupled photoconductive antennas (PCA) were employed for both THz generation and detection. The transmitted signal was focused onto the metasurface sample using a parabolic mirror, which was further directed towards the THz receiver in an optimized configuration. The THz-TDS spectrum was obtained initially for a bare silicon substrate, serving as the reference signal. Subsequently, the spectrum was obtained for the metasurface sample. The time-domain signals were transformed into frequency-domain signals using fast Fourier transformation (FFT), and the ratio of the metamaterial spectrum to the reference spectrum provided the transmission through the sample. The schematic of the THz-TDS setup used for this study is shown in Figure 3.4, and the fabricated samples and experimentally calculated transmission spectra (along with the simulation results) for single double and triple resonators-based MM are given in figure 3.5. The simulation and measured transmission spectra exhibit a close match, demonstrating FHWM broadening as the number of bending resonators gradually increases with an optimum angle.

3.4 Deep Subwavelength Coupling

To elucidate the physical mechanism behind the broadening of the transmission resonance spectrum, we conducted a comprehensive analysis by plotting the electric field distribution at various frequencies (position of the frequencies represented by the dashed line in the graph) of the terahertz transmission in an optimum configuration of strip resonators for three distinct cases (see the figure 3.6). The first case involved a straight single strip, while the second case comprised two strips, with one strip (SR_2) bent at an angle of $\theta_1=50^{\circ}$. In the third case, we examined a three-strip configuration, with the first strip (SR_2) bent at an angle of $\theta_1=50^{\circ}$ and the second strip (SR_3) bent at $\theta_2=8^{\circ}$. As illustrated in Figure 3.6(a), it clearly indicates that the

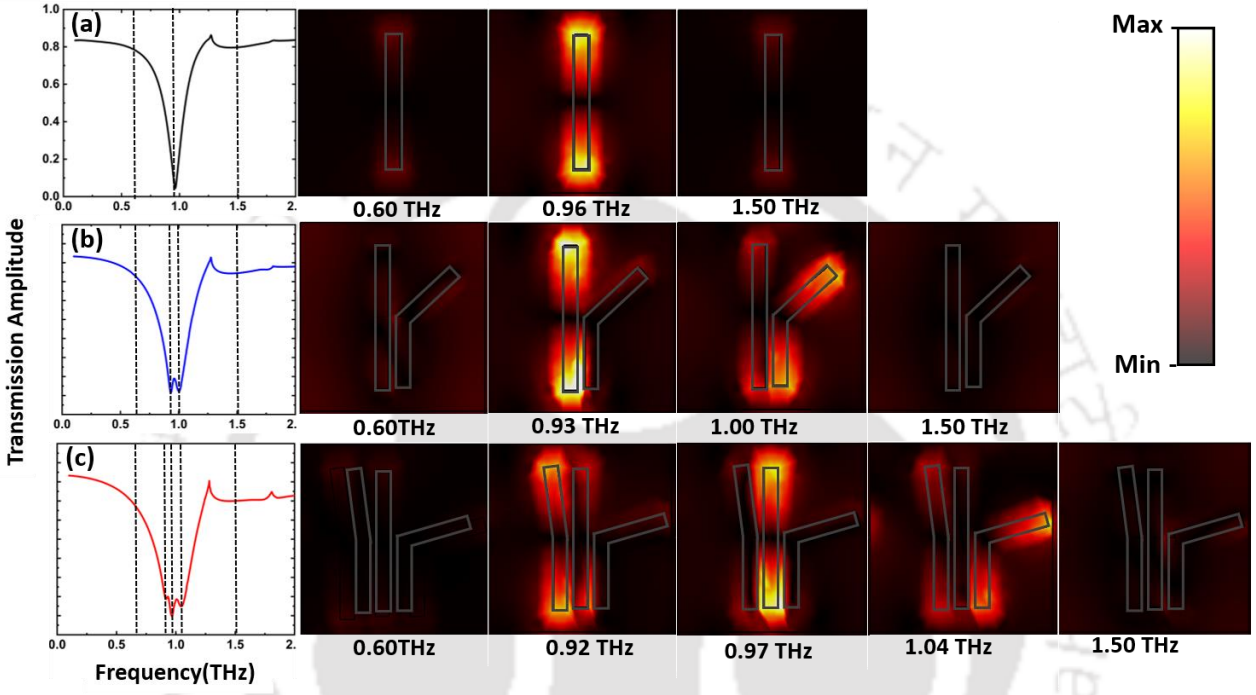

Figure 3.6: The electric field distribution at different resonances is shown. (a) illustrates the electric field resulting from a single resonator, while (b) and (c) demonstrate the electric field distribution caused by double and triple resonators based on metamaterials (MM). The single resonance is attributed to dipole interaction in the single straight resonators, while the merging of two or three resonances (broadening of resonance) is a result of coupling between the two or three resonators. The field at the off-resonance is also calculated, indicating that there is no excitation of the resonances apart from the resonant frequencies. This indicates that the broadening of the resonances is caused by the coupling between them.

resonance dip observed in a single resonator is a consequence of dipole interaction. Upon introducing an additional bending strip (SR_2) adjacent to the first strip (SR_1), dipole excitation occurred at frequencies of 0.97 THz and 1.12 THz, resulting in two close dips. Moreover, the figure reveals a partial coupling between the two strip resonators (figure 3.6(b)), leading to the merging of the two resonances into a single broadened resonance response. Furthermore, by incorporating a third bending strip (SR_3), a significant coupling effect was observed between the three resonators, amplifying the broadening of the fundamental resonance, as depicted in Figure 3.6(c). The electric field distribution outside the resonances does not indicate field confinement as expected. To verify the coupling between each resonator, transmission amplitude with respect to the separation of the resonators was studied, and the results are shown in Figure 3.7. Two cases were considered: one with two resonators and another with three

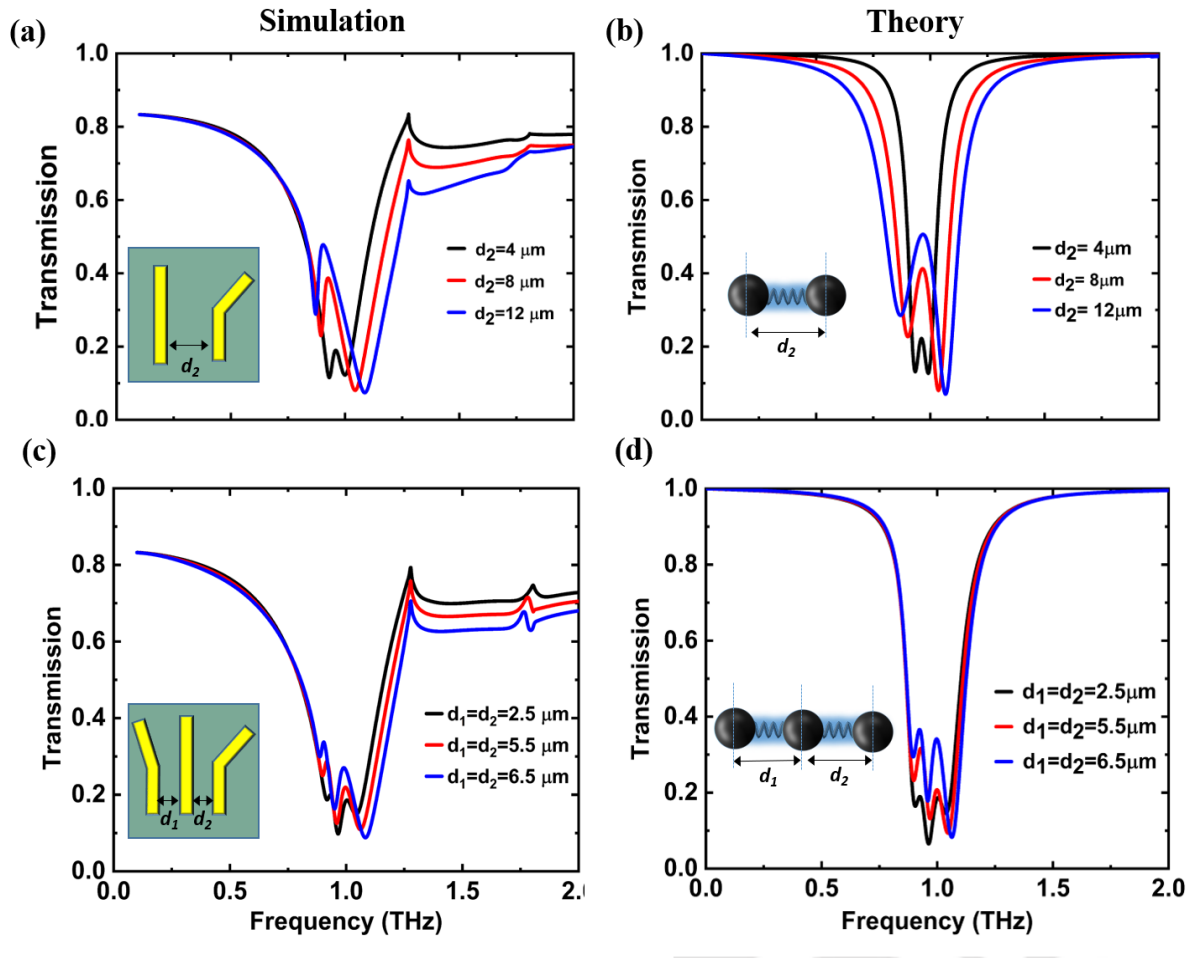

Figure 3.7: (a) depicts the transmission amplitude as a function of THz frequency for various separation distances (d_2). As the separation distance changes, the two merged resonances gradually separate, illustrating the decoupling of the resonators. (b) illustrates the transmission response for the three resonators. Similarly, as the separation distance ($d_1 = d_2$) between the three resonators increases, their individual responses become more distinct. (b) and (d) show the theoretically fitted transmission amplitude for different separation distances using the harmonic oscillator approach.

resonators. In the case of two resonators, it was observed from Figure 3.7(a) that increasing the separation distance (d_2) between the resonators led to the separation of the resonance frequencies. Initially, the two resonance frequencies were merged, but as d_2 was varied from 2 μm to 8 μm, they gradually separated from each other, indicating the decoupling of the

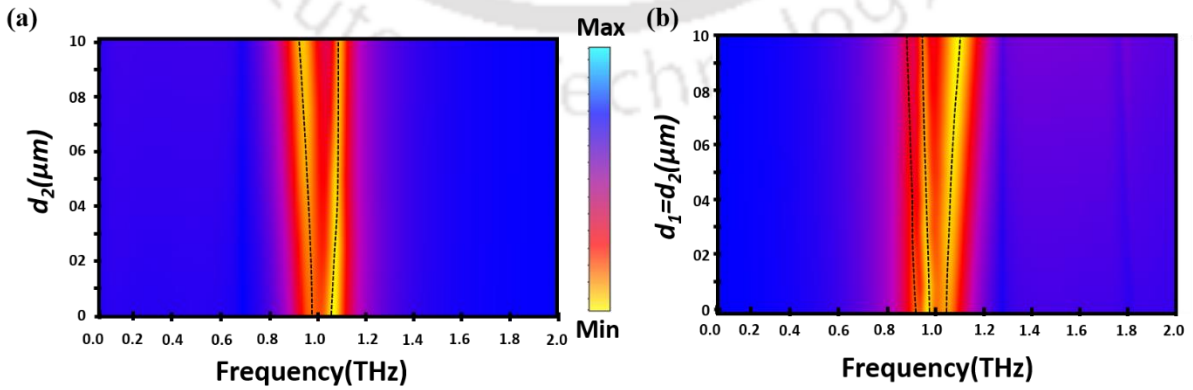

Figure 3.8(a) and (b) show contour plots for double and triple strip-based metamaterials, respectively, illustrating the effect of coupling between resonators concerning their separation. As the separation between the resonators increases, the resonance frequencies also move further apart from each other.

resonators. Similarly, for the three-resonator configuration, as the separation between three resonators ($d_1 = d_2$) was increased from 2.5 μm to 6.5 μm, the frequency dips were separated from each other, resulting in the decoupling of the resonators. These results clearly indicate the existence of strong coupling between the resonators, which is responsible for the broadening of the fundamental resonance from the straight resonators. Figures 3.7(b) and 3.7(d) show the theoretical fitting of the transmission amplitude with respect to the separation of the resonators using the harmonic oscillator approach. A detailed explanation is given in the next section. Figures 3.8(a) and 3.8(b) present the contour plots showing the coupling effect as the separation between resonators is varied. Notably, for larger values of "d_1" and "d_2", the resonances align closely with the resonance positions of individual resonators. These findings provide crucial insights into the coupling behaviour, frequency separation dynamics, and the underlying physical phenomena responsible for the broadening of the transmission spectrum in the studied configurations.

3.5 Theoretical modelling to understand the coupling between resonators:

To formally demonstrate the validation of transmission spectra obtained in simulation results, we employed a modelling approach based on the harmonic oscillator (OS), as outlined in references[102, 103]. In this context, each strip resonator can be treated as a harmonic oscillator. This section of the study is dedicated to a thorough investigation of the coupling strength between these strip resonators, achieved by varying both the separation distance(d) between the resonators and the bending angle(θ) of each individual resonator. The governing equations that describe the dynamics of the system involving three coupled resonators can be expressed in their differential form

$$\ddot{x}_1 + \gamma_1\dot{x}_1 + \omega_1^2 x_1 + \kappa_1^2 x_2 = \frac{Q_1}{M_1}E \tag{3.1}$$

$$\ddot{x}_2 + \gamma_2\dot{x}_2 + \omega_2^2 x_2 + \kappa_1^2 x_2 + \kappa_2^2 x_3 = \frac{Q_2}{M_2}E \tag{3.2}$$

$$\ddot{x}_3 + \gamma_3\dot{x}_3 + \omega_3^2 x_3 + \kappa_2^2 x_2 = \frac{Q_3}{M_3}E. \tag{3.3}$$

Here, the strip resonators, namely SR_1, SR_2, and SR_3, are represented as oscillators OS_1, OS_2, and OS_3, respectively. Additionally, the variables x_1, x_2, x_3 $\gamma_1, \gamma_2, \gamma_3, \omega_1, \omega_2$ and ω_3 correspond to the displacement, damping rate, and resonance frequencies of each resonator. These resonators have effective charges and masses denoted as (Q_1, Q_2, Q_3) and (M_1, M_2, M_3), respectively. The coupling strengths between oscillators OS_1 and OS_2, as well as between oscillators OS_2 and OS_3, are represented by κ_1 and κ_2. The incident THz electric filed is defined as $E = E_0 e^{\iota\omega t}$, here ω represent the frequency of incident THz radiation. We assumed a trial solution for displacement vector as $x_n = N_n e^{i\omega t}$, and solve equations (3.1), (3.2) and (3.3) for x_1,$x_2$and x_3 and relation between susceptibility(χ), polarization (P), and strength of incoming electric field (E) can be expressed as

$$\chi = \frac{P}{\varepsilon_0 E} = \frac{Q_1 x_1 + Q_2 x_2 + Q_3 x_3}{\varepsilon_0 E}$$

$$\chi = \frac{Q_1^2}{M_1\varepsilon_0}\left(\frac{\alpha_1\kappa_1^4+\alpha_2\kappa_2^4+\alpha_3\kappa_1^2+\alpha_4\kappa_2^2+\eta+\beta\kappa_1^2\kappa_2^2}{\kappa_2^4 C_2+\kappa_1^4 C_1-C_1C_2C_3}\right). \tag{3.4}$$

Where, $C_1 = \omega_1^2 - \omega^2 + i\omega\gamma_1, C_2 = \omega_2^2 - \omega^2 + i\omega\gamma_2, C_3 = \omega_3^2 - \omega^2 + i\omega\gamma_3, \beta = \frac{B_1+B_2}{A_1A_2}, \eta = C_2C_3 + \frac{B_1C_2C_3}{A_1^2} + \frac{B_2C_1C_2}{A_2^2}$ also, $\alpha_1 = -\frac{B_2}{A_2^2}, \alpha_2 = -\frac{B_1}{A_1^2}, \alpha_3 = -\frac{C_3}{A_1}(1+B_1), \alpha_4 = -\frac{C_2}{A_2}(1+B_2)$

and A_1, B_1, A_2 and B_2 are represented as, $A_1 = \frac{Q_1}{Q_2}, A_2 = \frac{Q_1}{Q_3}, B_1 = \frac{M_1}{M_2}$ and $B_2 = \frac{M_1}{M_3}$.

For two harmonics oscillators, we can reduce the three-differential equation into two [104, 105], and for this case, the relation between susceptibility(χ), polarization (P), and strength of incoming electric field (E) can be expressed as

$$\chi = \frac{P}{\varepsilon_0 E} = \frac{Q_1x_1+Q_2x_2}{\varepsilon_0 E}$$

$$\chi = \frac{K}{A_1^2B_1}\left(\frac{A_1(B_1+1)\kappa_1^2+A_1^2(\omega^2-\omega_2^2)+B_1^2(\omega^2-\omega_1^2)}{\kappa_1^4-(\omega^2-\omega_1^2+\iota\omega\gamma_1)(\omega^2-\omega_2^2+\iota\omega\gamma_2)} + i\omega\frac{A_1^2\gamma_1+B_1\gamma_2}{\kappa_1^4-(\omega^2-\omega_1^2+\iota\omega\gamma_1)(\omega^2-\omega_2^2+\iota\omega\gamma_2)}\right) \quad (3.5)$$

where all the symbols have the same meaning as described in the three-harmonic oscillator. The Transmission in the theoretical fitting is defined as $T = 1 - Im(\chi)$, which is the Kramers-Kronig relation and is derived from the conservation of energy principle: $T + A = 1$, where absorption (losses) within the medium is defined as $A = Im(\chi)$. The Kramers-Kronig relation [106] was used for fitting the models based on two-strip and three-strip resonators by varying the separation distance between the resonators and the bending angles of the individual resonators. Figures 3.7(b) and 3.7(d) depict the theoretically predicted transmission in relation

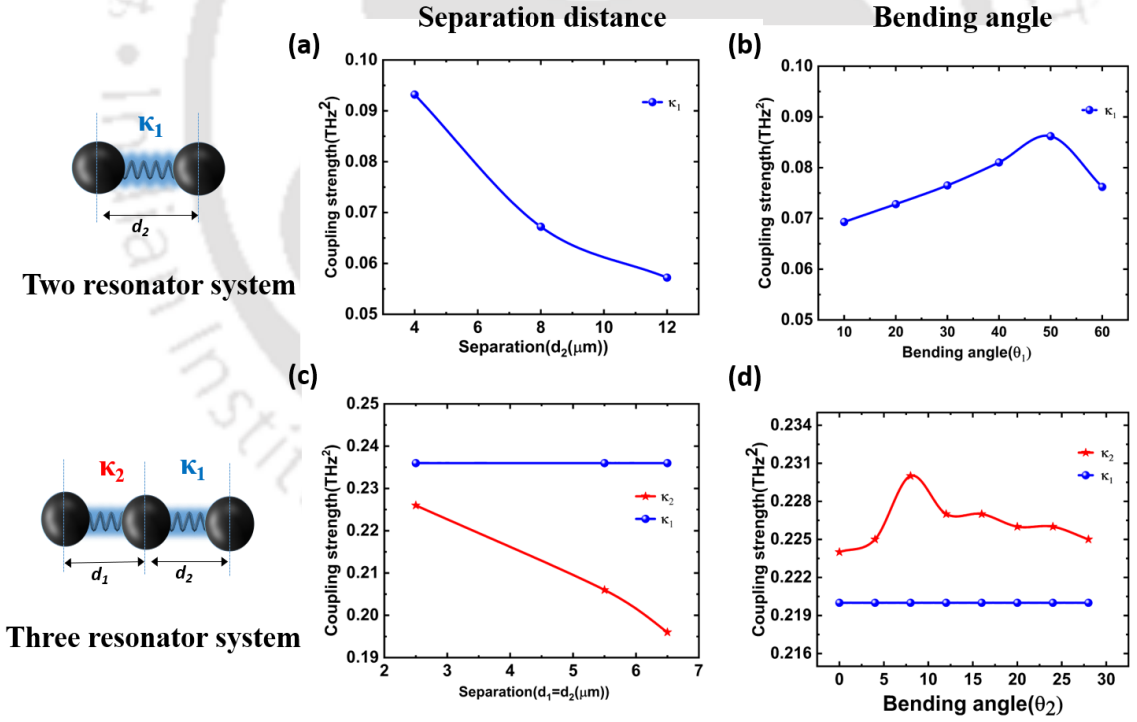

Figure3.9: (a) and (b) depicts the coupling strength between the resonators as the separation between resonators and bending angle θ_1 changes for two harmonic oscillator systems. (c) and (d) shows the change in coupling strength as the separation distance between the resonators and bending angle θ_1 changes (keeping θ_2 fixed at 50°). The coupling coefficient follows a similar trend to FWHM. This observation validates a proportional relationship between the coupling coefficient and FWHM.

to changes in the resonator's separation. This demonstrates a strong agreement with simulation results and validates the transmission amplitude spectrum. Observations from Figure 3.9(a) indicate that for the two-oscillator system, as d_2 increases from 4 µm to 12 µm, the coupling κ_1

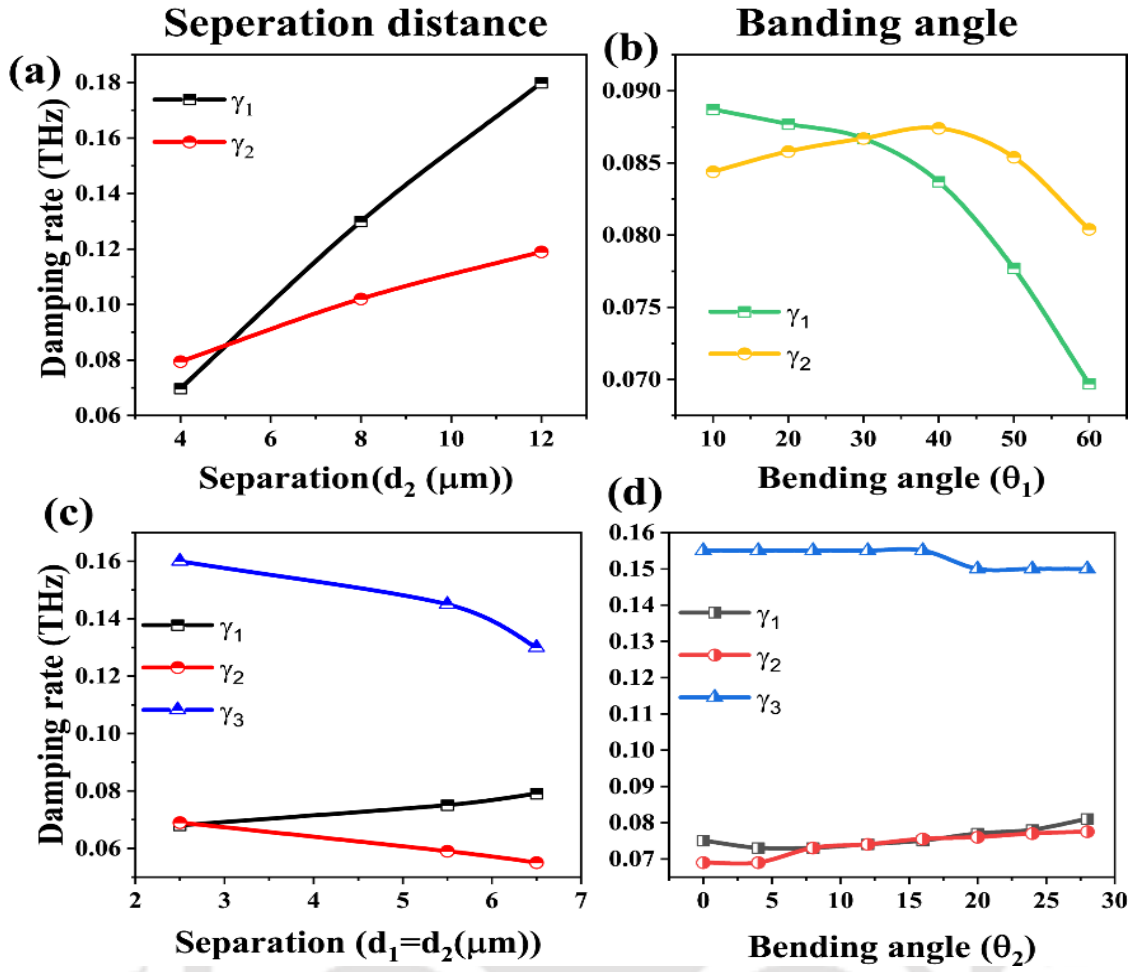

Figure 3.10: Damping rates with respect to the Separation distance between resonators and bending angles for the two and three-resonators-based MM. (a) and (b) represent the variation of γ_1 and γ_2 as the separation between resonators and bending angle increases, respectively, for the two-strip model. (c) and (d) represent the variation of γ_1, γ_2, and γ_3 for the 3-strip configuration as separation and bending angle (θ_2) increase.

coefficient significantly decreases from 0.095 THz² to 0.056 THz². This reduction is induced by a notable increase in the damping rates γ_1 and γ_2 of both oscillators (see Figure 3.10b). Similar trends are observed for the three-oscillator system. As the resonator's separation d_1 (keeping d2 fixed) increases from 2.5 μm to 6.5 μm, the coupling coefficient κ_1 (while κ_2 remains constant) decreases from 0.225 THz² to 0.195 THz² (Figure 9(c)). This decrease can be attributed to an increase in the damping rate γ_1 and a gradual decrease in γ_2 and γ_2 as can be seen in Figure 3.10(c). These coupling results also exhibit a strong agreement with the Full Width at Half Maximum (FWHM) calculated for different values of 'd' from the simulation results.

The variation in coupling strength concerning changes in the bending angle was also analyzed for both the two-resonator and three-resonator-based harmonic oscillators. For the two-resonator system, upon varying θ_1 from 0° to 60°, it was observed that the coupling coefficient κ_1 gradually increases up to 50°, after which it attenuates as θ_1 further increases (Figure 3.9(b)). In the case of the three-resonator system, similar trends are evident when varying θ_2 (while keeping θ_1 constant). As θ_2 increases from 0° to 30°, the coupling strength κ_2 (while κ_1 remains approximately constant) increases up to 10° and subsequently decreases with further increases in θ_2 (Figure 3.9(d)). In both cases, the coupling coefficient follows a similar trend to the FWHM. This observation validates a proportional relationship between the coupling

coefficient and FWHM.

3.6 Polarization-Dependent Transmission Characteristics

The response of metamaterial structures to terahertz (THz) radiation is highly dependent on the polarization of the incident electric field. In particular, anisotropic structures, such as those based on bending strips, exhibit distinct transmission characteristics when the electric field is oriented along different axes. To investigate this polarization dependence, we performed a numerical simulation study on the bending-strip metamaterial introduced earlier in this chapter.

Figure 3.11(a) shows the simulated transmission spectra for two orthogonal orientations of the incident THz electric field: one parallel to the axis of the bending strips, and the other perpendicular to it. When the electric field is aligned parallel to the strips, the structure exhibits a broadband rejection behavior. This effect arises due to strong electromagnetic coupling between the three closely spaced strips. As discussed in detail in Section 3.4, the mutual interactions among the strips result in broaden the THz transmission response, effectively functioning as a broadband band-reject filter.

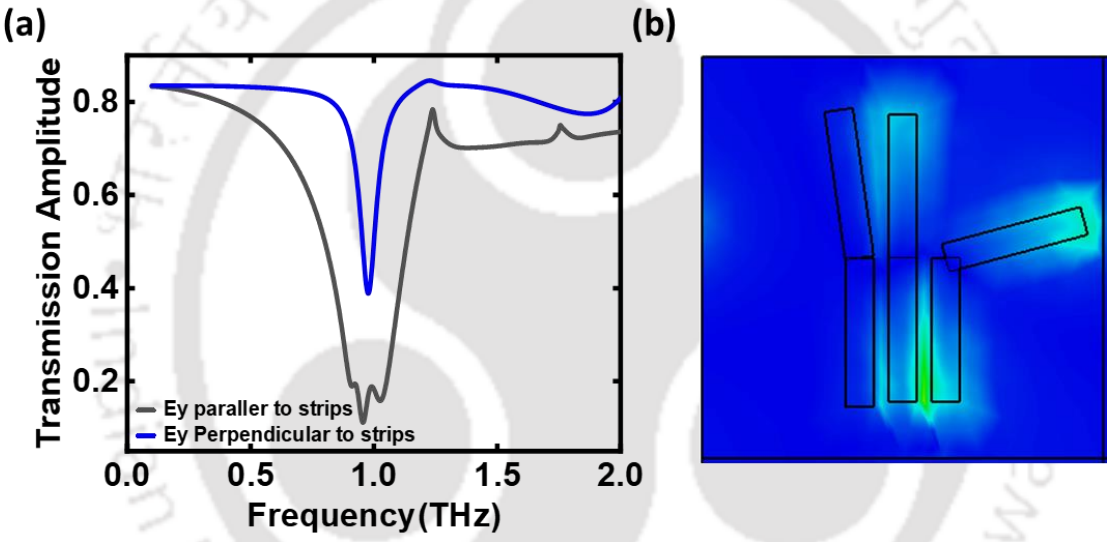

Figure 3.11 :(a) Simulated transmission spectra of the bending-strip metamaterial for THz electric fields parallel (black) and perpendicular (blue) to the strips. Parallel polarization shows a broadband rejection due to strong inter-strip coupling, while perpendicular polarization results in a narrow resonance. (b) Electric field distribution at resonance for perpendicular polarization, showing dominant excitation of the rightmost strip with minimal coupling to the center strip.

In contrast, when the electric field is oriented perpendicular to the bending strips, the transmission spectrum reveals a single, narrow resonance. This is attributed primarily to the excitation of the rightmost strip, as illustrated in the electric field distribution shown in Figure 3.11(b). The figure reveals that, under perpendicular excitation, the coupling between the right strip and the central strip is minimal, and the left strip remains largely unexcited. As a result, the resonant interaction is highly localized, producing a sharper and narrower spectral feature.

These findings underscore the importance of polarization control in the design and application of THz metamaterials. The observed anisotropic behavior highlights the capability of such structures to function as polarization-sensitive devices, which could be exploited in applications such as polarization filtering, sensing, and tunable THz components.

3.7 Summary

In summary, we introduce a planar single-layer metamaterial design aimed at broadening the bandwidth of the fundamental resonance by integrating multiple bending strip resonators

alongside the straight-strip resonator. Our findings demonstrate a notable enhancement in the FWHM and reject bandwidth (RBW) within 20% terahertz transmission. For the two-resonator-based metamaterial, we calculated FWHM and RBW to be 270 GHz and 120 GHz, respectively. With the incorporation of three-strip resonators in the MM design, the FWHM and RBW are further elevated to 350 GHz and 160 GHz, respectively. The overall improvements in FWHM and RBW for the two-resonator-based and three-resonator-based MM in comparison to the single resonator are 110 GHz and 25 GHz, and 190 GHz and 65 GHz, respectively. Enhancements were observed only for specific angles of bending of neighboring strip resonators with respect to the central resonator. We attribute the broadening of the resonance to the strong coupling between the resonators. Our experimental results and coupling strength calculated from the harmonic oscillator are found to be in very good agreement with the simulation findings. The study reveals that significant resonance broadening can be achieved in the planar configuration with the addition of strips in a strongly coupled configuration without much altering its electromagnetic strength. This study can find applications in developing planar broadband THz photonics devices, particularly terahertz filters, broadband modulators, etc. Avoiding the complexity involved in the fabrication of multilayer structures.

Chapter 4: Multi-stacked polarization insensitive ultra-broadband Terahertz Metamaterial

4.1 Introduction:

Broadband planar metamaterials have garnered significant attention due to their potential to advance THz technology in applications such as high-speed wireless communication, imaging, and sensing. By exploiting multi-resonance phenomena and introducing structural asymmetries, planar designs have demonstrated broadband transmission responses. However, as discussed in Section 1.6.1, these configurations often face inherent challenges, including limited resonance strength and reduced efficiency due to inter-resonator coupling and low resonator densities at specific frequencies. These constraints hinder further enhancement of

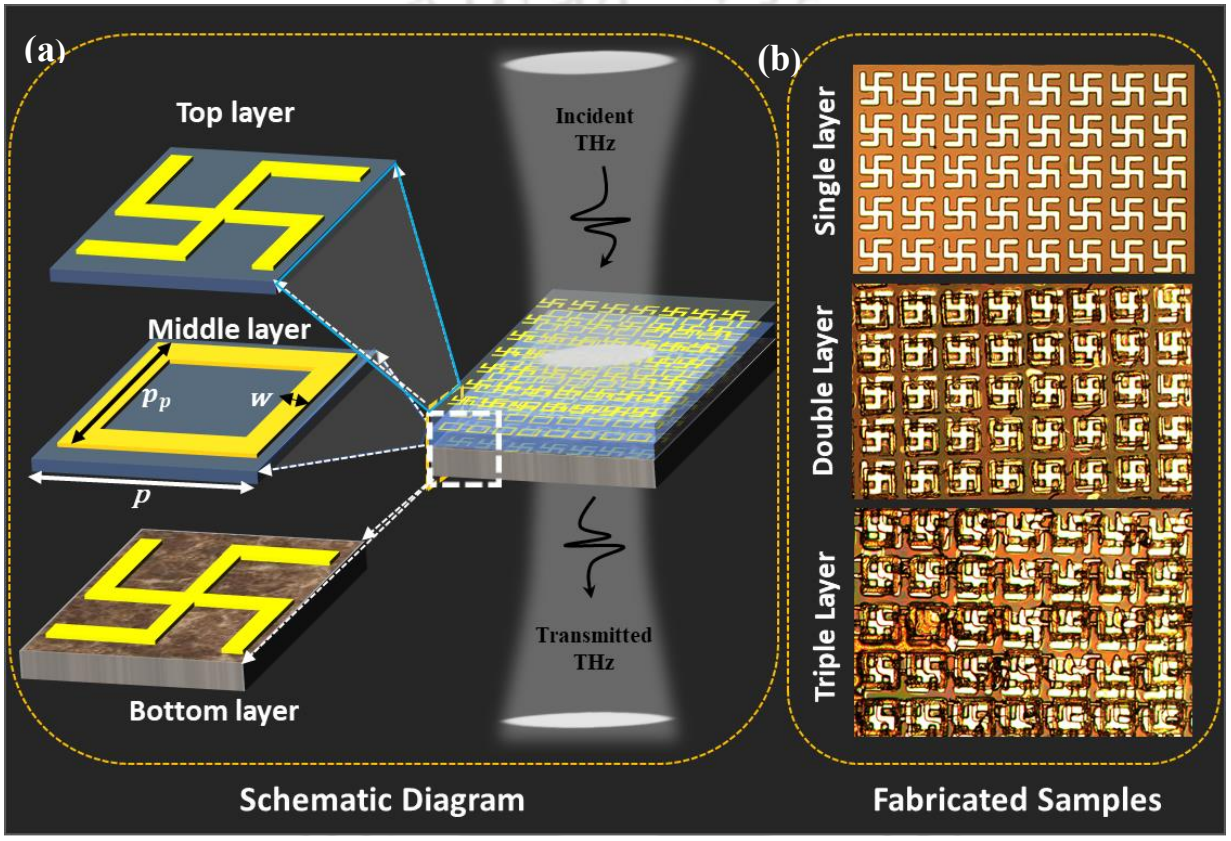

Figure 4.1: 3D metamaterials structure. The (a) shows the schematic diagram and the unit cell of the metamaterial structure. The periodicity, Length, and width of each resonator of the MM structure were p=80, Pp=55 µm, and w=5 µm, respectively. The silicon substrate and aluminium resonator thickness were taken as t=40 µm and tm=0.2 µm. (b) shows the fabricated samples from single layer to multi-layered.

broadband responses in planar geometries, necessitating alternative approaches.

Multi-stacked metamaterials offer a promising solution to these limitations. By stacking multiple resonator layers separated by low-loss dielectric spacers, it is possible to achieve ultra-broadband responses without compromising resonance strength. This approach facilitates improved coupling between layers and supports the superposition of multiple resonances, significantly enhancing bandwidth. Notable advancements in multi-stacked metamaterials include the work of N.R. Han et al., who demonstrated substantial broadband enhancement using split-ring resonators[78], and Ruan et al., who developed a broadband metamaterial filter with excellent flat-top characteristics[79]. Despite these successes, optimizing spacer thickness, resonator positioning, and interlayer coupling remains a critical challenge for

achieving even broader responses. Further supporting this direction, Li and Ding [107] demonstrated broadband-stop filtering in the THz region using vertically stacked identical resonators, leveraging mode coupling to enhance spectral performance. Similarly, Ansari et al.[108] investigated a multilayer Yagi-Uda absorber composed of stacked circular ring elements functioning as director, feed, and reflector. Although primarily designed for narrowband directional absorption, their structure also exhibits filtering behaviour in the transmission spectrum, attributed to plasmon hybridization between the layers. While these studies confirm the effectiveness of multilayer designs, they predominantly focus on identical resonator stacking, highlighting the need for new geometrical configurations and broadband filtering strategies.

In this chapter, we present a three-layer metamaterial structure designed to overcome these challenges and extend current multilayer design approaches. The proposed structure consists of a square ring resonator layer sandwiched between two windmill-shaped resonator layers, with polyimide films serving as dielectric spacers. Unlike previous studies that rely on symmetric or identical resonators, our hybrid design intentionally introduces geometrical diversity across layers. This results in enhanced near-field coupling and a broadened, flatter stopband response. The design process involves extensive numerical simulations to optimize geometrical and material parameters, with a particular focus on spacer thickness and interlayer alignment. The fabricated structure is characterized experimentally using terahertz time-domain spectroscopy (THz-TDS), and the observed transmission characteristics are compared with simulation results. Additionally, the electric field distributions within the multilayer structure are analysed to understand the origin of broadband behaviour. A transmission line model is further employed to quantitatively interpret interlayer coupling effects and validate the broadband performance analytically.

This chapter is structured as follows: Section 4.2 details the design and optimization of the multi-stacked metamaterial. Section 4.3 examines the broadband transmission spectrum and compares simulated and measured responses. Sections 4.4 and 4.5 investigate the effects of spacer thickness, resonator alignment, and interlayer coupling. Section 4.6 applies a transmission line model to further elucidate the broadband response. Finally, Section 4.7 summarizes the key findings and discusses their implications for THz applications.

4.2 Design and fabrication: multi-layer structures

The proposed metamaterial configuration is designed using commercially available finite element method and finite integration technique-based CST microwave studio suite software. The multistacked metamaterial configuration consists of a square ring resonator sandwiched between two windmill resonators, as shown in Figure 4.1. The resonators are separated with a loss-free polyimide thin film thickness of $t_p=40\ \mu m$. The periodicity, length, and width of each resonator of the MM structure are $p=80\ \mu m$, $P_p=55\ \mu m$, and $w=5\ \mu m$, respectively. The silicon substrate and the thickness of the aluminium-based resonator thickness were taken as t=30 µm and tm=0.2 µm, respectively, for the simulation. The thickness of the metallic resonator was chosen to be more than the skin depth of the aluminium to avoid the penetration of the terahertz wave through the resonators. Figure 4.1 shows a full view of the proposed metamaterial configuration. The schematic diagram of the unit cell is shown in Figure 4.1(a). The single, double and multilayer metamaterials fabricated and captured by the optical microscope are shown in Figure 4.1(b). The permittivity of the silicon substrate and polyimide spacer was taken as 11.9 and 3.5, respectively. The simulation was performed using a frequency domain solver with tetrahedral meshing. A normal incident plane electromagnetic wave was used, accommodating both TE (transverse electric) and TM (transverse magnetic) metamaterial designs. For the TE and TM polarized waves, the electric field of the incident THz wave is

directed along the y- and x-direction, respectively.

The proposed metamaterial structure was fabricated using a conventional photolithography technique. The $1cm \times 1cm$ array of a structure on the clean silicon substrate was developed by UV-photomask by using an appropriate positive photoresist. To realize the desired array of the different designs, a thin aluminium film of thickness 200nm was deposited on the developed silicon substrate using the e-beam evaporator, and subsequently, the liftoff method was performed in the acetone solution. The second and third layers of the metasurfaces are fabricated on the polyimide, stacking one onto the other. A thin film of the polyimide was spin-coated, followed by the annealing from room temperature to 200℃ in multiple steps of increasing temperature to ensure uniform thickness. All the samples were fabricated in a clean and dry environment at room temperature. Figure 4.1(b) shows a micrograph of a single layer of windmill resonators (top), a ring resonator developed onto windmill resonators (middle), and the final multilayered structure consisting of ring resonators sandwiched between the windmill resonator (bottom).

Choice of the windmill resonator: The windmill resonator was selected over more conventional designs, such as the cross-shaped resonator or ring resonator, to optimize the multi-stacked metamaterial. The initial exploration involved a cross-shaped configuration,

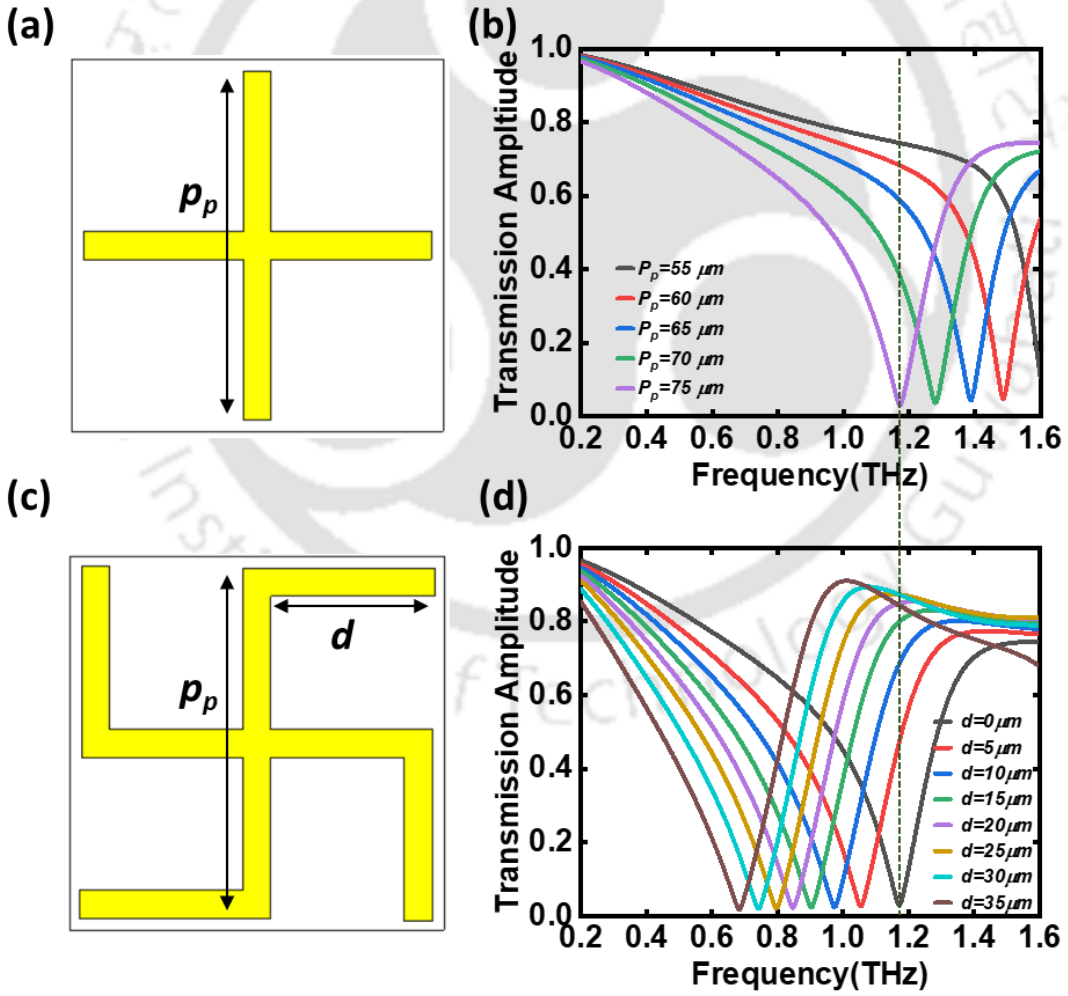

Figure 4.2. (a) Cross-shaped resonator structure. (b) Redshift in the resonance due to the change in the length of the resonator. (c) The extended unit cell (windmill resonator) is derived from the cross-shaped resonator. In this windmill structure, apart from the length of the resonator, the extended fork can also contribute to the red or blue shifting of the resonance. (d) Redshift in the resonance due to the increase in the fork length.

where it was observed that the terahertz resonance position is significantly influenced by the arm length of the cross-shaped resonator. The resonance frequency *(f)* and the resonator length *(P_p)* exhibit an inverse relationship *($f = 1/P_p$)*, as supported by the simulated results in Figure 4.2(b). The results demonstrate that increasing the length of the cross-shaped resonator *(P_p)* shifts the resonance position to lower frequencies within the spectrum (redshift).

In contrast to the cross-shaped resonator, a windmill structure introduces two independent variables, namely P_p and d, which can alter the position of the resonance. This versatility is absent in the cross-shaped structure, where only one independent variable, P_p, can be modified to change the resonance position. In the case of the windmill resonator, the resonance position can be related as $f = {}^{1}/_{(P_p + d)}$.

The windmill resonator offers significant advantages for targeting the terahertz frequency range of 0.2 THz to 1.6 THz, which is crucial for 6G wireless communication systems due to its various applications. Achieving band rejection within the 0.8 THz to 1.2 THz range necessitates precise control of the resonator's frequency response. Specifically, targeting a resonance near 1 THz presents challenges when using a fixed periodicity of P = 80 µm for cross resonators with Pp = 75 µm, as shown in Figure 4.2b. To address this limitation and enable a further redshift toward 1 THz, an additional fork was integrated into the cross-shaped resonator, effectively extending the length of the resonator arms. This modification not only facilitated the desired frequency adjustment (as illustrated in Figures 4.2c and 4.2d) but also preserved the essential four-fold symmetry required for a polarisation-insensitive response in the terahertz spectrum.

4.3 Ultra-broadband-stop transmission of designed MM:

The final sample was characterized by using the switch-based terahertz time-domain spectroscopy (THz-TDS), where a 1550 nm femtosecond laser was used to generate the terahertz signal through a source antenna using the commercially available system Teraflash (Toptica Photonics). The Laser's repetition rate and pulse width are 100 MHz and 60 fs, respectively. The terahertz detector and generator are made of a 25-µm metallic dipole antenna and a 100-um strip-line antenna fabricated on the InGaAs/InP. The transmitted time domain signal was collected through the pump-probe spectroscopy principle, as discussed in detail in section 2.3. The collected terahertz time domain signal is then converted into the frequency domain using Fast-Fourier transformation. The Terahertz signal was first passed through an identical bare silicon sample. This transmitted signal was treated as a reference signal. The spectrum transmitted through the fabricated sample was then normalized with the reference signal to obtain the transmission amplitude.

To understand the transmission response of each resonator and the combined effect of the multi-layered structure, we presented the transmission characteristics of each layer in Figure 4.3. Figure 4.3(a) shows the simulated, theoretically calculated, and experimentally measured transmission response of a single windmill resonator, along with the unit cell structure. The calculated FWHM of the single-layer windmill MM is 0.22 THz. In Figure 4.3(b), we have added another layer, a square ring resonator, and shown the transmission results accordingly. The FWHM through simulation is calculated as 0.38 THz. As we add another layer, i.e., a square ring resonator on top, we observe an increase in the bandwidth. To explore the possibility of further enhancement in the transmission bandwidth and a better transmission profile, we added another layer of Windmill structure on top of the square ring resonator. This resulted in a further increment in the bandwidth with a better transmission profile. Figure 4.3(c) depicts the transmission results of the final multi-stacked metamaterial structure. In this case, FWHM, through simulation, is observed to be 0.50 THz. From Figures 4.3(a) to 4.3(c), it is

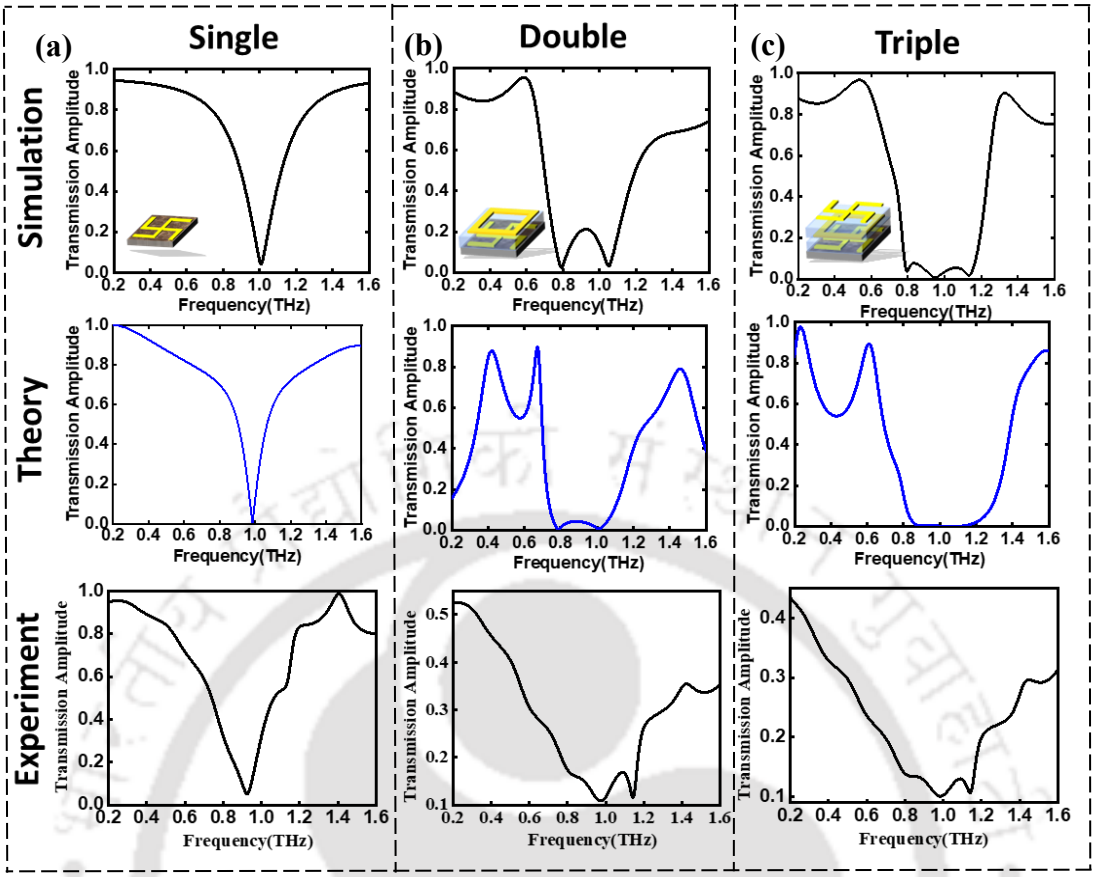

Figure 4.3: (a) simulated, theoretically calculated and experimentally measured transmission characteristics for single resonator along with their unit cell structure, (b) double layer (square ring resonator on the Swastik), and (c) multi-stacked MM configuration (square ring resonator sandwiched with Swastik structure). The FWHM calculated through simulation for single, double and multi-layered structure are 0.22 THz, 0.38 THz, and 0.5 THz respectively.

clear that the addition of layers of resonators on top of each other leads to the broadening of transmission characteristics. More than a 200% enhancement in FWHM of the final configuration has been achieved compared to the single layer. Therefore, our design is promising in providing a broader transmission response. In order to provide an extra degree of freedom for practical usage, we have also studied the polarization dependency of the multi-stacked material. Since the design is orthogonally symmetric, the transmission response will be the same for TE and TM modes of incident light.

The anomalies between the transmission amplitude and frequency shift of the simulated and measured spectrum may be due to several reasons, such as non-uniformity of the thickness of the coated polyimide, the difference in the permittivity of the polyimide and metallic resonators as compression to the perimetries chosen for the simulation, and plasmonic losses due to metallic resonators.

4.4 Optimization of spacer thickness and resonator's position

The thickness of the metamaterial device has been optimized for optimal broadband terahertz transmission. It was found that within the range of 40 µm to 55 µm, the transmission characteristics exhibit high bandwidth with negligible response between 0.79 THz and 1.15 THz (see Figure 4.4(a)). For fabrication purposes, we selected an optimized design with a thickness of 40 µm (see Figure 4.4(b)), where the full width at half maximum (FWHM) is relatively higher and the transmission band is more consistent compared to other spacer thicknesses.

To investigate how the position of the resonators affects broadband transmission, we simulated a multi-stacked structure with the resonators positioned at slightly shifted locations. Each resonator was translated by small distances $\delta_1, \delta_2, and\ \delta_3$(in μm) from its center (refer to Figure 4.4(d)). Figure 4.4(c) illustrates the transmission amplitude for these shifted positions, which were determined by selecting random combinations of varying distances, as well as for the resonators that were perfectly aligned perpendicularly. The results indicate that the transmission responses are nearly identical across all configurations. This suggests that the position of the resonators does not significantly impact the transmission response, indicating that precise alignment is not necessary. This finding simplifies the fabrication process of the multi-layer structure.

4.5 Deep subwavelength coupling

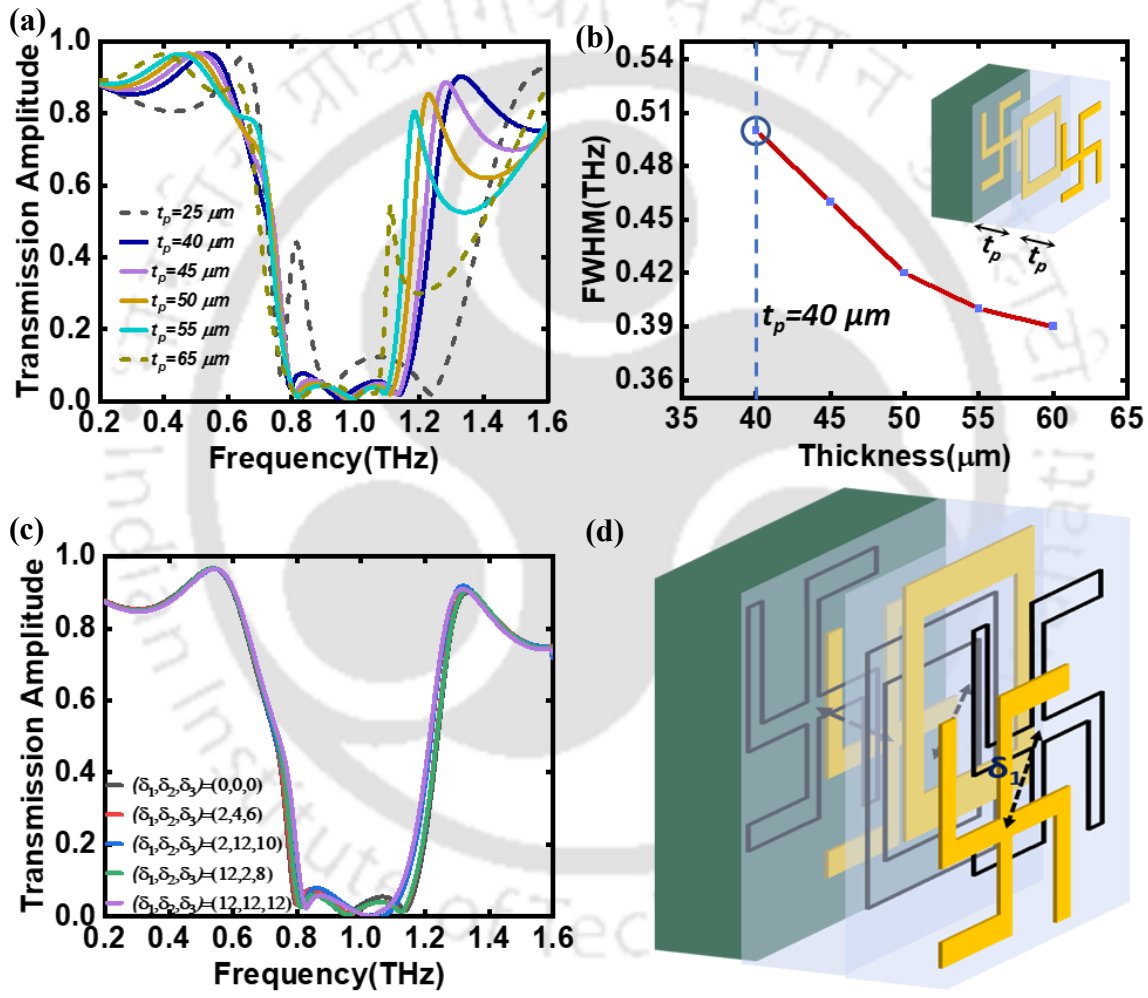

Figure 4.4: (a) Transmission spectrum w.r.t the thickness of the spacer. The optimized thickness of the spacer is between 40μm to 55μm. (b) For the fabrication, the thickness of the spacer, t=40μm taken since The FWHM at this thickness is relatively higher, and the transmission band is reasonably flat compared to the other thickness of the spacer. (c) transmission spectrum w.r.t the relative positions of the resonator. Each resonator translates with small distances from the center of the MM. Random combinations of translation distances of the resonator have been chosen and compared with the perpendicularly aligned resonator. The transmission amplitude is independent of the position of the resonators. The 3d view of the shifted resonators with respect to the center of the resonators.

To understand the contribution of the different subwavelength micro resonator structures, electric field distributions were calculated for TE polarized light using numerical simulation with CST software. Field distribution at three frequencies, 0.79 THz, 0.95 THz, and 1.15 THz,

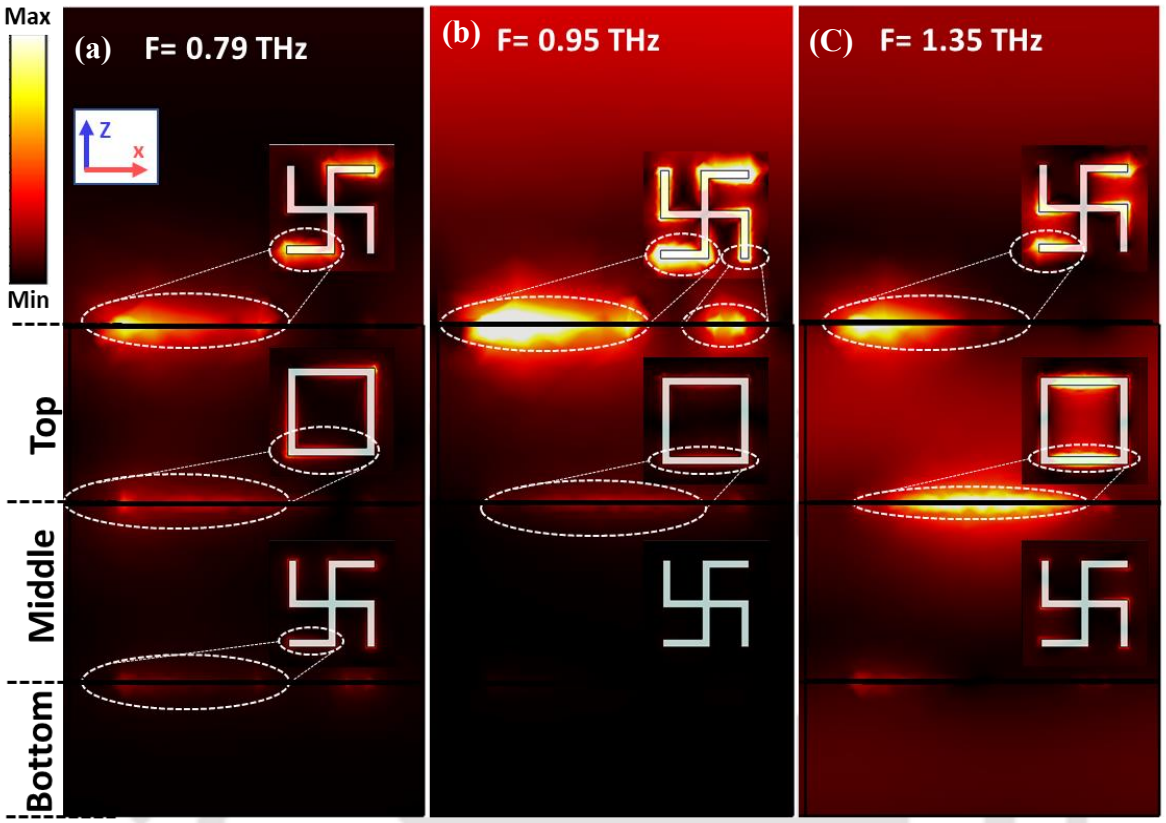

Figure 4.5: The cross-sectional plane of field distribution (along the x-z plane cuts through the centre of resonators) and the front view of the MM. Field distribution at three frequencies, 0.79 THz, 0.95 THz, and 1.35 THz plotted to realize coupling between the resonators.

was observed, with the understanding that these frequencies show minimum transmission amplitude within the band. The cross-sectional plane of the field distribution (along the x-z plane, cutting through the edge of the resonators), as well as the excited resonators corresponding to each layer (front view), are presented at the corner of each layer (Figure 4.5. The dashed circles corresponding to each layer represent the excitation of the layer at different frequencies. The field distribution at these frequencies reveals that the resonator excitation is due to electric dipoles, and it is also evident from the front view of the excited resonators in Figure 4.5. It's important to note that each metallic resonator plays a distinct role in broadening the transmission bandwidth and maintaining resonance strength. The first and second metallic layers of the proposed design contribute to producing resonance dips. For example, the resonance dip at the frequency of 0.79 THz is mainly due to the excitation of the two upper layers, with very minimal contribution from the bottom layer, as can be seen from field confinement in Figure 4.5(a). Meanwhile, the resonance dips at 0.95 THz and 1.15 THz frequencies are primarily due to the excitation of the upper Windmill and the middle ring resonator, with almost negligible contribution from the third resonator, the bottom layer (windmill). The third metallic resonator at these frequencies exhibits much lower field concentration compared to the first and second layers, indicating that the third metal resonator plays a role in widening the resistive band, increasing the resistive band absorption, and optimizing the steep cut-off performance of the filter, rather than directly contributing to the resonance dip formation. The presence of strong electrical resonance due to different metallic resonators ensures that when the frequency of the incident electromagnetic wave matches the

resonant frequency, almost all the energy of the incident wave is used to sustain the oscillation of the electrons inside the structure. As a result, the energy of the electromagnetic wave passing through the metamaterial is nearly nullified, further demonstrating that the broadband resonance arises from electric dipole resonance [109]. To further understand the role of different resonators and their contribution to broadening the bandwidth of the resonance, we have employed transmission line models in the next section.

4.6 Transmission line model

In this section, TL models were used to investigate the role of different resonators in the transmission Full Width at Half Maximum (FWHM). The cases examined include: a windmill-shaped resonator, a windmill-shaped resonator paired with a square ring resonator, and finally, a square ring resonator sandwiched between two windmill-shaped resonators separated by a polyimide spacer. The constructed circuit models provide S-parameter values for each case, which align well with the transmission results obtained from simulations. Resistance (R) is introduced in each model to account for optical losses, primarily influencing the transmittance amplitude. R is assumed to be always in series with the inductance due to the flow of the induced current. Circuit models of the unit cells for the windmill and ring resonator are

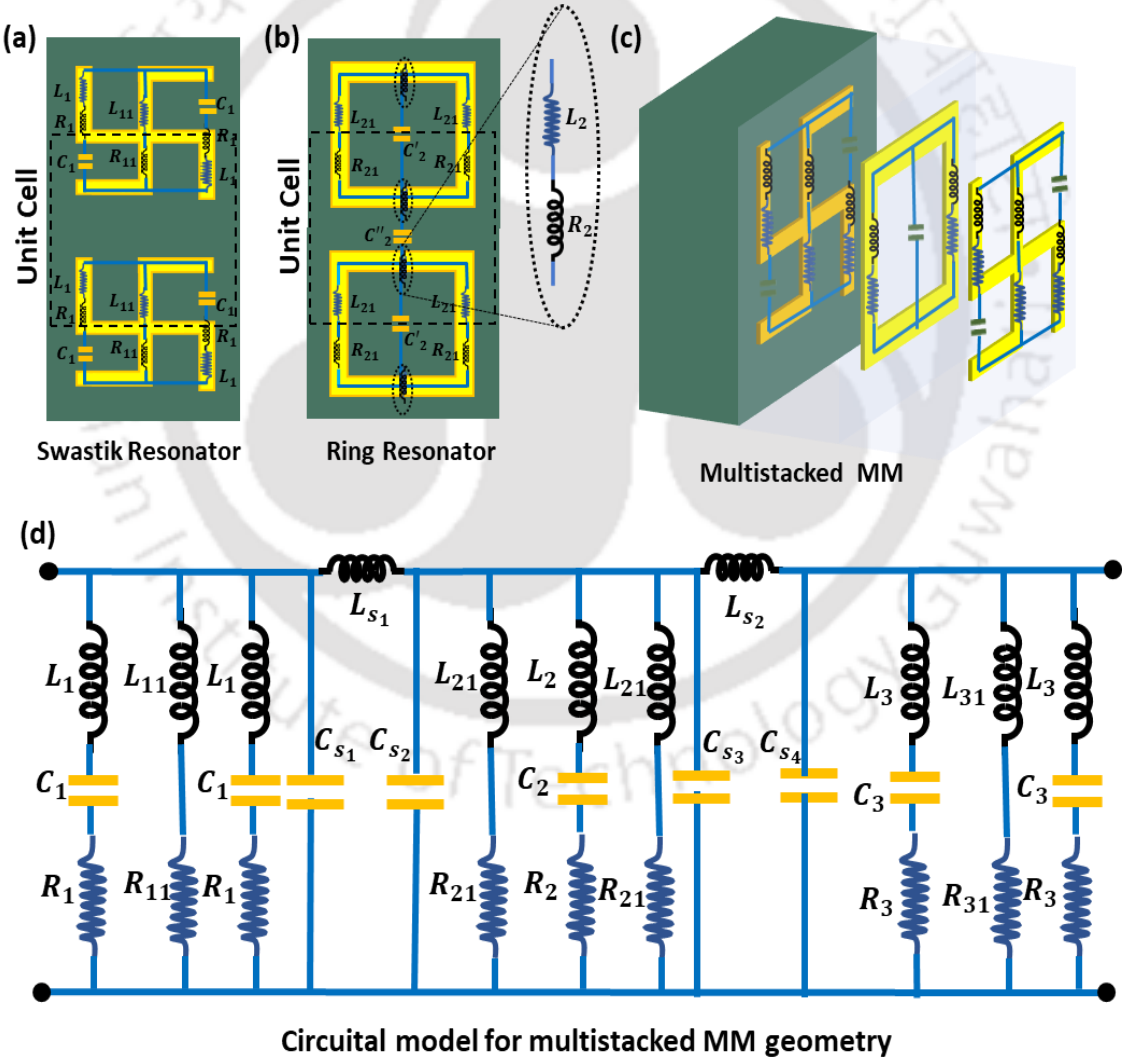

Figure 4.6: Transmission line model for the proposed metamaterial (MM) geometry. (a) shows the unit cell of windmill resonators with its equivalent lumped circuit model. (b) represents the unit cell of the ring resonator with its lumped circuit model. (c) depicts the unit cell of the multistacked resonators with the equivalent circuit model. And (d) shows the final equivalent circuit model for the proposed design consisting of the three resonators.

presented in Figure 4.6a and Figure 4.6b, respectively. Capacitance C_1 and inductance L_1 are the total equivalent capacitance and inductance determined by the electric resonance of the single-layer metasurface. Using the values of L_1, C_1, and R_1 tabulated in Table 4.I, the calculated spectra of a single layer can reproduce the numerical results very well, as shown in Figure 4.3a). Furthermore, the TL model is also identical to that of the capacitive plates at far-infrared frequencies[110]. Series inductor L_s and shunt capacitor C_s in Figure 4.6(d) denote the dielectric substrate modelled by transmission line according to the Telegrapher's equations[111]. Specifically, inside the stop band determined by L_1 and C_1, the inductor of L_s and capacitor of C_s can be considered as short and open circuits, respectively, due to the relatively small values. As shown in Figure 4.3, the fitted transmission of the TL equivalent circuit model agrees well with the CST simulation results. A windmill-shaped resonator and a square ring resonator were represented by a lumped equivalent circuit directly built by cascading two series LC circuits. The whole double-layered structure is still situated on the substrate. Herein, the original series LC circuit is kept modelling the top (first) metasurface that faces the incident electromagnetic wave, and the other LC circuit was introduced to model the bottom (second) metasurface. These two layers are separated by a polyamide spacer with a thickness of t_p=*40 μm*. TL model for double layers was constructed by combining the circuit composed of R_1, L_1, and C_1, and R_2, L_2, and C_2 ($C_2 = C_2' + C_2''$). In addition, L_s and C_s remain short and open circuits within the stop band determined by L_1, C_1, L_2, and C_2. The circuit parameters of the double layer model obtained through fitting the numerical parameters by the circuit model are listed in Table I. Calculated responses of the model are displayed in Figure 2(b), which agree well with the simulation results.

Table 4.1: Different parameters and corresponding values to fit the transmission response calculated form the simulation and Transmission line model.

Parameter	Value	Parameter	Value	parameter	value	Parameter	value
L_1	48 pH	C_1	0.68 fF	R_{11}	2.9 Ω	Cs_1	0.83fF
L_2	15 pH	C_2	1.56 fF	R_{21}	2.2 Ω	Cs_2	0.90fF
L_3	85 pH	C_3	0.25 fF	R_{31}	2.0 Ω	Cs_3	0.95fF
R_1	10 Ω	L_{11}	188 pH	LS_1	29 pH	Cs_4	0.91fF
R_2	5 Ω	L_{21}	300 pH	LS_2	32 pH	-	-
R_3	5 Ω	L_{31}	389 pH	-	-	-	-

To achieve a higher degree of freedom in spectral tuning for broadband regulation, we introduce a third metasurface for a tri-layer cascaded model. An equivalent circuit for this setup is developed in a manner similar to previous models. Additionally, a new series of LC circuits is introduced to reflect the third resonant mode of hybrid spectral behaviour, with interconnections among the layers. In this model, the inductance (L_1) and capacitance (C_1) branches represent the top layer metasurface, while the inductance (L_2) and capacitance (C_2) branches correspond to the middle layer metasurface, as discussed previously. The parameters for the third layer, inductance L_3 and capacitance C_3, can be estimated similarly for a windmill-shaped resonator.

A transmission line (TL) equivalent circuit model is established, which fits well with both simulation and experimental results, as illustrated in Figure 4.3. The accurate values of the

lumped elements, as shown in Figure 5(c), have been determined through a fitting procedure and are presented in Table 4.1. Consequently, Figures 4.3a, 4.3b, and 4.3c demonstrate that the measured transmission spectra from the TL circuit model align closely with simulations and experimental outcomes for all three configurations: single-layer, double-layer, and triple-layer devices. Three typical transmission line circuits have been studied using transmission line theory. The constructed models are validated by their strong agreement with the transmittance spectra and nonlocal material parameters in the simulations.

4.7 Summary:

In this work, we have designed and fabricated a broadband, polarization-independent terahertz metamaterial capable of achieving a full width at half maximum (FWHM) of 500 GHz. This FWHM, calculated through simulation, shows an enhancement of over 200% compared to the FWHM of a single resonator at resonance. The field distribution of the multi-stacked metamaterial indicates that the resonators are selectively excited at different frequencies across the broadband spectrum. To better understand the near-field coupling between the resonators, we employed a transmission line model. The results derived from circuit theory align well with our experimental and simulation observations. The stopband between 0.79 THz and 1.15 THz is suppressed to -25 dB, which is highly beneficial for the fabrication of broad stopband filter devices and has the potential for use in developing functional broadband THz devices.

Chapter 5: Actively tunable multistacked broadband metamaterial

This chapter consists of two subchapters. Subchapter 5.1 examines the development of an activity-tunable multi-stacked metamaterial, emphasizing its application as an activity-tunable broadband bandpass filter. Subchapter 5.2 focuses on the design of an activity-tunable broadband band-reject filter, utilizing toroidal metamaterials to achieve near-perfect reflection.

5.1 Ultra-Broadband Actively Tunable Terahertz Modulator Based on Multi-Stacked Metamaterial

5.1.1 Introduction:

Multi-stacked metamaterials have emerged as a promising solution for achieving ultra-broadband terahertz responses, overcoming the limitations of planar designs. By stacking resonator layers with optimized interlayer coupling and using low-loss spacers, these configurations enable broader bandwidths while preserving resonance strength. This approach addresses challenges inherent in planar structures, such as reduced resonance efficiency and limited bandwidth due to low resonator densities and coupling effects, as discussed in Section 1.6.1. Multi-stacked designs have demonstrated significant advancements in broadband transmission, making them highly suitable for terahertz applications requiring high-speed wireless communication, imaging, and sensing.

To further enhance the functionality of broadband metamaterials, active tunability has become a critical area of focus. Actively tunable terahertz devices, such as modulators and filters, are essential for dynamic applications in communication and sensing. Various methods, including optical, mechanical, and electrical modulation, have been explored to achieve tunability[112-115]. However, these approaches often face limitations, such as the high-power requirements of optical modulation, the fabrication complexity of mechanical systems, and the restricted modulation depth of electrical techniques.

Vanadium dioxide (VO_2), a phase-change material, offers a promising alternative for tunable terahertz applications. VO_2 undergoes a reversible insulator-to-metal transition when subjected to temperature changes, resulting in significant variations in its electrical conductivity and permittivity[116-118]. This property enables VO_2-based metamaterials to achieve wideband modulation and deep tunability with excellent thermal responsiveness. The integration of VO_2 into multi-stacked designs combines the benefits of broadband operation with dynamic tunability, paving the way for advanced terahertz modulators.

In this study, we introduce an ultra-broadband terahertz transmission modulator that integrates multi-stacked metasurfaces with a VO_2 thin film. The hybrid metamaterial design leverages the broadband capabilities of multi-stacked configurations and the phase transition properties of VO_2 for tunable performance. The flexible metamaterial is fabricated using photolithography and carefully transferred onto a VO_2 film deposited on quartz, preserving the film's integrity. The VO_2 film's phase transition characteristics, including its temperature-dependent conductivity, plasma frequency, and relaxation time, are thoroughly analyzed. The hybrid structure's modulation performance is evaluated using terahertz time-domain spectroscopy (THz-TDS), and a transmission line model is employed to understand the coupling mechanism and phase transition behaviour.

This subchapter is organized as follows: Section 5.1.2 details the design and fabrication of the multi-tacked hybrid metamaterial. Section 5.1.3 discusses the characterization of the VO_2 film

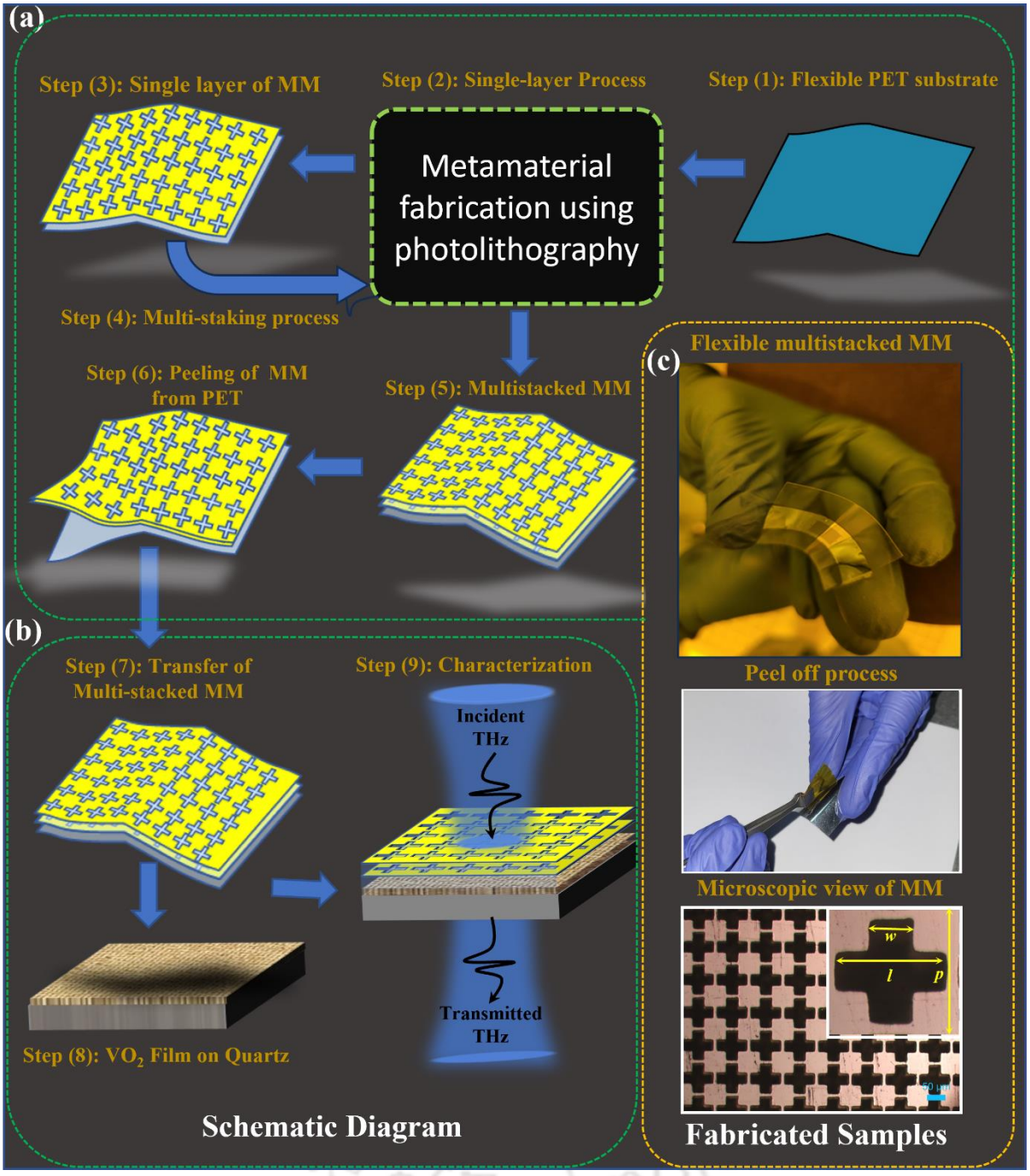

Figure 5.1.1: (a) Schematic of the multi-stacking and peel-off process of the metamaterial. (b) Transfer of the flexible metamaterial onto a VO_2 thin film on quartz, with the terahertz characterization scheme of the final MM. (c) Images of the flexible metamaterial, the peel-off process, and the fabricated sample.

and its integration with multilayered metamaterial. Section 5.1.4 presents the experimental results and discussion. Section 5.1.5 introduces a transmission line model to analyse the coupling mechanism and modulation behaviour. Finally, Section 5.1.6 summarizes the findings and their implications for future tunable terahertz devices.

5.1.2 Design and fabrication of hybrid metamaterial:

To demonstrate active terahertz broadband modulation in VO_2-deposited multistacked MM, we prepared three samples. The first sample was a VO_2 thin film deposited on a quartz substrate via chemical vapour deposition (CVD), with a thickness of $d = 1.5$ µm. The second sample is a flexible, multi-layered metamaterial comprising five layers: A Polyethylene Terephthalate

(PET) substrate, a polyimide spacer, a complementary cross-shaped aluminium resonator (conductivity of 3.5×10^7 S/m), and another identical resonator layer separated by polyimide as shown in Figure 5.1.1a (step 5). Each metallic resonator is 0.2 µm thick, exceeding the skin depth of aluminium in the terahertz range. Complementary cross-shaped resonators were chosen for their ease of fabrication and symmetric nature, providing polarization-insensitive transmission responses due to fourfold rotational symmetry. The unit cell periodicity was set at $p = 95$ µm, with resonator dimensions of $l = 80$ µm and $w = 20$ µm (see inset of bottom Figure 5.1.1c). The polyimide spacer thickness was optimized to t_p=50 µm to achieve a balance between a higher full width at half maximum (FWHM) and a relatively flat transmission band. Increasing the thickness beyond 50 µm further enhanced the FWHM but compromised the flatness of the transmission band. The detailed discussion on the optimization process and its impact on the terahertz response, please refer to Section A2 (Figure A2) of the Appendix A. For Sample 3, we peeled off the multi-layered metamaterial from Sample 2 and transferred it onto the VO_2 layer of Sample 1, as illustrated in Figure 5.1.1(see steps 6 to 8). Thus, the final sample consists of two functional components: the VO_2 thin layer on the quartz substrate and the multistacked resonators separated by the polyimide layer. The metamaterial fabrication was carried out using standard photolithography techniques. The multi-stacking, peeling-off, and transfer processes are depicted schematically in Figures 5.1.1a and 5.1.1b, illustrated in steps 1 to 8. The fabricated samples are shown in Figure 5.1.1c. Detailed descriptions of the fabrication and characterization processes can be found in the supplementary material (Sections 2 and 3).

5.1.3 VO_2 characterisation using THz-TDS

Prior to combining the VO_2 thin film with the multi-layered metamaterial (MM), we conducted an in-depth analysis of its basic properties within the terahertz spectrum. The temperature-dependent complex terahertz conductivity of the VO_2 thin film during the metal-insulator transition was assessed by THz-TDS. To compute this conductivity, the complex refractive index of the VO_2 thin film was initially obtained by using Equation (5.1)[119]:

$$T_{VO_2} = \frac{F_{sample(\omega)}}{F_{ref(\omega)}} = \frac{2\eta_2(\eta_1+\eta_3)}{(\eta_2+\eta_1)(\eta_2+\eta_3)} \exp\left[-j(\eta_2-\eta_1)\frac{\omega d}{c}\right] FP(\omega), \tag{5.1}$$

where $FP(\omega)$ represents the Fabry-Perot term given by:

$$FP(\omega) = \left[1 - \left(\frac{\eta_2-\eta_1}{\eta_2+\eta_1}\right)\left(\frac{\eta_2-\eta_3}{\eta_2+\eta_3}\right) exp\left(-2j\eta_2\frac{\omega d}{c}\right)\right]^{-1} \tag{5.2}$$

Here $\eta_1, \eta_2 and\ \eta_3$ are the complex refractive indices of the air, VO_2 thin film and quartz substrate, respectively. The complex transmission coefficient of the sample T_{VO_2} were measured experimentally by THz-TDS. For each measurement, the temperature was stabilized for 10 minutes to minimize temperature deviations. Subsequently, the complex refractive(η_2) index was determined using an algorithm referred to as the 'downhill method', as mentioned in the work of Da-Xiang Zhou[119]. Since VO_2 is a non-magnetic material ($\eta_2 = \sqrt{\boldsymbol{\varepsilon}_2}$), complex conductivity ($\boldsymbol{\sigma} = \sigma_1 + \boldsymbol{i}\sigma_2$) can be calculated by the well-known formula derived from Maxwell's equations given by [120].

$$\boldsymbol{\sigma} = \omega\varepsilon_o\big(\varepsilon' - j(\varepsilon'' - 1)\big), \tag{5.3}$$

where ε' and $\varepsilon''$is the real and imaginary components ($\boldsymbol{\varepsilon}_2 = \varepsilon' + j\varepsilon''$) of the permittivity of the VO_2 thin film. A detailed analysis is provided in the supplementary material in chapter 2, section (2.3.4). The real(σ_1) and imaginary(σ_2) components are plotted in Figure 5.1.2b for

temperatures ranging from T=50°C to T=90°C. It is observed that σ_1 is nearly flat with a slightly positive slope, consistent with terahertz studies of VO_2 conducted by other groups[116, 118, 121]. Meanwhile, σ_2 remains negative at all temperatures. The behaviours of σ_1 and σ_2, persisting into the fully metallic state, are characteristic of localized charge carriers[117]. To describe the conductivity in relation to temperature changes, the conductivity calculated from Equation (5.3) is fitted with the Drude-Smith model, a classical generalization of the Drude model. The most common form of the Drude-Smith model is given in Equation (5.4)[121]:

$$\sigma_{DS}(\omega) = \frac{ne^2\tau}{m^*(1-j\omega\tau)}\left(1+\frac{c}{(1-i\omega\tau)}\right), \tag{5.4}$$

where n represents the electron density, τ denotes the Drude-Smith scattering time (often referred to as the relaxation time of electrons), $m^* = 2m_e$ is the effective mass of electrons in VO_2, and c is a parameter varying between 0 for free carriers and -1 for fully localized charges. The fitting results, displayed in Figure 5.1.2b, illustrate the conductivity fitting from the Drude-Smith model (dotted line). It is evident from Figure 5.1.2b that both the dielectric and metallic phases of VO_2 are consistent with the Drude-Smith model. The obtained scattering time from the best fit for the VO_2 thin films is approximately 14±2 fs, while the c factor is around -0.95 ± 0.03 for the VO_2 thin film. Notably, the c values being close to -1 suggest that strong carrier

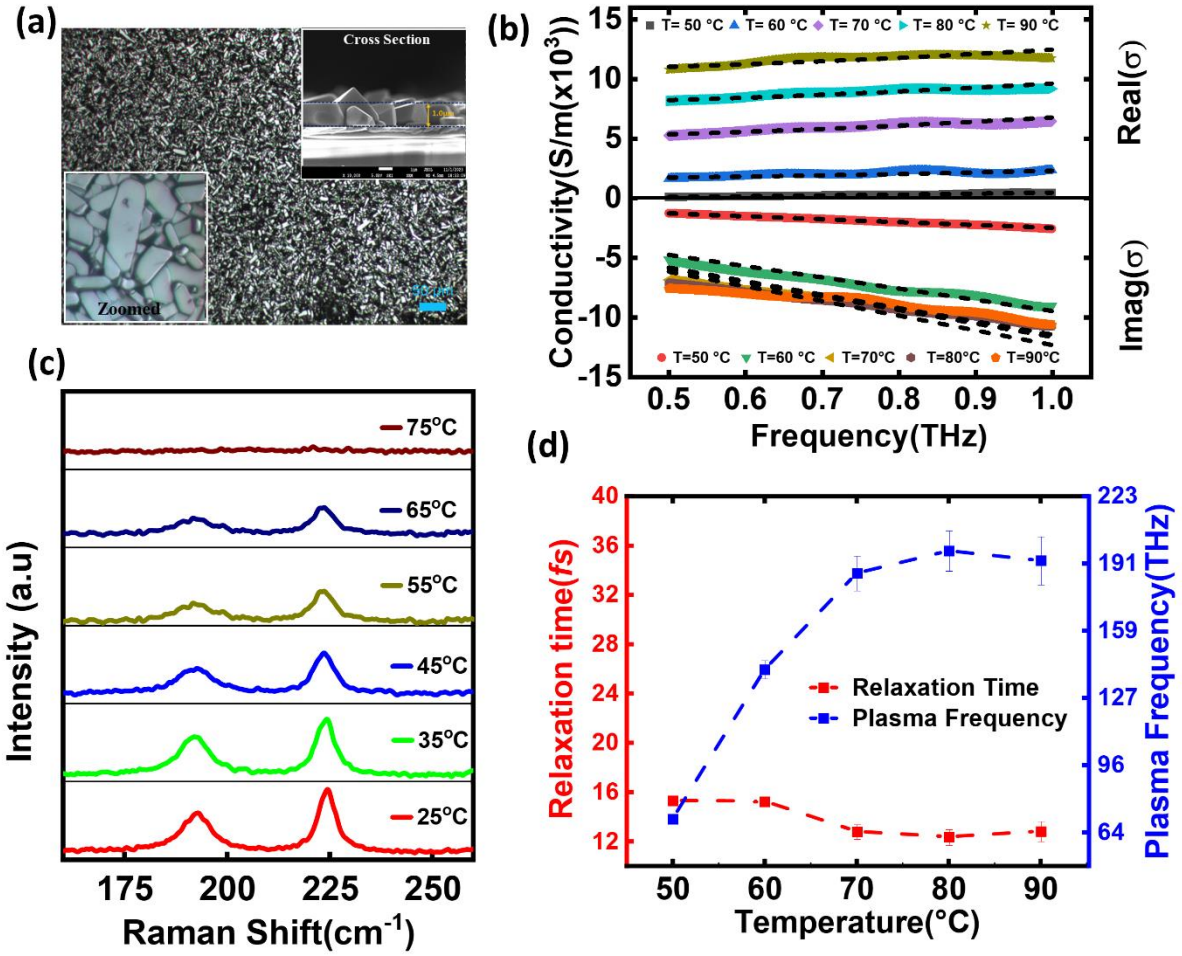

Figure 5.1.2: (a) FESEM image of VO_2 thin film surface morphology; insets show zoomed and cross-sectional views, with thickness calculated as 1.5 µm. (b) Real and imaginary components of conductivity fitted using the Lorentz-Drude model. (c) Temperature-dependent Raman data revealing the phase transition behaviour of the VO_2 thin film. (d) Plasma frequency and relaxation time from Drude-Lorentz fitting.

backscattering and localization may dominate electron transport in the THz range[117, 121]. VO_2 deposition via Chemical Vapor Deposition leads to smaller grains compared to other techniques, and these smaller grain sizes result in stronger backscattering. The plasma frequency, calculated from the fitting for the different temperatures, is plotted in Figure 5.1.2(d). These values fall within a reasonable range and are consistent with the findings reported by James Lourembam[118]. Finally, the Raman shift data presented in Figure 5.1.2(c) further confirm the phase transition properties of VO_2 materials as a function of temperature[122]. The detailed analysis of the VO_2 deposition and characterization can be found in the supplementary material Appendix A (section A1).

5.1.4 Results and Discussions:

To demonstrate thermally active modulation in a VO_2 thin-film-based multistacked metamaterial, numerical simulations were conducted using CST Microwave Studio software, which operates in the frequency domain and employs finite integral techniques to solve Maxwell's equations. Three simulation sets were performed: Sample 1 (VO_2 thin film), Sample 2 (flexible multistacked metamaterial), and Sample 3 (VO_2 thin film integrated with

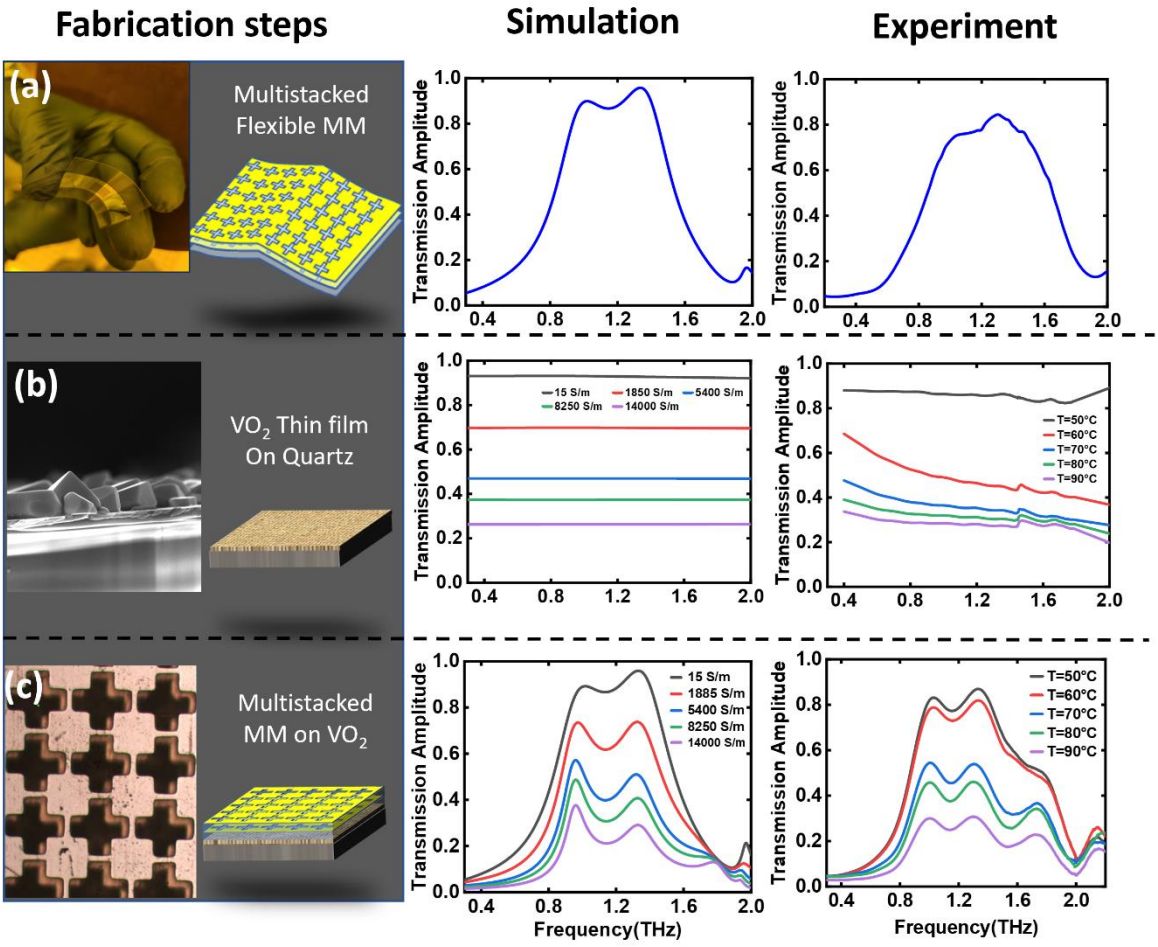

Figure 5.1.3: (a) Simulated, theoretically calculated, and experimentally measured transmission characteristics for a flexible MM, alongside their schematic and fabricated sample image. (b) VO_2 thin film, deposited on the quartz substrate, where the transmission amplitude decreases as the temperature changes from 50 °C to 90 °C. (c) Illustration of the multi-stacked MM integrated with the VO_2 thin film and transmission modulation w.r.t change in temperature.

multistacked metamaterial). The permittivities of quartz and PET substrates were set at 3.7 and 3.5, respectively, while the permittivity of the polyimide spacer was calculated using THz-TDS as 2.89. The conductivity of the VO_2 material, derived from Drude fitting, was utilized in the

simulations, with both real and imaginary parts extracted at different temperatures (as shown in Figure 5.1.2b) to modulate the transmission amplitude. Boundary conditions for all cases were taken as unit cells in the X and Y directions.

Figure 5.1.3 presents the simulated and corresponding experimental results for each set of samples. Figure 5.1.3(a) depicts the simulated and experimentally calculated transmission amplitudes of the flexible multistacked filter. FWHM for this bandpass filter, calculated from THz-TDS and obtained from CST simulation, is found to be 0.90 THz and 0.76 THz, respectively, which is substantially higher compared to earlier reported works[123-127]. This broader transmission response is attributed to the multi-stacking of the metamaterial layers and the optimized polyimide spacer thickness, which enhances the coupling between the resonators in adjacent layers. Figure 5.1.3b shows the simulated and experimentally calculated transmission amplitudes of the VO_2 thin film. It indicates that when the temperature of the VO_2 thin film changes from T=50℃ to T=90℃, the conductivity of the VO_2 film changes from 15 S/m to 14,000 S/m. As a result, the transmission amplitude calculated from THz-TDS (and obtained from CST simulation), decreases from a maximum of 85% (95%) to a minimum of 27% (25%). The final sample, multistacked metamaterial on the VO_2 thin film, is shown in Figure 5.1.3(c). The FWHM for this hybrid metamaterial, calculated through THz-TDS (and obtained via CST), is 1.02 THz (0.76 THz). The discrepancies between the FWHM and minor frequency shift of the resonance peak in the simulated and measured spectra may be due to factors such as non-uniform polyimide thickness, differences in the permittivity of the polyimide and metallic resonators compared to simulation parameters, and plasmonic losses from the metallic resonators. Another factor affecting the FWHM is the thickness of the polyimide spacer. If it exceeds the optimized thickness ($t_p = 50$ μm), the FWHM of the transmission can increase, but the band flatness of the terahertz filter may be compromised. More details on optimizing the polyimide thickness are provided in the Appendix A, section A2. As indicated in Figure 5.1.3c, as the temperature of the multistacked MM integrated with the VO_2 thin film changes from T=50°C to 90°C, the transmission amplitude calculated through THz-TDS (and obtained from CST simulation) changes from 78% (92%) to 24% (27%) at the central frequency (Fc=1.15 THz). To understand the modulation characteristics, we define the intensity modulation depth[127] as $M_d = \{(|T - T_0|)/T_0\} \times 100\%$, where T is the transmittance of the sample when the temperature is highest i.e. T=90℃ and T_0 is the transmittance when the temperature is the below phase transition that is T=50℃. As the temperature increases from T=50℃ to T=90℃, the modulation depth at the center frequency (fc=1.15 THz) achieved through the experiment (and from CST simulation) was 55% (77%), which is reasonably higher for the multi-stacked bandpass filter spanning in the range of more than 200 GHz.

5.1.5 Subwavelength coupling in multistacked metamateial:

To elucidate the impact of subwavelength micro-resonator structures on the broadening of the transmission amplitude bandwidth, we computed electric field distributions for TE-polarized light using numerical simulations in CST software. Field distributions at four frequencies $F_1 = 0.24$ *THz*, $F_2 = 1.05$ *THz,* $F_3 = 1.34$ *THz,* and $F_4 = 1.90$ *THz* were examined. Frequencies F_2 and F_3 exhibited maximum transmission amplitude, whereas F_1 and F_4 showed minimum amplitude, as indicated by dashed lines in Figure 5.1.4a. The cross-sectional field distribution (along the X-Z plane intersecting the resonators' edge) and the excited resonators for each layer (front view) are depicted in Figures 5.1.4(c)–(f), with dashed circles representing the excitation of the individual resonators at different frequencies. The orientation of the cutting plane is shown in Figure 5.1.4b. Analysis of the field distribution at these frequencies reveals that resonator excitation is predominantly due to electric dipoles, evident from the front view of the excited resonators in Figure 5.1.4 (c)-(f). Both metallic resonators(top and bottom) distinctly

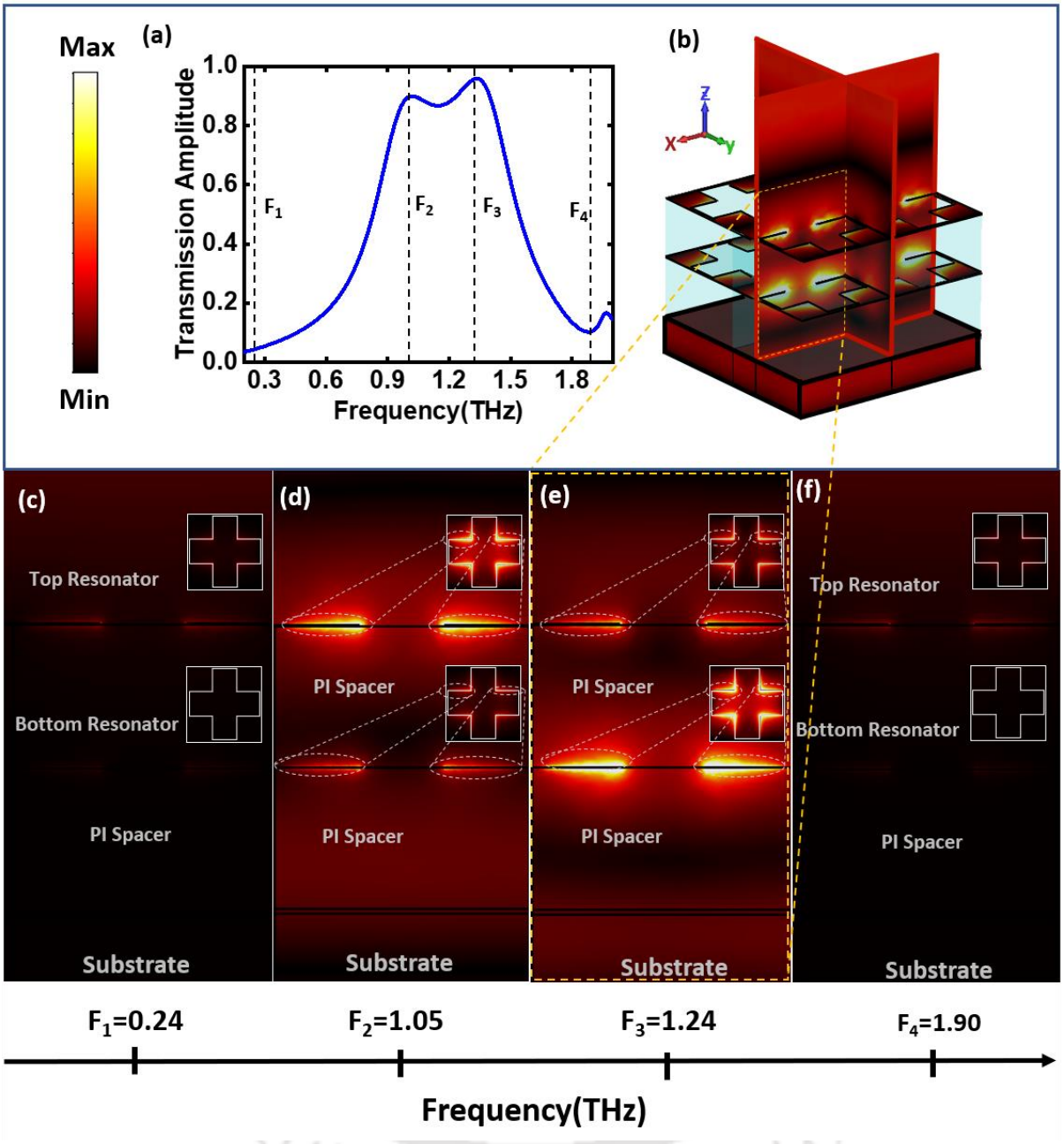

Figure 5.1.4: (a) Electric field distributions at four frequencies: F_1 = 0.24 THz, F_2 = 1.05 THz, F_3 = 1.34 THz, and F_4 = 1.90 THz. (b) Cross-sectional plane of the field distribution (along the x-z plane cutting through the edge of the resonators). (c–f) Side view of the MM and field distributions of the excited resonators at the four frequencies, illustrating coupling between the resonators.

contribute to bandwidth broadening and resonance strength. Specifically, the resonance peak at F_2 is primarily due to excitation of the upper layers, with minimal contribution from the bottom layer (Figure 5.1.4d), while the resonance dip at F_3 is mainly due to excitation of the lower resonators, with negligible upper resonator contribution. The simultaneous excitation of both resonators at F_2 and F_3 signifies the role of coupling in broadband enhancement. Figures 5.1.4(d) and 4(e) confirm that the broadening in terahertz transmission amplitude results from the superimposition of resonance frequencies due to individual resonators and their coupling. The electric field distribution at frequencies F_1 and F_4 indicates that excitation occurs only within the transmission band (F_3–F_2), and the broadening is primarily due to the excitation of resonators within this band range. To further understand the role of different resonators and their contributions to bandwidth broadening, transmission line models have been explored in

the subsequent section.

5.1.6 Transmission line model

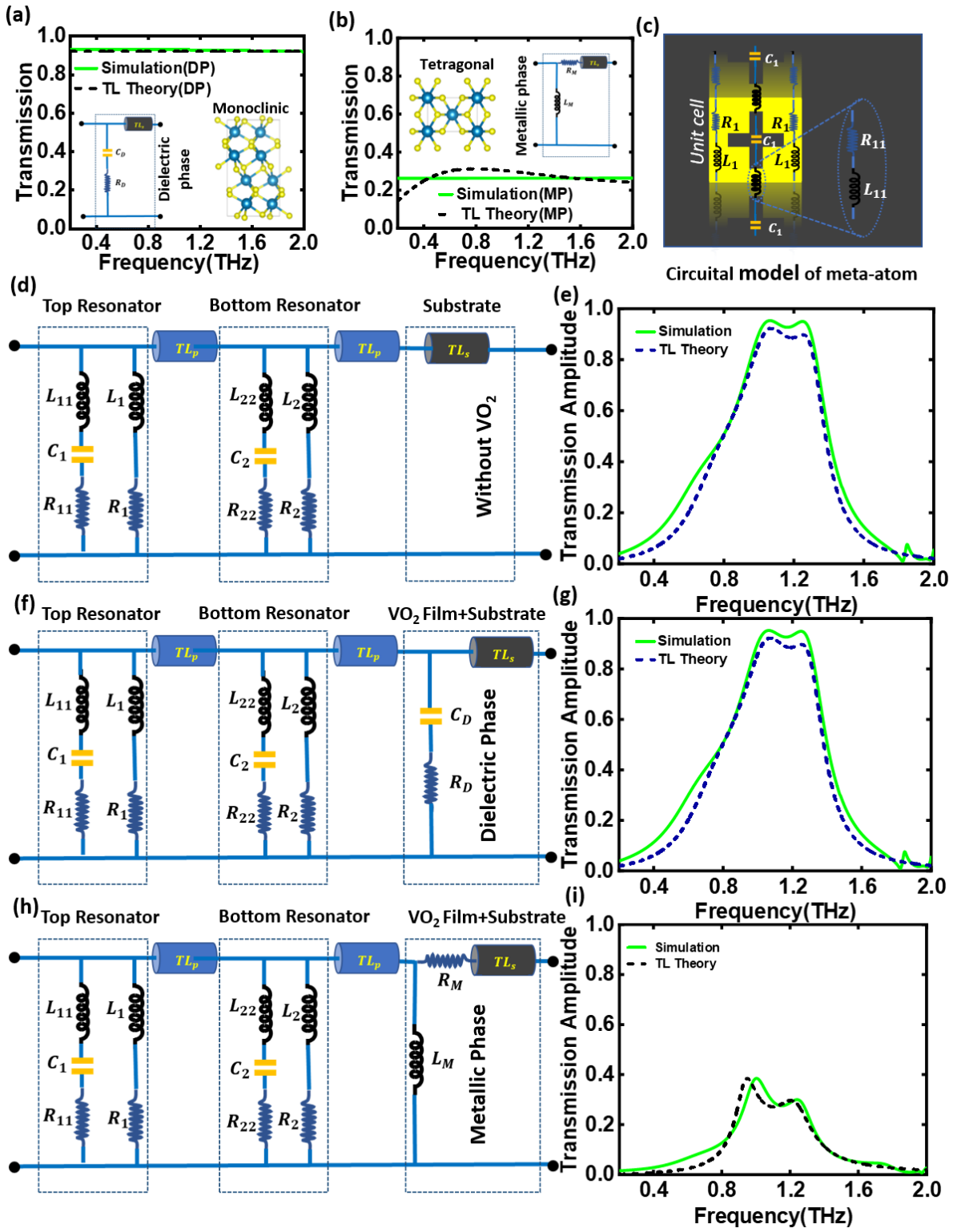

Figure 5.1.5: (a, b) Simulated and circuit-modeled transmission amplitudes for VO_2 in its dielectric (monoclinic) and metallic (tetragonal) phases, respectively, including their circuit representations. (c) Unit cell MM with its equivalent lumped circuital model. (d) Circuital model of the multistacked MM without the VO_2 layer, and (e) its corresponding simulated and calculated transmission amplitude. (f, h) Equivalent circuit representations of the multistacked MM when VO_2 is in the dielectric and metallic phases, respectively. (g, i) Corresponding transmission amplitudes fitted with circuit theory for the dielectric (DP) and metallic phases (MP).

Building on the previous discussion, VO_2 transitions from an insulating to a metallic phase near 67 °C, altering its lattice structure from monoclinic to tetragonal[122]. In its dielectric phase ($\sigma = 15$ S/m), the VO_2 film can be modelled as a transmission line comprising a shunt capacitor (C_D) and a resistor (R_D). Conversely, in the metallic phase ($\sigma = 14{,}000$ S/m), it can be represented by a shunt inductance (L_M) and a series resistance (R_M). The capacitance C_D in the dielectric phase can be calculated using Equation (5.5) [128, 129]:

$$C_D = \frac{\varepsilon_0 \varepsilon_r A}{d} = \frac{\varepsilon_0 \varepsilon_r (p \times p)}{d} \tag{5.5}$$

Where ε_0 is the permittivity of free space, $\varepsilon_r = 36$ is the dielectric constant[129] of VO_2, A is the meta-atom's area, and d is the film thickness. R_D accounts for dielectric losses and is determined by fitting the simulated transmission amplitude to the transmission line model. Figures 5.1.5(a) and 5(b) show the simulated transmission amplitudes fitted with the transmission line model for the dielectric and metallic phases, respectively, along with their circuit representations and structural phases.

To gain a better understanding of the resonance mechanism of the broadband active modulator, a circuital model of coupled resonators, with and without the integration of the VO_2 thin film, was employed. Two identical resonators, when multistacked and coupled to each other, enhance the bandwidth of the transmission spectrum. The VO_2 layer modulates the transmission amplitude in response to temperature changes. The polyimide spacer and quartz substrate are treated as short-length transmission lines with impedances calculated as $z = z_0/\sqrt{\varepsilon_s}$ (where ε_s is the permittivity of the material), yielding 221 Ω for polyimide and 196 Ω for quartz. Figure 5.1.5(c) presents the circuit representation of a single complementary cross-shaped resonator. Inductors (L) and capacitors (C) are added in parallel for the metamaterial (MM) unit cell, with resistance (R) in series with inductors to account for optical losses[110, 123, 130, 131]. Figure 5.1.5(d) shows the circuit representation of the multistacked MM without the VO_2 film. The simulation results closely match the Transmission Line Model, as depicted in Figure 5.1.5(e).

Table 5.1: Circuit parameters for calculating the electromagnetic response of the TL models.

Parameter	Value	Parameter	Value	Parameter	Value
R_1	03.20 Ω	R_2	0.96 Ω	C_D	1.97 pF
L_1	17.70 pH	L_2	9.14 pH	R_D	20.00 KΩ
C_1	1.40 Ff	C_2	2.11 fF	L_M	44.00 pH
R_{11}	0.99 Ω	R_{22}	0.98 Ω	R_M	00.43 KΩ
L_{11}	0.13 pH	L_{22}	1.6 pH		

Figures 5.1.5(f) and 5.1.5(h) illustrate the circuit models for the coupled MM with VO_2 in its dielectric and metallic phases, respectively. The transmission responses from simulations align well with the TL models, shown in Figures 5.1.5(g) and 5.1.5(i). In the dielectric phase (Figure 5.1.5(f)), VO_2 is represented by a shunt capacitor (C_D) and resistor (R_D), resulting in maximum transmission amplitude due to higher R_D, indicating insulating behaviour. In the metallic phase (Figure 5.1.5(h)), VO_2 is modelled with a shunt inductor (L_M) and a series resistor, leading to a decrease in transmission amplitude. A higher L_M value signifies the metallic behaviour of the VO_2 film. The fitting parameters L, C, and R are provided in Table 5.1.

5.1.7 Summary:

In this work, we have developed an ultra-broadband, multistacked, tunable metamaterial-based modulator integrated with a VO_2 thin film. This hybrid MM provides ultra-broadband transmission with an FWHM of 1.02 THz and a modulation depth of 55% at the center

frequency of 1.15 THz, observed with a temperature change from 50 °C to 90 °C. Our simulations indicate an FWHM of 0.76 THz and a modulation depth of 75%. The difference between calculated and simulated spectra is primarily due to variations in the polyimide spacer thickness, non-uniformity in polyimide thickness, discrepancies in permittivity values, and plasmonic losses from metallic resonators. Prior to integration, we thoroughly examined the thermal properties of the VO_2 film. The metamaterial on the PET substrate exhibited an FWHM of 0.90 THz (0.76 THz) through THz-TDS (and CST simulation). Using a transmission line model, we analysed the role of resonators in bandwidth broadening and the effect of the VO_2 thin film on transmission amplitude modulation. This adaptable approach can be applied to various terahertz wave control applications by adjusting resonator designs and thin films, including 2D materials. The straightforward fabrication process allows for metamaterial translation onto different substrates. Our versatile and scalable hybrid phase-change photonic framework holds promise for future advancements in phase-change terahertz photonics.

5.2 Tunable Broadband Terahertz Modulation in a Multi-Stacked Toroidal Metamaterial

5.2.1 Introduction

In this study, we presented an ultra-broadband terahertz band reject filter that can be actively tuned to function as a nearly perfect reflector. This was achieved using a hybrid metamaterial approach, which combines toroidally excited, multi-stacked metamaterial with a VO_2 thin film. The VO_2 film, with a thickness of 1.5 µm, was deposited on a quartz substrate using chemical vapour deposition (CVD) and characterized through temperature-dependent terahertz time-domain spectroscopy (THz-TDS), as discussed in the relevant section. The phase transition Raman peaks (Figure 3(b)) confirmed the deposition of a high-quality VO_2 film (details can be found in Appwndix A, Section A1).

By utilizing the extracted dispersive permittivity of VO_2 (as discussed in Section 5.1.3), we designed a multi-stacked metamaterial based on VO_2 and optimized its broadband transmission response. This optimization involved adjusting parameters such as spacer thickness, resonator positioning, and the near-field coupling between resonators. The integration of VO_2 enabled active modulation of the transmission properties, allowing for tunable broadband enhancement, which is crucial for terahertz photonics and next-generation wireless communications.

This subchapter is organized as follows: Section 5.2.2 details the design and optimization of the thickness and position of the multilayered metasurfaces. Section 5.2.3 discusses the role of toroidal excitation in bandwidth enhancement. Section 5.2.4 addresses the characterization of the VO_2 film and its integration with the multilayered metamaterial. Section 5.2.5 presents the experimental results and discussion.

5.2.2 Design of hybrid metamaterial

A hybrid multilayered metamaterial was designed in CST software, consisting of six layers arranged from bottom to top: a quartz substrate, a VO_2 thin film, a polyimide spacer, an aluminium toroidal ring resonator, another polyimide spacer, and an aluminium resonator. The polyimide thickness was optimized to 36 µm. To minimize the field screening effect and achieve a flat transmission band, a 2 µm polyimide layer was applied on top of this multi-stacked metamaterial. Each resonator's thickness was set to 0.2 µm. The toroidal resonator features a periodicity (P) of 44 µm, arm lengths (l) of 36 µm, a width (w) of 5 µm, and a gap

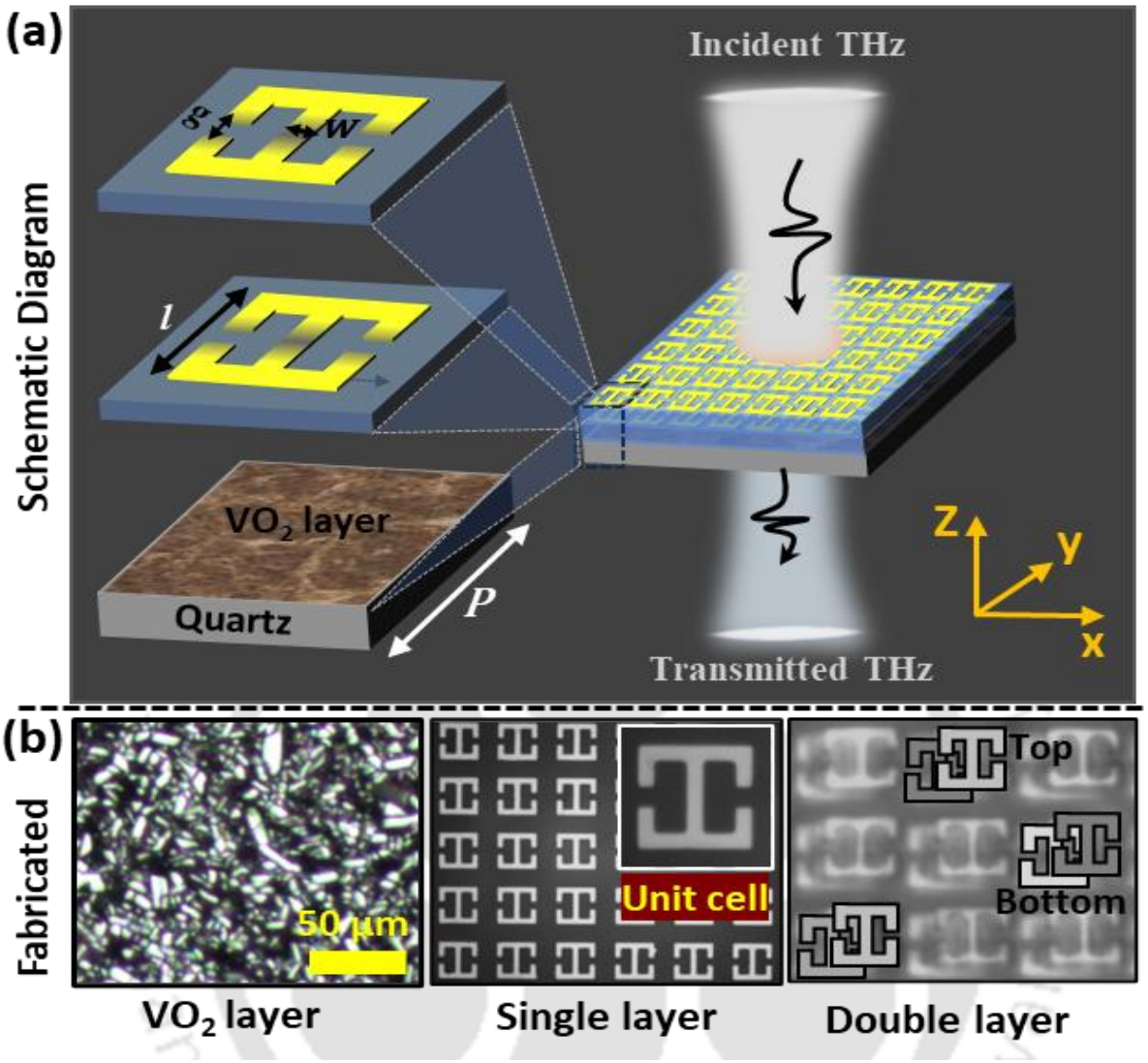

Figure 5.2.1: (a) Schematic of the multi-stacked THz modulator with metamaterial resonators on a VO_2-coated quartz substrate. (b) Optical images: VO_2 layer on a quartz substrate(left), metamaterial array of a single layer with unit cell (centre), and top/bottom resonator layers in stacked alignment (right).

(*g*) of 5 µm, positioned on a 30 µm thick quartz substrate as shown in Figure 1(a). The design utilizes quartz and polyimide materials with permittivities of 4.4 and 3.5, respectively. We evaluated the designed metamaterial's transmission response using a frequency-domain solver with tetrahedral meshing and a normally incident plane wave for both TE polarization.

Optimization of spacer thickness and resonator's position: The thickness of the multistacked metamaterial device has been optimized for broadband terahertz transmission and found to be 36 µm. The transmission characteristics at t_1=t_2=36 µm show high bandwidth with a comparatively flat transmission response in comparison to other thickness values, as seen in Figure 5.2.2(a). As the thickness of the polyimide increases, FWHM significantly improves, but the flatness of the transmission band is compromised. To optimize the flatness of the band-reject filter in the range of 1.05 THz to 1.2 THz, we added an additional layer (t_3) of polyimide on top of the multistacked metamaterial, as shown in Figure 5.2.2(c). We optimized the thickness t_3 for a flat transmission response and determined that t_3=2 µm yields the best results (see Figure 5.2.2(b)). For fabrication purposes, we selected an optimized design with spacer thicknesses of t_1=t_2=*36* µm, where the FWHM is relatively higher, and the transmission band

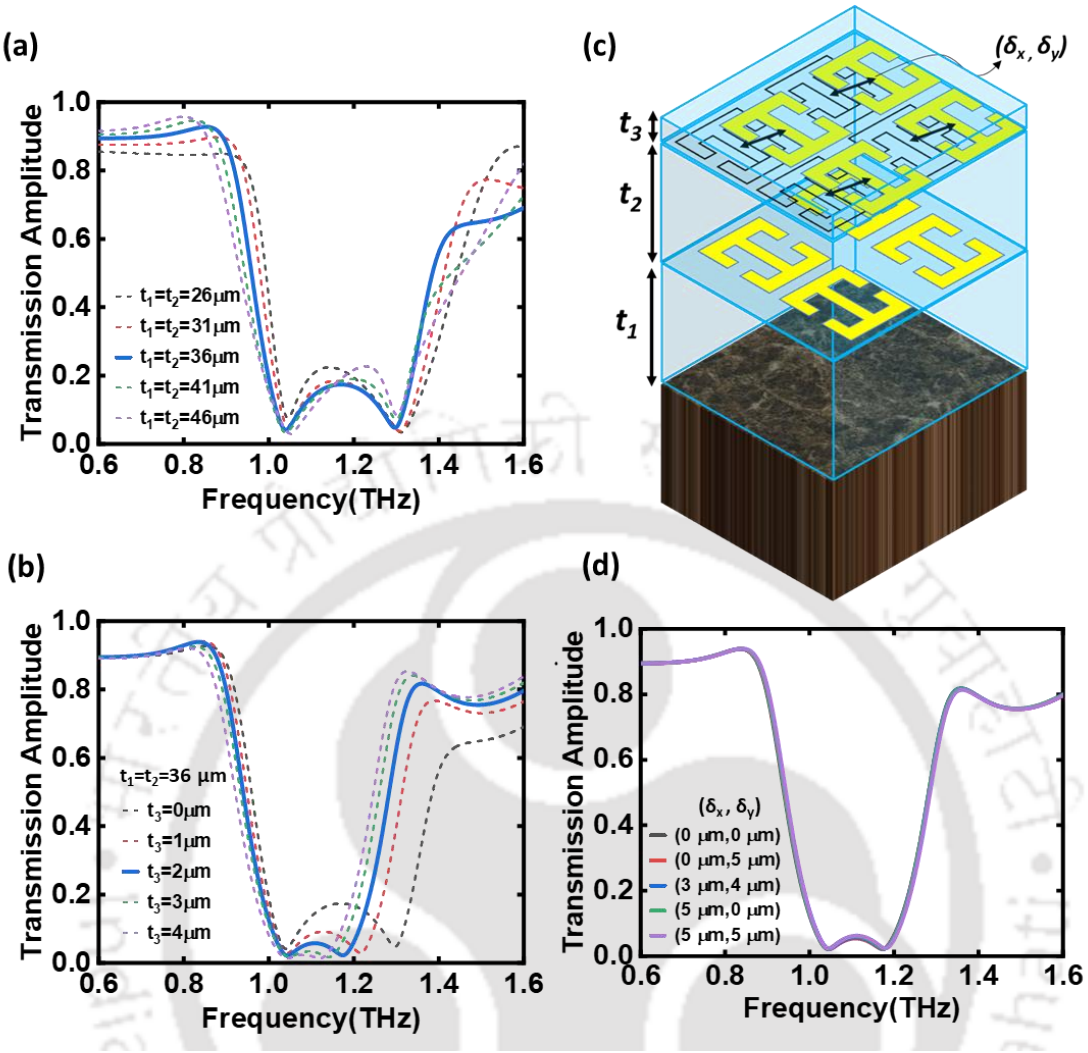

Figure 5.2.2: (a) Transmission spectrum with respect to the thickness of the spacer, highlighting the optimized spacer thickness of t_1=t_2=36 μm. (b) keeping the t_1 and t_2 fixed, added another polyimide layer t_3 for the flat band response, and optimized the t_3= 2 μm. (c) A 3D view of the resonators shifted with respect to the centre of the resonators. (d) Transmission spectrum with respect to the relative positions of the resonators. Each resonator is shifted by small distances from the centre of the metamaterial's resonator, indicating that the transmission amplitude is largely independent of the resonators' positions.

remains reasonably flat.

To examine the effect of the resonators' positions on broadband transmission, we simulated the multistacked structure with shifted positions of the resonators. We translated the upper resonator by small distances (δ_x, δ_y) from the centre of each resonator (see Figure 5.2.2(c)). Figure 5.2.2(d) shows the transmission amplitude for the shifted resonator. It is clear that the transmission responses are approximately the same for all cases. This indicates that the position of the resonator does not affect the transmission response; therefore, exact alignment of the resonators is not required, which significantly reduces the complexity of fabricating the multilayer structure. The effect of single to double metasurface layer on the FWHM is discussed in the following section.

5.2.3 Role of toroidal excitation in bandwidth enhancement

Analyzing the resonance of metamaterial resonators and their cumulative effects when toroidal metasurfaces are stacked reveals a significant improvement in transmission bandwidth. Initially, a single layer of the toroidal resonator exhibited a bandwidth of 0.27 THz (see Figure

5.2.4(a)). When an additional toroidal resonator was stacked, the Full Width at Half Maximum (FWHM) increased to 0.37 THz. This represents a bandwidth increase of over 150% compared to the single metasurface, as shown in Figure 5.2.4(b). The broadband transmission results from the superposition of closely spaced individual toroidal resonances, highlighting the benefits of the multi-stacked approach.

To demonstrate the broadening response of the terahertz transmission amplitude in both single and multistacked toroidal metamaterials, we calculated the radiated power for the electric, magnetic, and toroidal dipoles, denoted by WP, WM and WT, respectively. The equations are as follows[132]:

$$P = \frac{1}{i\omega}\iiint J dv \tag{5.6}$$

$$M = \frac{1}{2c}\iiint (r \times J) dv \tag{5.7}$$

$$T = \frac{1}{10c}\iiint [(r.J)r - 2r^2 J] f dv \tag{5.8}$$

$$WP = \frac{2\omega^4}{3c^3}|P|^2 \tag{5.9}$$

$$WT = \frac{2\omega^6}{3c^5}|T|^2 \tag{5.10}$$

$$WM = \frac{2\omega^4}{3c^3}|M|^2 \tag{5.11}$$

Where r is the position vector, J is the volume current density, and ω is the angular frequency of the incident radiation. The speed of light in a vacuum is represented as c. The P, T, and M denote the electric, toroidal, and magnetic moments, respectively. The red, black and green curves in Figures 5.2.3(a) and 5.2.3(b) illustrate the power radiated by the electric, toroidal, and magnetic dipoles for single and multistacked MM, respectively. It is evident that in both cases, the toroidal dipole exhibits a prominent feature at resonance, confirming that the excitation is associated with toroidal excitation. This toroidal excitation can be further

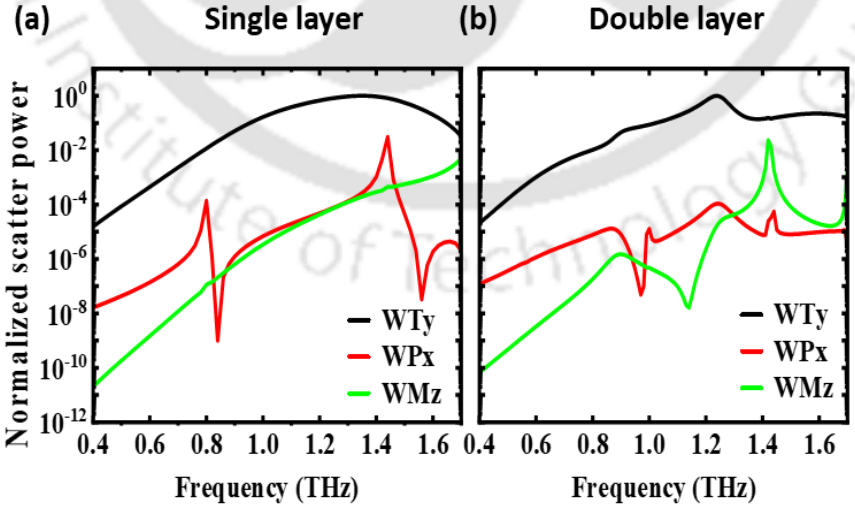

Figure 5.2.3: (a) and (b) Multipolar analysis for single and multi-stacked configurations over the simulated frequency range, showing the dominance of toroidal dipolar excitation over electric and magnetic dipolar contributions.

elucidated by correlating the scatter plots with the corresponding current profiles. In Figures 5.2.4(a) and 5.2.4(b), we present the current profiles, transmission spectra, and toroidal

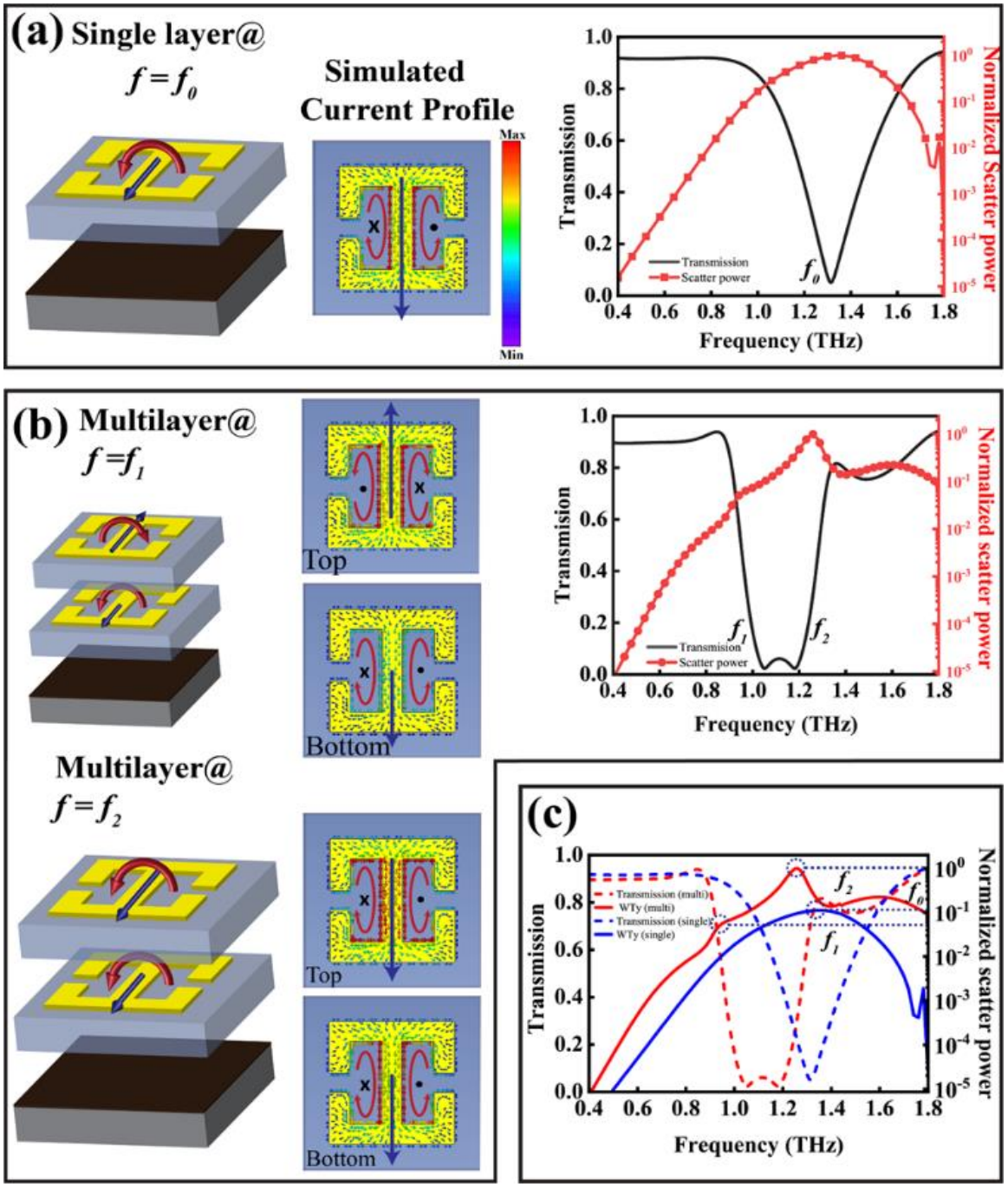

Figure 5.2.4: (a) Transmission response and electric field distribution for a single-layer toroidal resonator at the fundamental frequency $f=f_0$, illustrating the initial field confinement and scattering characteristics. (b) Transmission response and electric field distribution for a double-layer configuration at resonance frequencies $f=f_1$ and $f=f_2$, showing enhanced field confinement and scattering power in the stacked configuration, demonstrating the impact of multi-layer stacking on resonance behaviour. (c) Represents the comparison of the scattering power of the single and multilayered toroidal MM

scattering powers for both single and multistacked metamaterials (MM). Figure 5.2.4(a) shows a 3D illustration and the current profile for a single-layered MM. The current flows counterclockwise on the right side and clockwise on the left side of the MM, resulting in a magnetic field emerging from the right and penetrating the left, which gives rise to a downward-directed toroidal dipole. To further confirm the toroidal excitation, the transmission spectrum and the normalized toroidal scattering power, represented by black and red traces, respectively, are plotted in Figure 5.2.4(a). Notably, at f_0=1.31 THz, the toroidal scattering power reaches its maximum at resonance, supporting the toroidal nature of the excitation.

In the case of the multistacked MM, two resonances are observed at f_1=1.05 THz and f_2=1.18 THz. Figure 5.2.4(b) presents the 3D representation of the toroidal direction, transmission spectrum, and normalized scattering power for toroidal scattering. At both resonances, an increase in scattering power is evident, with the scattering at f_2 being significantly higher than at f_1. This behaviour can be understood by examining the surface current profiles at both resonances. At the f_1 resonance, the bottom resonator exhibits the same current flow as in the single-layer case, resulting in a downward-directed toroidal dipole. In contrast, the top resonator displays an opposite current flow with a higher concentration, leading to an upward toroidal excitation. For the f_2 THz resonance, both top and bottom resonators exhibit downward toroidal excitation, with the top resonator showing a slightly higher current concentration. This aligned excitation results in an enhancement of toroidal scattering, reflected in the increased scattered power observed in Figure 5.2.4(b). Comparing the toroidal scattering power for the single and multistacked MM, as shown in Figure 5.2.4(c), the toroidal scattering is highest at $f_2$and lowest at f_1, while the single-layer toroidal scattering power (at f_0) lies between the scattered power at f_2 and f_1.

5.2.4 Characterization of the VO_2

To create an actively tunable metamaterial (MM), we integrated the toroidal multistacked MM with a VO_2 thin film. Before integrating the VO_2 with the multistacked MM, the temperature-dependent transmission amplitude of VO_2 was calculated using THz-TDS (Figure 5.2.5(c)),

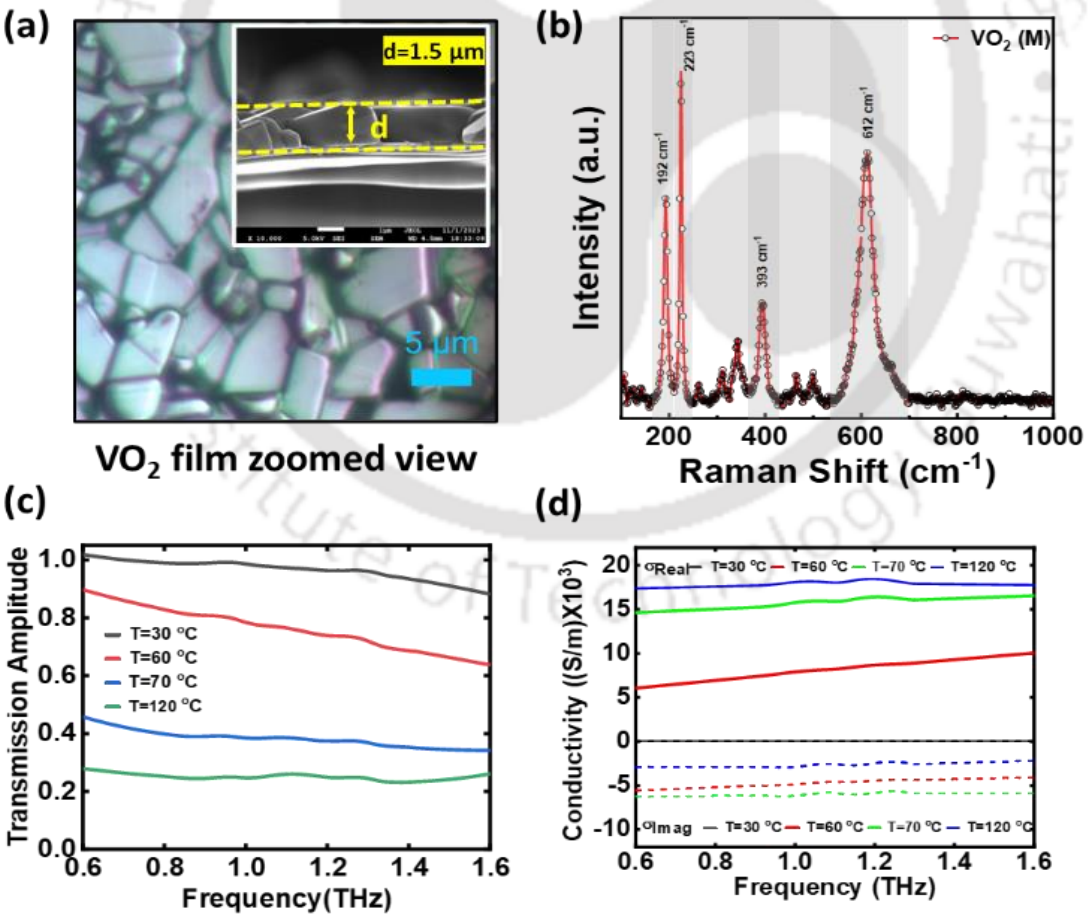

Figure 5.2.5: (a) Optical zoomed micrograph of the VO_2 film, with an inset showing a cross-sectional FESEM image indicating a thickness of 1.5 µm. (b) Raman spectra of the VO_2 film highlight phase transition peaks. (c) Temperature-dependent transmission amplitudes extracted using THz-TDS. (d) Complex conductivity with respect to the variation of different temperatures.

and the complex refractive index of the VO_2 thin film was calculated using equation (5.1)[119] as discussed in section 5.1.3. The real (σ_1) and imaginary (σ_2) components are plotted in Figure 5.2.5(d) for temperatures ranging from T = 30 °C to T = 120 °C. Figure 5.2.5(d) shows that as the temperature increases from 30 °C to 120 °C, the conductivity(σ_1) changes from 10 S/m to 17,500 S/m. It is also observed that σ_1 is nearly flat with a slightly positive slope, consistent with terahertz studies of VO_2 conducted by other groups. Meanwhile, σ_2 remains negative at all temperatures. The behaviours of σ_1 and σ_2, persisting into the fully metallic state, are characteristic of localized charge carriers. The detailed analysis of the VO_2 layer is discussed in section 5.1.3.

5.2.5 Reuslt and discussions

To modulate the transmission amplitude of the hybrid MM, we increased the thin film conductivity from 10 S/m to 17,500 S/m by raising the temperature from 30 °C to 120 °C (Figure 5.2.5(d)). This temperature-induced change in conductivity transformed the band-reject filter into a partial reflector, as illustrated in Figure 5.2.6. Figures 5.2.6(a) and 5.2.6(b) present the simulated and THz-TDS measured transmission modulation of terahertz radiation in the single-layer MM configuration, while Figures 5.2.6(c) and 5.2.6(d) show the corresponding results for the broadband terahertz multistacked MM. The optical images of the fabricated single and multistacked MM are shown in Figure 5.2.1(b). As shown in Figure 5.2.6, increasing the temperature of the hybrid metamaterial causes the device to transition from exhibiting a band-reject filter response to acting as a reflector. This tunable transition from a band-reject filter to a reflector in the hybrid MM holds promising applications in adaptive optics,

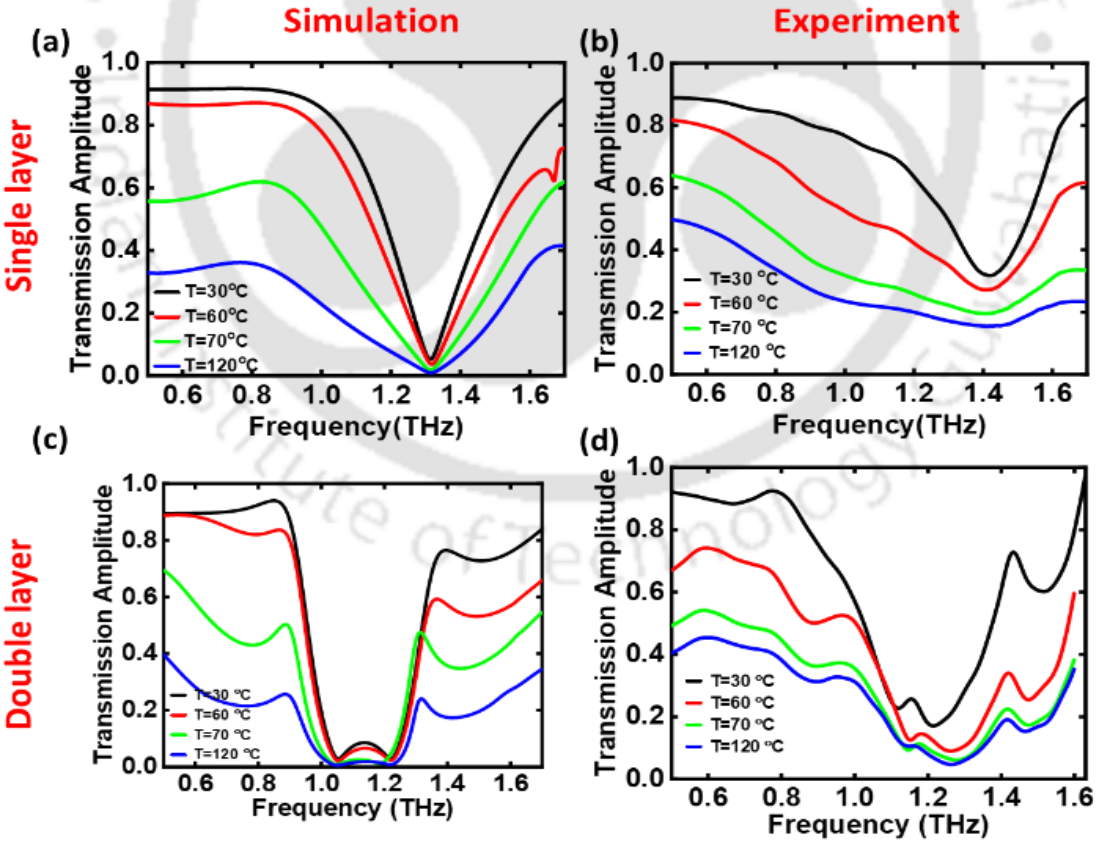

Figure 5.2.6: (a, c) Simulated transmission amplitude modulation for single and double-layered metamaterials, respectively, (b, d) The corresponding experimentally measured transmission amplitude modulation. The graphs depict the temperature-dependent modulation, where an increase in temperature from 30°C to 120°C transforms the band-reject transmission filter into a reflector.

switchable reflective coatings, and communication systems.

Band-Reject Filter to Broadband Reflector:

We analyzed the dynamic response of the proposed multistacked metamaterial by calculating its transmittance, reflectance, and absorption under two distinct temperature conditions: room temperature and a higher temperature (T=120°C), which is above the phase transition temperature of VO_2. At room temperature, VO_2 is in its insulating phase, while at 120°C, VO_2 transitions to its metallic phase. The results, presented in Figures 5.2.7(a) and 5.2.7(b), illustrate the influence of temperature on the metamaterial's optical behaviour.

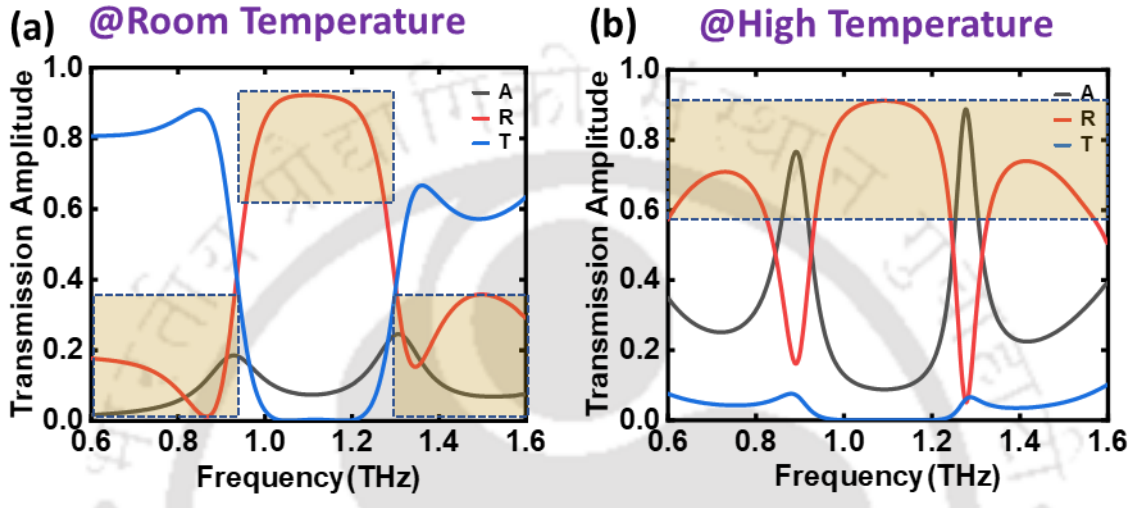

Figure 5.2.7: Temperature dependent transition of the band reject filter into broadband reflector. (a) transmission response of multistacked MM at low temperature behaving as band reject filter. (b) Transmission amplitude at higher temperature behaving as broadband reflector.

At room temperature (Figure 5.2.7(a)), the metamaterial exhibits maximum reflectance in the frequency range of 1.0 to 1.3 THz, while outside this band, the reflectance is minimal (as represented by the shaded region), allowing significant transmission. This behaviour demonstrates that the metamaterial functions as a band-reject filter, selectively reflecting terahertz waves within the specified frequency range and transmitting waves outside it.

In contrast, at the higher temperature of 120°C (Figure 5.2.7(b)), where VO_2 is in its metallic phase, the reflectance increases dramatically across the entire frequency range (as shown in the shaded region), resulting in a pronounced suppression of transmittance. This transition is driven by the phase change in the VO_2 layer, which enhances the overall reflective properties of the metamaterial. Consequently, the metamaterial evolves into a broadband terahertz reflector, capable of reflecting most of the incident terahertz waves across the spectrum.

The absorption plots confirm minimal absorption in both temperature conditions, indicating that the metamaterial efficiently manages terahertz waves by either reflecting or transmitting them, depending on the temperature. The shift from a selective band-reject filter at room temperature to a broadband reflector at higher temperatures is a direct result of the tunable conductivity of the VO_2 layer.

5.2.6 Summary

In this work, we designed an actively tunable broadband terahertz metamaterial achieving an FWHM of 370 GHz, a 150% enhancement over the 0.27 THz FWHM of a single-layer resonator. The broadband response is driven by toroidal excitation in the stacked resonators, enabling the superposition of individual resonances and significantly broadening the

transmission bandwidth. A detailed multipolar analysis highlights the dominance of toroidal dipolar excitation in the multi-stacked metamaterial, demonstrating its role in enhancing spectral selectivity and resonance bandwidth. The temperature-dependent properties of the fabricated VO_2, characterized using THz-TDS, further enabled the development of a tunable multi-stacked metamaterial. By varying the VO_2 layer's temperature from 30°C to 120°C, the device transitions from a band-reject filter to a nearly perfect reflector. This actively tunable metamaterial is ideal for controlling transmission amplitude or data rate in terahertz wireless communication systems.

Chapter 6: Machine learning-driven ultra-broadband terahertz Multilayer Metamaterial

6.1 Introduction

The development of robust terahertz components, such as absorbers, polarizers, phase shifters, sensors, switches, modulators, and THz lenses, is vital for advancing next-generation terahertz communication systems. Metamaterials have emerged as exceptional candidates for designing and fabricating such components due to their unparalleled ability to manipulate electromagnetic waves and confine light at subwavelength scales. Researchers have predominantly relied on computational modelling and numerical simulations to design both planar and multi-stacked metamaterials for various broadband applications, including filters, frequency selectors, wave plates, and detectors.

The design and fabrication of metamaterials, however, present significant challenges due to the complex interaction of their subwavelength structures with electromagnetic waves. Traditional design approaches, which rely on computational techniques, patterning, and self-assembly, often involve an extensive trial-and-error process[133, 134]. These methods utilize analytical and numerical techniques, such as Finite-Difference Time Domain (FDTD) simulations and genetic algorithms, which are computationally intensive and require substantial manual adjustments. Addressing these limitations, machine learning (ML) techniques, including deep learning, have emerged as transformative tools for designing and optimizing metamaterials. Deep learning-assisted design is particularly advantageous over conventional methods [84, 135, 136]. Once a neural network is appropriately constructed and trained on initial data, it can swiftly predict the properties of a metamaterial based on its structural input, eliminating the need for repetitive computational cycles. ML techniques expedite the discovery and design of novel metamaterial compositions and structures by predicting properties and optimizing configurations efficiently[137-142].

This work introduces a machine learning-driven ultra-broadband terahertz multilayer metamaterial. Section 6.2 elaborates on the design of multi-stack metamaterials, detailing the geometric configuration, material selection, and simulation methodologies. Section 6.3 focuses on data pre-processing, including parametric sweeps, data normalization, and training dataset preparation. In Section 6.4, the results and discussions present the performance of various ML models, including forward and inverse methods, alongside an experimental validation of the fabricated samples. Subtopics like subwavelength coupling and mode splitting provide insights into the broadband transmission mechanism. These results, supported by experimental measurements, establish a comprehensive workflow for designing and validating ultra-broadband metamaterials. This work demonstrates a machine learning approach, particularly the Random Forest method, can effectively predict structural parameters for broadband applications, paving the way for innovative THz metamaterial designs.

6.2 Design of multistacked metamaterial

The proposed metamaterial configuration was designed using the CST Microwave Studio Suite software, which employs finite element and finite integration techniques. The multistacked metamaterial consists of a cross-shaped resonator on top of a hexagonal resonator, as shown in Figure 6.1(a). The selection of these resonators was driven by their ease of fabrication and symmetric design, which facilitate polarization-insensitive ultra-broadband transmission responses. The proposed metamaterial consists of a total of 12 structural parameters, of which 7 are variable. The dimensions of the fixed parameters are as follows: the periodicity of the unit cell (P) is 100 µm, the width of each resonator (w) is 7 µm, the thickness of the polyimide layer (t_p) is 50 µm, the thickness of the aluminium metallic resonator (t_m) is 0.2 µm, and the thickness

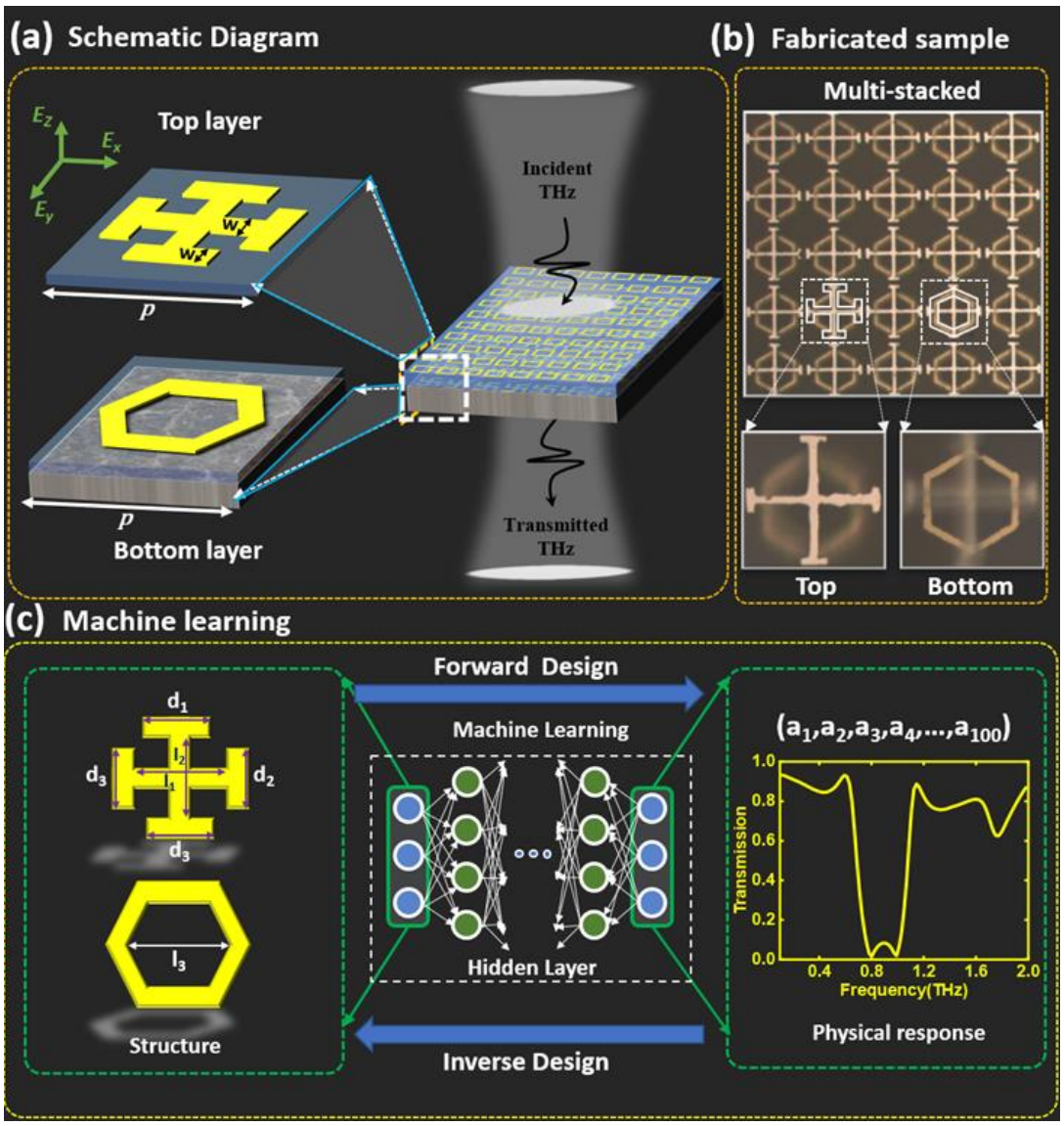

Figure 6.1: 3D metamaterials structure. (a) Shows the schematic diagram and the unit cell of the metamaterial structure. (b) Shows the microscopic pictures of the fabricated multi-layered metamaterial and the zoomed view of the top and bottom layers of the unit cell, respectively. (c) The architecture of machine learning model. (Forward) - Forward model that predicts transmission spectrum from structures. (Inverse) – Inverse model that predicts structures from the transmission spectrum.

of the substrate (t_s) is 25 µm. The ranges of the variable parameters (d_1, d_2, d_3, d_4, l_1, l_2, and l_3) are provided in Table 6.1. Since the periodicity of the MM is 100 µm, in order for the length of the structure to be compatible with the unit cell, it has to be smaller than the periodicity; therefore, the maximum length was 85 µm. In a similar manner, to avoid the overlap or coupling between the extended fork (d_1, d_2, d_3, and d_4), the maximum range was taken to be 20 µm, which is approximately half of the minimum range of resonator length (l_1, l_2, and l_3). The permittivity of the quartz and polyimide was chosen as 4.4 and 3.5, respectively. The simulation was performed using a frequency domain solver with tetrahedral meshing. Unit cell boundary conditions were applied to the x and y axes, while open-add space and open boundary conditions were imposed along the positive and negative z-axes, respectively. The incident terahertz radiation was predominantly oriented perpendicular to the sample plane, with the electric field (E-field) aligned along the y-axis of the resonators.

Table 6.1: Different variable parameters corresponding to their range.

Variable parameters	Dimension (µm)	Variable parameters	Dimension (µm)
d_1	10-20	l_1	45-85
d_2	10-20	l_2	45-85
d_3	10-20	l_3	45-85
d_4	10-20		

6.3 Data pre-processing

Approximately 2187 data points (transmission plots corresponding to the different combinations of the unit cell parameters) were extracted using a parametric sweep in the CST software for the meta-atom. Each input parameter was varied independently within specified ranges and steps: d_1 from 10 to 20 with a step of 5 (3 steps), d_2 from 10 to 20 with a step of 5 (3 steps), d_3 from 10 to 20 with a step of 5 (3 steps), d_4 from 10 to 20 with a step of 5 (3 steps), l_1 from 45 to 85 with a step of 20 (3 steps), l_2 from 45 to 85 with a step of 20 (3 steps), and l_3 from 45 to 85 with a step of 20 (3 steps). By applying the Multiplication Principle, the total number of combinations (or total data points) can be calculated as:

$$\prod_{i=1}^{n} S_i = 3 \times 3 \times 3 \times 3 \times 3 \times 3 \times 3 = 2187,$$

where n is the total no. parameters and S_i is the number of steps for the i^{th} parameter.

Before feeding data into the ML model for training, we averaged the transmission amplitude data from 1000 data points down to 100 points to minimize large errors in the output parameters. These 100 data points were compared with the original 1000 data points to ensure the nature of the transmission spectra remained consistent. A random sample was taken from

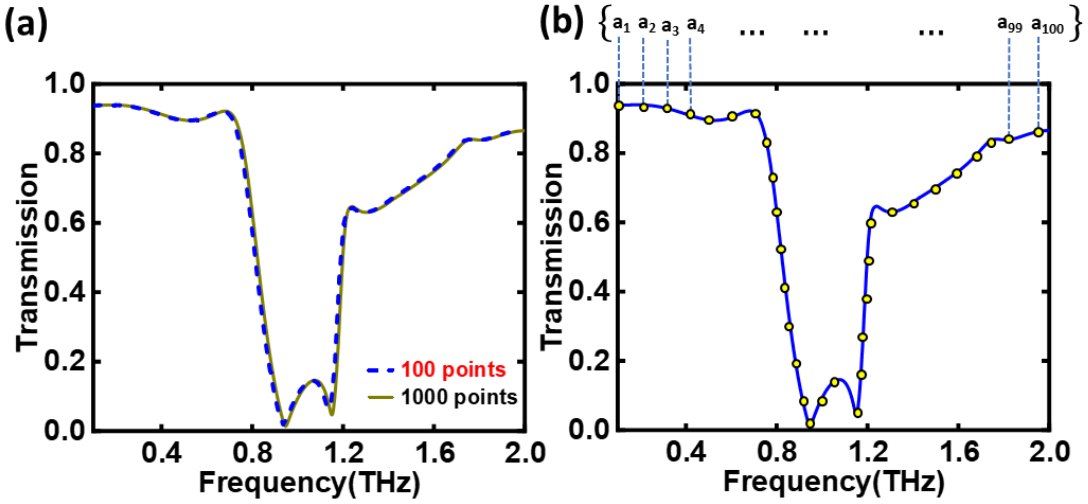

Figure 6.2:(a) Comparison of transmission spectra with 100 data points (dashed line) and 1000 data points (green solid line). The negligible change justifies using 100 data points for output. (b) Transmission amplitude spectrum with each point (x, y) representing frequency and corresponding transmission amplitude. Only the y-values are used to form a 1-D array for the output data.

the data sets to observe any changes in the transmission spectra, as shown in Figure 6.2(a). The 100 data points are denoted by the dashed line, and the 1000 data points by the green solid line. As shown in Figure 6.2(a), the change is negligible after averaging to 100 data points. Therefore, instead of using 1000 data points as output, we have used 100 data points.

Next, the graphical data (transmission amplitude consisting of 100 points) were converted into a one-dimensional (1-D) array for the output data. In the dataset, the input points are the structural parameters of the metamaterial, and the output is the projection of the transmission amplitude spectrum, represented as a 1-D array. These spectra are received as text files from CST, and further processing is performed on these files. By focusing on the projection, only the points on the y-axis of the transmission spectrum are considered. For example, in Figure

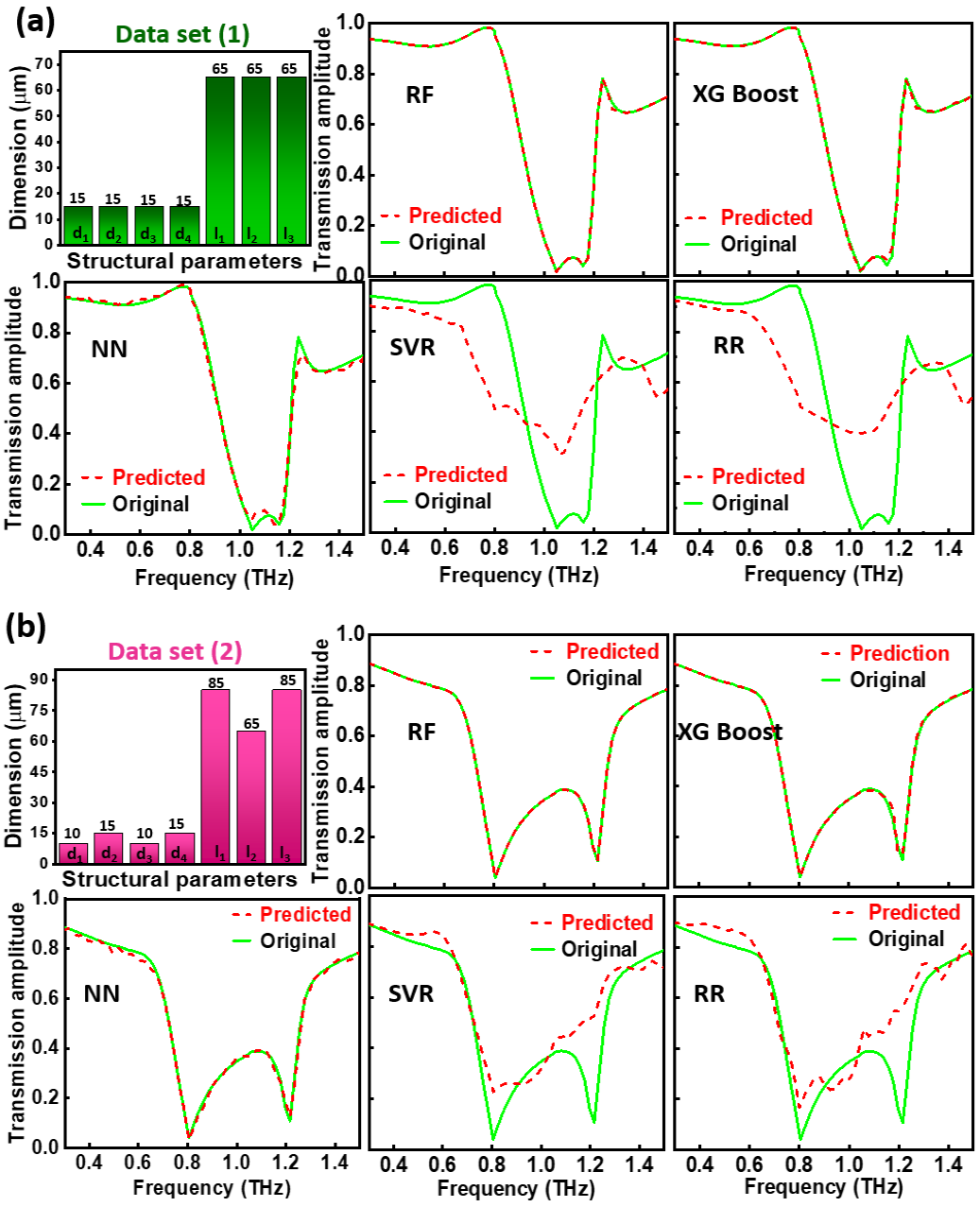

Figure 6.3: (a) and (b) present the verification of the forward method using two random test datasets, Data Set (1) and Data Set (2), tested with NN, RF, SVR, XGBoost, and RR methods. The bar charts represent input structural parameters (d_1, d_2, d_3, d_4, l_1, l_2, l_3), and the plots compare the corresponding output transmission amplitudes. The dashed red line shows the predicted transmission from all models, while the green solid line represents the original transmission amplitude from the CST simulation.

6.2(b), each point (x, y) indicates that x is the frequency, and y is the corresponding transmission amplitude at that frequency (with 100 such points in the plot). Therefore, only the y-values are considered in the dataset, creating a 1-D array. The plot can then be reconstructed from the array using 100 equidistant points as x-values. Hence, the final dataset for training contains seven input parameters and 100 points of transmission amplitude values as the output data. For machine learning training, we used 10-fold Cross-validation to provide a reliable estimate.

6.4 Results and discussions:

After generating the training data, the pre-processed data was fed into the forward model as well as the inverse model. In the forward model, variable structural parameters of MM are considered input features, while the transmission amplitude data points are output data points. The main objective of the forward model is to predict the transmission amplitude spectrum from the structural parameters using a machine-learning technique. Conversely, the inverse model takes a specific transmission spectrum as input and structural parameters as output data

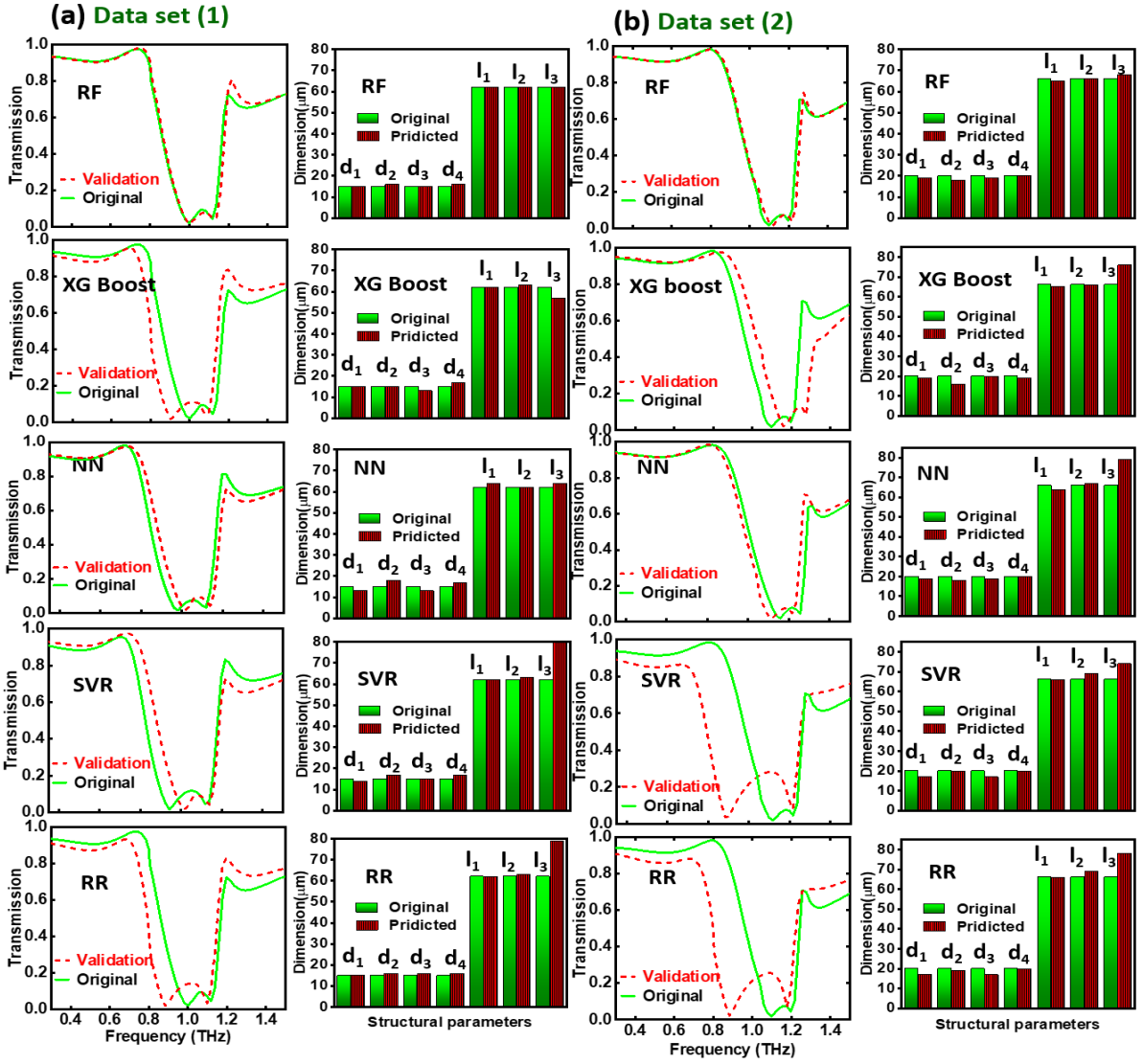

Figure 6.4: (a) and (b) presents verification of the inverse method using two randomly selected test datasets. The transmission amplitude spectrum (100 data points) is taken as input, while the 7 structural parameters (d_1, d_2, d_3, d_4, l_1, l_2, l_3) are the output. The green chart bars represent the predicted structural parameters, and the red chart bars represent the original parameters from the CST simulation. Additionally, the transmission amplitude from CST simulation using the predicted parameters is compared with the original transmission amplitude.

points. The inverse model aims to predict the structural parameters of a metamaterial structure with the desired properties.

We evaluated a diverse set of regression models for a multi-output regression task, including Ridge Regression (RR), Support Vector Regression (SVR), Random Forest Regressor (RF), XGBoost Regressor, and a Multi-Layer Perceptron (MLP) Regressor neural network (NN). Ridge Regression, with L_2 regularization, effectively handles correlated features by stabilizing estimates[87], while SVR uses a kernel-based method to approximate input-output relationships in high-dimensional spaces[90]. The Random Forest Regressor, an ensemble method, improves accuracy and handles complex patterns by averaging multiple decision trees[89]. XGBoost, a gradient-boosting technique, efficiently manages large and sparse datasets through optimization and regularization[92]. Finally, the MLP Regressor, with its multi-layer neural network structure, captures intricate, non-linear relationships using ReLU activation and the Adam optimizer, making it suitable for tasks with highly non-linear data[93]. More detail about the different models is given in appendix B2.

To verify the forward and inverse models, two random test datasets (namely Data Set (1) and Data Set (2)) were selected and tested using the NN, RF, SVR, XGBoost, and RR models. For the forward method, a set of structural parameters ($d_1, d_2, d_3, d_4, l_1, l_2, l_3$) was chosen as input data, while 100 data points of the transmission amplitude spectrum were taken as output points. In Figures 6.3(a) and 6.3(b), the input parameters (represented by the chart bar) and corresponding output transmission are plotted for the different regression models. The predicted transmission from all the models are shown in the dashed red line, while the green solid line represents the original transmission amplitude calculated from the CST simulation for the same data sets (Data Set (1) and Data Set (2)). Figures 6.3(a) and 6.3(b) show that the transmission amplitude calculated from the RF model is a much more accurate comparison to all other models.

Similarly, two randomly selected datasets were chosen from the test data files for the inverse method. The transmission amplitude spectrum (100 data points) was taken as input, while the 7 structural parameters ($d_1, d_2, d_3, d_4, l_1, l_2, l_3$) were taken as output. The predicted structural parameter datasets were calculated using all five models shown in Figures 6.4(a) and 6.4(b). The predicted (Red chart bar) and original sets of parameters (Green chart bar) are shown in Figure 6.4 for all the models, and it can be concluded that the RF model is predicting the nearest structural parameters in comparison to the original structure parameters extracted from the CST simulation. In order to validate the predicted structural parameters from different models, we also compared the transmission amplitude with respect to the original structure parameters and the transmission amplitude calculated using the predicted structural parameters (again ran the CST simulation with the predicted structural parameters and compared it with the original transmission amplitude).

The average mean absolute error (average MAE) for both the forward and inverse models using all five algorithms was calculated. The results show that the RF, XGBoost, and NN algorithms have a lower average mean error than the SVR and RR algorithms. It is clear from Table 6.2 that the most accurate model for the multistacked metamaterial design is the RF model, while the RR is the worst in predicting the actual input and output parameters from both methods. It is also important to note that for the randomly chosen two data sets (Data Set (1) and Data Set (2)), we found that RF and XGBoost are always able to predict more accurate results, while for another random data set, it may be possible that other models can give the best results. Here, we calculated various metrics to obtain optimal results, including the average Mean Absolute Error (MAE), R-squared value, and Root Mean Square Error (RMSE). These metrics collectively represent the overall error contributed by all data points (from a total of 2187 data

sets). The formulas for calculating the average MAE, R-squared value, and RMSE are provided in **Appendix B**, specifically in Section B1. To further refine the analysis, we placed particular emphasis on reducing the Mean Absolute Error (MAE) by improving the methodology to enhance the accuracy and reliability of the results.

Table 6.2: Comparison between different matrices for the different algorithm.

Classifier	**Average R-squared**	**Average RMSE**	**Inverse Avg. R-squared**	**Inverse Avg. RMSE**	**Avg. MAE**	**Inverse Avg. MAE**
Ridge	0.68	3.2362	0.4869	0.1009	3.3182	0.0885
SVR	**0.6545**	3.3645	**0.2657**	0.1066	3.3118	0.0954
RandomForest	0.7928	2.4428	0.9739	0.0138	**2.2391**	**0.0053**
XGBoost	0.8353	**2.2642**	0.9783	0.0128	2.2476	0.0061
NN	0.8247	3.4985	0.8633	**0.0644**	3.5431	3.3231

6.4.1 Ultra-broadband terahertz metamaterial using ML and Experimental verification

After a rigorous study of different machine learning models for harnessing the multistacked terahertz broadband metamaterial, we concluded that the desired multistacked metamaterial could be effectively designed using the random forest method. This method accurately predicts both the transmission amplitude and structural parameters using the forward and inverse models. We employed the random forest model to determine the structural parameters and designed an ultrabroad terahertz metamaterial, specifically a band-reject filter, targeting a range from 0.5 THz to 1.5 THz with a full width at half maximum (FWHM) of more than 250 GHz. Notably, the data points (transmission amplitude of 100 points) for this filter were not included during the training of the random forest model, making it unknown to the model. Figure 6.5(a) displays the transmission amplitude of the desired filter, for which we needed to predict the structural parameters using the random forest model. Figure 6.5(b) presents the predicted structural parameters, while Figure 6.5(c) compares the transmission amplitude of the unknown band reject filter with that calculated using CST based on the predicted parameters. The close match between the transmission amplitude calculated from predicted structural parameters and the actual transmission amplitude demonstrates the accuracy of the machine-learning model.

To experimentally verify the ultra-broadband response of the multistacked MM (predicted band-reject filter using ML), a series of fabrication steps were performed to create the desired multistacked pattern on a quartz substrate[143]. The quartz sample was initially cleaned using acetone, isopropyl alcohol (IPA), and deionized (DI) water, then dried with N_2 gas and heated at 100°C for 10 minutes. A 200 nm thick layer of aluminium was deposited onto the clean substrate using a thermal evaporator ensuring the thickness exceeded the skin depth in the terahertz range to prevent partial transmission[144]. To enhance the adhesion of the photoresist, hexamethyldisilazane (HMDS) was applied at 3500 RPM for 60 seconds, followed by heating at 150°C for 30 minutes. The substrate was then coated with a positive photoresist (S1813) at 3000 RPM for 60 seconds and baked at 100°C for 2 minutes for uniformity and stability. A mask writer was used to expose the substrate to UV light, forming the desired pattern. The

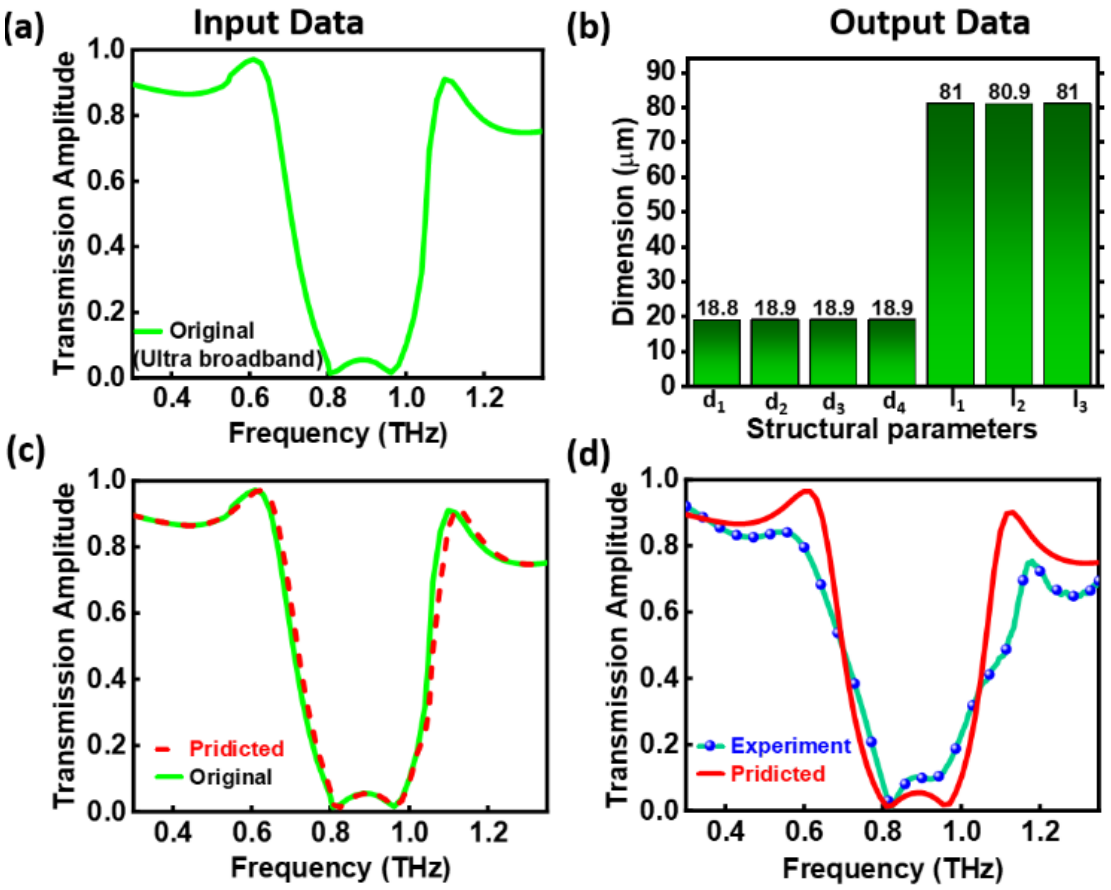

Figure 6.5: (a) Transmission amplitude of the desired ultra-broadband band-reject filter for predicting structural parameters using the random forest model. (b) Predicted structural parameters. (c) Comparison of the transmission amplitude of the unknown filter with CST simulation based on predicted parameters. (d) Experimentally measured transmission spectra alongside predicted transmission amplitude, demonstrating a close match and validating the machine learning approach for designing multistacked metamaterials.

exposed patterned substrate was then developed in M319 solution for 60 seconds, and an aluminium etchant was used for 2-3 minutes to form the pattern. The sample was cleaned with acetone and DI water, dried with N_2 gas, and heated at 100°C for 5 minutes. For the multistacked layer, a 50 µm thick layer of Kapton polyimide layer was applied on the single-layered fabricated metamaterial, and the same lithography process was repeated for the second layer. The alignment of one resonator with the other was achieved using the three-point method with the Kloe Dialse 250 mask writer.

Terahertz transmission measurements were conducted using a THz time-domain spectroscopy (THz-TDS) setup from LUNA Innovations (Terametrix 5000 T-Ray) with fibre-coupled photoconductive antennas (PCA) for both generation and detection. The transmitted signal was focused onto the metasurface sample using a parabolic mirror and directed to the THz receiver. The THz-TDS spectrum was initially obtained for a bare quartz substrate as a reference and then for the multistacked MM sample. The time-domain signals were transformed into frequency-domain signals using fast Fourier transformation (FFT), and the ratio of the metamaterial spectrum to the reference spectrum provided the transmission through the sample[99, 100, 145]. Figure 6.1(c) shows the micrograph of the fabricated multistacked metamaterial structure. Figure 5(d) presents the experimentally measured transmission spectra alongside the predicted transmission amplitude, demonstrating a close match and validating the machine learning approach for designing multistacked metamaterials.

6.4.2 Subwavelength coupling and mode splitting

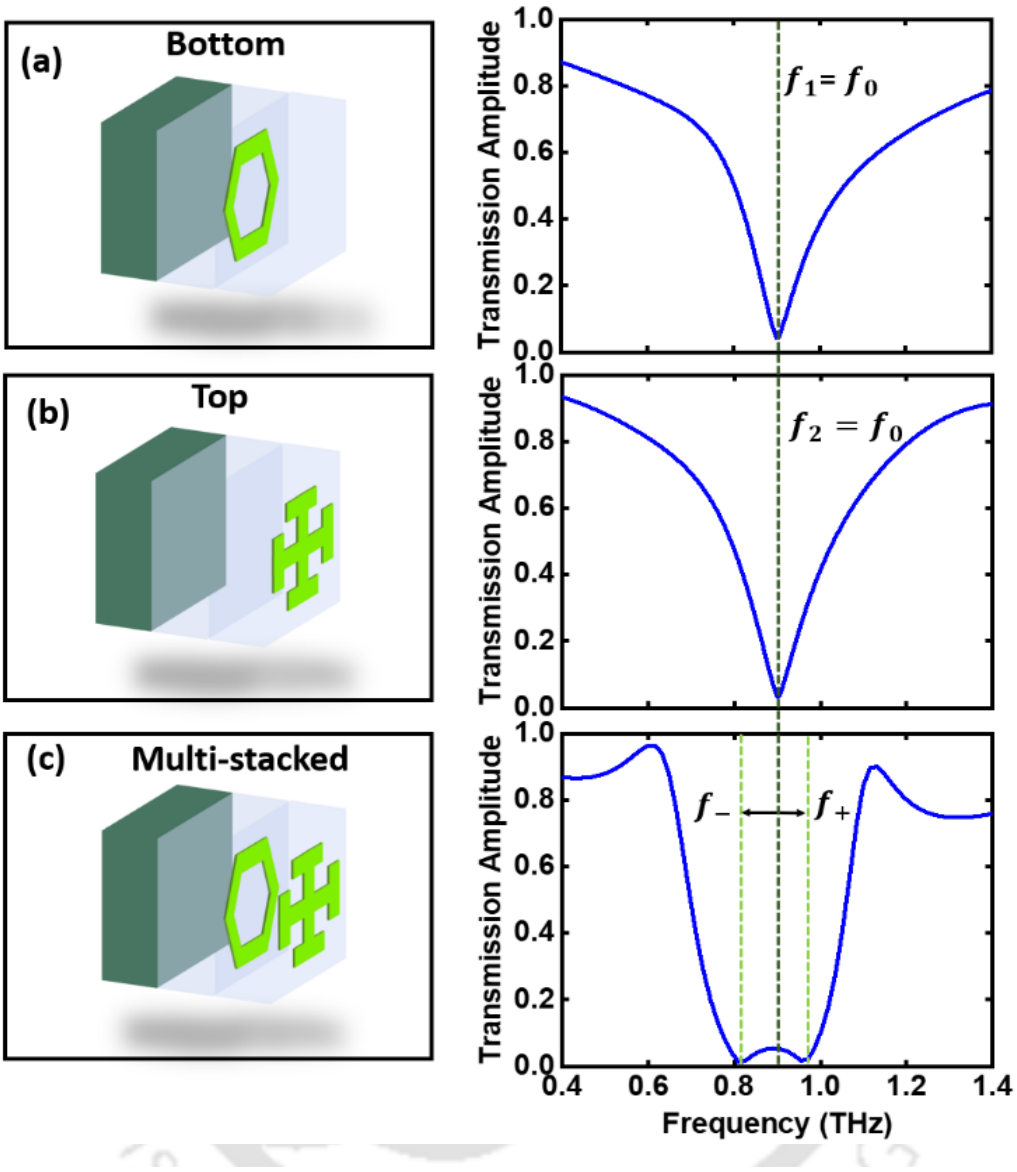

Figure 6.6: (a) Transmission amplitude due to the bottom resonator. (b) Transmission amplitude due to the top resonator. (c) transmission amplitude due to multistacked resonators. The Individual resonators (hexagonal or cross) have a resonance dip at f_0 = 0.90 THz. When stacked (multistacked configuration), this dip splits into two resonances (f_- and f_+), broadening the transmission amplitude. The coupling between the resonators hybridizes the single mode into two plasmon modes.

To elucidate the impact of subwavelength microresonator structures on the broadening of the transmission amplitude bandwidth, we studied the hybridization scheme of the plasmon modes of both individual resonators and multistacked resonators. From Figure 6.6, it can be seen that for the individual resonators (the hexagonal resonator and the cross resonator), the resonance dip coincides at f_0 = 0.90 THz. These resonances are predominantly due to electric dipoles in the THz regime and can also be interpreted in terms of localized plasmon resonance [146-148].

However, when the cross resonator is stacked onto the hexagonal ring resonator (multistacked configuration), the single resonance dip splits into two closely positioned resonances (f_- and f_+), resulting in a broadening of the transmission amplitude. For the multilayer, the coupling between the bottom and top resonators lifts the degeneracy of the single resonator mode, hybridizing it into two plasmon modes. One mode is symmetric and corresponds to in-phase

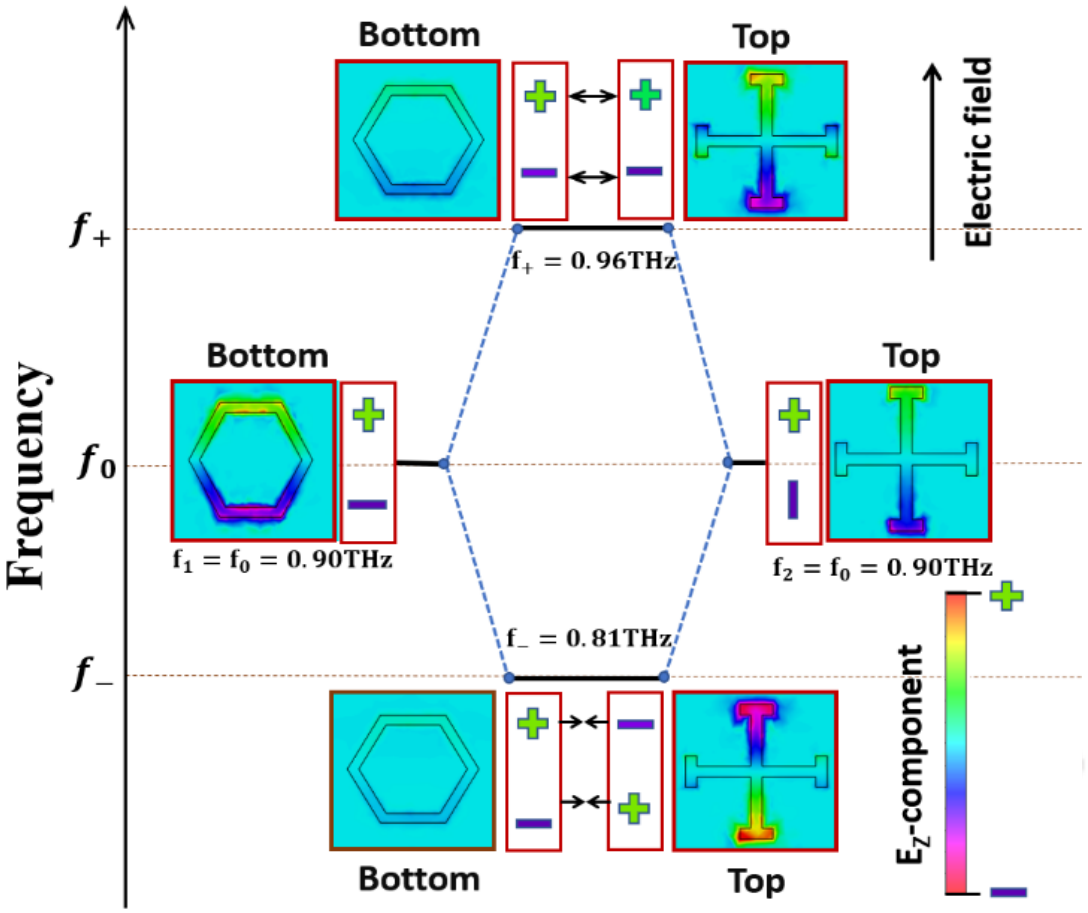

Figure 6.7: Illustration of the hybridization scheme of plasmon modes in multistacked metamaterials. The z-components of the electric field distributions for TE-polarized light are shown at four frequencies: f_1 = 0.90 THz, f_2 = 0.90 THz, f_+ = 0.96 THz, and f_- = 0.81 THz. The antisymmetric mode (low-energy) and symmetric mode (high-frequency) arise from in-phase and out-of-phase charge oscillations, respectively.

charge oscillations, while the other mode is antisymmetric and corresponds to out-of-phase charge oscillations. This can be seen in Figure 6.7, where the z-components of the electric field depict the charge distribution in the metallic resonator. The z-component of the electric field distributions for TE-polarized light was computed using numerical simulations in CST software. The field distribution was examined at four distinct frequencies: f_1 = 0.90 THz, f_2 = 0.90 THz, f_+ = 0.96 THz, and f_- = 0.81 THz. For a multistacked MM with a vertical alignment of the two resonators, the antisymmetric mode is the low-energy mode due to attractive forces in the system. Conversely, repellent forces are present in symmetric mode, making it the high-frequency mode. The stronger the coupling and the closer the spacing between the dipoles, the larger the frequency difference between the two modes. The broadening of the fundamental resonance in the multistacked metamaterial mainly depends on the separation and length of the stacked resonators and, hence, on the coupling between them. The separation and length of the resonators have been optimized to ensure that the mode splitting creates a broadband spectrum.

6.5 Summary

In this study, we successfully demonstrated the application of machine learning techniques to the design of ultra-broadband multistacked terahertz metamaterials. By employing forward and inverse ML methods using algorithms such as RR, SVR, RF, NN, and XGBoost, we were able

to predict transmission spectra from structural parameters and vice versa with high accuracy. Among the models tested, RF and XGBoost emerged as the most effective for achieving the desired ultra-broadband spectrum, with Random Forest particularly excelling in predictive accuracy for both forward and inverse tasks, as indicated by the lowest calculated average mean absolute error (average MAE for forward and inverse methods being 0.0053 and 2.2390, respectively) compared to other regression models. We then validated our RF regression model by predicting the structural parameters of an ultra-broadband band-reject filter (with an FWHM of 250 GHz) not included in the training data and confirmed these predictions through simulations and experimentally measured transmission amplitudes. The transmission spectrum calculated from the THz-TDS of the fabricated multistacked metamaterial closely matched the model predictions, further validating our approach. The analysis of electric field distribution and near-field coupling between resonators using a hybridization mode-splitting model confirmed that the broadening of the resonance is due to the mode splitting when stacking one resonator onto the other. This research highlights the significant potential of ML-driven approaches in the design of complex metamaterials, offering a more efficient alternative to traditional simulation-based methods. The methodology presented here not only accelerates the design process but also enhances the ability to explore and optimize new metamaterial structures for advanced terahertz applications.

Chapter 7: Summary and Future Direction

This thesis explores the design, fabrication, and characterization of terahertz metamaterials, with a focus on achieving enhanced broadband performance. The research starts by investigating passive metamaterials, utilizing both planar and multi-stacked configurations to significantly improve bandwidth. A planar single-layer metamaterial design was developed, which incorporated multiple bending-strip resonators alongside a straight-strip resonator. This innovative approach resulted in a substantial enhancement of the full width at half maximum (FWHM). Specifically, the two-resonator configuration achieved an FWHM of 270 GHz, while the addition of a third resonator increased the FWHM to 350 GHz, representing the highest reported broadband bandwidth in comparison to earlier studies. However, further improvements in planar designs faced limitations, as increasing the density of resonators led to trade-offs in resonance strength due to coupling effects and reduced resonator effectiveness at specific frequencies. To address these challenges, a multi-stacked metamaterial approach was explored as a solution for achieving broadband performance without compromising resonance strength. A polarization-independent multi-stacked metamaterial was designed and fabricated, achieving an FWHM of 500 GHz. This improvement was attributed to the selective excitation of resonators at different frequencies across the broadband spectrum. Field distribution analysis confirmed that the multi-stacked arrangement effectively combined individual resonances, resulting in a broader bandwidth while maintaining strong resonance dips.

Building on the foundation of passive designs, the thesis further explores active tunability by integrating a vanadium dioxide (VO_2) thin film with the multi-stacked metamaterial. The unique phase-transition properties of VO_2, which switches from an insulator to a metal with temperature changes, enabled dynamic control of the metamaterial's transmission. By utilizing complementary cross-shaped resonators stacked on one another and integrating them with the VO_2 layer, an ultra-broadband tunable modulator was developed. This design achieved an FWHM of 1.02 THz and a transmission modulation depth of 55% near 1.15 THz, with tunability achieved by varying the temperature from 50 °C to 90 °C. Additionally, a toroidal metamaterial design with stacked resonators demonstrated a tunable FWHM of 370 GHz, representing a 150% enhancement compared to a single-layer configuration. By adjusting the VO_2 layer's temperature from 30 °C to 120 °C, the toroidal metamaterial-based device transitioned from a band-reject filter to a nearly perfect reflector, showcasing its potential for dynamically controlling data rates and transmission amplitudes in terahertz communication systems.

The thesis also addresses the challenges associated with the complex design and optimization of metamaterials. Traditional approaches, which rely on extensive simulations and iterative adjustments, are time-intensive and computationally expensive. To overcome these limitations, machine learning (ML) techniques were employed to streamline the design process, as discussed in Chapter 6. Algorithms such as linear regression, support vector regression, random forest, neural networks, and XGBoost were applied to both forward (predicting spectral responses from structural parameters) and inverse (determining structural parameters from target spectra) design problems. Among these, Random Forest and XGBoost demonstrated superior performance, with Random Forest achieving the highest accuracy. A key validation involved predicting the parameters for an ultra-broadband band-reject filter with an FWHM of 250 GHz not included in the training dataset. The fabricated structure exhibited transmission characteristics closely matching the predictions from simulations and experimental measurements, confirming the reliability of the ML-based approach.

Overall, this thesis investigates diverse approaches to enhance broadband resonance in the terahertz range through advanced metamaterial designs. It also demonstrates the development of actively tunable modulators, enabling dynamic control for practical applications. Furthermore, machine learning techniques are applied to optimize the design process, offering new opportunities for advancing terahertz technologies and expanding their potential applications.

7.1 Future scope of work

Building on the advances in multistacked metamaterial-based terahertz modulators described in this thesis, future research should address current limitations in achieving broader bandwidth, enhanced tunability, greater modulation depth, and faster switching speeds. By integrating emerging materials, advanced design strategies, and novel computational tools, researchers can develop next-generation terahertz metamaterials for use in filters, switches, lenses, and modulators, ultimately driving transformative applications in communication, imaging, and sensing.

In this work, we expanded the terahertz bandwidth from 250–500 GHz for band-reject filters and above 1 THz for band-pass filters. Moving forward, three-dimensional and topological metamaterials can push these frequencies even higher while maintaining resistance to structural imperfections. Although VO_2-based metamaterials have shown promise for dynamic tunability, incorporating phase-change materials such as GeSbTe alloys and liquid crystals can further boost switching speed and modulation depth. Meanwhile, two-dimensional materials, graphene, transition metal dichalcogenides (e.g., MoS_2 and WSe_2), and Ge-based semiconductors offer lower power consumption and faster modulation, making them well-suited for reconfigurable terahertz devices.

While metallic resonators have been central to this thesis, combining plasmonic and dielectric elements can achieve ultra-wideband filtering with sharper filter edges, essential for communication systems that require precise frequency separation. Additionally, fabricating meta-atoms from two-dimensional semiconductors instead of metallic resonators can reduce ohmic losses, enhance nonlinear effects, and enable gate-controlled optical properties, thereby expanding the functionality of terahertz components.

Machine learning, as demonstrated with XGBoost, neural networks, and random forests, can be further enhanced through generative models (GANs, diffusion models) and physics-informed neural networks to discover novel metamaterial architectures. These data-driven approaches promise high performance, experimental feasibility, and rapid development of sophisticated, reconfigurable terahertz systems. By embracing these opportunities, terahertz technology will continue to evolve, opening new frontiers and driving significant breakthroughs in both fundamental research and practical applications across numerous industries.

.

APPENDIX A

A1. Synthesis of VO_2 thin films:

The synthesis of VO_2 thin films was achieved through the utilization of the Chemical Vapour Deposition (CVD) technique, as illustrated in Fig. A1(a)[149]. The experimental setup employed a single-zone tube furnace, with one end connected to a rotary pump. 100 mg of commercially available V_2O_5 powder (99.99%, Alfa Aesar) was placed inside an alumina boat, and a 1.5 cm wide quartz substrate was placed in a separate alumina boat at a 5 cm distance from the precursor powder (V_2O_5). All these were enclosed in a quartz tube and then the system was evacuated to a base pressure of 0.02 mbar using the rotary pump. To avoid any contamination Ar gas was purged multiple times before the experiment. Subsequently, the temperature of the hot zone (where the precursor is located) was raised to 900˚ C with a ramping rate of 15˚ C/min using a PID controller. Once the desired temperature was reached, it was maintained for 5 hrs with a continuous Ar flow at a rate 10 sccm. Then, the system was cooled down to room temperature at a slow cooling rate of 5˚ C/min. The Raman spectra of obtained VO_2 thin film is depicted in Fig. A1(b). The Raman peaks at 194 cm^{-1} and 223 cm^{-1} correspond to the stretching vibrational modes of the V-V dimers along the c-axis, whereas the broad peak at 612 cm^{-1} is due to the vibrations of the V-O bond. All these modes are the characteristics of the VO_2 phase. The X-ray diffraction (XRD) pattern of the as-obtained film (Fig. A1(c)) shows only one distinct peak at 27.80˚ which corresponds to the (011) plane of the VO_2 M1 phase, which also confirms a unidirectional growth of the film along [011] direction during the growth[122, 150, 151].

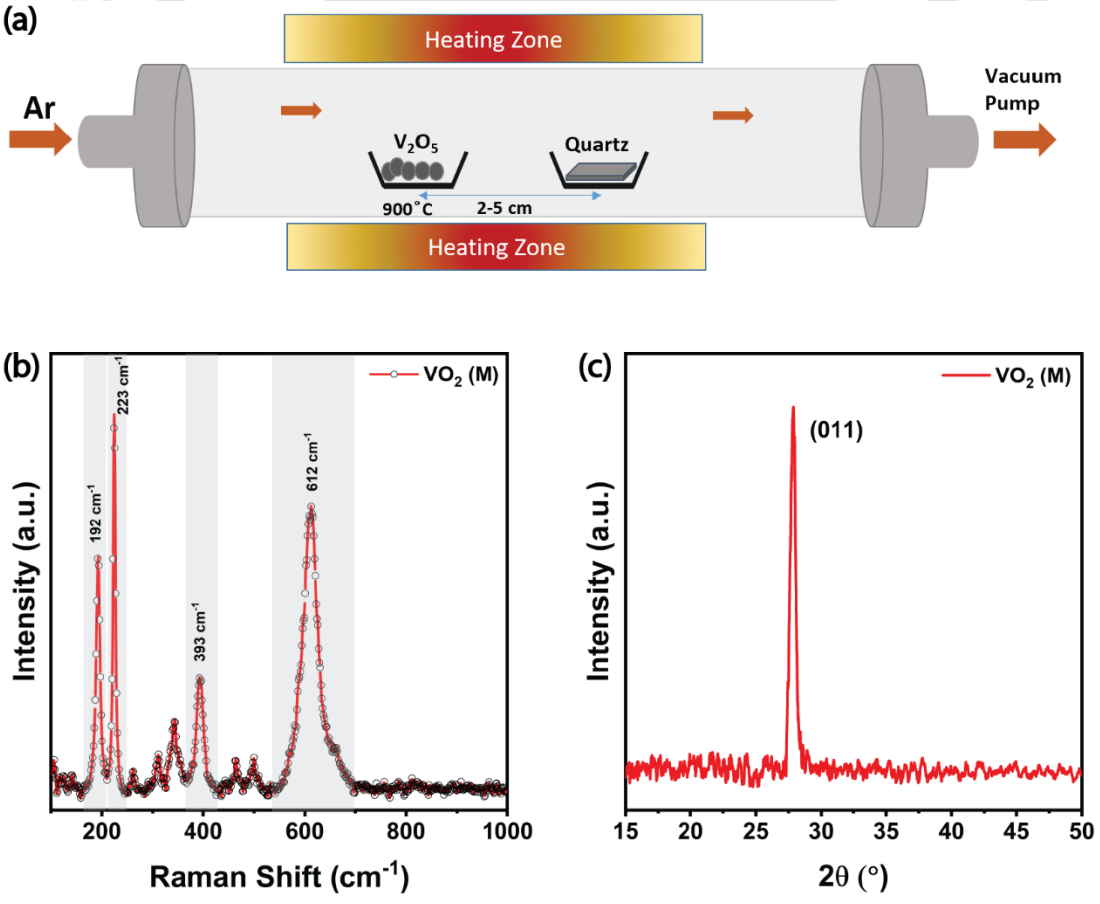

Figure A1: (a) Schematic diagram of the CVD setup for the synthesis of VO_2 thin films. (b) Raman spectrum of as-grown VO_2 thin films. (c) XRD pattern of the same.

A2. Optimization of spacer thickness and resonator's position

The thickness of the VO_2-based metamaterial device has been optimized for optimal broadband terahertz transmission and found to be *50 μm*. The transmission characteristics at t_p=*50 μm* show high bandwidth with a flat transmission response between the range of 1.05 THz to 1.35 THz, as seen in Figure A2(a). As the thickness of the polyimide further increases, the FWHM significantly enhances, but the flatness of the band will be compromised. Figure A2(b) illustrates the relationship between the FWHM and the spacer thickness, demonstrating that an increase in thickness leads to a corresponding increase in the FWHM. For fabrication purposes, we have chosen an optimized design with a spacer thickness of 50 μm, where the FWHM is relatively higher, and the transmission band remains reasonably flat compared to other thicknesses of the spacer. An important conclusion can also be drawn here regarding the mismatch in FWHM observed from simulated results and calculated from THz-TDS. This discrepancy arises because, for the simulation, we used a spacer thickness (t_p) of *50 μm*, while the actual polyimide layer used might deviate slightly from this exact thickness. This deviation

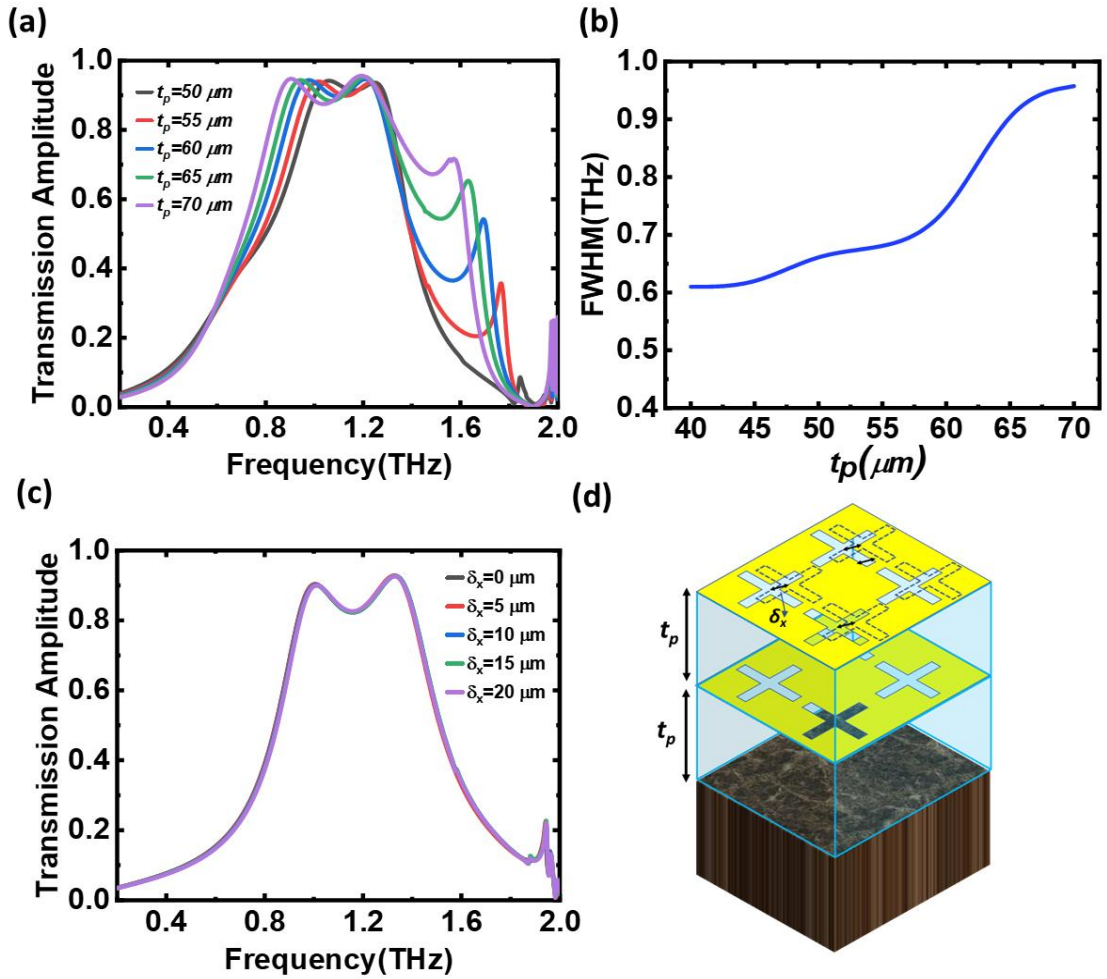

Figure A2: (a) Transmission spectrum with respect to the thickness of the spacer, highlighting the optimized spacer thickness of 50 μm. (b) FWHM of multistacked MM w.r.t spacer thickness. (c) Transmission spectrum with respect to the relative positions of the resonators. Each resonator is shifted by small distances from the center of the metamaterial's resonator, indicating that the transmission amplitude is largely independent of the resonators' positions. (d) A 3D view of the resonators shifted with respect to the center of the resonators, visually illustrating the experimental setup and findings.

is a possible reason for the enhancement of the FWHM in the fabricated metamaterial.

However, to verify this, we fabricated an additional hybrid multi-stacked metamaterial sample with more precise control over the polyimide spacer thickness (as shown in Figure A3), targeting the simulation-optimized thickness of 50 µm. Figures A3(a) and A3(b) show the simulated and experimentally calculated terahertz response of the hybrid multi-stacked metamaterial that we have reported in the manuscript, while Figures A3(c) and A3(d) show the

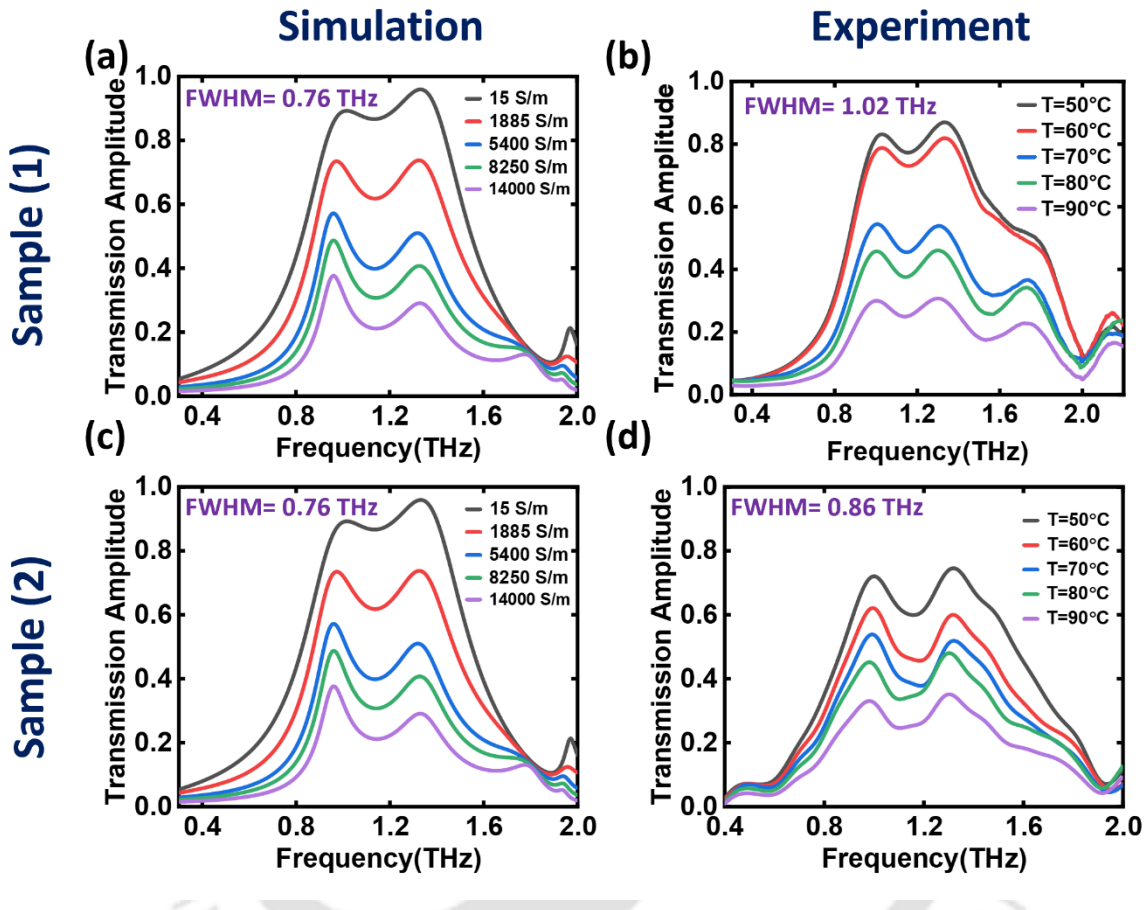

Figure A3: Simulated and experimental terahertz transmission of hybrid multi-stacked metamaterial samples. (a, b) Sample (1) with varying VO_2 conductivity and temperature. (c, d) Sample (2) with improved spacer thickness control, showing better agreement between simulation and experiment.

simulated and experimentally calculated response of one more extra sample (sample (2)). Characterization of this newly fabricated sample showed an FWHM of 0.86 THz (FWHM from the sample (1) is 1.02 THz), which is significantly closer to the simulated value of 0.76 THz.

From the comparison of these two samples, we can conclude that if the thickness of the spacer is precisely controlled, the FWHM can be improved to match the simulation results. Apart from spacer thickness, other factors such as fabrication imperfections, potential variations in resonator dimensions (e.g., changes in width or length of resonators), slight discrepancies in material parameters (VO_2, quartz substrate, and metallic layers), plasmonic losses from the metallic resonators, and minor defects introduced during the multi-step photolithography process also influence the FWHM. Despite these challenges, our results confirm that improved control of the spacer thickness substantially narrows the gap between experimental and simulated responses.

In order to see the effect of the resonator's position on the broadband transmission, we have simulated the multi-stacked structure with a shifted position of the resonators. We translate the

upper resonator with the small distances δ_x(in μm) from the center of each resonator (see Figure A3(d)). Figure A3(c) shows the transmission amplitude for the shifted resonator. It is clear that the transmission responses are approximately similar for all the cases. It shows that the position of the resonator does not affect the transmission response; therefore, the exact alignment of the resonators is not required, which significantly reduces the complexity of fabricating the multi-layer structure.

APPENDIX B

B1. Machine Learning details:

In this experiment, we investigated the application of different machine learning models for multi-output regression tasks. We aimed to predict numerous target variables from a collection of input features using a different regression model and then assess their effectiveness. Additionally, we studied the inverse problem, in which we swapped the roles of inputs and outputs to check how well the models predicted the original inputs from the desired outputs. Finally, we applied our technique to an unknown dataset to forecast previously undetected data points. The complete steps are:

Step (1). Load and Pre-process Data:

1. Load the dataset D from the *data_path.*
2. Split the dataset D into *inputs* X and *Output* Y with a ratio of 70:30, i.e., we used 70% of the datasets for training and 30% for testing.

$$\text{X} = \{x_1, x_2, \dots, x_n\}, \text{Y} = \{y_1, y_2, \dots, y_n\}$$

3. Standardize the *inputs* using *StandardScalar*

$$X_{scaled} = StandardScalar(X)$$

Step (2). Model Selection: Define the following regression models using Multi Output Regressor:

- Ridge Regression $\hat{Y} = Ridge(X)$
- Support Vector Regression (SVR) $\hat{Y} = SVR(X)$
- Random Forest Regressor $\hat{Y} = RandomForest(X)$
- XGBoost Regressor $\hat{Y} = XGBoost(X)$
- Neural Network (MLPRegressor) $\hat{Y} = MLPRegressor(X)$

Step (3). Cross-Validation Setup:

1. Initialize KFold with 10 splits and shuffle the data.
2. Create placeholders for storing predictions and errors.

Step (4). Perform Cross Validation for the Original Problem: For each model in classifiers:

1. Perform 10-fold cross-validation using cross_val_predict.

$$\hat{Y}_{ev} = cross\_val\_predict(model, X_{scaled}, Y, cv = 10)$$

2. Perform the evaluation using the below metrics:
    I. The Mean Absolute Error (MAE) for each target variable:

$$MAE = \frac{(\sum_i^n |y_i - \hat{y}_i|)}{n}$$

Where:

y_i represents the observed values,

$\hat{y}_i$ represents the predicted values,

n is the number of observations.

II. The R-squared for or each target variable

$$R^2 = 1 - \left(\frac{SS_{res}}{SS_{tot}}\right)$$

Where:

R^2 is the coefficient of determination.

SS_{Res} (sum of squares of residuals) is the sum of the squares of the prediction errors.

SS_{tot} (total sum of squares) relates to the total variance in the observed data.

III. The RMSE or each target variable

$$\text{RMSE} = \sqrt{\frac{\Sigma(y_i - \hat{y}_i)^2}{n}}$$

Where:

y_i represents the observed values,

$\hat{y}_i$ represents the predicted values,

n is the number of observations.

3. Store predictions and errors.
4. Save predictions to an Excel file.

Step (5). Inverse Problem Analysis:

1. Swap inputs and outputs to create input_inverse X_{in} and outputs_inverse Y_{in}.

$$X_{in} = Y\ , Y_{in} = X$$

2. Standardize *inputs_inverse.*

$$X_{inv\_scaled} = StandardScalar(X_{inv})$$

3. Repeat the cross_validation process for the inverse problem

$$\widehat{Y_{inv\_cv}} = cross\_val\_predict(model\ , X_{inv_{scaled}}, Y_{inv}\ , cv = 10$$

4. Save inverse predictions to an Excel file

Step (6). Save the Lowest Error Points

1. Define a function save_lowest_error_points to identify and save the five points with the lowest prediction errors.
2. Apply this function to both original and inverse problem results for each model.

Step (7). Predict Unknown Data Points

1. Load the unknown data $D_{unknown}$ from unknown_data_path.
2. Standardize the unknown data to match the training input structure.

$$X_{unknown\_scaled} = StandardScalar(X_{unknown})$$

3. Train the Neural Network model on the entire original dataset.

$$\text{Model.fit}\ (X_{scaled}, Y)$$

4. Predict the outputs for the unknown data points.

$$\widehat{Y_{unknown}} = model.predict(X_{unknown_{scaled}})$$

5. Save the predictions to an Excel file.

Step (8). Calculate Average Performance Metrics

1. Calculate the average MAE, R^2 and RMSE across all folds for each model.

$$MAE = \frac{(\sum_i^n |y_i - \hat{y}_i|)}{n}$$

$$R^2 = 1 - \left(\frac{SS_{res}}{SS_{tot}}\right)$$

$$\text{RMSE} = \sqrt{\frac{\Sigma(y_i - \hat{y}_i)^2}{n}}$$

2. Compare and analyse the average performance for each model for both original and inverse problems.

B2. Experimental Setup and Model selection for the ML methods.

The studies were carried out using a high-performance computing system equipped with an NVIDIA GeForce RTX 4090 GPU and 16 GB of dedicated graphics memory. This GPU is installed in a TITAN GT77HX 13VI workstation, which ensures peak performance and efficiency. The fast GPU accelerated the training and evaluation of various machine learning models, including complicated neural networks by allowing for the processing of massive datasets and computationally hard jobs. The arrangement ensured that the tests were carried out with high precision and in an acceptable timeframe by allowing for extensive cross-validation and regression model analysis. The improved hardware capabilities considerably increased the efficiency and effectiveness of the experimental processes and delivered consistent and reproducible findings. Additionally, various tools and libraries were utilized to implement, analyse, and validate machine learning models. In our experimentation, machine learning models were implemented using "*MultiOutputRegressor*" function from scikit-learn to handle the multi-output nature of the task. Table B1. provides a clear overview of the tools and libraries used in our research.

Table B1. Summarization of the used tools

S. No.	Tools	Purpose	Description
1.	Python	Basic Programming Language	Scripting and implementing machine learning models.
2.	Pandas	Data Manipulation & Analysis	Handling data operations such as loading, manipulating, and analysing datasets.

3.	NumPy	Numerical Computing	Supporting array operations and numerical calculations for data processing.
4.	Scikit-Learn	Machine Learning Framework	Implementing machine learning models, cross-validation, and data preprocessing.
5.	Jupyter Notebook	Interactive Coding Environment	Providing an environment for coding, testing, and documenting the experiments.

B2.1. Model Selection

We applied multiple regression models and evaluated their performance on the collected datasets. Table B2. highlights the initialized parameters of the machine learning models.

B2.1.1. Ridge Regression

Ridge Regression is a linear regression model [87]. It enables the model to predict several target variables at once by creating multiple ridge regression models for each output. Ridge Regression is particularly effective when the input features are highly correlated.

B2.1.2. Support Vector Regression (SVR)

SVR is a powerful kernel-based method [90]. It maps the input data into a higher-dimensional space by using a linear kernel, where a linear relationship can best approximate the outputs.

B2.1.3. Random Forest Regressor

Random Forest is an ensemble learning method that constructs a multitude of decision trees during training and outputs the average prediction of the individual trees [89]. The Random Forest regressor can handle complex and non-linear task.

B2.1.4. XGBoost Regressor

XGBoost is a scalable and efficient gradient boosting technique [92]. It works by combining the predictions of multiple weak learners (decision trees in this case) to produce a strong learner.

Table B2. Initialized Model Parameters of Machine Learning Models

S. No.	Model	Parameters
1.	Ridge	alpha (default=1.0), fit intercept (default=True), normalize (default=False), random state (default=None)
2.	SVR	kernel (default='rbf'), degree (default=3), gamma (default='scale'), C (default=1.0), epsilon (default=0.1)
3.	RandomForest	n_estimators (default=100), criterion (default='squared_error'), max_depth (default=None), random_state (default=None)
4	XGBoost	n_estimators (default=100), learning rate (default=0.1), max_depth (default=3), random state (default=None)

B2.1.5. Neural Network (MLPRegressor)

In our study we applied a Multi-Layer Perceptron (MLP) Regressor, which consists of multiple layers of interconnected neurons [93]. Each neuron applies a non-linear activation function to its inputs, which allow the network to capture complex and non-linear relationships in the data. The architecture chosen for this experiment included two hidden layers with 128 and 64 neurons, respectively, and utilized the ReLU activation function and the model was trained using the Adam optimizer. The initialized parameters details are highlighted in Table B3.

Table B3. Initialized Model Parameters of Neural Network Models

Layer Type	**Parameters**
Input Layer	Number of features: 100
Hidden Layer 1	Number of neurons: 128, Activation function: ReLU
Hidden Layer 2	Number of neurons: 64, Activation function: ReLU
Output Layer	Number of outputs: 7
Training Configuration	Solver: Adam, Learning rate: Adaptive, Max iterations: 500, Random state: 42

References:

[1] A. Barrios-Ulloa, P. P. Ariza-Colpas, H. Sánchez-Moreno, A. P. Quintero-Linero, and E. De la Hoz-Franco, "Modeling radio wave propagation for wireless sensor networks in vegetated environments: A systematic literature review," *Sensors,* vol. 22, no. 14, p. 5285, 2022.

[2] T. Kim Geok *et al.*, "Review of indoor positioning: Radio wave technology," *Applied Sciences,* vol. 11, no. 1, p. 279, 2020.

[3] A. A. Eteng, H. H. Goh, S. K. A. Rahim, and A. Alomainy, "A review of metasurfaces for microwave energy transmission and harvesting in wireless powered networks," *IEEE Access,* vol. 9, pp. 27518-27539, 2021.

[4] X. Zhu, K. Jin, Q. Hui, W. Gong, and D. Mao, "Long-range wireless microwave power transmission: A review of recent progress," *IEEE Journal of Emerging and Selected Topics in Power Electronics,* vol. 9, no. 4, pp. 4932-4946, 2020.

[5] J. A. Sobrino, F. Del Frate, M. Drusch, J. C. Jiménez-Muñoz, P. Manunta, and A. Regan, "Review of thermal infrared applications and requirements for future high-resolution sensors," *IEEE Transactions on Geoscience and Remote Sensing,* vol. 54, no. 5, pp. 2963-2972, 2016.

[6] A. Rogalski and K. Chrzanowski, "Infrared devices and techniques (revision)," *Metrology and Measurement Systems,* vol. 21, no. 4, pp. 565-618, 2014.

[7] S. U. Rehman, S. Ullah, P. H. J. Chong, S. Yongchareon, and D. Komosny, "Visible light communication: A system perspective—Overview and challenges," *Sensors,* vol. 19, no. 5, p. 1153, 2019.

[8] P. H. Pathak, X. Feng, P. Hu, and P. Mohapatra, "Visible light communication, networking, and sensing: A survey, potential and challenges," *IEEE communications surveys & tutorials,* vol. 17, no. 4, pp. 2047-2077, 2015.

[9] M. Mosayebnia, M. Ahmadi, M. Emzhik, and M. Hajiramezanali, "Gamma-ray involved in cancer therapy and imaging," in *Electromagnetic Waves-Based Cancer Diagnosis and Therapy*: Elsevier, 2023, pp. 295-345.

[10] C. Sirtori, "Bridge for the terahertz gap," *Nature,* vol. 417, no. 6885, pp. 132-133, 2002.

[11] F. H. Feres *et al.*, "Graphene nano-optics in the terahertz gap," *Nano letters,* vol. 23, no. 9, pp. 3913-3920, 2023.

[12] R. Kleiner, "Filling the terahertz gap," *Science,* vol. 318, no. 5854, pp. 1254-1255, 2007.

[13] A. Y. Pawar, D. D. Sonawane, K. B. Erande, and D. V. Derle, "Terahertz technology and its applications," *Drug invention today,* vol. 5, no. 2, pp. 157-163, 2013.

[14] M. Perenzoni and D. J. Paul, *Physics and applications of terahertz radiation*. Springer, 2014.

[15] D. Dragoman and M. Dragoman, "Terahertz fields and applications," *Progress in quantum electronics,* vol. 28, no. 1, pp. 1-66, 2004.

[16] Y. Jiang *et al.*, "Machine learning and application in terahertz technology: A review on achievements and future challenges," *IEEE Access,* vol. 10, pp. 53761-53776, 2022.

[17] S. K. Mathanker, P. R. Weckler, and N. Wang, "Terahertz (THz) applications in food

and agriculture: A review," *Transactions of the ASABE,* vol. 56, no. 3, pp. 1213-1226, 2013.

[18] Z. Chen *et al.*, "A survey on terahertz communications," *China Communications,* vol. 16, no. 2, pp. 1-35, 2019.

[19] L. Xie, Y. Yao, and Y. Ying, "The application of terahertz spectroscopy to protein detection: a review," *Applied Spectroscopy Reviews,* vol. 49, no. 6, pp. 448-461, 2014.

[20] G. Tzydynzhapov, P. Gusikhin, V. Muravev, A. Dremin, Y. Nefyodov, and I. Kukushkin, "New real-time sub-terahertz security body scanner," *Journal of Infrared, Millimeter, and Terahertz Waves,* vol. 41, pp. 632-641, 2020.

[21] M. C. Kemp, P. Taday, B. E. Cole, J. Cluff, A. J. Fitzgerald, and W. R. Tribe, "Security applications of terahertz technology," in *Terahertz for military and security applications*, 2003, vol. 5070: SPIE, pp. 44-52.

[22] G. Valušis, A. Lisauskas, H. Yuan, W. Knap, and H. G. Roskos, "Roadmap of terahertz imaging 2021," *Sensors,* vol. 21, no. 12, p. 4092, 2021.

[23] T. Bowman *et al.*, "Pulsed terahertz imaging of breast cancer in freshly excised murine tumors," *Journal of biomedical optics,* vol. 23, no. 2, pp. 026004-026004, 2018.

[24] A. Ion *et al.*, "Metamaterial mechanisms," in *Proceedings of the 29th annual symposium on user interface software and technology*, 2016, pp. 529-539.

[25] T. J. Cui, D. R. Smith, and R. Liu, *Metamaterials*. Springer, 2010.

[26] P. K. Choudhury, *Metamaterials: technology and applications*. CRC Press, 2021.

[27] D. D. Paul, "Optical metamaterials: fundamentals and applications," ed: American Institute of Physics, 2010.

[28] R. Balafendiev, C. Simovski, A. J. Millar, and P. Belov, "Wire metamaterial filled metallic resonators," *Physical Review B,* vol. 106, no. 7, p. 075106, 2022.

[29] J. B. Pendry, A. Holden, W. Stewart, and I. Youngs, "Extremely low frequency plasmons in metallic mesostructures," *Physical review letters,* vol. 76, no. 25, p. 4773, 1996.

[30] J. Pendry, A. Holden, D. Robbins, and W. Stewart, "IEEE Trans. Microwave Theory Tech," *IEEE Trans. Microwave Theory Tech,* vol. 47, no. 2075, 1999.

[31] W. Padilla, M. Aronsson, C. Highstrete, M. Lee, A. J. Taylor, and R. Averitt, "Electrically resonant terahertz metamaterials: Theoretical and experimental investigations," *Physical Review B—Condensed Matter and Materials Physics,* vol. 75, no. 4, p. 041102, 2007.

[32] D. Schurig, J. Mock, and D. Smith, "Electric-field-coupled resonators for negative permittivity metamaterials," *Applied physics letters,* vol. 88, no. 4, 2006.

[33] C. Imhof and R. Zengerle, "Pairs of metallic crosses as a left-handed metamaterial with improved polarization properties," *Optics express,* vol. 14, no. 18, pp. 8257-8262, 2006.

[34] N.-H. Shen, T. Koschny, M. Kafesaki, and C. M. Soukoulis, "Optical metamaterials with different metals," *Physical Review B—Condensed Matter and Materials Physics,* vol. 85, no. 7, p. 075120, 2012.

[35] G. Dolling, M. Wegener, C. M. Soukoulis, and S. Linden, "Negative-index metamaterial at 780 nm wavelength," *Optics letters,* vol. 32, no. 1, pp. 53-55, 2006.

[36] T.-J. Yen *et al.*, "Terahertz magnetic response from artificial materials," *science,* vol. 303, no. 5663, pp. 1494-1496, 2004.

[37] A. D. Boardman *et al.*, "Active and tunable metamaterials," *Laser & Photonics Reviews,* vol. 5, no. 2, pp. 287-307, 2011.

[38] W. Withayachumnankul and D. Abbott, "Metamaterials in the terahertz regime," *IEEE Photonics Journal,* vol. 1, no. 2, pp. 99-118, 2009.

[39] T. Gundogdu *et al.*, "Experimental demonstration of negative magnetic permeability in the far-infrared frequency regime," *Applied physics letters,* vol. 89, no. 8, 2006.

[40] X. Wei, C. Ren, B. Liu, Y. Peng, and S. Zhuang, "The theory, technology, and application of terahertz metamaterial biosensors: a review," *Fundamental Research,* 2024.

[41] W. J. Padilla, A. J. Taylor, C. Highstrete, M. Lee, and R. D. Averitt, "Dynamical electric and magnetic metamaterial response at terahertz frequencies," *Physical review letters,* vol. 96, no. 10, p. 107401, 2006.

[42] H.-T. Chen, W. J. Padilla, J. M. Zide, A. C. Gossard, A. J. Taylor, and R. D. Averitt, "Active terahertz metamaterial devices," *Nature,* vol. 444, no. 7119, pp. 597-600, 2006.

[43] S. Xiao, T. Wang, T. Liu, C. Zhou, X. Jiang, and J. Zhang, "Active metamaterials and metadevices: a review," *Journal of Physics D: Applied Physics,* vol. 53, no. 50, p. 503002, 2020.

[44] J. Li *et al.*, "A Review: Active Tunable Terahertz Metamaterials," *Advanced Photonics Research,* p. 2300351, 2024.

[45] J. H. Ko, Y. J. Yoo, Y. Lee, H.-H. Jeong, and Y. M. Song, "A review of tunable photonics: Optically active materials and applications from visible to terahertz," *IScience,* vol. 25, no. 8, 2022.

[46] W. Zhang *et al.*, "Terahertz metamaterials for biosensing applications: A review," *Biosensors,* vol. 14, no. 1, p. 3, 2023.

[47] T. Tan *et al.*, "Renewable energy harvesting and absorbing via multi-scale metamaterial systems for Internet of things," *Applied Energy,* vol. 254, p. 113717, 2019.

[48] J. He, X. He, T. Dong, S. Wang, M. Fu, and Y. Zhang, "Recent progress and applications of terahertz metamaterials," *Journal of Physics D: Applied Physics,* vol. 55, no. 12, p. 123002, 2021.

[49] W. J. Padilla, D. N. Basov, and D. R. Smith, "Negative refractive index metamaterials," *Materials today,* vol. 9, no. 7-8, pp. 28-35, 2006.

[50] B. S. Chouhan, B. Barman, L. K. Vaswani, A. Panwar, and G. Kumar, "Broadening of resonance with the bending of strongly coupled strip resonators in a planar terahertz metamaterial," *Journal of Lightwave Technology,* 2024.

[51] B. Singh Chouhan, N. Acharyya, A. Panwar, D. Roy Chowdhury, and G. Kumar, "Multi-stacked polarization insensitive broadband terahertz metamaterial," *Journal of Applied Physics,* vol. 135, no. 17, 2024.

[52] K. Yang, S. Liu, S. Arezoomandan, A. Nahata, and B. Sensale-Rodriguez, "Graphene-based tunable metamaterial terahertz filters," *Applied Physics Letters,* vol. 105, no. 9, 2014.

[53] H. Ou, F. Lu, Y. Liao, F. Zhu, and Y.-S. Lin, "Tunable terahertz metamaterial for high-

efficiency switch application," *Results in Physics,* vol. 16, p. 102897, 2020.

[54] F. Lu, H. Ou, Y. Liao, F. Zhu, and Y.-S. Lin, "Actively switchable terahertz metamaterial," *Results in Physics,* vol. 15, p. 102756, 2019.

[55] A. Bhattacharya, R. Sarkar, N. K. Sharma, B. K. Bhowmik, A. Ahmad, and G. Kumar, "Multiband transparency effect induced by toroidal excitation in a strongly coupled planar terahertz metamaterial," *Scientific reports,* vol. 11, no. 1, p. 19186, 2021.

[56] M. Gupta, Y. K. Srivastava, M. Manjappa, and R. Singh, "Sensing with toroidal metamaterial," *Applied Physics Letters,* vol. 110, no. 12, 2017.

[57] B. K. K. Bhowmik, R. KM, S. John, S. S. Prabhu, and G. Kumar, "High-quality factor Quasi-BIC mode via selective symmetry-breaking approach in a terahertz metasurface," *New Journal of Physics,* 2024.

[58] T. Chen, D. Zhang, F. Huang, Z. Li, and F. Hu, "Design of a terahertz metamaterial sensor based on split ring resonator nested square ring resonator," *Materials Research Express,* vol. 7, no. 9, p. 095802, 2020.

[59] M. Li, W. Li, H. Li, Y. Zhu, and Y. Yu, "Controllable design of super-oscillatory lenses with multiple sub-diffraction-limit foci," *Scientific Reports,* vol. 7, no. 1, p. 1335, 2017.

[60] J. Neu, B. Krolla, O. Paul, B. Reinhard, R. Beigang, and M. Rahm, "Metamaterial-based gradient index lens with strong focusing in the THz frequency range," *Optics express,* vol. 18, no. 26, pp. 27748-27757, 2010.

[61] F. Gaufillet, S. Marcellin, and E. Akmansoy, "Dielectric metamaterial-based gradient index lens in the terahertz frequency range," *IEEE Journal of selected topics in Quantum Electronics,* vol. 23, no. 4, pp. 1-5, 2016.

[62] H.-T. Chen, W. J. Padilla, M. J. Cich, A. K. Azad, R. D. Averitt, and A. J. Taylor, "A metamaterial solid-state terahertz phase modulator," *Nature photonics,* vol. 3, no. 3, pp. 148-151, 2009.

[63] K. Dhriti, A. K. Chowdhary, B. S. Chouhan, D. Sikdar, and G. Kumar, "Tunable terahertz absorption modulation in graphene nanoribbon-assisted dielectric metamaterial," *Journal of Physics D: Applied Physics,* vol. 55, no. 28, p. 285101, 2022.

[64] R. Degl'Innocenti, H. Lin, and M. Navarro-Cía, "Recent progress in terahertz metamaterial modulators," *Nanophotonics,* vol. 11, no. 8, pp. 1485-1514, 2022.

[65] A. K. Azad, A. J. Taylor, E. Smirnova, and J. F. O'Hara, "Characterization and analysis of terahertz metamaterials based on rectangular split-ring resonators," *Applied Physics Letters,* vol. 92, no. 1, 2008.

[66] C. Sabah, B. Mulla, H. Altan, and L. Ozyuzer, "Thermally and optically tunable sub-terahertz superconducting fishnet metamaterial," *Physica C: Superconductivity and its Applications,* vol. 544, pp. 46-53, 2018.

[67] A. Gopinath, S. V. Boriskina, N.-N. Feng, B. r. M. Reinhard, and L. D. Negro, "Photonic-plasmonic scattering resonances in deterministic aperiodic structures," *Nano letters,* vol. 8, no. 8, pp. 2423-2431, 2008.

[68] V. G. Achanta, "Plasmonic quasicrystals," *Progress in Quantum Electronics,* vol. 39, pp. 1-23, 2015.

[69] S. Pandey, B. Gupta, S. Mujumdar, and A. Nahata, "Direct observation of Anderson localization in plasmonic terahertz devices," *Light: Science & Applications,* vol. 6, no.

3, pp. e16232-e16232, 2017.

[70] S. Kasture *et al.*, "Plasmonic quasicrystals with broadband transmission enhancement," *Scientific reports,* vol. 4, no. 1, p. 5257, 2014.

[71] Y. Yuan *et al.*, "Dual-band planar electric metamaterial in the terahertz regime," *Optics Express,* vol. 16, no. 13, pp. 9746-9752, 2008.

[72] D. R. Chowdhury *et al.*, "A broadband planar terahertz metamaterial with nested structure," *Optics express,* vol. 19, no. 17, pp. 15817-15823, 2011.

[73] F. Miyamaru *et al.*, "Terahertz electric response of fractal metamaterial structures," *Physical Review B,* vol. 77, no. 4, p. 045124, 2008.

[74] D. Roy Chowdhury, R. Singh, A. J. Taylor, H.-T. Chen, W. Zhang, and A. K. Azad, "Coupling schemes in terahertz planar metamaterials," *International Journal of Optics,* vol. 2012, no. 1, p. 148985, 2012.

[75] W. Yang and Y.-S. Lin, "Tunable metamaterial filter for optical communication in the terahertz frequency range," *Optics Express,* vol. 28, no. 12, pp. 17620-17629, 2020.

[76] O. Rioul, "Shannon's formula W. log (1+ SNR): A historical perspective," in *Colloque Théorie de l'Information: nouvelles frontières dans le cadre du centenaire de Claude Shannon*, 2016.

[77] E. C. Pielou, "Shannon's formula as a measure of specific diversity: its use and misuse," *The American Naturalist,* vol. 100, no. 914, pp. 463-465, 1966.

[78] N. Han, Z. Chen, C. Lim, B. Ng, and M. Hong, "Broadband multi-layer terahertz metamaterials fabrication and characterization on flexible substrates," *Optics express,* vol. 19, no. 8, pp. 6990-6998, 2011.

[79] J. Ruan, F. Lan, L. Wang, and S. Ji, "Ultra-wideband THz metamaterial filter with steep cut-off," *Journal of Electromagnetic Waves and Applications,* vol. 35, no. 4, pp. 431-440, 2021.

[80] S. Lu, L. Hou, and F. Gan, "Preparation and optical properties of phase-change VO2 thin films," *Journal of materials science,* vol. 28, no. 8, pp. 2169-2177, 1993.

[81] C. M. Bingham, H. Tao, X. Liu, R. D. Averitt, X. Zhang, and W. J. Padilla, "Planar wallpaper group metamaterials for novel terahertz applications," *Optics Express,* vol. 16, no. 23, pp. 18565-18575, 2008.

[82] A. Bhattacharya, B. S. Chouhan, R. Singh, B. K. Bhowmik, and G. Kumar, "Polarization independent lattice-coupled terahertz toroidal excitation," *Journal of Physics D: Applied Physics,* vol. 56, no. 41, p. 415101, 2023.

[83] H. Liu, T. Li, S.-m. Wang, and S.-n. Zhu, "Hybridization effect in coupled metamaterials," *Frontiers of Physics in China,* vol. 5, pp. 277-290, 2010.

[84] A. Khaireh-Walieh, D. Langevin, P. Bennet, O. Teytaud, A. Moreau, and P. R. Wiecha, "A newcomer's guide to deep learning for inverse design in nano-photonics," *Nanophotonics,* vol. 12, no. 24, pp. 4387-4414, 2023.

[85] H. Wang, Z. Lei, X. Zhang, B. Zhou, and J. Peng, "Machine learning basics," *Deep learning,* pp. 98-164, 2016.

[86] D. Maulud and A. M. Abdulazeez, "A review on linear regression comprehensive in machine learning," *Journal of Applied Science and Technology Trends,* vol. 1, no. 2, pp. 140-147, 2020.

[87] D. W. Marquardt and R. D. Snee, "Ridge regression in practice," *The American Statistician,* vol. 29, no. 1, pp. 3-20, 1975.

[88] Y.-Y. Song and L. Ying, "Decision tree methods: applications for classification and prediction," *Shanghai archives of psychiatry,* vol. 27, no. 2, p. 130, 2015.

[89] L. Breiman, "Random forests," *Machine learning,* vol. 45, pp. 5-32, 2001.

[90] M. A. Hearst, S. T. Dumais, E. Osuna, J. Platt, and B. Scholkopf, "Support vector machines," *IEEE Intelligent Systems and their applications,* vol. 13, no. 4, pp. 18-28, 1998.

[91] Z. Zhang, "Introduction to machine learning: k-nearest neighbors," *Annals of translational medicine,* vol. 4, no. 11, 2016.

[92] T. Chen and C. Guestrin, "Xgboost: A scalable tree boosting system," in *Proceedings of the 22nd acm sigkdd international conference on knowledge discovery and data mining*, 2016, pp. 785-794.

[93] F. Murtagh, "Multilayer perceptrons for classification and regression," *Neurocomputing,* vol. 2, no. 5-6, pp. 183-197, 1991.

[94] A. Taflove and M. E. Brodwin, "Numerical solution of steady-state electromagnetic scattering problems using the time-dependent Maxwell's equations," *IEEE transactions on microwave theory and techniques,* vol. 23, no. 8, pp. 623-630, 1975.

[95] N. M. Burford and M. O. El-Shenawee, "Review of terahertz photoconductive antenna technology," *Optical Engineering,* vol. 56, no. 1, pp. 010901-010901, 2017.

[96] Y. Shen *et al.*, "Generation and detection of ultrabroadband terahertz radiation using photoconductive emitters and receivers," *Applied Physics Letters,* vol. 85, no. 2, pp. 164-166, 2004.

[97] A. Schneider, M. Neis, M. Stillhart, B. Ruiz, R. U. Khan, and P. Günter, "Generation of terahertz pulses through optical rectification in organic DAST crystals: theory and experiment," *JOSA B,* vol. 23, no. 9, pp. 1822-1835, 2006.

[98] Y.-S. Lee, *Principles of terahertz science and technology*. Springer Science & Business Media, 2009.

[99] J. Neu and C. A. Schmuttenmaer, "Tutorial: An introduction to terahertz time domain spectroscopy (THz-TDS)," *Journal of Applied Physics,* vol. 124, no. 23, 2018.

[100] W. Withayachumnankul and M. Naftaly, "Fundamentals of measurement in terahertz time-domain spectroscopy," *Journal of Infrared, Millimeter, and Terahertz Waves,* vol. 35, pp. 610-637, 2014.

[101] P. C. Planken, H.-K. Nienhuys, H. J. Bakker, and T. Wenckebach, "Measurement and calculation of the orientation dependence of terahertz pulse detection in ZnTe," *JOSA B,* vol. 18, no. 3, pp. 313-317, 2001.

[102] X. Su *et al.*, "Dynamic mode coupling in terahertz metamaterials," *Scientific reports,* vol. 5, no. 1, p. 10823, 2015.

[103] R. Yahiaoui *et al.*, "Electromagnetically induced transparency control in terahertz metasurfaces based on bright-bright mode coupling," *Physical Review B,* vol. 97, no. 15, p. 155403, 2018.

[104] T.-T. Kim *et al.*, "Electrically tunable slow light using graphene metamaterials," *Acs Photonics,* vol. 5, no. 5, pp. 1800-1807, 2018.

[105] J. Souza, L. Cabral, R. Oliveira, and C. Villas-Boas, "Electromagnetically-induced-transparency-related phenomena and their mechanical analogs," *Physical Review A,* vol. 92, no. 2, p. 023818, 2015.

[106] H. Tuononen, E. Gornov, J. A. Zeitler, J. Aaltonen, and K.-E. Peiponen, "Using modified Kramers–Kronig relations to test transmission spectra of porous media in THz-TDS," *Optics letters,* vol. 35, no. 5, pp. 631-633, 2010.

[107] Z. Li and Y. J. Ding, "Terahertz broadband-stop filters," *IEEE Journal of Selected Topics in Quantum Electronics,* vol. 19, no. 1, pp. 8500705-8500705, 2012.

[108] A. Pattanayak, S. Roy, G. Rana, S. P. Duttagupta, V. G. Achanta, and S. Prabhu, "Study of THz-Plasmon hybridization of a loop Yagi-Uda absorber," *Scientific Reports,* vol. 7, no. 1, p. 16961, 2017.

[109] H. Li, J. Wang, X. Wang, Y. Feng, and Z. Sun, "Design and characterization of wideband terahertz metamaterial stop-band filter," *Micromachines,* vol. 13, no. 7, p. 1034, 2022.

[110] S. Zhou, L. Liu, Q. Deng, S. Liao, Q. Xue, and M. Chan, "Intercoupling of cascaded metasurfaces for broadband spectral scalability," *Materials,* vol. 16, no. 5, p. 2013, 2023.

[111] L. Fu, H. Schweizer, H. Guo, N. Liu, and H. Giessen, "Synthesis of transmission line models for metamaterial slabs at optical frequencies," *Physical Review B—Condensed Matter and Materials Physics,* vol. 78, no. 11, p. 115110, 2008.

[112] Z. Han, K. Kohno, H. Fujita, K. Hirakawa, and H. Toshiyoshi, "Tunable terahertz filter and modulator based on electrostatic MEMS reconfigurable SRR array," *IEEE Journal of Selected Topics in Quantum Electronics,* vol. 21, no. 4, pp. 114-122, 2014.

[113] M. T. Nouman, H.-W. Kim, J. M. Woo, J. H. Hwang, D. Kim, and J.-H. Jang, "Terahertz modulator based on metamaterials integrated with metal-semiconductor-metal varactors," *Scientific reports,* vol. 6, no. 1, p. 26452, 2016.

[114] S. H. Lee, H.-D. Kim, H. J. Choi, B. Kang, Y. R. Cho, and B. Min, "Broadband modulation of terahertz waves with non-resonant graphene meta-devices," *IEEE Transactions on Terahertz Science and Technology,* vol. 3, no. 6, pp. 764-771, 2013.

[115] N. A. Butakov *et al.*, "Broadband electrically tunable dielectric resonators using metal–insulator transitions," *Acs Photonics,* vol. 5, no. 10, pp. 4056-4060, 2018.

[116] H. Liu, J. Lu, and X. R. Wang, "Metamaterials based on the phase transition of VO2," *Nanotechnology,* vol. 29, no. 2, p. 024002, 2017.

[117] T. Cocker *et al.*, "Terahertz conductivity of the metal-insulator transition in a nanogranular VO2 film," *Applied Physics Letters,* vol. 97, no. 22, 2010.

[118] J. Lourembam, A. Srivastava, C. La-o-vorakiat, H. Rotella, T. Venkatesan, and E. E. Chia, "New insights into the diverse electronic phases of a novel vanadium dioxide polymorph: a terahertz spectroscopy study," *Scientific Reports,* vol. 5, no. 1, p. 9182, 2015.

[119] D.-x. Zhou, E. P. Parrott, D. J. Paul, and J. A. Zeitler, "Determination of complex refractive index of thin metal films from terahertz time-domain spectroscopy," *Journal of Applied Physics,* vol. 104, no. 5, 2008.

[120] M. Walther, D. Cooke, C. Sherstan, M. Hajar, M. Freeman, and F. Hegmann, "Terahertz conductivity of thin gold films at the metal-insulator percolation transition," *Physical*

Review B, vol. 76, no. 12, p. 125408, 2007.

[121] Y. Luo *et al.*, "Terahertz conductivities of VO2 thin films grown under different sputtering gas pressures," *Journal of Alloys and Compounds,* vol. 655, pp. 442-447, 2016.

[122] Y. Huang *et al.*, "Phase transition analysis of thermochromic VO2 thin films by temperature-dependent Raman scattering and ellipsometry," *Applied Surface Science,* vol. 456, pp. 545-551, 2018.

[123] M. Lu, W. Li, and E. R. Brown, "Second-order bandpass terahertz filter achieved by multilayer complementary metamaterial structures," *Optics letters,* vol. 36, no. 7, pp. 1071-1073, 2011.

[124] Y.-J. Chiang, C.-S. Yang, Y.-H. Yang, C.-L. Pan, and T.-J. Yen, "An ultrabroad terahertz bandpass filter based on multiple-resonance excitation of a composite metamaterial," *Applied Physics Letters,* vol. 99, no. 19, 2011.

[125] F. Hu *et al.*, "Electrically triggered tunable terahertz band-pass filter based on VO 2 hybrid metamaterial," *IEEE Journal of Selected Topics in Quantum Electronics,* vol. 25, no. 3, pp. 1-7, 2018.

[126] S. Chase and R. Joseph, "Resonant array bandpass filters for the far infrared," *Applied optics,* vol. 22, no. 11, pp. 1775-1779, 1983.

[127] F. Hu *et al.*, "Broadband large-modulation-depth low-current-triggered terahertz intensity modulator based on VO2 embedded hybrid metamaterials," *Applied Physics Express,* vol. 11, no. 9, p. 092004, 2018.

[128] Z. Yang, C. Ko, V. Balakrishnan, G. Gopalakrishnan, and S. Ramanathan, "Dielectric and carrier transport properties of vanadium dioxide thin films across the phase transition utilizing gated capacitor devices," *Physical Review B,* vol. 82, no. 20, p. 205101, 2010.

[129] V. Sanphuang, N. Ghalichechian, N. K. Nahar, and J. L. Volakis, "Equivalent circuit for VO2 phase change material film in reconfigurable frequency selective surfaces," *Applied Physics Letters,* vol. 107, no. 25, 2015.

[130] L. Fu, H. Schweizer, H. Guo, N. Liu, and H. Giessen, "Synthesis of transmission line models for metamaterial slabs at optical frequencies," *Physical Review B,* vol. 78, no. 11, p. 115110, 2008.

[131] M. Al-Joumayly and N. Behdad, "A new technique for design of low-profile, second-order, bandpass frequency selective surfaces," *IEEE transactions on antennas and propagation,* vol. 57, no. 2, pp. 452-459, 2009.

[132] K. Marinov, A. Boardman, V. Fedotov, and N. Zheludev, "Toroidal metamaterial," *New Journal of Physics,* vol. 9, no. 9, p. 324, 2007.

[133] D. Zhang *et al.*, "Tunable Optical Properties in Self-Assembled Oxide-Metal Hybrid Thin Films via Au-Phase Geometry Control: From Nanopillars to Nanodisks," *Advanced Optical Materials,* vol. 8, no. 4, p. 1901359, 2020.

[134] J. Huang *et al.*, "Tailorable optical response of Au–LiNbO3 hybrid metamaterial thin films for optical waveguide applications," *Advanced Optical Materials,* vol. 6, no. 19, p. 1800510, 2018.

[135] W. Chen *et al.*, "Broadband solar metamaterial absorbers empowered by transformer-based deep learning," *Advanced Science,* vol. 10, no. 13, p. 2206718, 2023.

[136] J. Xiong *et al.*, "Real-Time On-Demand Design of Circuit-Analog Plasmonic Stack Metamaterials by Divide-and-Conquer Deep Learning," *Laser & Photonics Reviews,* vol. 17, no. 3, p. 2100738, 2023.

[137] A. Challapalli, J. Konlan, and G. Li, "Inverse machine learning discovered metamaterials with record high recovery stress," *International Journal of Mechanical Sciences,* vol. 244, p. 108029, 2023.

[138] L. Wu *et al.*, "A machine learning-based method to design modular metamaterials," *Extreme Mechanics Letters,* vol. 36, p. 100657, 2020.

[139] Y. Wang, Y. Zhu, Z. Cui, H. Jiang, K. Zhang, and X. Wang, "Ensemble learning: a bidirectional framework for designing data-driven THz composite metamaterials," *JOSA B,* vol. 39, no. 3, pp. 835-842, 2022.

[140] K. Donda *et al.*, "Ultrathin acoustic absorbing metasurface based on deep learning approach," *Smart Materials and Structures,* vol. 30, no. 8, p. 085003, 2021.

[141] Y. Chen, J. Zhu, Y. Xie, N. Feng, and Q. H. Liu, "Smart inverse design of graphene-based photonic metamaterials by an adaptive artificial neural network," *Nanoscale,* vol. 11, no. 19, pp. 9749-9755, 2019.

[142] M. Soni and S. Misra, "Machine-learning-assisted design of multiband terahertz metamaterial absorber," *ACS Applied Optical Materials,* vol. 1, no. 10, pp. 1679-1687, 2023.

[143] P. van Assenbergh, E. Meinders, J. Geraedts, and D. Dodou, "Nanostructure and microstructure fabrication: from desired properties to suitable processes," *Small,* vol. 14, no. 20, p. 1703401, 2018.

[144] R. Singh, E. Smirnova, A. J. Taylor, J. F. O'Hara, and W. Zhang, "Optically thin terahertz metamaterials," *Optics express,* vol. 16, no. 9, pp. 6537-6543, 2008.

[145] M. Naftaly and R. E. Miles, "Terahertz time-domain spectroscopy for material characterization," *Proceedings of the IEEE,* vol. 95, no. 8, pp. 1658-1665, 2007.

[146] B. Kanté, S. Burokur, A. Sellier, A. De Lustrac, and J.-M. Lourtioz, "Controlling plasmon hybridization for negative refraction metamaterials," *Physical Review B—Condensed Matter and Materials Physics,* vol. 79, no. 7, p. 075121, 2009.

[147] E. Prodan, C. Radloff, N. J. Halas, and P. Nordlander, "A hybridization model for the plasmon response of complex nanostructures," *science,* vol. 302, no. 5644, pp. 419-422, 2003.

[148] A. Cunningham, S. Mühlig, C. Rockstuhl, and T. Bürgi, "Exciting bright and dark eigenmodes in strongly coupled asymmetric metallic nanoparticle arrays," *The Journal of Physical Chemistry C,* vol. 116, no. 33, pp. 17746-17752, 2012.

[149] X. Guo, Y. Tan, Y. Hu, Z. Zafar, J. Liu, and J. Zou, "High quality VO2 thin films synthesized from V2O5 powder for sensitive near-infrared detection," *Scientific Reports,* vol. 11, no. 1, p. 21749, 2021.

[150] B. Rajeswaran and A. M. Umarji, "Defect engineering of VO2 thin films synthesized by Chemical Vapor Deposition," *Materials Chemistry and Physics,* vol. 245, p. 122230, 2020.

[151] W.-J. Lee and Y.-H. Chang, "Growth without postannealing of monoclinic VO2 thin film by atomic layer deposition using VCl4 as precursor," *Coatings,* vol. 8, no. 12, p. 431, 2018.